

Investigation of impact loads caused by the dynamic effect of falling debris initiating from a design failure scenario in an RC structure.

Master thesis

Kasper Steinbjørn Dyhr & Michael Winther Pedersen



AALBORG UNIVERSITY
STUDENT REPORT

10-6-2020



AALBORG UNIVERSITY
STUDENT REPORT

School of Engineering and science
Structural & Civil engineering
Thomas Manns Vej 23
9220 Aalborg
<http://www.civil.aau.dk/>

Title:

Investigation of impact loads caused by the dynamic effect of falling debris initiating from a design failure scenario in an RC structure.

Project type:

Master thesis

Project period:

February 2020 - June 2020

Authors:

Kasper S. Dyhr
Michael W. Pedersen

Supervisors:

Lars Damkilde
John Dalsgaard Sørensen

Page number: 89

Appendix: 64

Submitted 10-06-2020

Synopsis:

This report investigates a design failure scenario in a RC structure, where a chosen design failure scenario is modelled, after which the loads are compared with the Danish National Annex standard value of vertical replacement load. The chosen design failure scenario is determined from an example building known in the report as the DPCA-building, which is a high-rise building constructed with pre-cast RC elements. To model the design failure scenario in a numerical model, phenomenons such as shear and bending failure is firstly investigated, as well as rebar pullout. The design failure scenario is then simulated in a large numerical model, where the impact loads and reaction forces are determined, such that they can be compared with vertical replacement load. The overall phenomenones found in the complex model is studied further in a parametric study by investigating the design failure scenario using a simple approach with beam elements.

Preface

This Master's thesis in Structural and Civil Engineering at Aalborg University is written by Kasper Steinbjørn Dyhr and Michael Winther Pedersen in the period February 2020 to June 2020. The authors of this report would like to thank our supervisors Lars Damkilde and John Dalsgaard Sørensen. We would also like to thank Jesper Frøbert Jensen for his input on the topic of robustness in structures as well as for the material he provided us about the DPCA-building.

Reading guide

The project consists of a main report and appendices. The main report focuses on highlighting the investigated topics and the results, while the appendices describes some of the procedures in more detail. The appendices are not meant to be read independently but should be read in conjunction with the relevant sections in the main report.

Through the report references to sources are made using the Harvard method. A reference in a sentence is written as the authors name followed by the year of publication. Passive references are written similarly, after a sentence, but with square brackets. In the bibliography the sources are listed in alphabetic order.

Figures and tables are numbered by the chapter they are included in followed by the number of the respective figure or table. For instance the fifth figure in chapter seven is numbered as Figure 7.5. Equations are numbered similarly as figures and tables, and a reference to an equation is written as the number of the equation in parenthesis. For instance the fourth equation in chapter two is referred to as Equation (2.4). At the end of the main report the appendix is located, which are numbered according to the alphabet, meaning that the first appendix is numbered as Appendix A.

Resumé

Denne rapport undersøger et design brud scenarie i en armeret betonkonstruktion der igennem rapporten er omtalt som DPCA-bygningen.

I den initierede del af rapporten undersøges først metoder til at opnå robuste konstruktioner i overensstemmelse med det Danske Nationale Anneks. Heri blev det fundet at der benyttes en vertikal erstatningslast der skal imitere lasten der forekommer i et design brud scenarie. For at undersøge hvor godt denne last stemmer overens med virkeligheden er dette undersøgt nærmere ved brug af et design brud scenarie fra DPCA-bygningen.

Til at modellere design brud scenariet er det kommercielle finite element program Abaqus anvendt. I Abaqus er fænomener såsom forskydningsbrud, bøjningsbrud og udtræk af armering først undersøgt, for at sikre at de enkelte fænomener fungerer, så en model af design brud scenariet kan konstrueres. I simuleringen af design brud scenariet er stødlasten og reaktionskræfterne bestemt, som herefter er omregnet til en ækvivalent statisk last og sammenlignet med den vertikale erstatningslast.

Værdierne af den ækvivalente statiske last viste at den vertikale erstatningslast i nogle tilfælde ikke var tilstrækkelig, og brud kunne derfor forekomme. Resultaterne fra den komplekse model er herefter forsøgt gengivet ved brug af en mere simpel model konstrueret af bjælkeelementer i programmet Abaqus. Den simple model gav resultater der stemte overens med den komplekse model, og viste at der var situationer hvor den vertikale last ikke var tilstrækkelig til at beskrive lasten i design brud scenariet.

Baseret på undersøgelser af nedstyrtningslasten er der desuden blevet observeret fænomener som forekommer grundet den dynamiske stødlast fra det faldende materiale. I øjeblikket hvor det faldende materiale rammer det underliggende dæk, er snitkræfterne i dækket bestemt til at være flere gange højere end den vertikale erstatningslast, men grundet den korte varighed resulterer det kun i et stort omfang af revnedannelser som udbreder sig i hele dækket, uden at resultere i et komplet kollaps.

Desuden ses der store ækvivalente statiske laster når stødlasten er placeret nær understøtningerne, hvorfor der anbefales at anvende forskydningsarmering for at forhindre brud i dette tilfælde. Ud fra energibetragtninger kan det tilmed ses at for det undersøgte design brud scenarie vil det nedfaldende dæk optage en stor del af energien igennem elastisk og plastisk deformation og en mulighed er derfor at øge massen og stivheden af det underliggende dæk, så det nedfaldne dæk vil opnå en så stor skade at det vil bryde under sammenstødet, og derfor reducere stødlasten betragteligt.



Contents

1	Introduction	1
1.1	Problem definition	2
2	Robustness and Eurocodes	3
2.1	Ronan Point	3
2.2	Structural measures for increasing robustness	6
2.3	Eurocode guidelines	10
2.4	Danish National Annex	12
3	DPCA-building	25
3.1	Building properties	25
3.2	Robustness design principles of the DPCA-building	26
3.3	Segmentation and unidentified accidental actions	27
3.4	Selected design failure scenarios and further studies	37
4	Numerical modelling of collapse	39
4.1	Model setup considerations	39
4.2	Numerical modelling of RC elements	41
5	Modelling of a Design Failure Scenario	51
5.1	The Da Vinci collapse	51
5.2	Design Failure Scenario from DPCA-building	55
5.3	DFS without element deletion	57

5.4	DFS with element deletion	62
5.5	DFS with partwise element deletion	64
5.6	Equivalent static loads and parameter study	66
6	Simplified approaches	71
6.1	Beam model in Abaqus	71
6.2	2DOF approach	79
7	Comparison of vertical replacement load	81
7.1	Forces at the time of impact	81
7.2	Eurocode comparison with <i>LESF</i>	84
8	Conclusion	87
9	Discussion	89
	Literature	89

I	Appendix
----------	-----------------

A	Material modelling	95
A.1	Concrete modelling	95
A.2	Testing of material behaviour in Abaqus	100
A.3	Shell and solid element RCB	101
A.4	Modelling of hollow core slab	116
B	Eurocode approach RCB	121
B.1	Analytical RCB model	121
C	Abaqus procedures	127
C.1	Contact behaviour in Abaqus	127

C.2	Damping in dynamic explicit analysis	128
D	Energy and mesh convergence	131
D.1	Da Vinci Failure	131
D.2	Mesh convergence	133
D.3	Butterworth filter	138
E	Design failure scenario	139
E.1	Part-wise element deletion	139
E.2	Parameter study	140
E.3	Simplified beam shear force diagrams	141
E.4	Damage and moment caused by inertia effect	143
F	2DOF and Eurocode approach	145
F.1	Stiffness and Mass of the structure.	145
F.2	Response to Impact load	148
F.3	Eurocode approach of impact loads	154
F.4	Hard and soft impact comparison with 2DOF solution.	156



Nomenclature

The following list encompass the symbols and abbreviations that are emphasised and/or most commonly used throughout this report.

α	Yield surface parameter
$\bar{\sigma}_c(\bar{\varepsilon}_c^{pl}), \bar{\sigma}_t(\bar{\varepsilon}_t^{pl})$	Effective compressive and tensile cohesion stress
$\bar{\sigma}_{max}$	Maximum principal effective stress
\bar{p}	Hydrostatic pressure stress
\bar{q}	Mises equivalent effective stress
β	Yield surface parameter
$\bar{\sigma}$	Effective stress
ϵ	Eccentricity parameter
ν	Poisson ratio
ψ	Dilation angle
ρ	Density
$\sigma_1, \sigma_2, \sigma_3$	Principal stress
σ_c, σ_t	Compression and tension stress
σ_{b0}	Equibiaxial compressive yield strength
σ_{t0}	Uniaxial tensile yield strength
$\bar{\varepsilon}_c^{pl}, \bar{\varepsilon}_t^{pl}$	Equivalent plastic strains
$\bar{\varepsilon}_c^{in}, \bar{\varepsilon}_t^{ck}$	Inelastic and cracking strain
a	Acceleration
d, d_t, d_c	Damage, tensile damage and compression damage
E_0	Undamaged modulus of elasticity
f	Yield surface
$f_{ck, cube}$	Characteristic compression strength on a cube

f_{ck}	Characteristic compression strength on a cylinder
f_{ctk}	Characteristic tensile strength of concrete
G	Flow function
I	Area moment of inertia
K_c	Ratio of second stress invariants
l_b	Anchorage length
M	Moment force
T	Tensile force in rebar
T_I	Time of Initial Impact
u	Displacement
V	Shear force
v	Velocity
ALS	Accidental limit state
B31	Linear Timoshenko Beam Element
C.M	Compression meridian
C3D8R	Eight-node solid element with reduced integration
CDP	Concrete Damage Plasticity
DFS	Design failure scenario
DOF	Degree of freedom
DPCA	Danish Precast Concrete Association
DS	Danish Standard
EN	European Standard
HCS	Hollow core slab
LESF	Local Equivalent Static Force
RCB	Reinforced concrete beam
SC8R	Quadrilateral Continuum Shell element
SLS	Serviceability limit state
T.M	Tensile meridian
ULS	Ultimate limit state
VRL	Vertical Replacement Load
\varnothing	diameter

1. Introduction

Robustness of structures in Denmark is ensured through the rules and guidelines stated in the Eurocodes and the Danish National Annex, in which a set of requirements can be found depending on the consequence class of a structure. One of these requirements specifies the use of design failure scenarios, where part of the building is assumed to be removed due to some unknown event. When investigating the specific design failure scenario, robustness is assured when local failure does not exceed specified limits of collapse, and the structure is proven capable of redistributing the loads. In the design failure scenarios used to prove structural robustness, the dynamic aspects related to falling structural elements are not directly considered, as well as the failed area is assumed to disappear, without having an impact on the remaining structure.

These dynamic aspects are in this project investigated by firstly using a failure scenario which happened recently and near the University, which is referred to as the Da Vinci collapse. Furthermore, to investigate the dynamic effects of falling material in high rise buildings an investigation of the design failure scenarios in a typical multi-storey precast concrete structure is performed. This precast concrete structure has been provided by the Danish Precast Concrete Association, DPCA. The high rise building is throughout this report referred to as the DPCA-building. The overall dimensions of the DPCA-building are illustrated in Figure 1.1.

Analysis of chosen design failure scenarios are modelled in the FEM program Abaqus. From the results found in Abaqus, general guidelines are developed, including an estimation of an equivalent accidental load for precast concrete structures such as the DPCA-building.

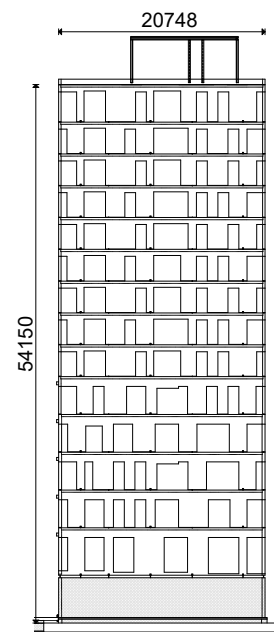
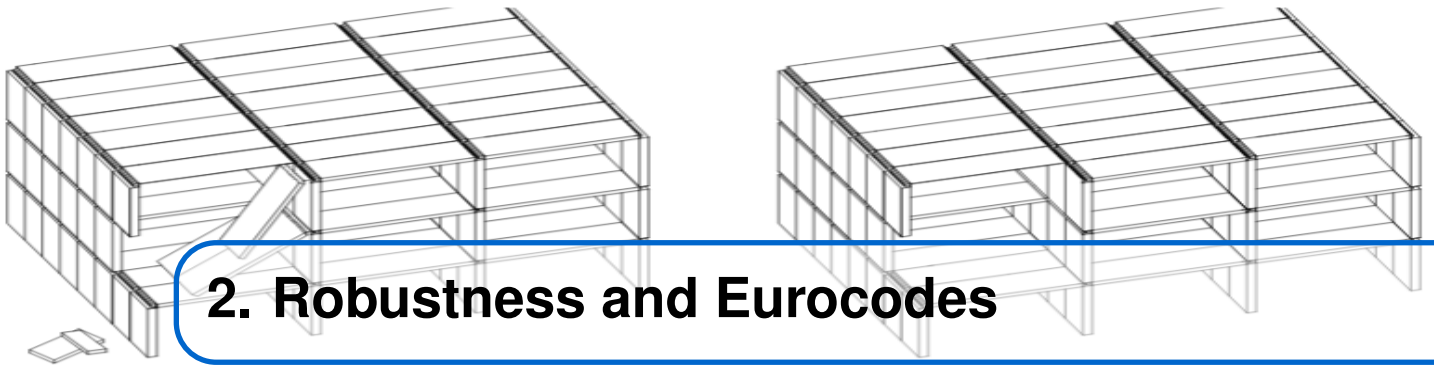


Figure 1.1: Facade of the DPCA-building, All measures in [mm].

1.1 Problem definition

What loads can be expected in identified design failure scenarios in precast concrete structures from the dynamic effects of falling materiel, and how well do these loads correlate with the vertical replacement loads in the Danish National Annex.



2. Robustness and Eurocodes

The requirements of documenting a certain degree of robustness of a structure have only recently been implemented in building standards such as the Eurocodes, which was firstly initiated in the United Kingdom after experiencing a collapse in a multi-storey concrete structure known as the Ronan Point. Along with the requirements of documenting robustness, a definition of a robust structure was developed, which has been revised multiple times over the years, some of which are described below.

- "When the safety-critical parts of the structure are only slightly sensitive to unintended influences and defects, or when there is no major failure of the structure if a limited part of the structure fails." [DS/INF-146, 2003]
- "The ability of a structure to withstand events like fire, explosions, impact or the consequence of human error, without being damaged to an extent disproportionate to the original cause." [DS/EN-1990, 2007]
- "A structure should be designed to have an adequate level of robustness so that, during its design service life it will not be damaged by adverse and unforeseen events, such as the failure or collapse of a structural member or part of a structure, to an extent disproportionate to the original cause." [prEN1990:2019, 2019]

Although the definition of a robust structure differs slightly, an overall agreement of important topics is seen, such as the safety of critical parts of the structure, so that collapse disproportionate to the initial failure is avoided.

Along with the description of a robust structure, building standards implemented the use of design failure scenarios, DFS, in which part of a structure is removed, and the remaining structure is to be proven capable of redistributing the loads without comprehensive damages. The dynamic actions arising from the local failure can have severe consequences on the remaining structure, with debris falling and gaining inertia, which has to be absorbed by the structure below. One event where a small initial failure resulted in a partwise collapse is the Ronan Point building.

2.1 Ronan Point

The Ronan Point structure was a 22 floors tall precast concrete, bearing wall construction located in London. The progressive collapse of the corner initiated from a gas explosion on the 18th floor, as illustrated in Figure 2.1. The gas explosion destroyed the peripheral load bearing wall, which removed the support of the overlying floors.



Figure 2.1: Progressive collapse of the corner of Ronan Point.

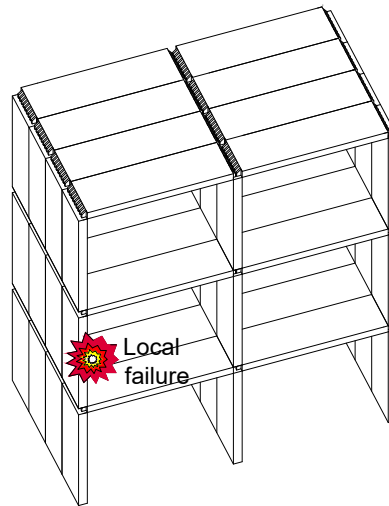


Figure 2.2: Simplified model of the Ronan Point initiating gas explosion.

The initial gas explosion, as illustrated on Figure 2.2 and resulting collapse of the structure can be described in four overall steps:

1. The initial gas explosion in the apartment, as illustrated on Figure 2.3, resulted in a blow-out of the peripheral load bearing wall.
2. The blow out of the load bearing wall results in sudden loss of support of the overlying floors, illustrated on Figure 2.4
3. The built up inertia of the overlying floors impacts and breaks the underlying slab, illustrated on Figure 2.5
4. Progressive collapse is developed, with the amount of debris and resulting inertia continuously increasing, illustrated on Figure 2.6

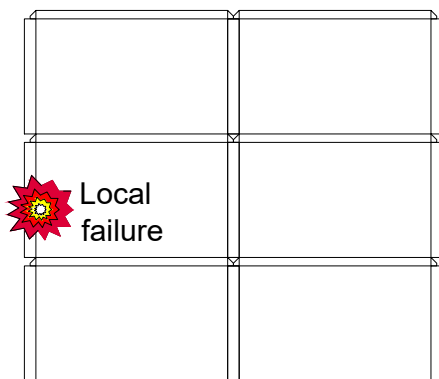


Figure 2.3: Initial failure of the peripheral wall.

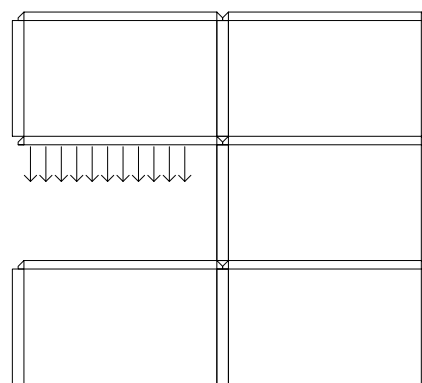


Figure 2.4: Loss of support results in increasing downward headed inertia of overlying floors.

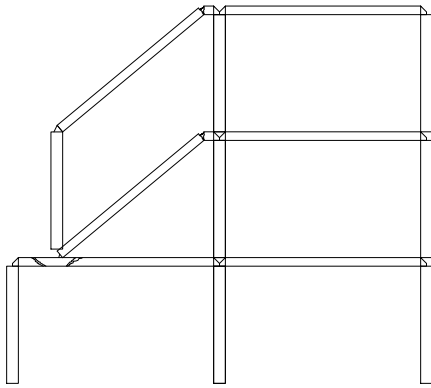


Figure 2.5: The built up inertia impacts and

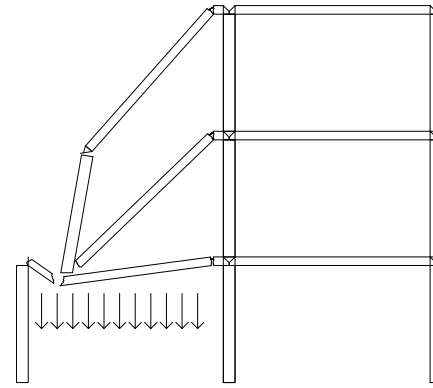


Figure 2.6: The slab breaks and debris continues.

The partwise progressive collapse of Ronan Point is one of many examples, where an initial failure resulted in a disproportionate collapse. In general, buildings are not designed to withstand loading conditions such as gas- and bomb explosions, vehicle collisions or aircraft collisions which have been experienced before. Although the accidental loading conditions in some cases will result in a local failure, precautions should be made, to produce an overall more robust structure, which is strong, ductile and capable of redistributing loads while not being too costly.

Following the Ronan Point collapse, regularity standards were formulated to prevent such incidents. Thorough investigations of the Ronan Point collapse began, and the error was found to be in the lack of continuity of reinforcement. The stringer reinforcement between slabs consisted of a single rebar placed at the site, with subsequent in-situ casting, as illustrated on Figure 2.7. The stringer reinforcement had no direct ties to the peripheral reinforcement, as illustrated on Figure 2.8.

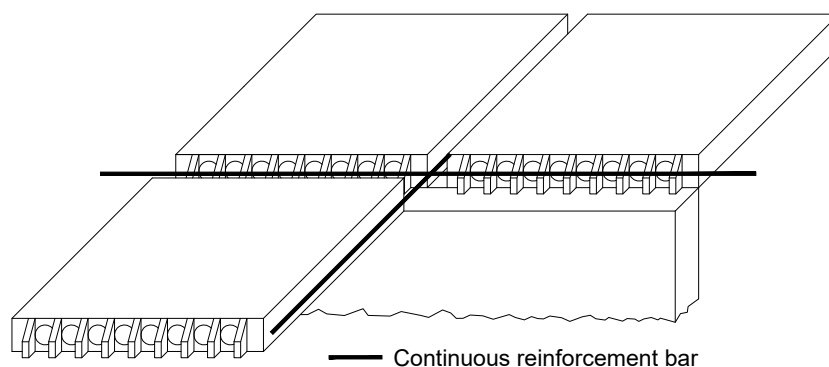


Figure 2.7: Sketch of the stringer reinforcement between slabs in the Ronan Point structure.

The design of the peripheral joints of Ronan Point consists of teathed hollow slab elements as illustrated on Figure 2.7. The teathed edges rest on the wall abutment, which results in greater surface area when pouring in-situ concrete. Even still, the improperly designed peripheral joints in the Ronan Point structure was found to be the direct cause for the

development of progressive collapse. If the building had been properly tied at the joints, e.g. Figure 2.9, severe cracking would be present in the concrete, but progressive collapse would be avoided.

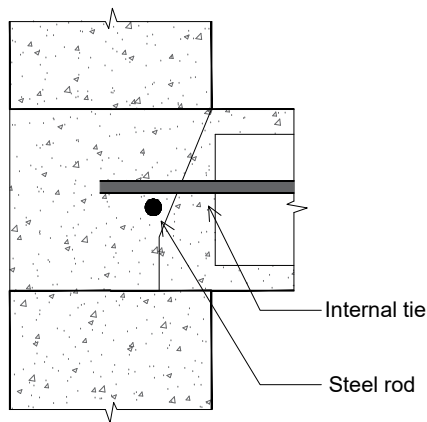


Figure 2.8: Joint at the external walls of the Ronan Point structure. [Pearson, 2005]

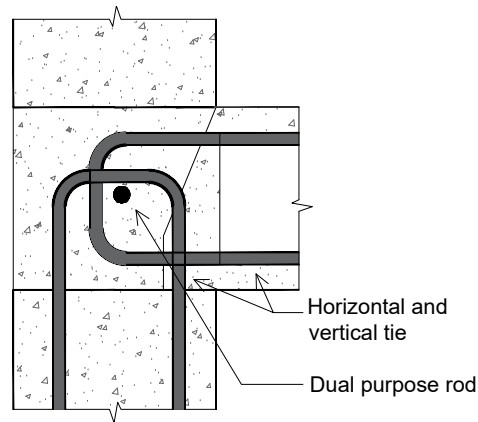


Figure 2.9: Example of joint which secures continuity.

The actions implemented in the later developed Eurocodes consisted of minimum reinforcements as the example in Figure 2.9, with several more measures to avoid such incidents.

2.2 Structural measures for increasing robustness

In section 2.1, the collapse of Ronan Point was found to be because of the lack of reinforcements/ductility in the joints. Additional methods of increasing robustness exist, such as increasing redundancy of the structure, or by dividing the structure into segments, which are described in the following.

2.2.1 Redundancy and ductility

The method of increasing the ductility and redundancy in concrete structures through the use of additional reinforcement is an often seen method of securing a robust structure. A structural element such as the concrete beam illustrated on Figure 2.10 a) will exhibit two very different types of failure depending on whether the section is reinforced or not. If the concrete section is not properly reinforced, the beam will experience a brittle type failure from tensile cracking or shear, where both the deformation and energy absorption capabilities are low as illustrated by the brittle failure on Figure 2.10 b). By properly reinforcing the beam to ensure a flexural ductile failure, the beam exhibits an increase in deformation capability's and therefore energy dissipation properties, as illustrated by the ductile failure. [Bruce R. Ellingwood and Dusenberry, 2007]

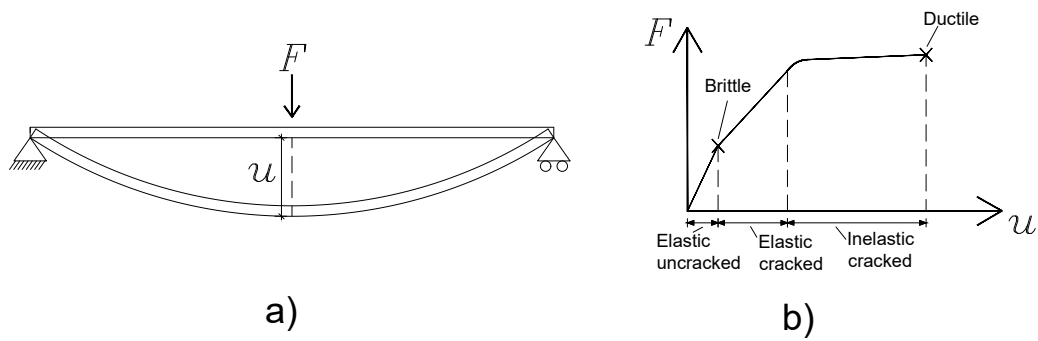


Figure 2.10: Brittle and ductile failure of a concrete beam.

As for increased ductile behaviour, properly placed reinforcement can increase the redundancy, being the number of load paths for the accidental load to be redistributed. When constructing systems of concrete slabs and walls, increased use of reinforcement can allow redistribution of loads through a secondary span direction as illustrated on Figure 2.11, although such actions will require interior partitions capable of carrying the load, and therefore reducing floor flexibility.

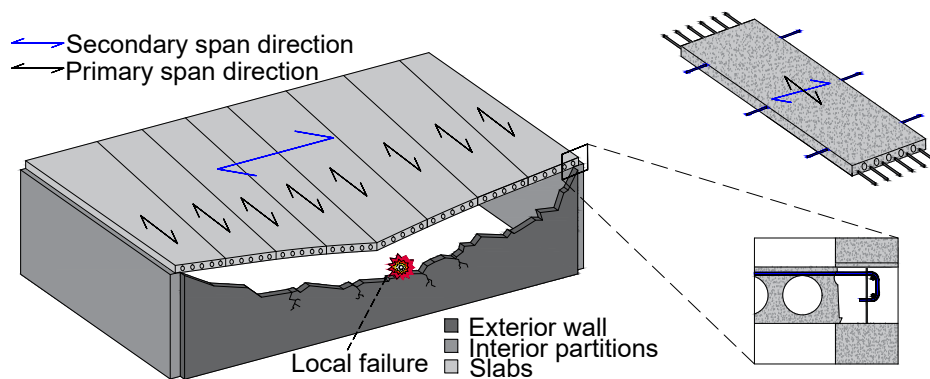


Figure 2.11: Secondary span direction through the use of transverse reinforcement.

If a secondary span direction is not an option, catenary action of the slab and wall structure is possible as illustrated on Figure 2.12, redistributing the vertical loads through membrane forces in the slabs to the adjacent walls.

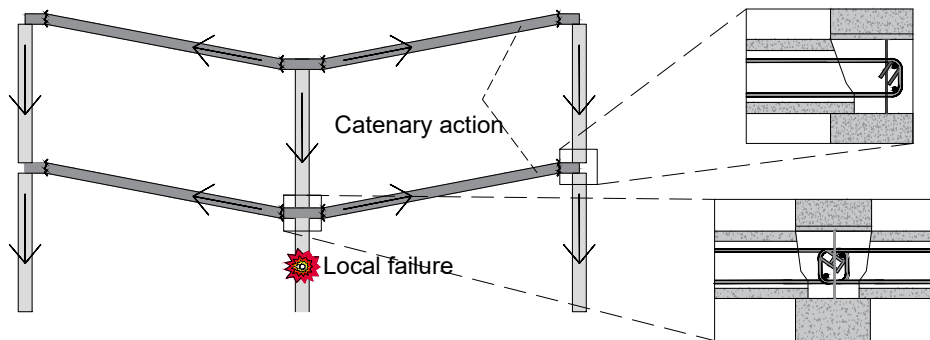


Figure 2.12: Catenary action of precast concrete slab/wall structure using the two illustrated joints.

Load redistribution is also possible by reinforcing walls and slabs to act as a beam, with the wall and slabs acting as the web and flanges as illustrated on Figure 2.13.

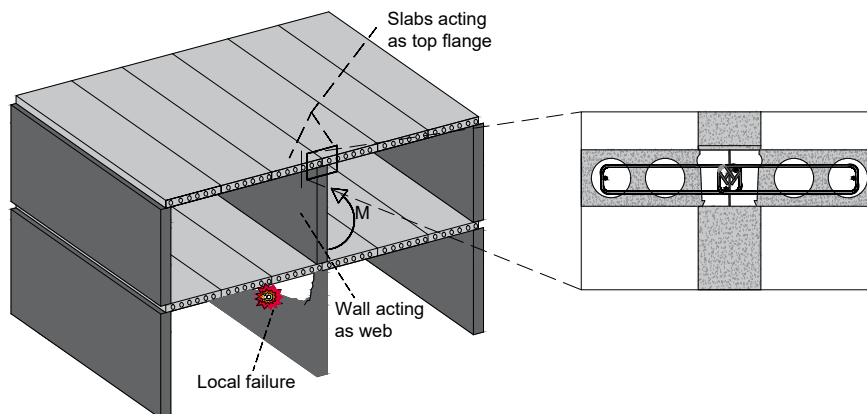


Figure 2.13: Wall spanning an opening using the slabs above and below the wall as flanges.

2.2.2 Segmentation

In some cases of securing a robust structure, the method of redistributing loads as previously described is not suitable, and the method of dividing the structure into segments can be used.

In the method of segmentation, the local failure of a structure is isolated between discontinuities in the structure, such as hinged joints with high ductility and low stiffness. The segment is created such that the extent of collapse is limited to that specific area in which the local failure began, similar to the use of fire compartments to confine a fire to the compartment of origin.

The use of segmentation is widespread in the design of larger structures, such as airport

terminals, bridges etc. The principal of segmentation and its advantages can be described by the Confederation bridge illustrated on Figure 2.14, which is constructed with prestressed box girders, each with a 250m span. In the design of the bridge, segmentation was found advantageous over the alternative load path method, because of the large expenses required to acquire the necessary strength and ductility to redistribute the loads through e.g. catenary action. In the early design of the Confederation bridge, the design failure scenarios were determined to be the failure of one of the bridge piers. Modelling of the pier failure concluded that the collapse could progress into the next span, resulting in a domino effect with failure of the whole bridge. The solution was to construct the bridge in segments, with joints as illustrated on Figure 2.15 to eliminate continuity and isolate the incipient collapse.

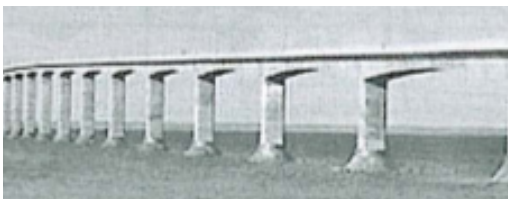


Figure 2.14: Confederation bridge (Canada) [Uwe Starossek, 2009]

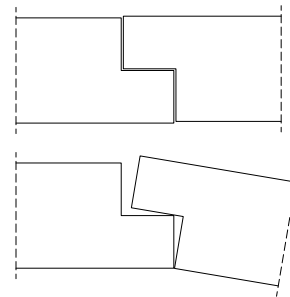


Figure 2.15: Hinge joint of girder element in Confederation bridge [Uwe Starossek, 2009]

A case of structural failure in segments was the airport terminal in Paris illustrated on Figure 2.16. The terminal consisted of rings which unintentionally was constructed as segments, with the discontinuity present as expansion joints. The failure initiated in the roof structure, which propagated to both sides until reaching the expansion joints.



Figure 2.16: Segmentation of airport terminal (Paris) [Uwe Starossek, 2009]

An assessment of the structure after the collapse concluded that if continuity in the joints had been present, it was likely that the collapse would propagate further.

It is thus important in the design that if the method of alternative load path is chosen, the strength required to redistribute the loads must be well documented. If this is not the case, the continuity present from the alternative load path method will in some cases promote rather than prevent failure progression [Uwe Starossek, 2009].

2.3 Eurocode guidelines

The following section encompasses a state of the art description of the current robustness rules in the EU and Denmark. The first European Standard, EN, were implemented in 1984 and the idea was to contribute to a functioning internal market and a uniform level of safety of construction across the EU. Since the EU consist of many countries there is some parameters that are left up to the individual country to decide. This is why an EN Eurocode part consist of rules and recommended values for certain parameters, which each country can either accept or change in a national standard with annexes. The national annex thus allow for nationally determined parameters if left open to change in accordance with the corresponding EN Eurocode part.

The Eurocodes discussed are the latest available versions, unless stated otherwise. The following Eurocodes will be discussed in this section:

- EN 1990:2002 - Basis of structural design
- EN 1990:2019 - Basis of structural design [Draft 2019-09]
- EN 1991-1-7:2007 - Actions on structures, (Accidental actions)
- EN 1992:2008 - Design of concrete structures

The Danish National Annexes developed in addition to the three Eurocodes are hereafter reviewed to investigate and discuss the national chosen methods for securing a robust structure.

- DS/EN 1990:2019 DK NA - Apply to EN1990:2002
- DS/EN 1991-1-7:2013 DK NA
- DS/EN 1992-1:2017 DK NA

2.3.1 EN1990 and EN1991-1-7

As described previously, the general guidelines for reaching a robust structure are found in the European Standard EN1990:2019 and EN1991-1-7. The distinction between robustness in compliance with EN1990 and design for identified actions in accordance with EN1991, where structural performance can increase robustness, is shown on Figure 2.17.

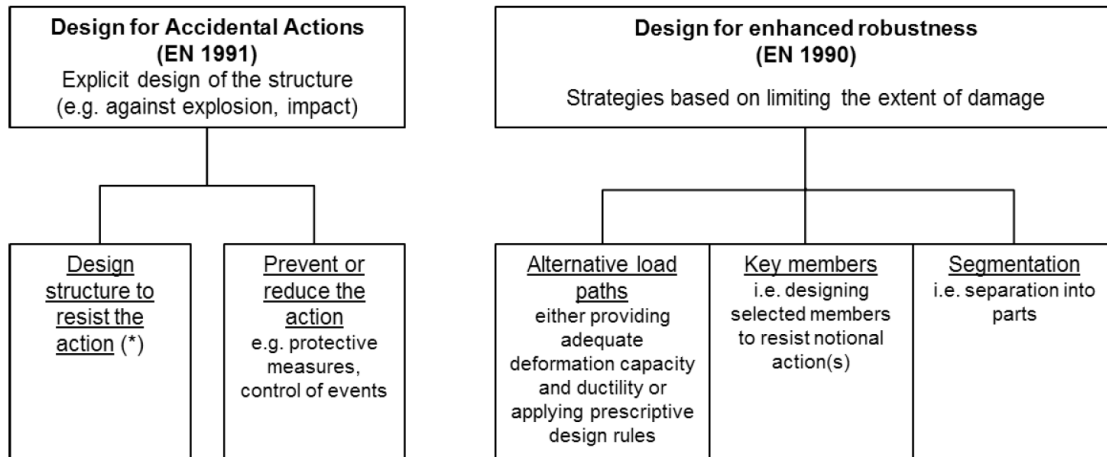


Figure 2.17: Strategies for designing for identified accidental actions and for general enhanced robustness. [prEN1990:2019, 2019]

As seen on Figure 2.17 when designing for accidental actions according to EN1991, a contribution to the robustness is possible through explicit design of the structure. The explicit design of the structure is described as designing the structure to resist known accidental actions, defined as:

- "An identified accidental action is one against which a structure is explicitly designed on having been identified as possible to occur during its design service life" [prEN1990:2019, 2019]

The identified accidental actions comprises of e.g. impact loads on a bridge from ships. The design against the accidental action will then comprise of structural measures such as increased strength, or protective measures to control or minimise the risk of the event. The explicit design method will therefore only partwise increase a structures robustness, and is advantageous if such an incident is the only one relevant.

As opposed to the strategies stated in EN1991, EN1990:2019 mentions three design strategies which instead of increasing the robustness to resist the specific action, they provide general enhanced robustness of the structure.

The three methods are described as follows:

1. Creating alternative load paths by increased ductility, deformation capacity and redundancy.
2. Increasing the resistance in selected structural members, known as key elements.
3. Separating the structure into segments, such that the structure is able to collapse independently of the remaining structure.

The design for enhanced robustness described in EN1990:2019 is only relevant in some cases, and the extent of the required investigation is dependent on the authorities choice and consequence class, CC. The consequence class are divided into three, as described in Table 2.1 [prEN1990:2019, 2019].

Table 2.1: The three different consequence classes and their definition. [prEN1990:2019, 2019]

Consequence class	Consequence of failure
CC1 (Low)	<ul style="list-style-type: none">• Low risk of loss of human life• Small or negligible economic, social or environmental consequences
CC2 (Medium)	<ul style="list-style-type: none">• Medium risk of loss of human life• Substantial economic, social or environmental consequences
CC3 (High)	<ul style="list-style-type: none">• High risk of loss of human life or -• Large economic, social or environmental consequences

2.4 Danish National Annex

The rules described in the Danish National Annex associated to the Eurocodes previously described is investigated in this section.

2.4.1 National annex: DS/EN 1990:2019 DK NA

The guidelines described in the national annex for enhanced robustness is dependent on the consequence class described previously from the European Standards. Structures placed in CC1 does not require any design methods to provide enhanced robustness. If the structure is placed in CC2, it is a requirement to make an assessment of the robustness, along with the use of prescriptive design rules for increased structural integrity and ductility, as described in section 2.4.2 governing the Danish National Annex approach [DK-NA, 2017].

Structures with high consequence of failure, CC3, requires in addition to the rules stated for CC2, documentation of sufficient robustness through the use of Annex E1 and E2.

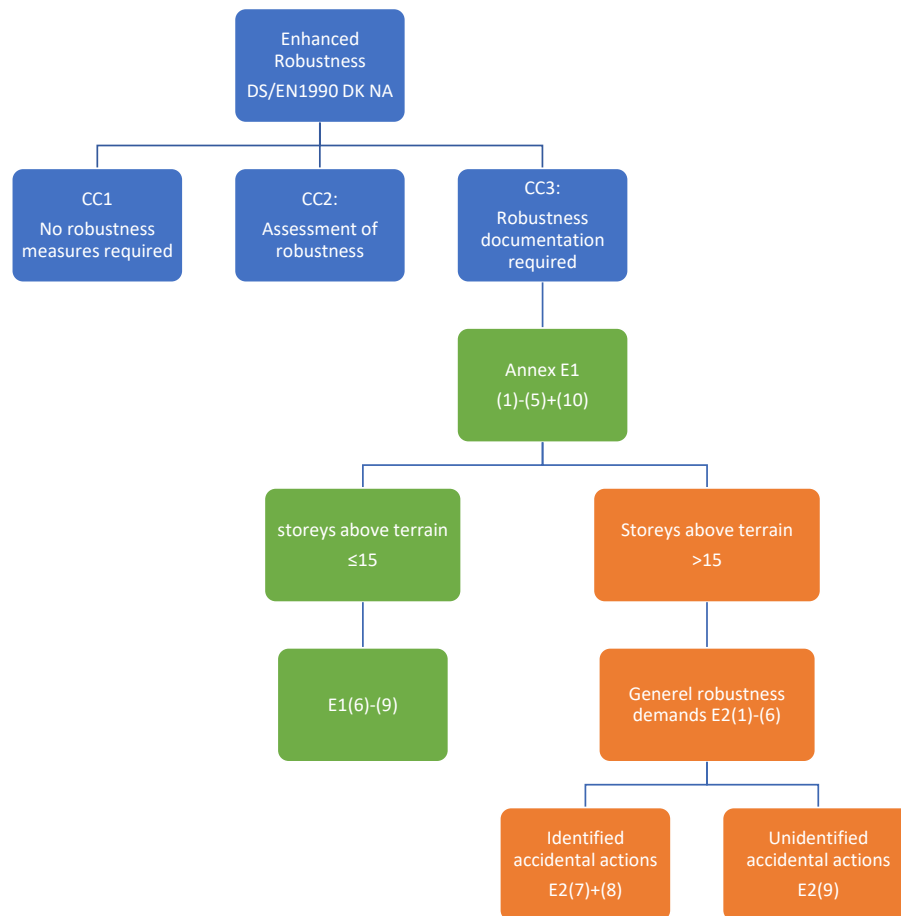


Figure 2.18: An overview of the robustness requirements in the Danish National Annex.

The guidelines described in the national annex for enhanced robustness divides the requirements into two different areas, depending on the number of storeys above terrain in the structure that occupies people, as illustrated on Figure 2.18. The Danish National Annex E1 states both the general robustness rules in topics E1(1)-(5)+(10), such as the definition of a robust structure etc. as well as the methods used to document robustness described in (6)-(9), which is investigated further. Structures with 15 or less storeys above terrain follow the rules stated in Annex E1, and structures with more than 15 storeys above terrain that occupies people are classified as high rise buildings, which partly follow Annex E1, and in addition follow rules stated in E2 [1990DK-NA:2019, 2019].

Annex E1 - Robustness - (6)-(9)

The documentation required in CC3 for structures with 15 or less storeys above terrain, is comprised of calculations to prove that overall stability of the structure is not at risk, if a local failure should occur. To document the robustness in CC3, at least one of the three following methods must be fulfilled.

1. Secure that essential structural components, known as "Key elements", has little sensitivity against unintended influences.

2. Proving that progressive collapse is unlikely in the case of local failure
3. Securing that key elements has sufficient security against collapse, such that the structure reaches robustness equivalent to a corresponding structure which has been proven through criterion #2.

To secure sufficient robustness using method #1, firstly requires that all members identified as key elements are found, after which a process of assessing which unintended influences are of high relevance towards the failure of the structure, followed by documentation that proves that the sensitivity is low towards that unintended influence. The identification of unintended influences is open to interpretation, since this may include anything and nothing, which often will lead to disagreements in the case of third party verification. The above also makes it clear why method #1 is mentioned as not being recommended.

Method #2 is an often used method, and is documented by the use of alternative load path method, described in section 2.4.3

If choosing to use method #3, the structural system chosen in the design is limited, such that it resembles structural systems which previously has been proven through method #2. Benefits of the approach consist of low costs and low risk of error, although limiting the extent of which the structural system can be changed.

Additional to the technical documentation through one or more of the above mentioned methods, the engineer responsible must thoroughly review the design for possible weak points, identifying key elements and critical load scenarios.

Comparing the three criterion's with the methods described in EN section 2.3.1, it is clear that they differ in formulation, however two of the topics have the same idea, first of which being the importance of key elements, and secondly being the robustness against progressive collapse, referred to as the method of creating alternative load paths. The method of creating segments described in method #3 in EN does however not appear in the Danish National Annex E1, and is instead replaced with the method of using previously robustness documented structural systems through method #2, to secure a robust structure. The replacement of method #3 can be explained by how the Danish National Annex divides the robustness measures depending on the number of storeys above terrain, such that segmentation only is seen as a useful method in larger structures, and therefore implemented in annex E2.

Annex E2 - Robustness for High rise buildings

In the case of structures with more than 15 storeys above terrain which is used to occupy people, rules additional to the ones stated in annex E1 (1)-(5) + (10) as described on Figure 2.18 apply, which are described in annex E2.

The procedure of securing the robustness of high-rise buildings is divided into the overall requirements, followed by two approaches as illustrated on Figure 2.18. The two methods are both based on identified design failure scenarios, and the differences emerge at whether or not the accidental action is identified.

The overall requirements state that the assessment of the robustness of high rise buildings is done through the use of relevant design failure scenarios. In each of the design failure scenarios, the expected number of fatalities must not surpass 500, meaning that if necessary the structure is required to be divided into segments, with each segment occupying less than or equal to 500 people. The expected number of fatalities pr. square meter varies depending on live load category, with values shown in Table 2.2

Live load category	Pers. pr. m ²
A, B, C1, D1	1 pers. pr 15 m ²
C2, C3, C4, C5, D2	1 pers. pr 4 m ²

Table 2.2: Expected number of fatalities dependent on the live load category.

To design the horizontal segmentation of the high rise building, the national annex E2 suggests the use of a vertical replacement load, VRL, to imitate the impact loads from the failure of overlying floors. The loads are divided in three sizes depending on the number of overlying floors in the created segment, as illustrated on Figure 2.19. As the figure suggests, the idea does satisfy the requirement of segmentation, as long as the replacement loads are sufficiently accurate to describe the real world behaviour of multiple storey failure in high rise buildings.

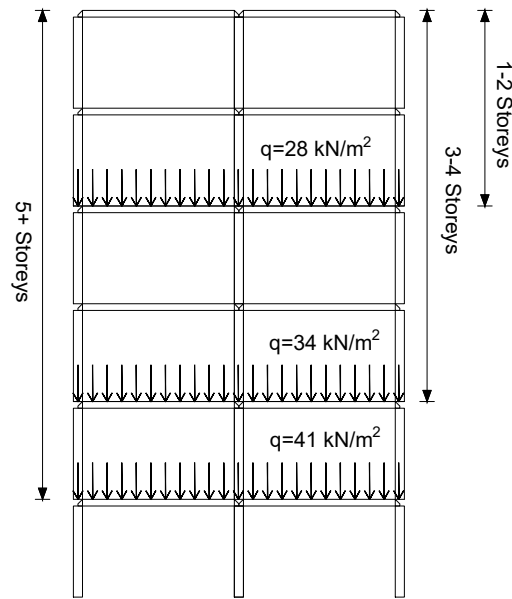


Figure 2.19: Vertical Replacement Loads, VRL, used to design high rise buildings into segments according to annex E2.

Further assessment of the high rise building is done through the use of identified design failure scenarios, which is determined based on whether the actions on the structure is identified or unidentified. The identified accidental actions consist of hazards such as abnormal loads, impact loads or deformation related as described in Table 2.3, along with unidentified accidental actions, such as faulty practice.

Table 2.3: Structure relevant hazards and their possible consequences [Bruce R. Ellingwood and Dusenberry, 2007].

Hazard scenario	Type of loads
Abnormal loads	Pressure loads from explosions or wind pressure
Impact loads	Vehicular collisions, falling debris and swinging objects under construction or demolition
Deformation related	Strength and stiffness reduction from temperature changes, foundation subsidence
Faulty practice	Errors in concept, design and execution

The procedure for identified design failure scenarios with identified accidental actions, consist of documentation of the possibility of developing progressive collapse, as well as documentation of the most appropriate structural measures to prevent progressive collapse, such as increased ductility, segmentation and reducing risk of errors through third party verification.

More specifically, the procedure for identified accidental actions is illustrated on Figure 2.20. As seen on the figure, the documentation consists of two steps, being the persistent and transient design situations described in (7), and the identified design failure scenarios described in (8).

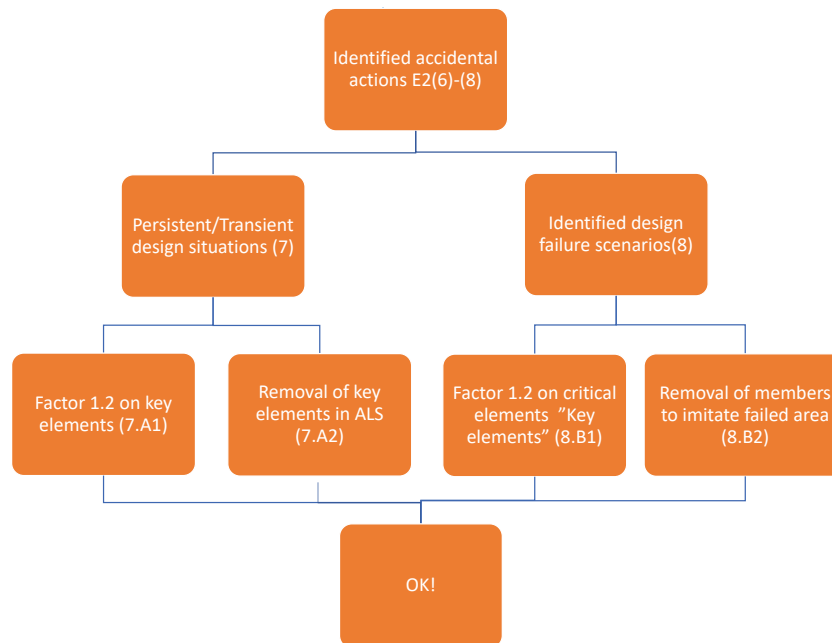


Figure 2.20: Flowchart for which Eurocode design approach to apply regarding identified accidental actions.

The choice of approach within the persistent and transient design situation step is up to the engineer responsible. The first approach, (7.A1) ensures robustness by increasing the size of the key elements known to be affected in the design failure scenario. The increase in size is achieved through increasing the safety factor by 1.2 in the persistent and transient design situation. The approach is illustrated on Figure 2.21 (7.A1).

The second approach secures robustness by documenting sufficient strength in the accidental limit state, where the design failure scenario is simulated by removal of elements such as joints, slabs etc, and the remaining structure is documented to remain stable and not promote progressive collapse, further described in section 2.4.3 The approach is illustrated on Figure 2.21 (7.A2).

The identified design failure scenarios which are related to accidental failure scenarios is documented by either using the key element approach (8.B1) illustrated on Figure 2.21 (8.B1), where partial coefficients is increased with a factor 1.2 on strength parameters, and loads relevant for the identified accidental action is found in the Danish National

Annex for identified accidental actions [NA:2013, 2013]. The second approach, (8.B2), introduces limited damage as illustrated on Figure 2.21 (8.B2), after which the structure is documented to not promote progressive collapse as described in section 2.4.3, both methods are documented in the accidental limit state.

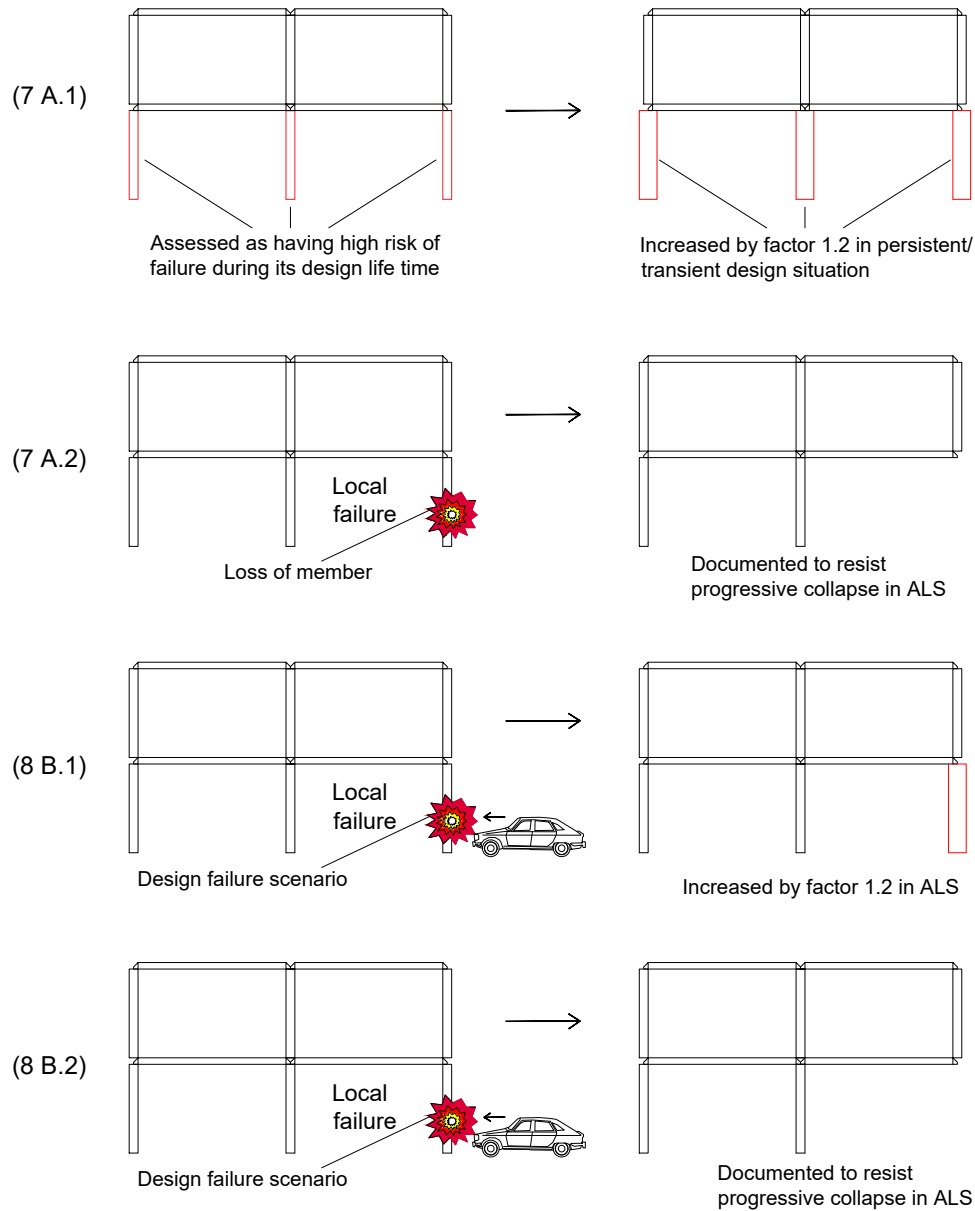


Figure 2.21: The four possible approaches of documenting the robustness in structures against identified accidental actions.

For identified design failure scenarios with unidentified accidental actions, the approach is different than described previously, and the procedure now consists of two possible approaches, as illustrated on Figure 2.22. In the first approach, (9.C1), the critical members must firstly be identified, after which they are designed to resist a accidental replacement load applied in ALS. The accidental replacement loads is chosen to be the most unfavourable of either a surface load or point load as illustrated on Figure 2.23.

In the second approach, (9.C2), illustrated on Figure 2.23, the critical members are removed, and sufficient robustness of the remaining structure is proven in ALS.

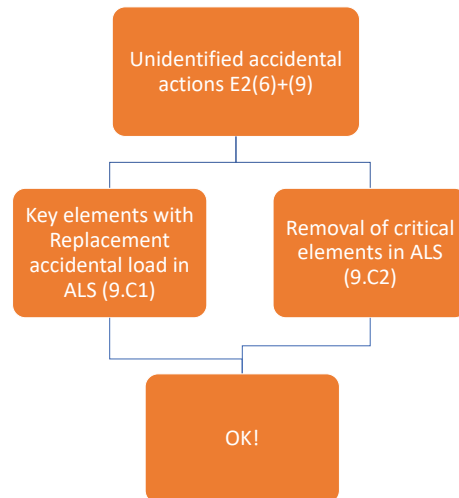


Figure 2.22: Description of the robustness demands regarding unidentified accidental actions.

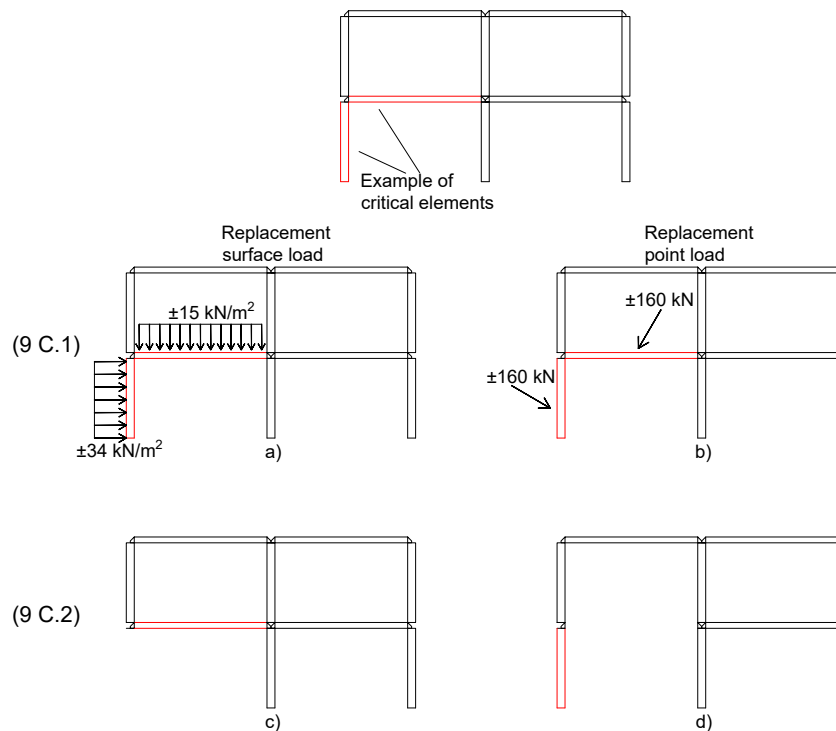


Figure 2.23: Illustration of method of securing robustness against unidentified accidental actions (9.C1) and (9.C2).

2.4.2 Minimum reinforcements (DS/EN1992 DK NA)

In addition to the requirements stated in annex E1 and annex E2 described previously, rules of minimum reinforcement present in concrete structures exist [DK-NA, 2017]. The rules of minimum reinforcement states that the robustness of concrete structures must be further increased by placing rebar in joints, beams and walls, to increase structure

continuity and ductility. One example of the benefits is illustrated on Figure 2.24, which in the design only requires reinforcement as illustrated to the left. In the case of a change in the support conditions, the moment section forces change, as illustrated to the right on Figure 2.24. The demands of minimum reinforcement as stated in the Danish National Annex assists these incidents, which to some extent ensures redistribution of loads instead of structural failure.

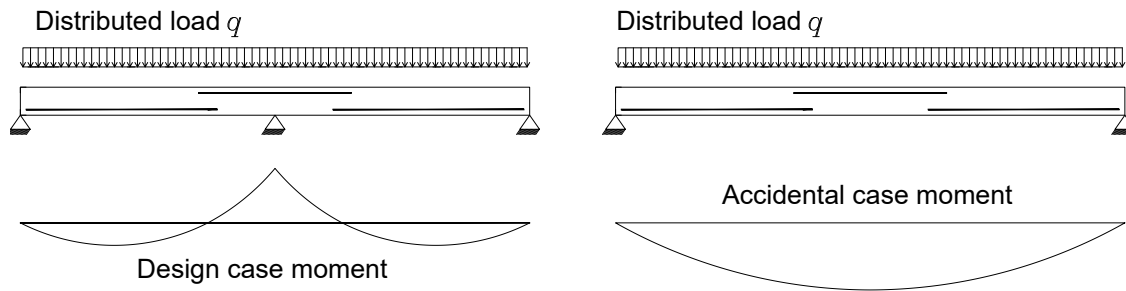


Figure 2.24: Consequences of not including accidental design situations in the placement of reinforcement.

The minimum demands to reinforcement are in the Danish National Annex stated as a requirement when considering concrete structures, because of the lack of tensile strength and low ductility properties. The minimum reinforcement act as ties, to increase the overall redundancy of the structure, increasing the number of load paths for a possible load redistribution. The amount of reinforcement necessary is based on the consequence class, where a higher consequence class requires more reinforcement.

The ties required are divided into four types, being:

- Peripheral ties
- Internal ties
- Horizontal ties to columns and walls
- Vertical ties

The peripheral ties are secured by placing reinforcement in the joints with exterior walls. The vertical ties secure vertical tensile capacity, giving walls the potential of spanning a local failure. The peripheral and vertical ties can be combined with horizontal ties as illustrated on Figure 2.25, which together secures a strong connection between horizontal movement of the slab, and vertical movement of the exterior walls. Furthermore, internal ties are required, which are spread evenly in the floor and tied to the peripheral ties with the use of horizontal tie.

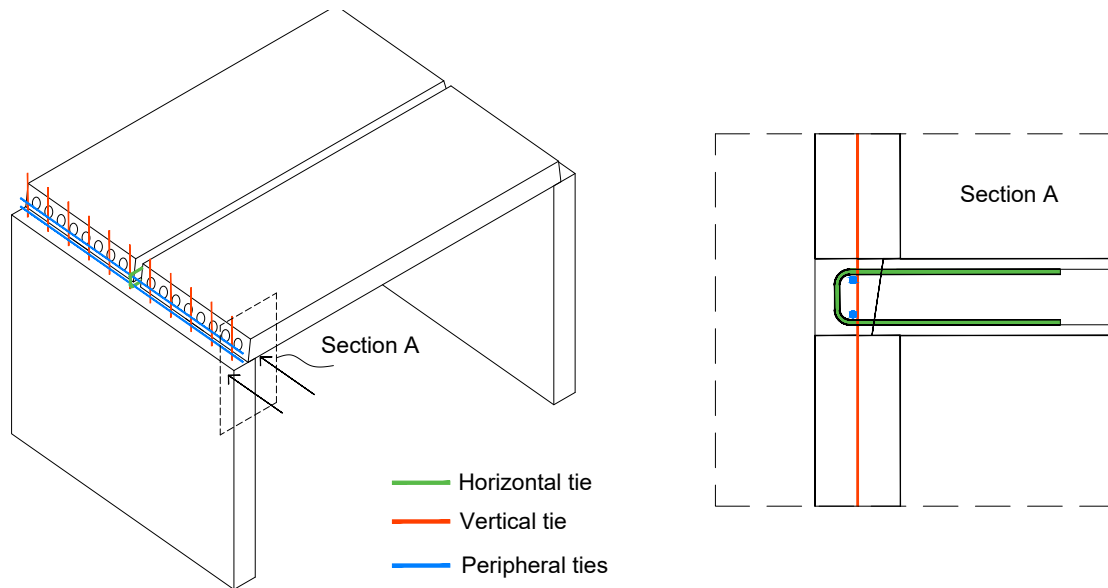


Figure 2.25: Example of combining Internal, Vertical and Peripheral ties.

The reinforcement requirements can in some cases counteract other measures taken to secure robustness. Especially when following the mandatory requirements of segmentation in high rise buildings, the segmentation approach assures robustness by containing the collapse to designated areas without affecting the remaining structure. If large amounts of reinforcement is used to increase the continuity, the failed structure may have a negative impact on the segmentation strategy, such that the failed structure tries to "pull down" some of the surrounding structure, resulting in a strategy that promotes rather than prevents progressive collapse, a phenomenon which is also described in section 2.2.2.

2.4.3 Loss of member method

In the previous sections describing the European Standard and Danish National Annex approach of securing robustness of structures, the method of documenting sufficient resistance against progressive collapse in the design failure scenario, meaning after the removal of the member in question, is mentioned as a viable method independent of structure type, size or whether the accidental action is identified or not. The reason for this can be explained by how the robustness is documented directly in the case of failure, and not only by increasing material safety factors, to improve factors such as redundancy and ductility.

The loss of member method assumes that some part of the structure is removed in the design failure scenario, where the extent of removal is dependent on whether the design failure scenario is with identified or unidentified accidental actions;

- If the accidental action is identified as defined in section 2.3.1, only the affected structure is removed
- If the accidental action is unidentified, area representative to the specific design failure scenario is used

The Danish National Annex [1990DK-NA:2019, 2019] mentions scenarios such as

- A slab and a column
- A slab and an arbitrary 3 m wall piece

or equivalent failure areas, if the engineer responsible considers that there is a risk if the structural part fails. After removal of the member or area, the structural stability is proven to be sufficient to not promote progressive collapse in an accidental limit state.

The limits of acceptance for the localised failure is described as being maximum two on top of each other floors. On each of the two floors, the maximum collapsing area must be lower than 15% of the floor area, however the area must not exceed 240 m² pr. floor, and no more than 360 m² total.

One example of the loss of member approach is illustrated on Figure 2.26 where a wall is removed, resulting in a failed area. The failed area is acceptable if it is below the limit of collapse area previously described.

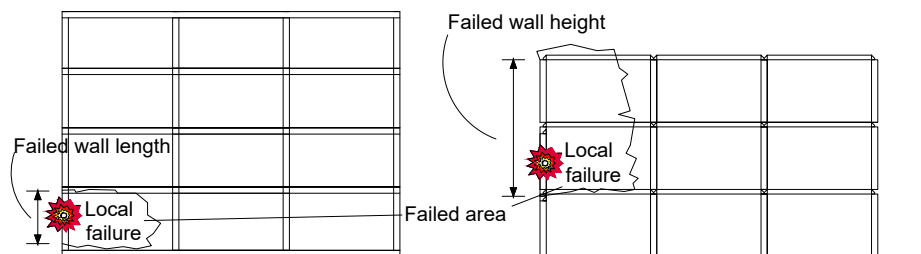


Figure 2.26: Example of failed area resulting from the failure of a peripheral wall.

In the example illustrated on Figure 2.26, only one of the failure scenarios is investigated, meaning that the robustness requirements are only documented in one of the failure cases. Documenting the robustness can therefore be a comprehensive and time-consuming process, where each of the identified design failure scenarios are investigated, e.g. failure in joints, columns, walls etc. where the section forces is documented to be redistributed to the surrounding load bearing system, without promoting progressive collapse of the structure.

2.4.4 Including the dynamic aspects

In the loss of member method, one important assumption is made, being that

- The failed area, comprising of slabs, walls etc. is assumed to disappear when failed, having no influence on the remaining structure.

The assumption is illustrated with the local failure described in Figure 2.26, where the failed area in reality is expected to act like illustrated to the left on Figure 2.27, as opposed to the assumption of disappearing area illustrated to the right.

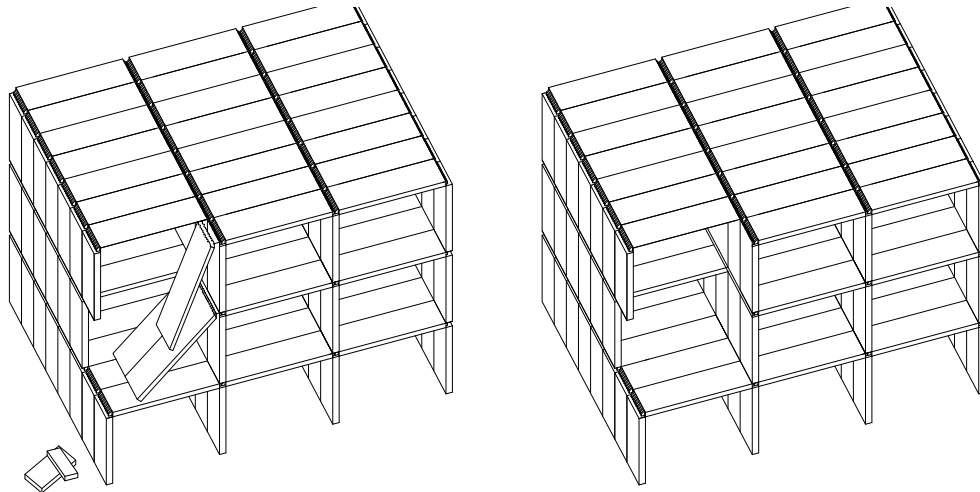
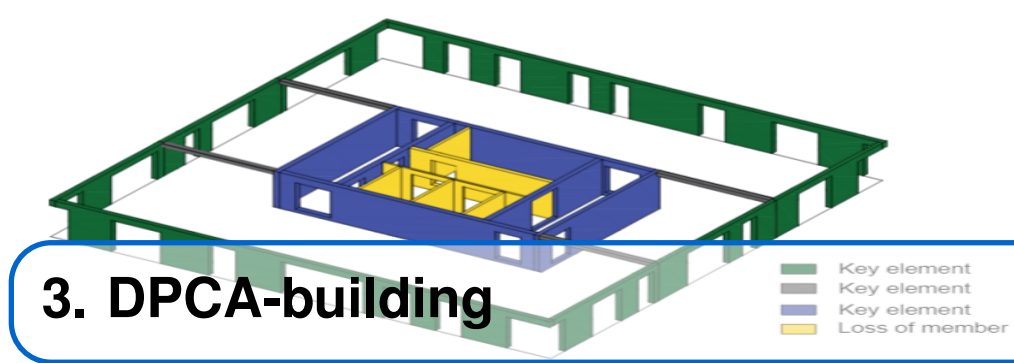


Figure 2.27: Left, collapsing area resulting from local failure. Right, assumption of disappearing area.

Assuming that the failed area is removed in the design failure scenario, the dynamic aspects of the failure is removed from the analysis, and the resulting loads is not taken into account. The failure is in reality expected to include phenomenons described in the Ronan Point failure in Section 2.1, involving the built up inertia of moving members and high impact forces.

Although not included in the loss of members method, the loads from falling structural members are previously used and was mentioned as replacement loads in the method of securing segmentation in high rise buildings described in the Danish National Annex, [prEN1990:2019, 2019]. The replacement loads are dependent on the number of storeys which are assumed to fail, as illustrated on Figure 2.19. The replacement load size originates from the previous used Danish norm for loads on constructions, [DS410, 1999], in which the loads was assigned by the ministry of internal affairs, without any further documentation.

The assumption of disappearing failed area proposes further analysis of the consequences thereof, in which a concrete structure is investigated for design failure scenarios and resulting loads from collapsing area.



In this chapter a typical precast concrete element structure will be investigated where some of the proposed actions used to document the robustness principles in annex E1 and annex E2 are used and explained. The chapter is based on the Danish National Annex [1990DK-NA:2019, 2019], and proposed actions developed by Jesper Frøbert Jensen to comply with the robustness requirements.

3.1 Building properties

The structure used in the analysis is a typical precast multi-storey concrete building as illustrated on Figure 3.1. The structural properties and measures was delivered by Jesper Frøbert Jensen, and describes a building projected for the Danish Precast Concrete Association as an example of a multi-storey concrete structure, and is throughout the report referred to as the DPCA-building [Jensen, 2020]. The building consists of a site-cast basement, followed by 14 floors in which precast elements are used. Even though the DPCA-building is 1 storey short of being classified as a high rise building it is investigated in accordance with the design principles for a high rise building. These design principles are described in Danish National Annex [1990DK-NA:2019, 2019] and a description of the most important parts are detailed in section 2.4. The overall structural measures are illustrated on Figure 3.1, with the floor plan illustrated on Figure 3.2.

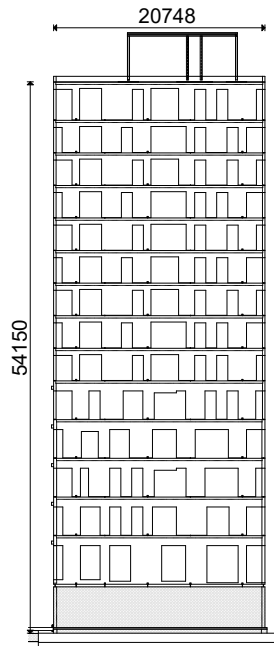


Figure 3.1: Facade of the DPCA-building. Measures in [mm].

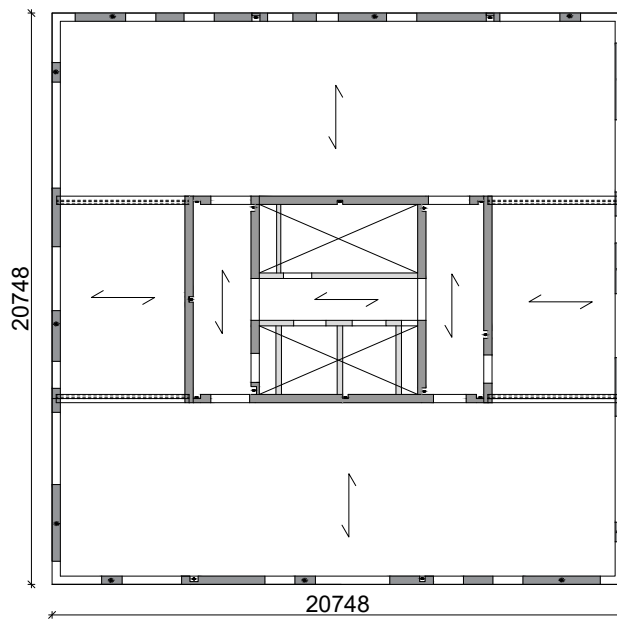


Figure 3.2: Floor plan of the DPCA-building. Measures in [mm].

3.2 Robustness design principles of the DPCA-building

To document sufficient robustness of the DPCA-building in accordance with Danish National Annex E1 and E2, the following requirements must be met;

- Since the DPCA-building is considered a high rise structure, Annex E2 requires the structure to be divided into segments, such that the expected number of fatalities do

not exceed the limits described in section 2.4.

- In addition to the segmentation requirement, the DPCA-building must be documented to have sufficient robustness against identified design failure scenarios, arising through both unidentified and identified accidental actions.
- The DPCA-building is a concrete structure and therefore requires minimum reinforcements as described in EN1992-1-1 DK NA.

3.3 Segmentation and unidentified accidental actions

To document the above stated requirements using the approach of design failure scenarios with unidentified accidental actions, and at the same time considering the rules for segmentation, a proposed method is to first design parts of the structure with the key element approach. This way an overall robust frame of the building is reached, after which only the remaining walls, slabs etc. are investigated with the use of design failure scenarios. [Jensen, 2020]

To illustrate the issues which can arise when designing the structural system for enhanced robustness using a combination of a robust frame and failure scenarios, firstly an example of a not so robust structure is discussed, after which the actions proposed by Jesper Frøbert Jensen are implemented and discussed.

An example of enhancing robustness by creating an overall robust frame with key elements, and members which are allowed to collapse can be seen on Figure 3.3. On the Figure the peripheral walls and parts of the core structure are shown to be designed in the accidental limit state to withstand the replacement accidental loads described on Figure 2.23.

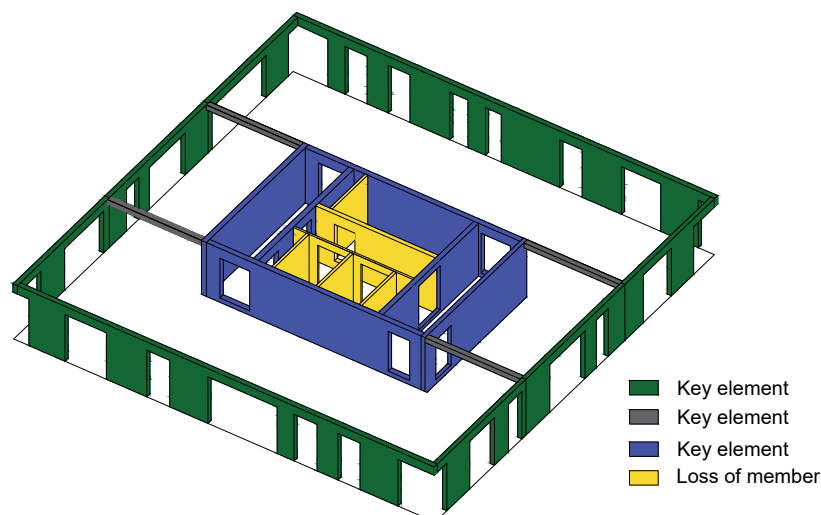


Figure 3.3: Illustration of key elements in the floor plan design.

The remaining structure must now be designed such that the identified design failure scenarios do not result in damage greater than the stated limits. Since the design failure scenario is a result of an unidentified accidental action, limits comes from segmentation requirements of the structure, meaning that there are no restrictions to the number of

floors or size of the area affected directly, only restrictions governing the expected number of fatalities.

In compliance with the requirements for segmentation, the horizontal segmentation of the DPCA-building is determined based on the placement of the key elements, which form the boundaries of the segment area, as illustrated on Figure 3.4. Within each of the boundaries of the segmented area which in this case is the floors, the design failure scenario with unidentified accidental actions may be the complete collapse of one storey. The collapse may as an example be as a result of poor design and improper placement of reinforcements, after which the joint along the periphery of a segment fails, resulting in a collapse as illustrated on Figure 3.5.

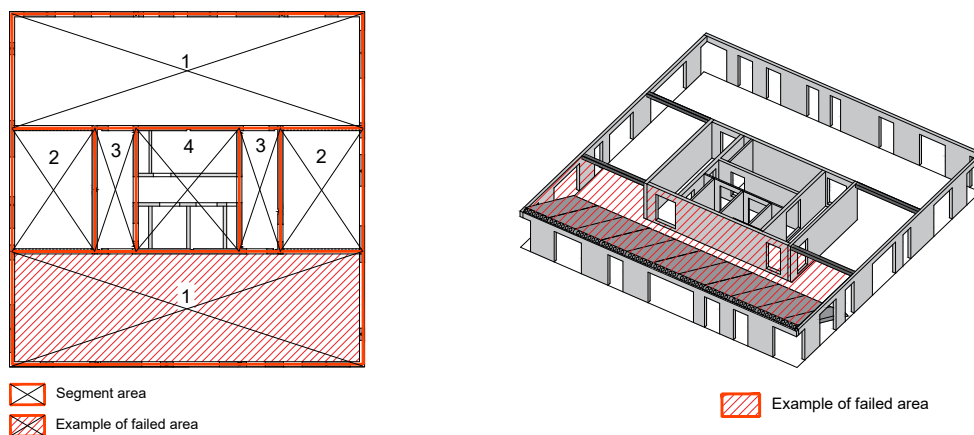


Figure 3.4: Horizontal segmentation of the floor plan.

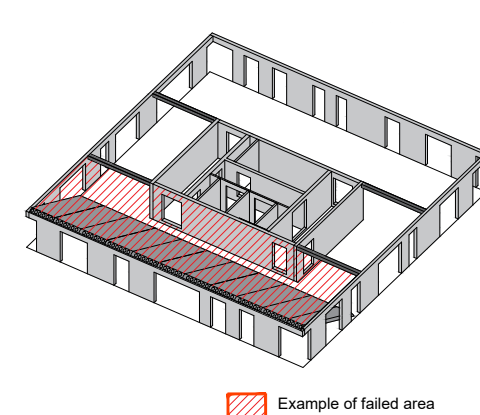


Figure 3.5: Example of failure in one of the segmented areas.

In the design of the vertical segmentation, the marked area on Figure 3.5 is assumed to break in some unidentified accidental event, after which the failed area is collapsed, hitting the floors beneath as illustrated on Figure 3.6 A). The number of floors beneath which are affected by the failure is here chosen by the design engineer, such that the total number of expected fatalities remain within the limits. If it is assumed that 4 storeys are affected by the collapse, the 5th floor must be designed to withstand the loads from the falling debris, which results in a surface load of 41 kN/m^2 , as illustrated on 3.6 B) and C). If the limits of expected fatalities is reached within the segmented area after e.g. 4 storeys, the subsequent floor must be designed to withstand the replacement accidental load in the accidental limit state. Since the remaining floors are assumed to collapse, they are only designed in the Transient/persistent design situation as illustrated on Figure 3.6

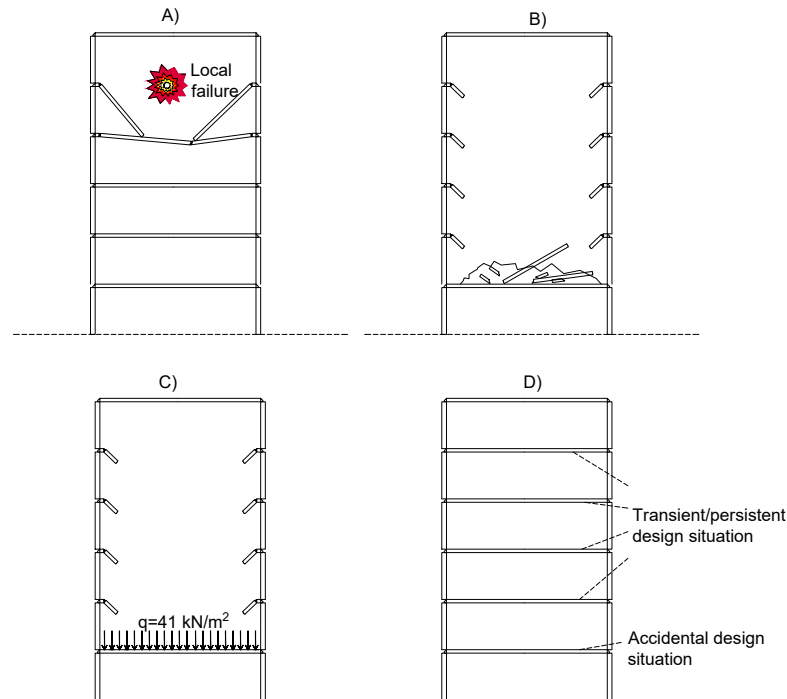


Figure 3.6: Sketch of the failure in one segment and resulting boundaries for the vertical segmentation.

In the scenario illustrated on Figure 3.6, the vertical segmentation was described, but for the structure to remain stable it must also be proven to have sufficient stability in the key element structure such that these do not fail because of the disappearing floors. An example of this issue is shown on Figure 3.7, where it can be seen that the removal of floors in the chosen segment will result in loss of stability for the key element boundaries.

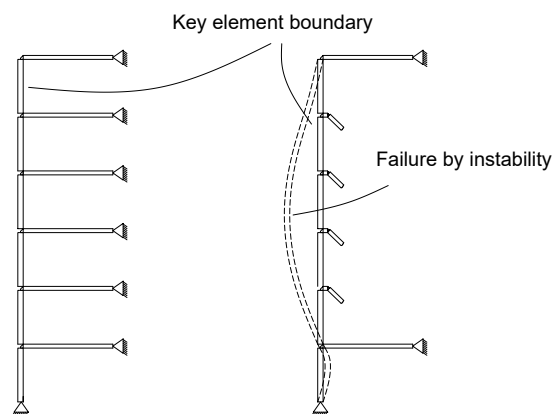


Figure 3.7: Sketch of instability of key element segment boundary.

In this example four floors collapsed, which with a floor height of e.g. 3m, results in a wall which is unsupported horizontally for a total of 15m, which will result in instability problems. Therefore to secure that the overall structure can act as a robust frame, it must be noted that stability and capacity of this frame structure must be demonstrated in the accidental scenario where members allowed to collapse have collapsed.

It can therefore be concluded that additional key elements must be used to secure an overall robust frame structure, an example of which can be seen on Figure 3.8, where some of the proposed actions mentioned by Jesper Frøbert Jensen is implemented [Jensen, 2020].

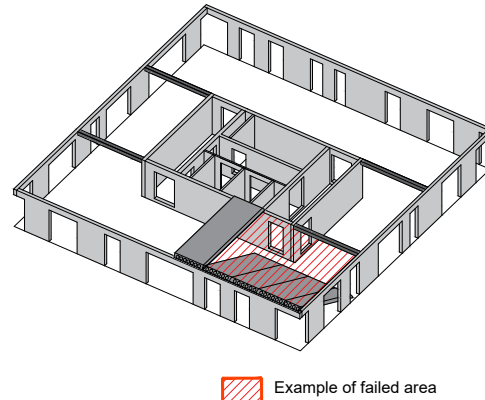
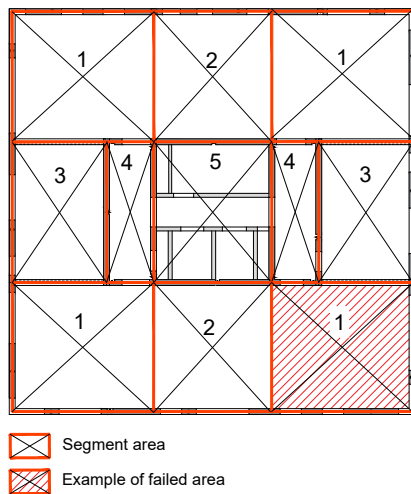


Figure 3.8: Potential method of reducing the segment area and also securing horizontal stability of a key element structure.

Figure 3.9: Example of failed area in a smaller segment.

When implementing additional key elements to secure stability, the resulting segment area will also change as illustrated on Figure 3.9. Increasing the number of key elements to reduce the segment area illustrated on Figure 3.9 is not always a disadvantage when considering the total cost of the structure, since the smaller segment floor area results in a larger vertical span of floors required to reach the expected number of fatalities. A higher number of floors which are allowed to collapse means fewer floors designed using the accidental replacement load, and therefore less costly.

Furthermore choosing to have large floor areas within each segment, the resulting load on the supporting walls along the periphery as shown on Figure 3.10, may be significant compared to the loads in the Transient/Persistent design situation. Comparing the replacement accidental load with the imposed load values described in the National Annex for Eurocode 1991-1-1, the largest values of the imposed load reaches up to 7 kN/m^2 , which even with the load combination and partial factors does not reach anywhere near the values for replacement accidental load [NA:2013, 2013]. Therefore the floors chosen to be the boundaries for the vertical segment will have to be significantly stronger than the remaining floors.

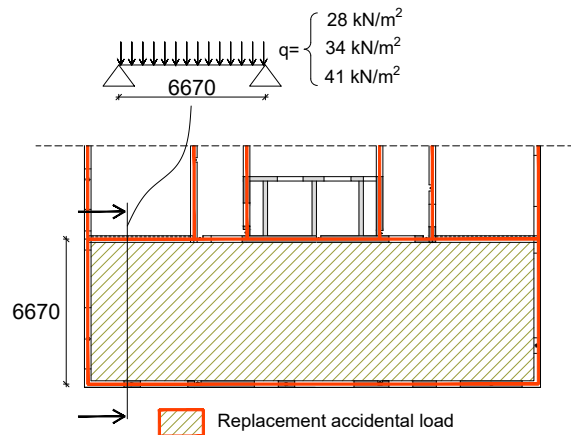


Figure 3.10: Resulting loads on the wall abutment along the periphery of a segment. Measures in [mm].

Considering the total load on the wall abutment along the periphery of each of the segments, it may be advantageous to divide the floor plan into smaller segments as illustrated on Figure 3.8, such that the total load in each of the failure scenarios becomes smaller, and therefore reducing the loads in each of the accidental limit states. This will however require the use of more key elements designed for accidental loads, a choice of which method to proceed with remains up to the engineer.

3.3.1 Identified accidental actions

In addition to the design against unidentified accidental actions previously described, the engineer responsible must consider the identified accidental actions, which are the actions deemed possible to occur during its design service life. Depending on the placement and use of the building, the identified accidental actions can vary from impact loads from cars, trucks, or from explosions. Assuming that the DPCA-building is placed in a high risk environment close to a frequently used road, or with a high risk of gas-explosions, the engineer responsible has multiple approaches available of documenting sufficient robustness. The approach is either to design the member to resist the action, use the key element approach or by the loss of member approach, the latter of which is investigated in the following.

Loss of member approach

In the loss of member approach, the identified design failure scenarios are simulated by the removal of an area which to some extent represents the damage caused by the hazard. The resulting damage from a local failure is determined based on the use of the structural component in the structural system, and therefore the floor plan is divided into groups as illustrated on Figure 3.11, with the use shown in Table 3.1.

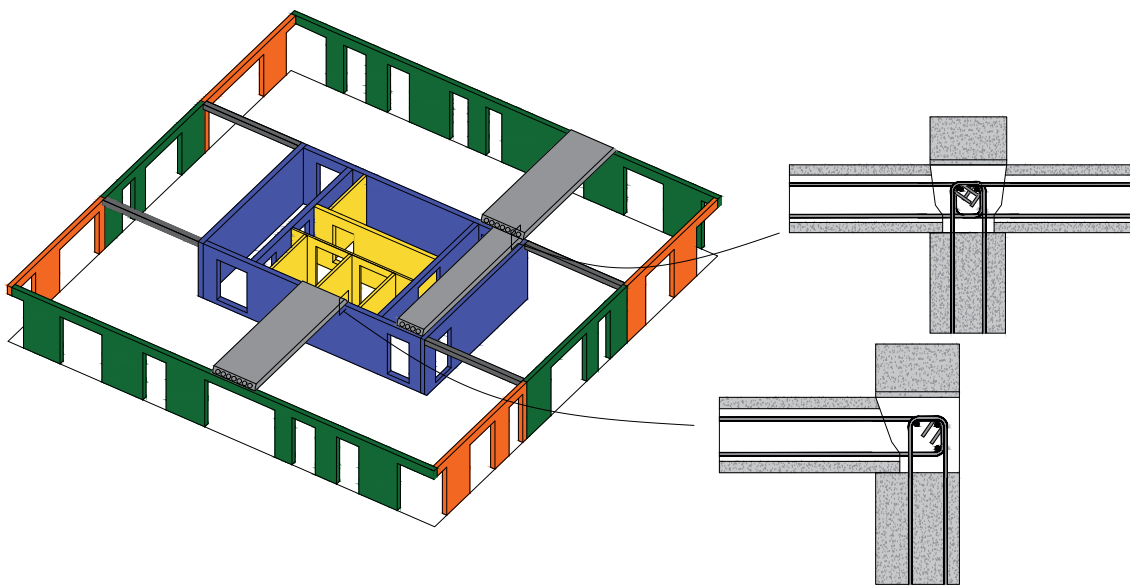


Figure 3.11: Illustration of the groups present in the DPCA-building along with joint description.

Table 3.1: Group location and use in the DPCA-building.

Element group	Location	Use
#1 Green	Periphery	Support of walls and slabs
#2 Orange	Periphery	Support of walls
#3 Blue	Core structure	Support of walls and slabs
#4 Yellow	Core structure	Elevator and staircase structure, supporting walls

Group 2 is seen to only act as a support of the walls above, and the failure will therefore result in the loss of support of the walls above. Group 1 and 3 is used as both the support of walls above and as the support of slabs. Failure of these structural parts will therefore result in removed floor area, which must be investigated to be within the limits of acceptance. The 4th group consists of the staircase and elevator structure, which as group 2 only acts as the support of walls above.

Additional to the use of each member, the placement of reinforcements in the structure, and how the slabs are placed has a big influence on the area which are assumed to fail. In this building, the slabs rest on the wall abutment, where all vertical load is transferred to the wall abutment and down to the ground. Each of the slabs are reinforced such that they are fixed from moving in the horizontal direction.

Knowing the use of each of the structural components, and how each of the members are tied together, the engineer may create an overview of which failure scenarios are critical, and should be investigated further. In reality, the loss of member procedure is comprehensive with a great number of investigated design failure scenarios. In the DPCA

example structure, only some of the design failure scenarios are determined, where the initial local failure is based on the examples of removed area described in 2.4.3. The design failure scenarios are illustrated on Figure 3.13-3.19, where the removed component is marked with red, and resulting failed floor area is sketched with diagonal lines.

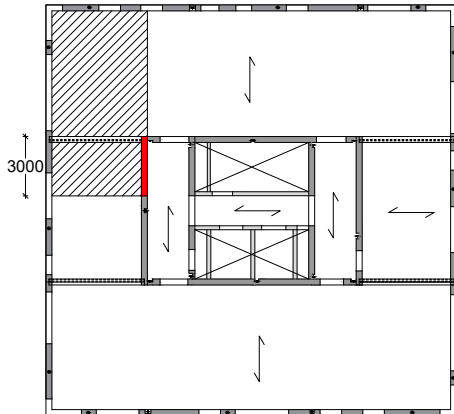


Figure 3.12: DFS1; Failure of a 3m wall piece, which acts as support of both slabs and beams.

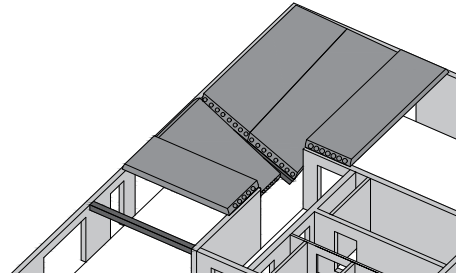


Figure 3.13: DFS1; Example of failure resulting from removal of 3m wall piece.

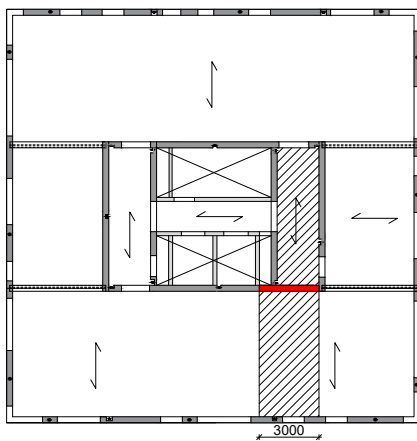


Figure 3.14: DFS2; Initial failure of the core structure peripheral wall.

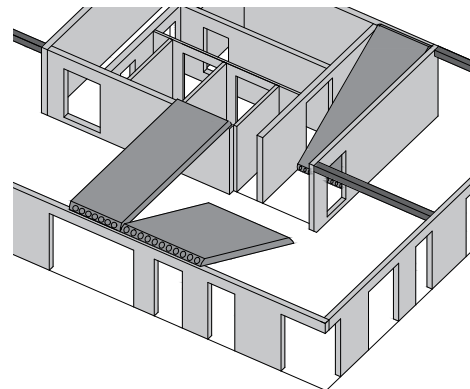


Figure 3.15: DFS2; Example of failure resulting from removal of 3m wall piece.

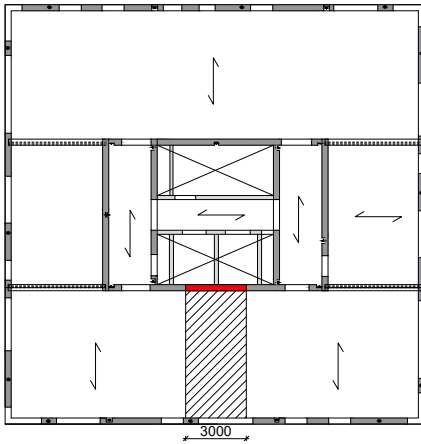


Figure 3.16: DFS3; Initial failure of core structure peripheral wall.

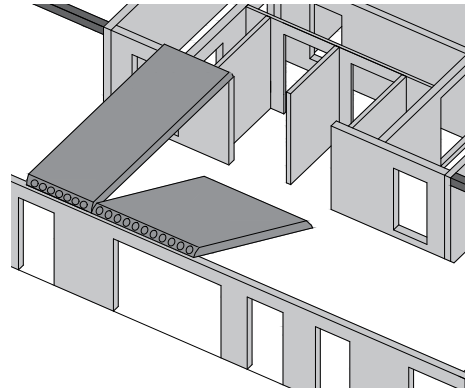


Figure 3.17: DFS3; Example of failure resulting from removal of 3m wall piece.

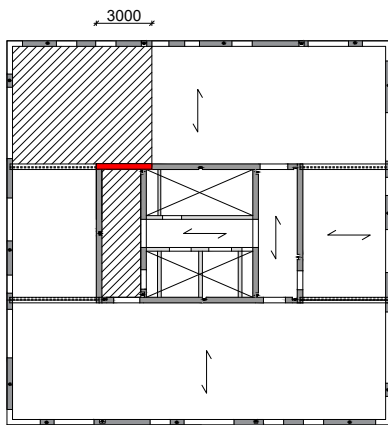


Figure 3.18: DFS4; Initial failure of core structure peripheral wall.

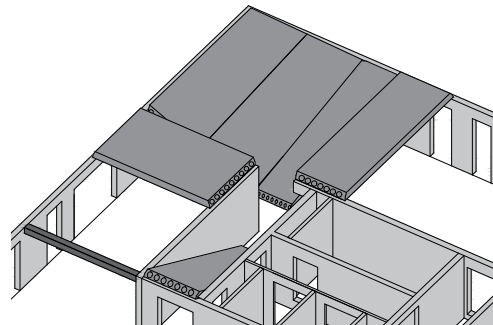


Figure 3.19: DFS4; Example of failure resulting from removal of 3m wall piece.

After identifying the design failure scenarios, documentation of sufficient robustness is performed by proving through static calculations that the loads can be redistributed to the surrounding structure. In these calculations, focus should be on the wall structure removed, since the wall above has lost its support, and it is therefore critical that the wall above is documented to be well connected to the remaining wall, such that bridging over the localised failure is possible.

3.3.2 Minimum reinforcements

Since the DPCA-building is designed with concrete members, minimum reinforcements is required, and an example of the placement of the four types of ties is described in this section. The rules of minimum reinforcement is implemented to provide the ability to redistribute the loads in the case of a local failure. The minimum reinforcements are divided into four types of ties, described as

- Peripheral ties

- Internal ties
- Horizontal ties to columns and walls
- Vertical ties

The ties are implemented in floor plan design illustrated on Figure 3.20, using the gaps in joints between precast members, after which site casting is used.

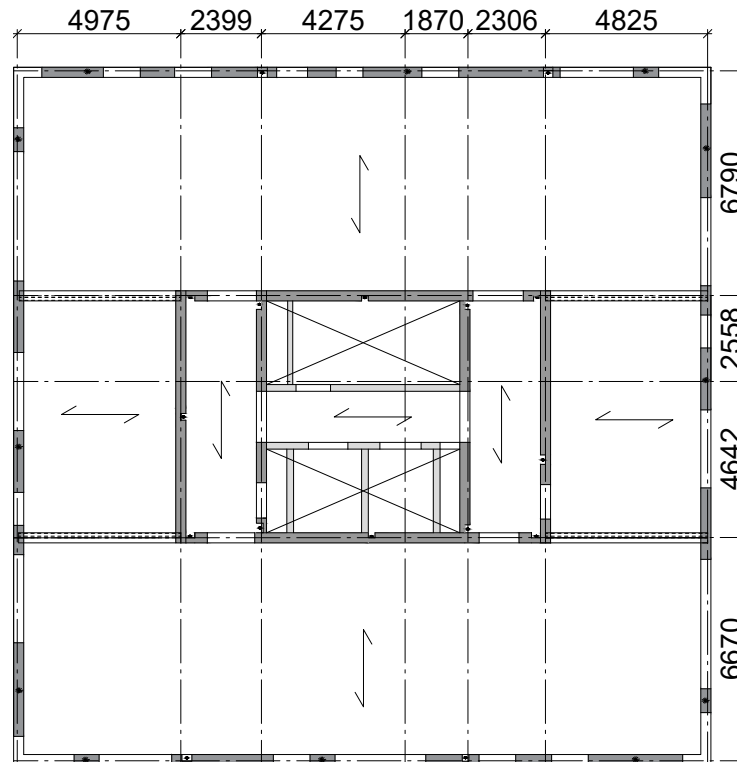


Figure 3.20: Floor plan of the DPCA-building. All measures in [mm]

The required reinforcements are determined in accordance with the Danish National Annex DK NA EN1992-1-1 as the reinforcement required to resist a tensile force dependent on the adjacent area. The reinforcement required for the four different ties are described in Table 3.2

Table 3.2: Robustness required minimum reinforcement.

Type	Size	Placement
Peripheral tie	2 Y12	Continuously in the joint between peripheral walls and slabs
Internal tie	2 Y16 & 2 Y20	Distributed parallel to the peripheral walls and connected to peripheral reinforcement
Horizontal tie	2 Y12	Placed in the concrete core structure and at column reinforcements to secure tying of the walls
Vertical tie	2 Y20	Distributed in the concrete core structure

The minimum required reinforcements are illustrated on Figure 3.21-3.24, for the peripheral, internal, horizontal and vertical tie respectively.

To ensure compliance of horizontal ties, the internal ties illustrated on Figure 3.22 is utilised as horizontal tying of the peripheral walls, with additional horizontal tying of the vertical column reinforcements, illustrated as blue circles.

The vertical ties are illustrated with a yellow circle on Figure 3.24, and are placed in areas of lacking vertical column reinforcements, mainly being the concrete core structure.

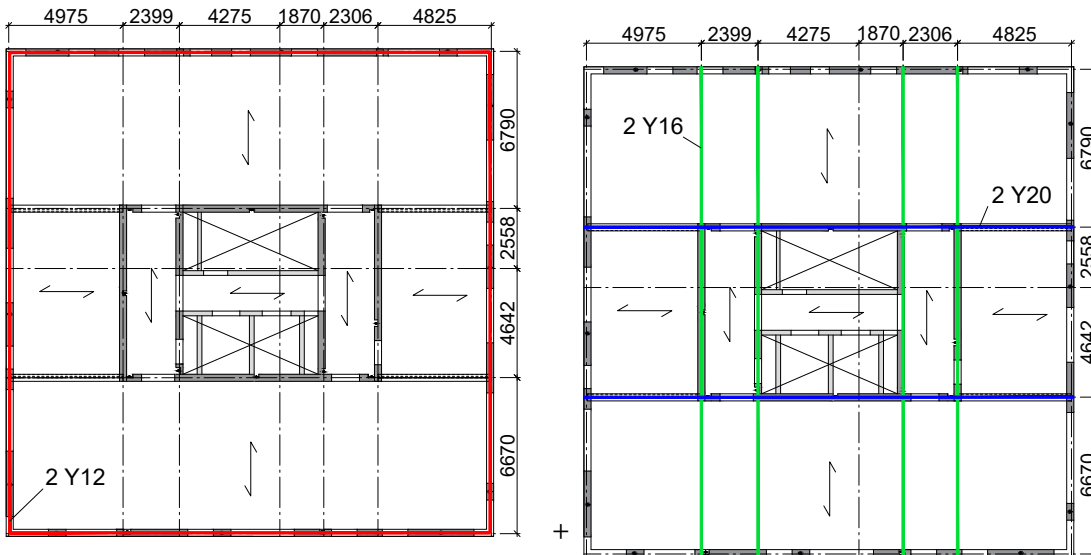


Figure 3.21: Peripheral ties in the DPCA-building.

Figure 3.22: Internal ties in the DPCA-building.

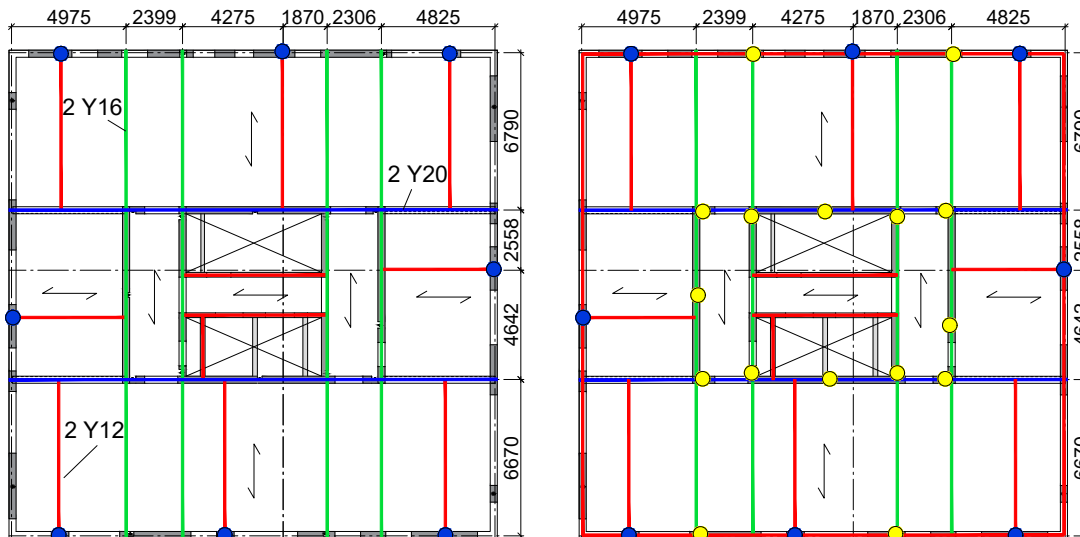


Figure 3.23: Horizontal tie of walls in DPCA-building.

Figure 3.24: Vertical reinforcement and total resulting reinforcement of DPCA-building.

The design of minimum reinforcements will consequently lead to a more continuous structure, with positive effects such as the ability to bridge over local failures, or prevent

incidents like the previously mentioned Ronan Point accident. Therefore the rules for minimum reinforcements may in general be a positive action, although exceptions should be made in the case of the segmentation approach, where the minimum reinforcements directly counteracts the wanted segmentation type of failure. Looking at the resulting minimum reinforcement plan illustrated on Figure 3.24, especially the internal ties will in this case create problems, where the slab collapse in one segment will have a direct effect on the adjacent segments.

3.4 Selected design failure scenarios and further studies

In the previous sections two important assumptions are made which has high influence on the validity of the procedure, them being;

- The procedure to secure vertical segmentation in high rise buildings depends on the fact that the accidental replacement loads imitate the real resulting load from falling material in the form of multiple collapsing floors.
- The assumption of disappearing floor area in the loss of member approach.

A study of the dynamic effects related to falling material in structures is therefore relevant, to secure that future design of structures are not done on the wrong premise.

To investigate the effects of falling material, the design failure scenario with the slab failure illustrated on Figure 3.25 is further investigated using a simplified model shown on Figure 3.26, such that the equivalent static loads can be compared with the values described by the Danish National Annex.

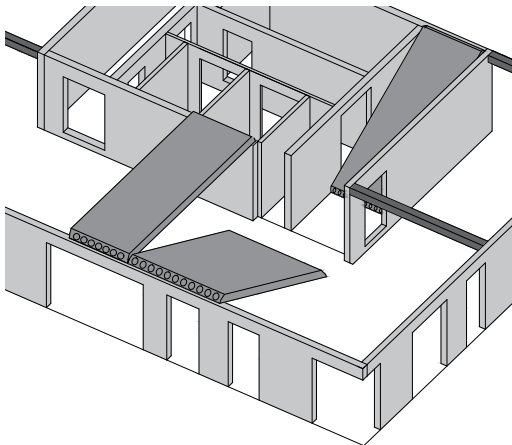


Figure 3.25: Design failure scenario 2.

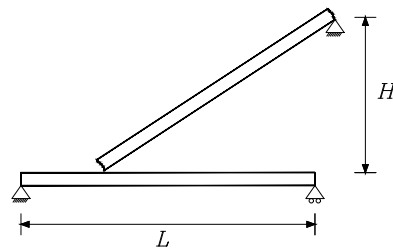
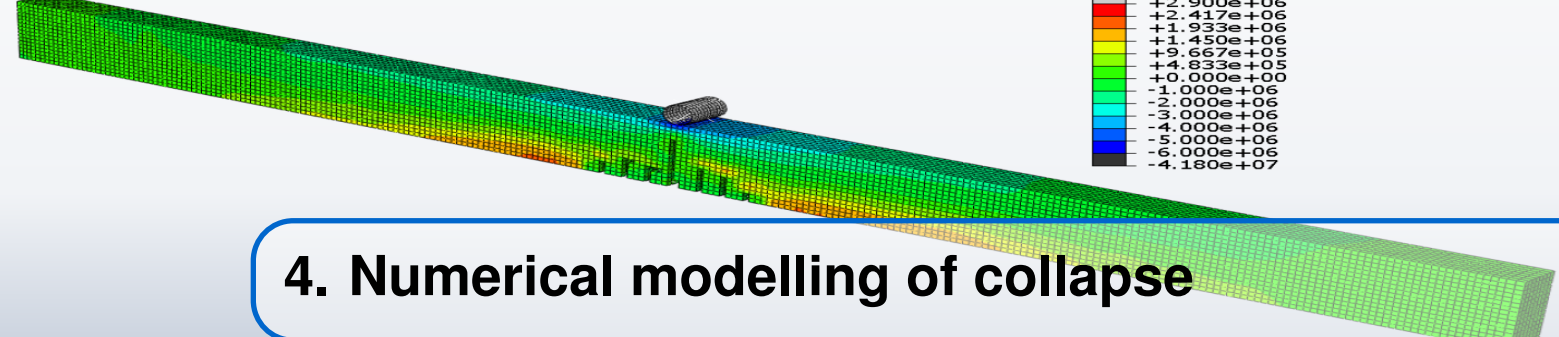


Figure 3.26: Simplified model of DFS2 which is chosen for further study.



4. Numerical modelling of collapse

The phenomena relevant in the design failure scenario is discussed in this chapter, followed by the modelling approach used in the Finite Element Program Abaqus, in which the simplified model of the design failure scenario illustrated on Figure 3.26 is built and investigated.

4.1 Model setup considerations

To model the design failure scenario, multiple phenomena must be considered to give the correct response of the overall structure. In the design failure scenario, the model must describe the built up inertia of the damaged body from stationary, and how the kinetic energy is distributed through impact of the moving and stationary adjacent structure, as sketched on Figure 4.1 a). To describe the properties and forces relevant in the impact, the simplified model on Figure 4.1 b) is used as reference, in which the impact forces are denoted F , and reaction forces are denoted R , along with a displacement of the structure u .

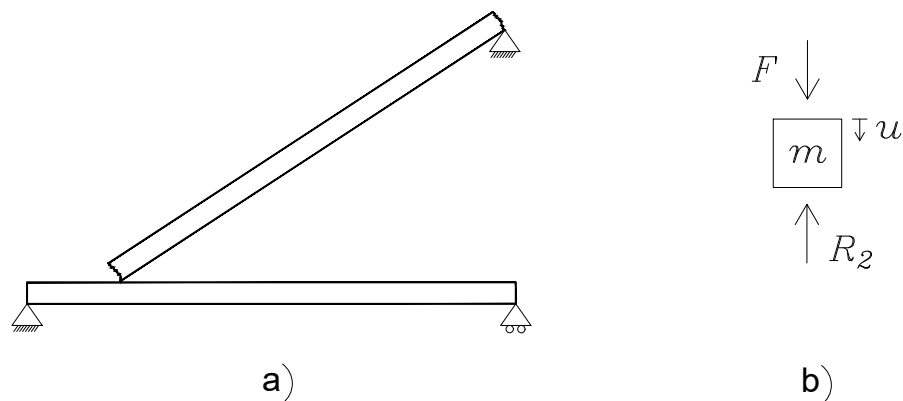


Figure 4.1: Simplified design failure scenario approach.

The magnitude of the reaction R , in the impact between a moving and stationary object is described by the structural response of the structure, in which three responses are relevant illustrated on Figure 4.2, showing a simplification of real world behaviour of different structures and materials.

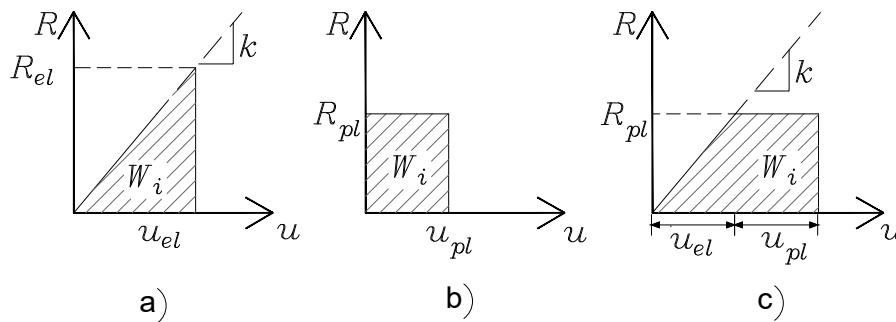


Figure 4.2: Showing the response of a) Elastic, b) plastic and c) elasto-plastic material behaviour.

The magnitude and variation of reaction force, R , depends on the ability of increasing internal energy, W_i , through plastic and elastic deformation of the structure, m , illustrated on Figure 4.1 b). In the elastic response, the reaction capacity, R_{el} , is assumed to be infinite, resulting in a displacement which is fully reversible, with no permanent deformation of the structure. In the plastic response, the material stiffness is irrelevant, and the deformation is permanent. The elasto-plastic behaviour combines the elastic and plastic model, with an elastic range, followed by plastic deformation.

Along with the reaction forces, the impulse created during the impact is of high importance. The shape of the impulse depends on the material properties of the masses in question, such as the stiffness, mass and loading capacity. On Figure 4.3, three different impulses are illustrated, with the shape indicating the response of a, a) elastic material, b) plastic material and c) elasto-plastic material.

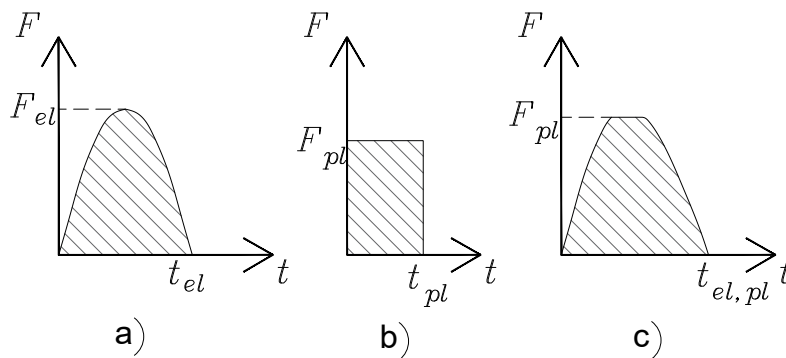


Figure 4.3: Impulse as a result of a) Elastic, b) plastic and c) elasto-plastic material behaviour.

In the case of collision, the ability of the structure to absorb the incoming external energy, W_e , through deformation energy, W_i , is of high importance in the determination of loads. The change in external to internal energy in the case of collision is sketched on Figure 4.4

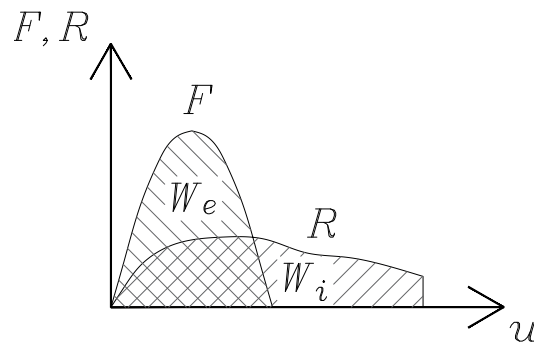


Figure 4.4: Sketch of the change in external and internal energy in a collision.

In general, structures with high stiffness will result in small deformations, but as a consequence with increased reaction force R . Additionally, low stiffness results in increased deformation and lower reaction force R . The latter is preferred in the design of structures, where increased ductility is at focus to ensure the ability of absorbing loads through extensive deformation.

In the real world scenario of a structural failure, the stiffness and mass of the impacting body's are complex, and properties needed to describe such parameters are of high influence on the results.

To secure realistic results of force and deformation in the time of collision, it is important to model the behaviours of the structural components such as

- The elastic deformation properties of steel and concrete
- The cracking of concrete and its influence on the structure stiffness
- The plastic capacity of concrete and steel

4.2 Numerical modelling of RC elements

To create a numerical model that describes the behaviour of reinforced concrete in failure, several material and structural phenomena must be considered and verified as mentioned previously. The material models are described in this section for both concrete and steel. Considering the numerical model size required to model the design failure scenario, the use of continuum shell elements is investigated to reduce compute time, explanation of the benefits of these elements are described in Appendix A.3.5. The initial studies will therefore consist of two numerical models, one with a coarse mesh using shell elements, and one with a fine mesh using solid elements. In the numerical model, two structure types are investigated, initially being a reinforced concrete beam, RCB, to document that simple geometry can be modelled accurately in a failure scenario, followed by a more complex hollow core slab, which is required to model the design failure scenario in the DPCA-building.

4.2.1 Stiffness and deformation parameters

To model the concrete behaviour, the Concrete Damage Plasticity model is used, in which the stiffness of the material is able to vary depending on the damage accumulated through tension and/or compression. The change in stiffness as function of damage is illustrated on Figure 4.5 and 4.6, further described in Appendix A.1.

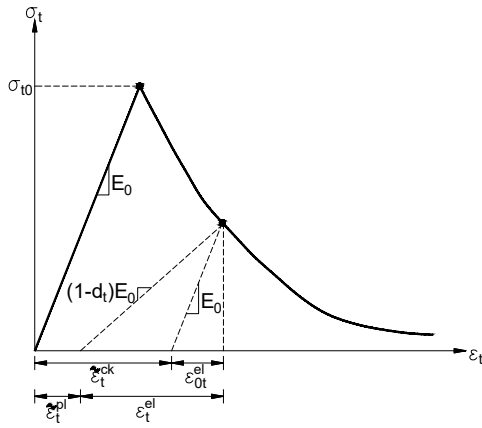


Figure 4.5: Stress-strain curve in uniaxial tension [Dassault Systèmes, 2020]

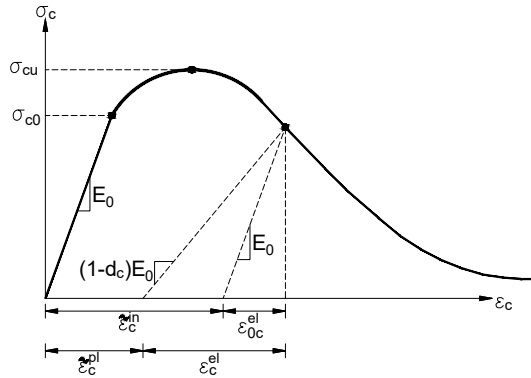


Figure 4.6: Stress-strain curve in uniaxial compression [Dassault Systèmes, 2020]

To use the concrete damage plasticity model, data is required from uniaxial compression and tension tests. These tests are not performed in this project, and therefore data from previously performed experiments are used, obtained by [Tomasz and Łodygowski, 2013]. These experiments are performed on concrete class B50, with a compression strength $f_{ck,cube}$ of 50 MPa. Further description of the data used can be seen in Appendix A.1.

The reinforcement steel is modelled as an elasto-plastic material with hardening. Further explanation of the material model and the values used for rebar material can be seen in Appendix A.1.1 and A.1, respectively.

4.2.2 Bending failure in reinforced concrete

To verify the bending failure of a reinforced concrete element, a reinforced concrete beam element is used as illustrated on Figure 4.7 and 4.8, with measures $h \cdot b \cdot l = 65\text{cm} \cdot 30\text{cm} \cdot 10000\text{cm}$. The bending failure of a concrete beam is investigated in a three point bending test using two different models, being a shell and solid element model, which is further described in Appendix A.3.

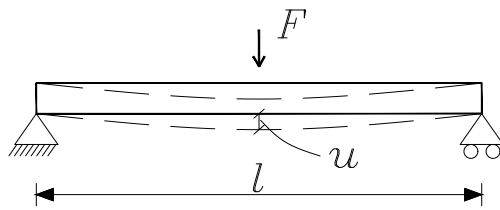


Figure 4.7: Concrete beam support conditions.

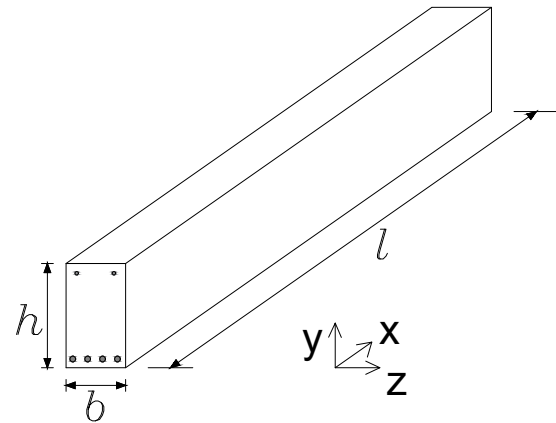


Figure 4.8: Concrete beam orientation.

The RCB is tested using a three point bending test, where the force is increased linearly until failure. In the numerical model of the RCB, element deletion algorithm is used, such that the development of cracks can be illustrated, and the influence of the cracks on the behaviour can be investigated. Since element deletion algorithm is used, the analysis is forced to be explicit, and testing of the bearing capacity can therefore not be static. Since the results from the three point bending test are later used in a comparison with an analytical approach based on static assumptions, quasi-static behaviour in the three point bending test is investigated to assure this condition, and can be seen in Appendix A.3.2. To assure that the failure mode is not a combination of both bending and shear, the RCB is equipped with enough shear reinforcement such that this is not an issue, further explained in Appendix B.1. The shear failure phenomenon is further investigated using a different test as explained in Appendix A.3.4.

The RCB used in the three point bending test is reinforced with non-tensioned rebars, using 4 $\varnothing 20$ and 2 $\varnothing 10$ in the bottom and top respectively. Modelling of the rebar material within the RCB is done through a constraint method known as "Embedded Region" in Abaqus, which is further described in Appendix A.3.3. In this appendix it is shown that the rebar model method has been verified through a test where the rebar is pulled out of the concrete.

The numerical model of the RCB created in Abaqus can be seen on Figure, 4.9. The beam is subjected to a force, F , which is increased linearly over a time span of 10 seconds, further described in Table 4.1.

Table 4.1: Applied load at mid span in three point bending test.

Symbol	Load [kN]	Applied	Time [s]	Steps/s	Total steps
F	180	Incremental	10	50	500

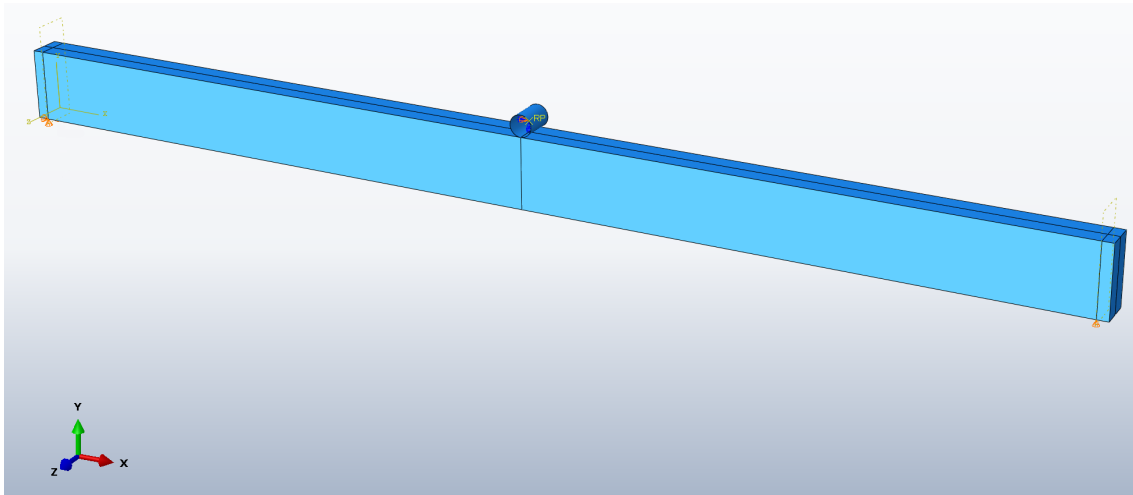


Figure 4.9: RC-beam model in Abaqus.

From the explicit dynamic analysis, the force-displacement curve is obtained as illustrated on Figure 4.10 for both the continuum shell and continuum solid element model. As seen on the figure, the displacement is linear and without sudden changes until the applied force reaches a value of $\approx 38\text{kN}$, where the stiffness of the beam suddenly drops, which originates from the first crack appearing in the beam, as shown on Figure 4.11 for the solid element beam model. The appearance of cracks results in oscillating behaviour of the beam caused by the sudden free fall motion, and the remaining force-displacement curve is affected by this phenomenon. At the appearance of the first crack the two models start to deviate from each other, and the shell element model is seen to predict a higher stiffness than the solid element model, which can be explained by the fewer number of finite elements, making the shell model less susceptible to development of cracks.

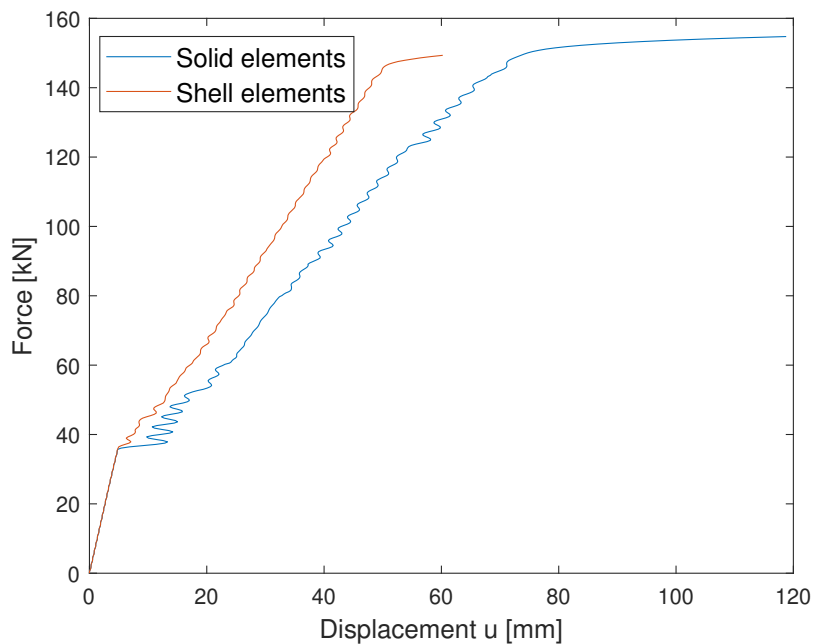


Figure 4.10: Force-displacement curve of the shell and solid element model.

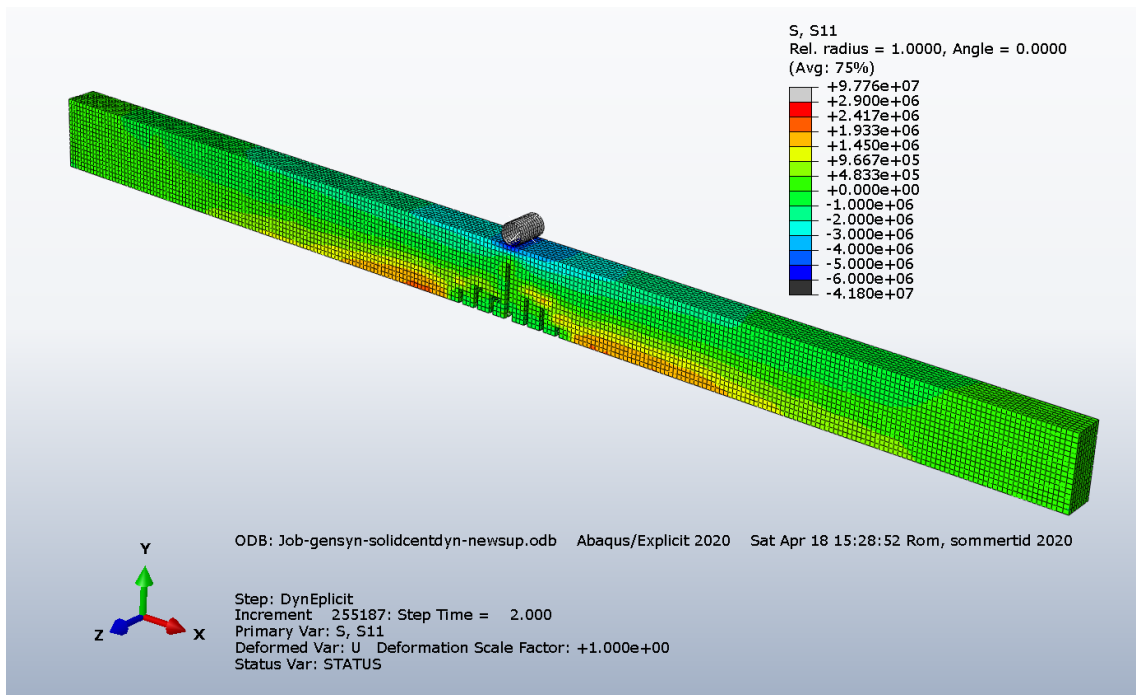


Figure 4.11: Cracked RCB modelled with solid elements. The normal stress in the x-direction is shown, with red indicating tension and blue indicating compression.

Element type	Abaqus model setup (Figure 4.11)		
	No. of elements	Material	Other
Solid continuum C3D8R	34178	Concrete-01	Element deletion and Contact
Timoshenko beam B31	1296	Steel-01	Embedded region
Analysis type:		Explicit dynamic	

The results of the two numerical models are compared with the RCB moment capacity determined with the use of Eurocode [DS/EN-1992, 2007], described in Appendix B.1. The shell and solid element solution is seen to show small deviations in moment capacity as shown in Table 4.2. These deviations are evaluated as being small considering that the analytical approach neglects concrete tension strength and therefore is expected to be lower. The solid and shell element model is therefore deemed capable of describing the failure behaviour of a RCB.

Table 4.2: Moment capacity of the beam calculated with two different element types. Both moment capacities are larger than the analytical solution that showed a moment capacity of 372 kNm.

	Solid	Shell
Moment capacity [kNm]	376.4	379.9
Deviation from analytical solution [%]	1.14	2.08

From the RCB three point bending test it was found that the beam had both an uncracked bending stiffness, k_1 , and a cracked bending stiffness, k_2 , both of which was determined in

Appendix A.3.1 in the shell and solid element model, and can be seen in the following table.

Element type	k_1 [MN/m]	k_2 [MN/m]
Solid	7.4	2.3
Shell	7.5	3.0

4.2.3 Hollow core slab verification

In the design failure scenarios described in section 3, the RC-elements used consist of hollow core slabs, HCS, and therefore it deviates from the solid RCB investigated previously. The most important deviations from the solid RCB consist of:

- The slab elements use pre-stressed bottom reinforcement
- The geometry is significantly more complex with longitudinal cylindrical holes to reduce weight

To verify the HCS in Abaqus it is compared to an identical HCS model from CHR Concrete. The HCS used is a DB220 with section dimensions as shown on Figure 4.12 with the meshed model in Abaqus illustrated on Figure 4.13. To accurately describe the geometry of the slab with holes, a fine mesh is used. Further description of the model and test results is shown in Appendix A.4.

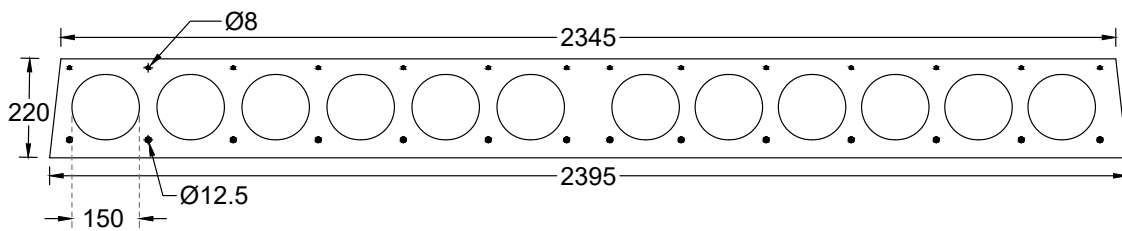


Figure 4.12: HCS cross section with dimensions. All measures in [mm]

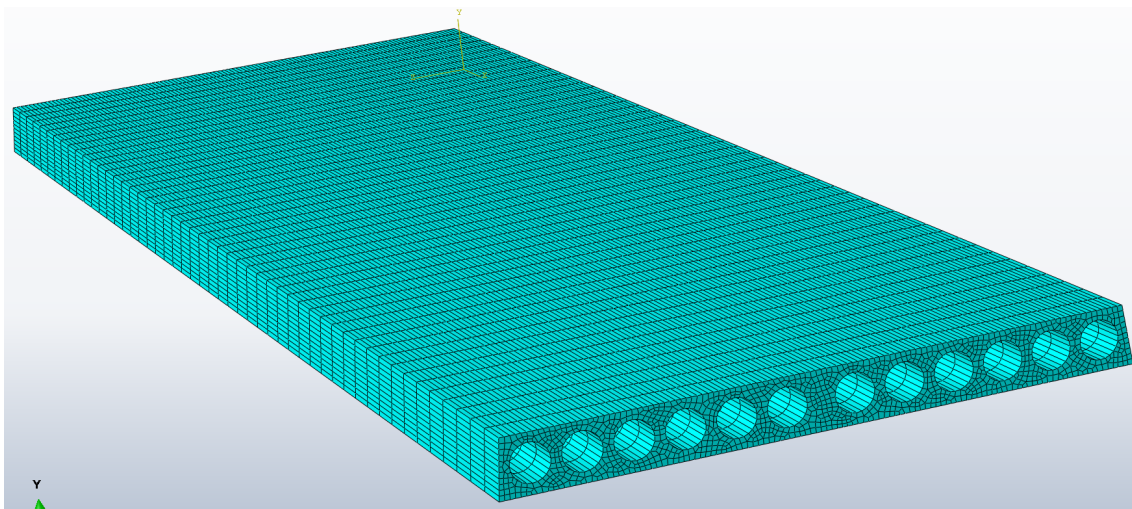


Figure 4.13: Full model of HCS meshed in Abaqus.

To assure that the bearing capacity of the slab can be compared with the manufacturer CHR concrete stated load capacity, prestressed reinforcement is implemented by cooling down the embedded rebars placed in the bottom until sufficient values of tension have been reached.

The testing conditions follow the same procedure as described in the RCB section. Modelling of the HCS model is only done using solid elements, since the number of elements required to describe the complex geometry requires a large amount of elements, and the stated benefits of the continuum shell disappears. The failure load capacity determined from the numerical calculation along with the design moment capacity stated by the manufacturer CHR Concrete is shown in the table below.

	Solid elements
Characteristic moment capacity in Abaqus [kNm]	180.1
Design moment capacity from manufacturer [kNm]	164.6
Deviation from manufacturer specification [%]	9.4

The concrete strength data in the CDP model is based on a model with a characteristic strength, f_{ck} , of 40 MPa as described in Appendix A.1. This limits the ability to recreate the HCS from CHR Concrete since CHR concrete uses a characteristic strength, f_{ck} , of 55 MPa [CHR Concrete, 2020]. Specifically the pre-tension rebars can not be loaded to 1050 MPa as CHR concrete specifies since the concrete in the model fails. Therefore the pre-tension in Abaqus is set to 825 MPa instead. The moment capacity stated by the manufacturer CHR Concrete is a design moment capacity, and is therefore expected to include safety factors resulting in a decrease in value. However when taking into consideration the lower pre-tension stress and the weaker concrete strength, it is expected that the moment capacity of the HCS in Abaqus should be comparable with the capacity stated by CHR Concrete. The difference in moment capacity between the two slabs was found to be 9.4% and the finite element model is assessed as a good description of the real HCS.

To use the HCS in the description of the design failure scenario described in section 3.4 would require large computational performance. The possibility of creating a simplified model is therefore investigated. The pretension effect in the HCS was found to have large effects on the dynamic behaviour of the HCS, and a small influence on the computational costs, and pretension is therefore used continuously in simpler models.

Changes to the geometry does however have large influences on the computational cost, and therefore the cylindrical holes are removed, and the material properties are changed such that the bending stiffness and total mass of the slab remains close to the HCS model, further described in Appendix A.4. Although the solid slab replica of the HCS behaves like the original HCS, further simplifications is done, since it still would be very time consuming to use a model that size in a dynamic explicit analysis, without gaining much more information about the dynamic loads. This is why the slab width is reduced from 2.4 m to 1 m, thereby reducing the number of elements with 85%. This is considered a reasonable choice since the change of the width will result in a negligible difference on the end result for the DFS case that is selected for investigation. Although the Youngs modulus of the simplified model is decreased to reduce the bending stiffness, the shear stiffness

will increase because of the increased cross-section area. This effect is not investigated further, since the response of the slab during the design failure scenario is assessed as being primarily bending orientated. The simplified cross section of the slab is seen on Figure 4.14.

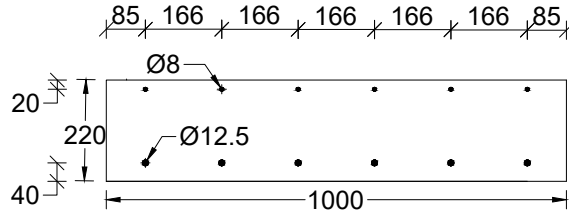


Figure 4.14: Simplified HCS cross section with dimensions. All measures in [mm]

To ensure that all the changes does not result in a change in the behaviour of the slab, a frequency analysis is performed in Abaqus. For bending behaviour the first and third mode is relevant, where the first mode can be seen on Figure 4.15 and Figure 4.16 for the full HCS model and the simplified version, respectively, with the belonging Abaqus model parameters shown in the table below. Comparison of the third mode frequency can be seen in Appendix A.4.1. From the first and third mode comparison it is seen that the frequency deviates by less than 3% for both the natural frequencies. Furthermore the bending stiffness after crack development is also verified which can be seen in Appendix A.4.

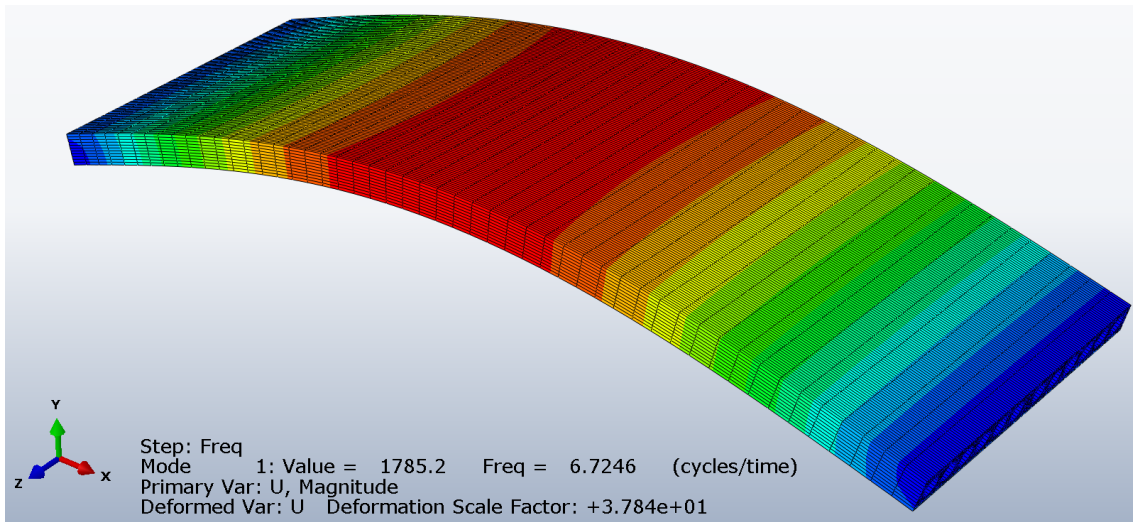


Figure 4.15: The first mode of the full HCS model: Mode 1: 6.725 Hz

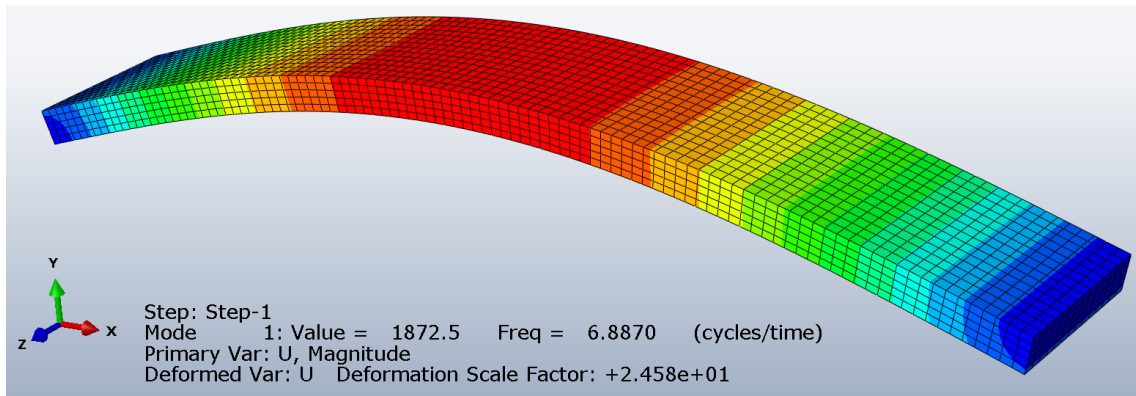
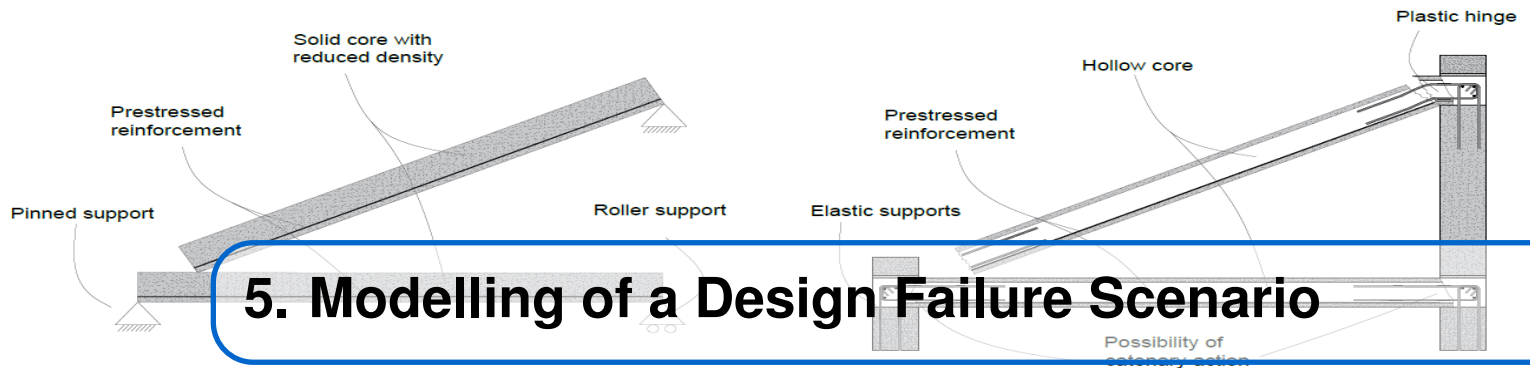


Figure 4.16: The first mode of the simplified HCS model. Mode 1: 6.887 Hz

Abaqus model setup (Figure 4.15)			
Element type	No. of elements	Material	Other
Solid continuum C3D8R	48800	Concrete-01	No
Timoshenko beam B31	504	Steel-02	Embedded region
Analysis type:		Frequency analysis	

Abaqus model setup (Figure 4.16)			
Element type	No. of elements	Material	Other
Solid continuum C3D8R	7210	Concrete-02	No
Timoshenko beam B31	216	Steel-02	Embedded region
Analysis type:		Frequency analysis	



In this chapter the previously used modelling techniques are tested in a large numerical model for a real world scenario referred to as the Da Vinci collapse. The results are hereafter discussed, and the effects present in the simulation is investigated using a simpler model referred to as the DFS which were discussed in section 4.1. The static equivalent loads are furthermore investigated for the DFS, and the position of impact and drop height is investigated in a parametric study.

When investigating shell elements it was found that even though they were continuum shell elements with translational degrees of freedom which should be able to calculate shear stress they were not very accurate in transverse shear, as demonstrated in Appendix A.3.4. In the design failure scenario the shear stress is important since especially concrete structures are susceptible to shear failure and unlike the previous quasi-static bending test that gave good results, the lack of through thickness change in the simulations will result in the shell being too stiff and thus give inaccurate results. Therefore will other models in the following chapters only use solid elements for the concrete material and beam elements for the rebar.

5.1 The Da Vinci collapse

When modelling the design failure scenario that is chosen to be investigated further, both of the concrete slabs are expected to deform extensively, which will result in severe cracking from a combination of bending and shear. In reality the behaviour of concrete slabs in dynamic failure is not a well documented topic, and therefore it is difficult to verify how well a complex numerical model will imitate reality. One known and recent dynamic failure of a concrete structure is the failure of a balcony, where the support of two concrete slabs failed, resulting in complete failure of the corner. The collapse happened in an area known as the "Da Vinci parken" in Denmark, and the collapse is in this report referred to as the Da Vinci collapse.

Images from the event is seen illustrated in Figure 5.1 and 5.2, furthermore it should be noticed that the bottom slab have experienced a bending type crack at the mid-span of the slab which is shown in the red circle.



Figure 5.1: Image from the Da Vinci failure. Image: Nordjyske Stiftstidende [2019].



Figure 5.2: The Da Vinci collapse with the crack in the slab circled in red. Image: Nordjyske Stiftstidende [2019].

Since there is no detailed description of the behaviour in the small time span of failure, it can only be guessed on how the slabs fell. It is suggested that it originated from only one of the supports, such that the slab started to pivot around one of the supports for the first few milliseconds, after which the remaining support is assumed to fail resulting in complete failure. The support which started to fail is estimated to be the wall furthest away on Figure 5.1, since this wall contained a large door opening.

A sketch of the failure is illustrated in Figure 5.3, where the failure originates in the right bottom wall.

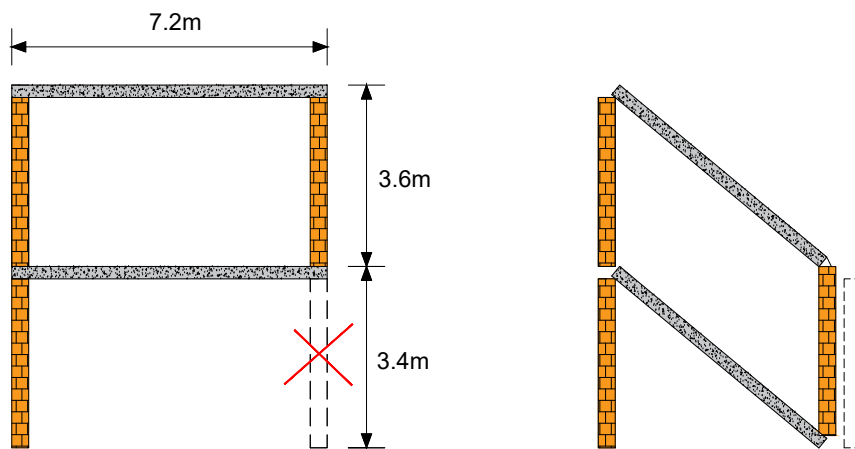


Figure 5.3: Simplified model of the Da Vinci collapse.

The Da Vinci collapse is modelled in one complete model, where the slabs and walls are created without the presence of the right lower wall. The white/grey rectangular shapes is meant to simulate the ground and the remaining structure, where they are modelled without any degrees of freedom and therefore are fully rigid. In reality both the ground and the back wall would be able to deform, and this could mean that the event would collapse in a different manner. However this model is mostly meant to show how well the RC structural members work in a complex numerical model, in order to determine possible issues. Further description of the model is shown in Appendix D.1

During the numerical simulation the energies present in the whole model is extracted for further analysis. Three figures are extracted from the numerical analysis as shown on Figure 5.4, 5.6 and 5.8 along with the belonging internal energy present in the whole model as illustrated on Figure 5.5, 5.7 and 5.9.

The behaviour of the brick walls and concrete slabs can be described in three steps;

- Figure 5.4, After ≈ 600 ms of free fall motion the first crack appears in the concrete bottom and top slab.
- Figure 5.6, the right end of the bottom slab reaches the ground and damage increases rapidly.
- Figure 5.8, shortly after the first impact with the ground, the damage continues to develop through the slabs.

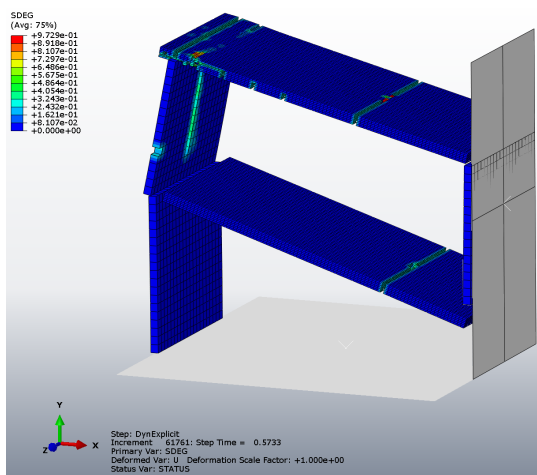


Figure 5.4: Appearance of first cracks.
Time = 600ms.

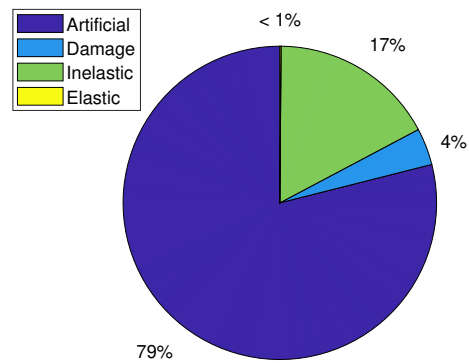


Figure 5.5: Internal energy distribution at 600ms.

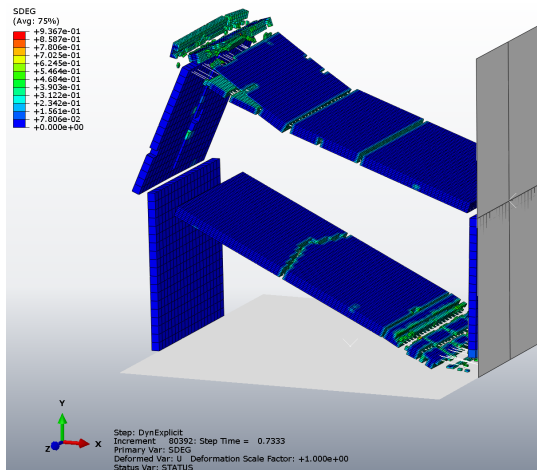


Figure 5.6: Slab reaches rigid barrier.
Time = 750ms.

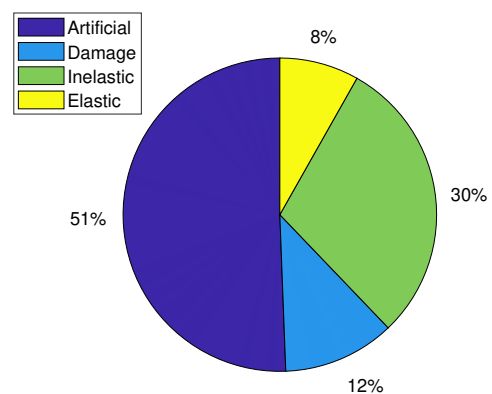


Figure 5.7: Internal energy distribution at 750ms.

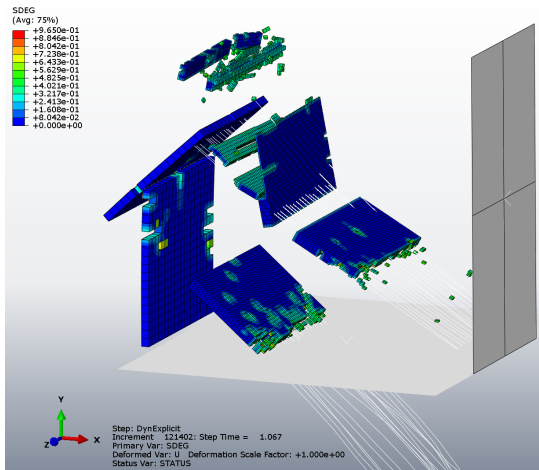


Figure 5.8: Model continues to show extensive damage behaviour. Time = 1150ms

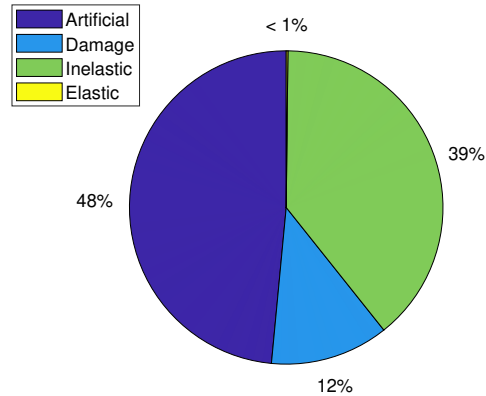


Figure 5.9: Internal energy distribution at 1150ms.

When considering the accuracy of the simulation, both positive and negative observations can be made on the behaviour seen on the three figures above. Some of which are:

- In the initial first milliseconds the two slabs are seen to experience bending type cracks which was the expected response.
- When continuing the simulation, the model shows signs of improper physical behaviour, where excessive damage and separation is present.
- Both the slabs and walls seems to show behaviour of element deletion in the time of impact with the rigid barrier, where instead of bouncing back or laying on the barrier, all elements modelled with element deletion disappears, leaving only the rebar material.

The errors present on the numerical model makes it necessary to further study the energies present in the model, which is advantageous to look at in large numerical simulations which model multiple physical phenomena, since it can help understand what happens.

The energy present in the model consist of multiple contributions, which is described in detail in Appendix D.1. The interest is in how the kinetic energy built up from the falling motion is distributed to internal energy. In reality, all of the kinetic energy built up from the falling motion must be distributed purely by the elastic and inelastic deformation of the body. In Abaqus however, internal energy also consist of artificial energy, which indicates the energy used in the algorithm to counteract hour-glassing phenomenon, and can be used to conclude whether or not the results are trustworthy.

The internal energy of the model therefore consist of four main contributions, being Artificial, Damage, Inelastic and elastic strain energy. The four energy contributions to the internal energy is extracted at the times identical to the three Figures illustrating the damage behaviour.

Examining the internal energy on Figure 5.5 in the time of initial cracking, several observations can be made about the behaviour, such as:

- The absence of elastic strain energy is explained by the fact that the main structure is

in free fall motion.

- The inelastic and damage energy is the product of initial cracking in the bottom and top slab.
- The energy used to control hour-glassing phenomenon is seen to be much higher than the remaining contributions, which indicate that improvements should be made towards mesh refinement.

Following the time of initial cracking, the internal energy is in general seen to increase as shown in Appendix D.1, furthermore the energy distribution changes at the time of impact between the slab and rigid body as shown on Figure 5.6. The impact results in an increase in both the inelastic and damage energy, as well as elastic energy, which stems from the impact force being distributed through the bottom slab.

At time 1150ms, the internal energy shown on Figure 5.9 is again seen to lack the elastic energy caused by the free fall motion, as well as the inelastic and damage energy seen to have increased, which continues to rise until complete deterioration of the model.

In general some of the phenomenon expected in a failure scenario with concrete elements are seen in the Da Vinci failure model, but considering the real life failure shown on Figure 5.1 and 5.2, adjusting of the model is required. Factors such as mesh refinement, time increment, element deletion and damage all have large influence on the results. From the Da Vinci model it shows that it is important that studies are conducted using a more simple and manageable numeric model, where the mentioned factors are investigated.

5.2 Design Failure Scenario from DPCA-building

From investigating the DPCA-building, one relevant design failure scenario is the collapse of a wall, which acts as support of slabs. The sudden loss of support results in the slab now being a mechanism, such that it is expected to rotate around the remaining support, and finally impacting the bottom slab with the corner. In this type of impact, multiple structure characteristics are present which has an effect on the results, some of which are illustrated on Figure 5.10 B). To include all of these characteristics in one single model requires large computational effort, and would make the problem too time consuming for a project of this size.

The DFS is in this project simplified to a case illustrated on Figure 5.10 A), where the hollow core slab is simulated with a solid core model with reduced stiffness and mass, and the support conditions now are either pinned or with roller support.

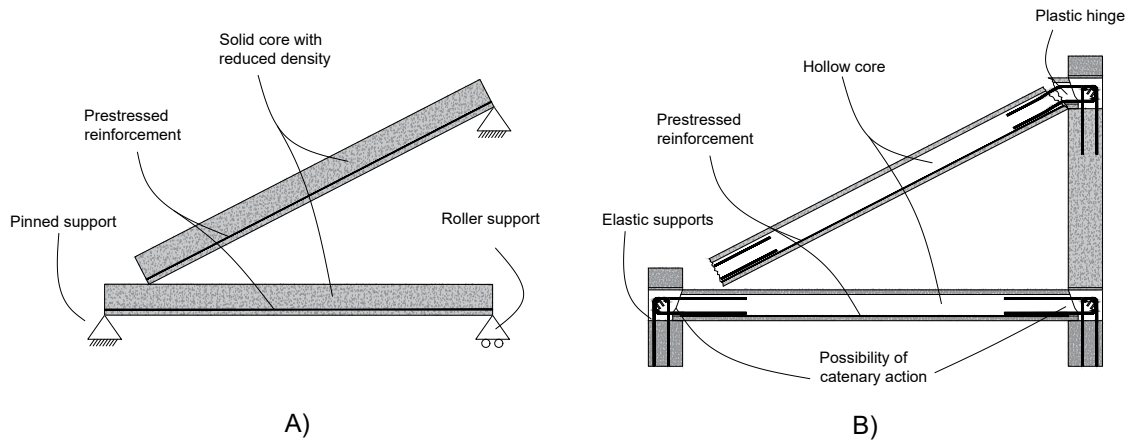


Figure 5.10: Sketch of the impact and reaction force.

In the design failure scenario, the top slab is initially horizontal, after which the top left support are removed to simulate a sudden removal of a wall. Shortly after removal, the top slab will impact the bottom slab, and all of the kinetic energy built up from the free fall motion is converted into deformation and damage of the two slabs. The impact load phenomenon is mentioned in the Eurocodes when determining loads from e.g. cars or trucks, which is relevant in the case of identified accidental actions. [DS/EN-1991, 2007].

The Eurocode divides the type of impact into two, being either a hard or soft impact. There are two different assumptions about the impact:

- The hard impact assumes that the kinetic energy of the impacting object is dissipated through elastic strain energy in the impacting object.
- The soft impact assumes that the kinetic energy of the impacting object is dissipated through elastic and plastic deformation of the structure.

If assuming that either of these two definitions are true for the impact case, simple calculations can be made to determine the impact force between the falling slab and bottom slab, which is further investigated in Appendix F.3 and later in the report.

Even though that the impact force between the two objects can be determined with a simple approach, the interest in this project is the response of the bottom slab, and whether it may hold when subjected to the large impact forces from the falling slab. The ratio between the reaction force in the bottom slab and the force applied in the impact is in the Eurocodes referred to as the dynamic load factor, DLF, illustrated on Figure 5.11. Even though that methods exist to determine the impacting force, the reaction force and therefore dynamic load factor is in the Eurocodes not mentioned how to calculate, only a recommendation that a direct dynamic analysis should be used.

$$DLF = \frac{\text{Reaction force}}{\text{Impacting force}} \quad (5.1)$$

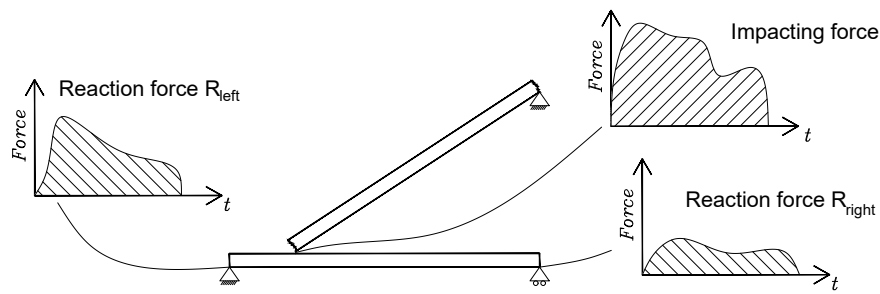


Figure 5.11: Sketch of the impact and reaction force.

The forces in the impact are determined in three different points, being at the area of impact, referred to as the "impacting force", and at the right and left support referred to as R_{right} and R_{left} respectively, as sketched on Figure 5.11. The reaction and impacting force distribution can vary in both size and shape depending on several factors as described previously in section 4.1.

To investigate the impact force, two models are created, where the only difference is the element deletion algorithm, which is not used for the first model, and then later used for the second.

5.3 DFS without element deletion

The DFS model setup is illustrated on Figure 5.12. The top slab is supported at the right most end using pinned supports, and the bottom slab is supported by pinned and simple support conditions for the left and right end respectively, as illustrated on Figure 5.13. Throughout the report the position of impact is referred to using a position parameter, α , and the height difference is referred to as, H , both of which is shown on Figure 5.13.

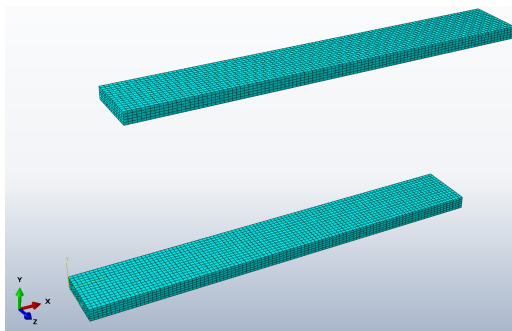


Figure 5.12: Numerical model of DFS in Abaqus.

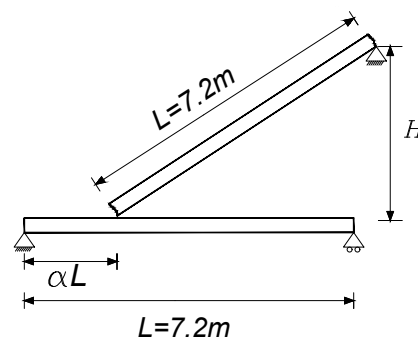


Figure 5.13: Definition of position parameter, α , and height, H .

Since the aim of the project is to determine the size of the reaction forces, influence on the reaction force and energy distribution from mesh refinement is investigated using four

different levels of mesh refinements as described in Appendix D.2. In the mesh refinement analysis, the position parameter is kept at $\alpha = 0.3$, with a height, H , of 3m.

The mesh refinement investigation indicates that convergence is reached with the second most refined mesh, which is chosen for further studies. The impact behaviour of the two slabs 8ms after the time of initial impact, T_I , and 136ms after is shown on Figure 5.14 and 5.15

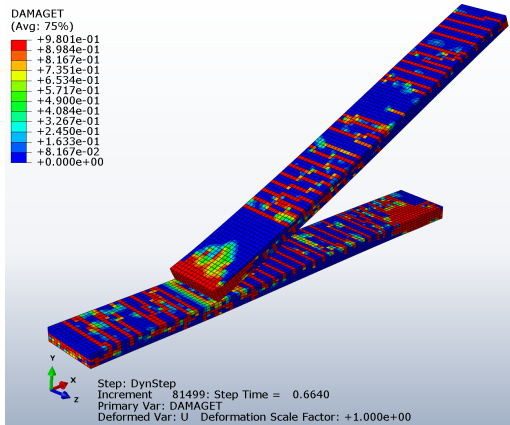


Figure 5.14: Tension Damage at $T_I + 8\text{ms}$ [$\alpha = 0.3$ & $H = 3\text{m}$]

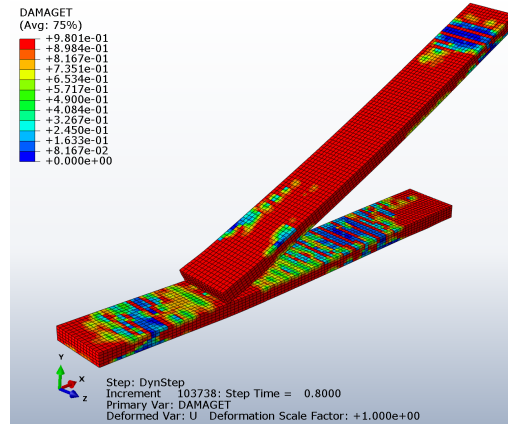


Figure 5.15: Tension Damage at $T_I + 136\text{ms}$ [$\alpha = 0.3$ & $H = 3\text{m}$]

Abaqus model setup (Figure 5.14)			
Element type	No. of elements	Material	Other
Solid continuum C3D8R	14420	Concrete-02	Contact
Timoshenko beam B31	432	Steel-02	Embedded region
Analysis type:		Explicit dynamic	

From the numerical simulation, the reaction force and impact force are extracted for analysis, which can be seen on Figures 5.16, 5.17 and 5.18 for the impact force, left and right reaction force respectively. Because of the large variety in force, the peak force are stated in Table 5.1, such that the response after is visible.

Table 5.1: Peak force determined with GS005 mesh [$\alpha = 0.3$ & $H = 3\text{m}$]

Mesh type	Impact force [kN]	R_{left} [kN]	R_{right} [kN]
GS005	1578	250	105.6

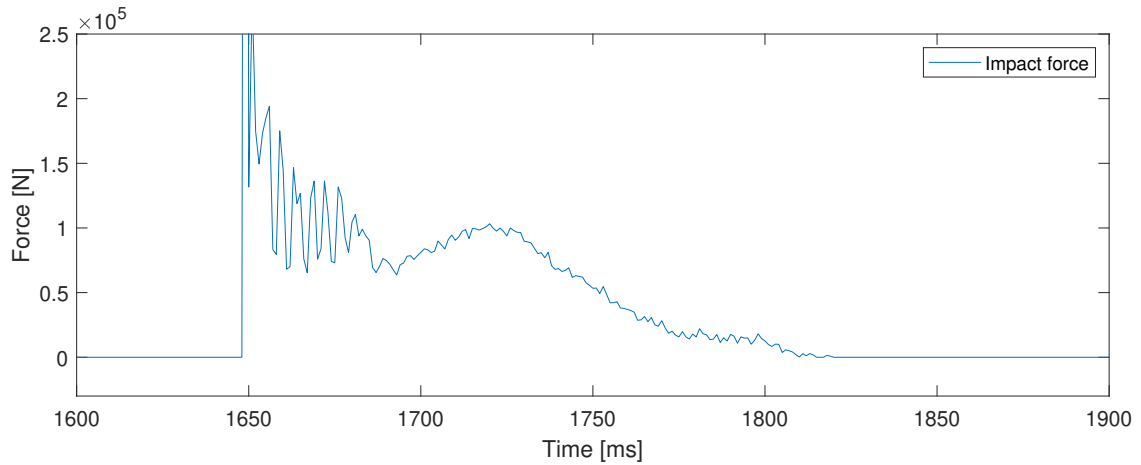


Figure 5.16: Impact force, [$\alpha = 0.3$ & $H = 3\text{m}$, GS005]

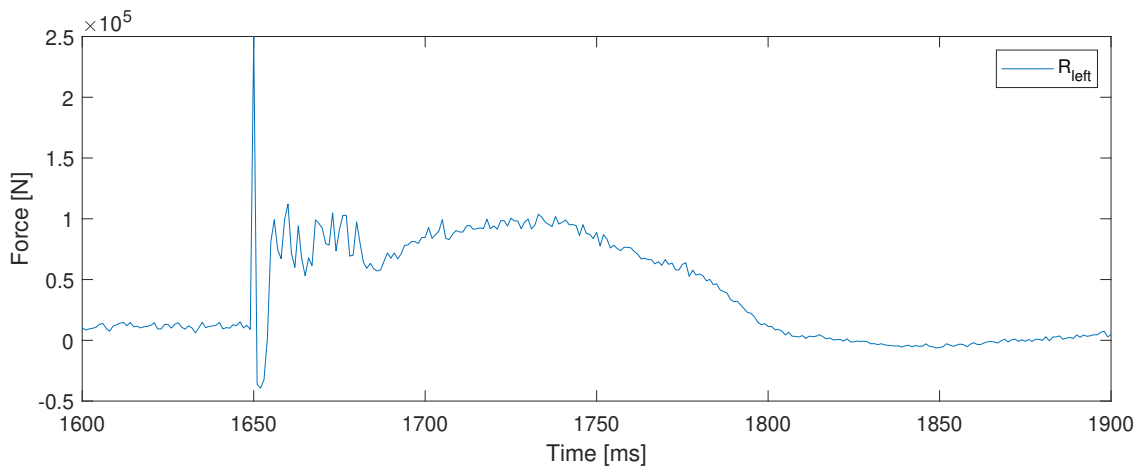


Figure 5.17: Left reaction force, R_{left} . [$\alpha = 0.3$ & $H = 3\text{m}$, GS005]

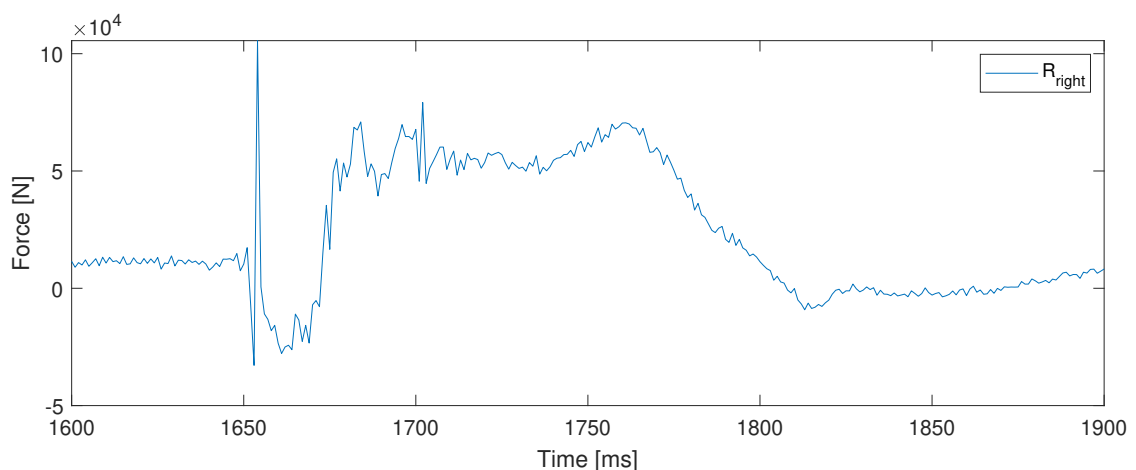


Figure 5.18: Right reaction force, R_{right} . [$\alpha = 0.3$ & $H = 3\text{m}$, GS005]

As seen on the impact force 5.16, the initial contact results in very large forces, with the largest spike reaching a value of 1.57 MN. The initial large spikes are, however, not

considered as an accurate representation of the real world behaviour since a much finer mesh is required to model this accurately, and furthermore the chosen contact algorithm, "hard contact", can result in large spikes in the initial steps of contact, further described in Appendix C.1.

The reaction force from the bottom slab illustrated on Figure 5.17 and 5.18 for the left and right support respectively, is seen to show the same sudden spike behaviour, after which the estimated force shows a more smooth representation. From the reaction forces it can furthermore be seen that the initial impact force results in a negative reaction force, indicating that the ends of the slab below is forced upwards in the initial stages of impact.

Investigation of this phenomenon is done through the deflection curve found in the numerical simulation, as illustrated on Figure 5.19. Although very small, the phenomenon is seen present on both sides of the applied impact force, and to greatest extent on the right side, where the deflection at time of impact plus 12 ms, $T_I + 12$ ms, after impact is above the initial deflection curve. This phenomenon is present because of several factors, such as the arc effect from the pre-tensioned reinforcement, and the effect of inertia of the bottom slab, further investigated in a more simple model.

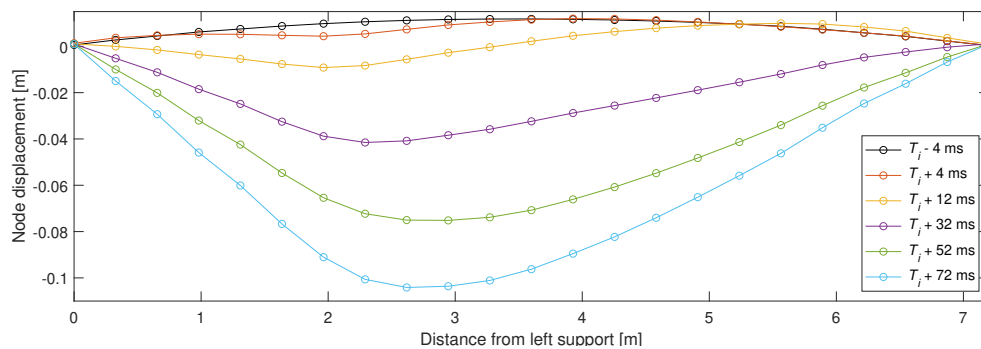


Figure 5.19: Displacement behaviour of the bottom slab before and during impact. [$\alpha = 0.3$ & $H = 3$ m, GS005]

The reaction force following the sudden lift follows a smooth pattern where the kinetic energy is gradually converted to deflection of the slabs, after which the bottom slab is seen to experience vertical oscillation behaviour at ≈ 1800 - 1900 ms, identified by both the sudden drop in reaction force which briefly is in tension. Furthermore it can be seen by how the contact force reaches zero, indicating that the impacting slab is bouncing upwards away from the bottom slab.

In static conditions, the sum of applied force is equal to the sum of reaction force felt at the support, this condition may be far from true when the behaviour is dynamic. Investigation of this condition is done through comparison of the impact force and sum of reaction forces as seen on Figure 5.20. It must be noted that the reaction force and impact force is smoothed using a Butterworth filter, such that high-frequent behaviour is smoothed out, an example of the use of the filter can be seen in Appendix D.3, and is applied for comparison reasons. As seen by the comparison, the two forces are far from equal. In the initial few milliseconds of the impact, the impact force is larger than the reaction forces, caused by the inertia of the bottom slab, and the reaction forces therefore do not feel the

total applied force. Following the peak in impact force, the reaction forces are seen to increase to values larger than the applied force, and there is no sign of compliance with the static conditions.

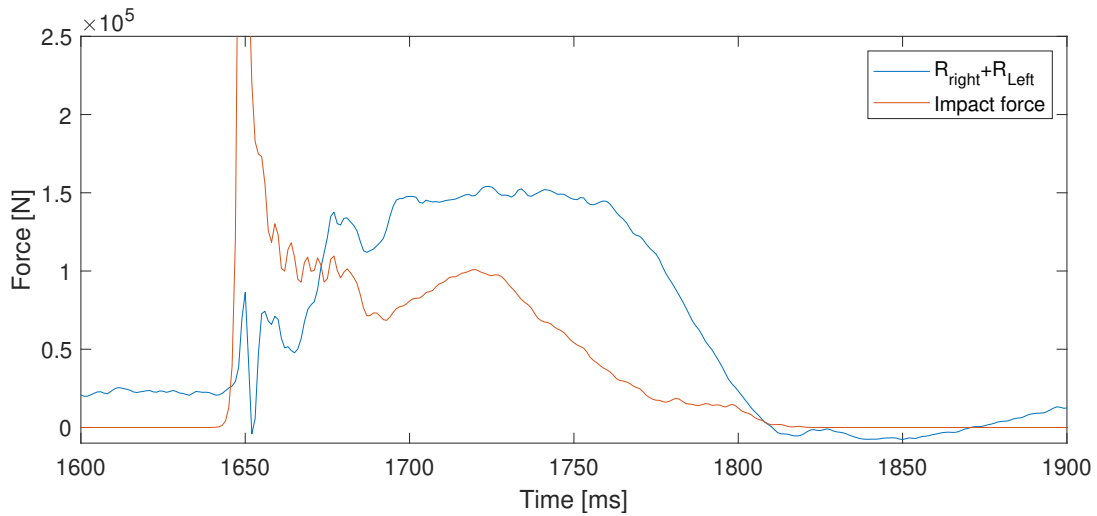


Figure 5.20: Total reaction force comparison with impact force, [$\alpha = 0.3$ & $H = 3\text{m}$, GS005]

The behaviour of the model is furthermore investigated using the individual contributions to energy in the model. The total and internal energy contributions can be seen on Figure 5.21 and 5.22. The total energy of the model is seen to start at 20kJ, which originates from the prestressed reinforcement performed in a previous step in the analysis in Abaqus. The top slab is dropped at 1000ms, after which the kinetic energy is increasing exponentially until impact at approximately 1650 ms. From the time of impact and forward, the kinetic energy is seen to decrease rapidly, while the internal energy and viscous dissipated energy increases. The contributions to internal energy is seen to mainly consist of the elastic and inelastic strain energy, with small contributions to damage and artificial energy. The behaviour from an energy point of view does in the initial 50 ms show expected behaviour. After this point, the elastic strain energy and therefore internal energy starts to decrease far below zero which physically does not make sense. This error in elastic strain energy is accompanied with suspicious high values of viscous dissipated energy used to dampen the structure. This damping is part of how Abaqus run the explicit dynamics analyses and this is further described in Appendix C.2.

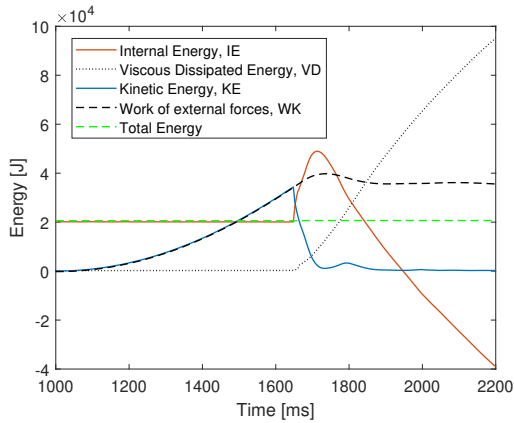


Figure 5.21: Total energy contributions. [$\alpha = 0.3$ & $H = 3m$, GS005]

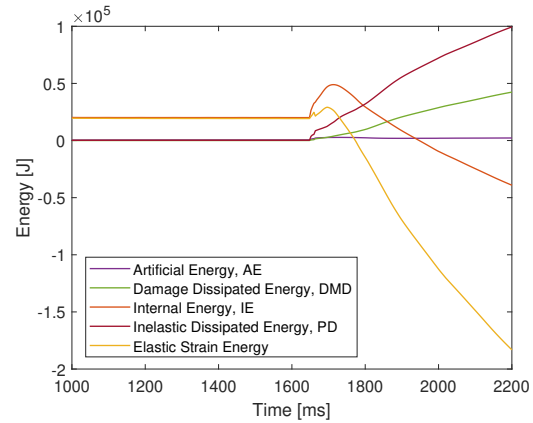


Figure 5.22: Internal energy contributions. [$\alpha = 0.3$ & $H = 3m$, GS005]

5.4 DFS with element deletion

The effect of using element deletion on the results is further investigated using the same DFS as was used previously, with the mesh refinement being GS007 described in Appendix D.2.

The DFS with element deletion is seen on Figure 5.23 and 5.24, which illustrates the behaviour at the exact same two time steps as was illustrated previously.

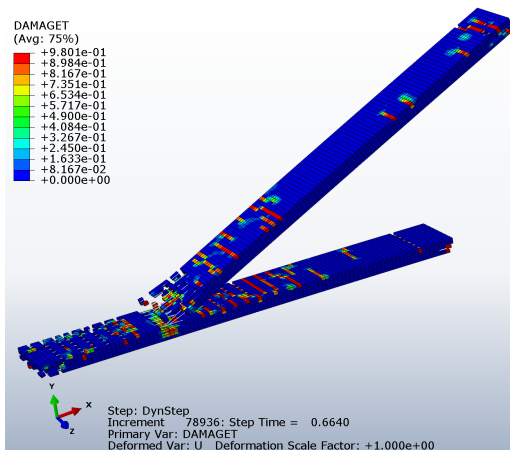


Figure 5.23: Tension Damage at $T_I + 8ms$ [$\alpha = 0.3$ & $H = 3m$]

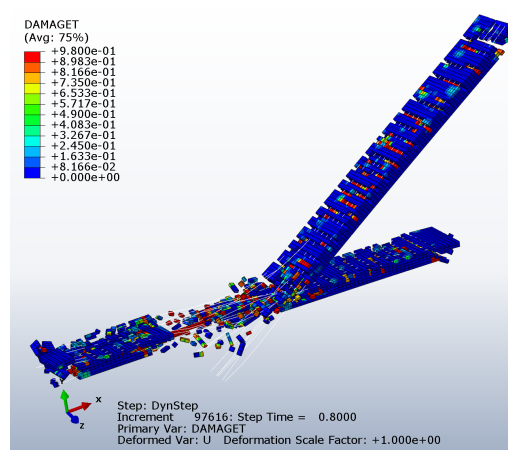


Figure 5.24: Tension Damage at $T_I + 136ms$ [$\alpha = 0.3$ & $H = 3m$]

It is clear from the two figures that the two slabs experience extensive damage right from start of impact. Furthermore the model experiences damage at the supports to an extent such the support fails for both the slab below and above, resulting in free fall motion for both of the slabs. The total and internal energy is seen illustrated on Figure 5.25 and 5.26 respectively. The dynamic simulation initiates at 1000ms, which can be seen by the exponential increase in kinetic energy and external work. at $\approx 1650ms$ the slabs impact each other, after which the elastic strain energy built up from the pre-tensioned rebars is

converted because of extensive damages, as well does the damage, inelastic and artificial energy increase which results in an increase in internal energy.

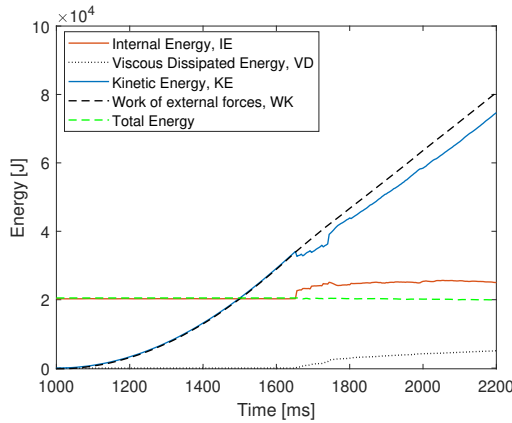


Figure 5.25: Total energy contributions. [$\alpha = 0.3$ & $H = 3m$]

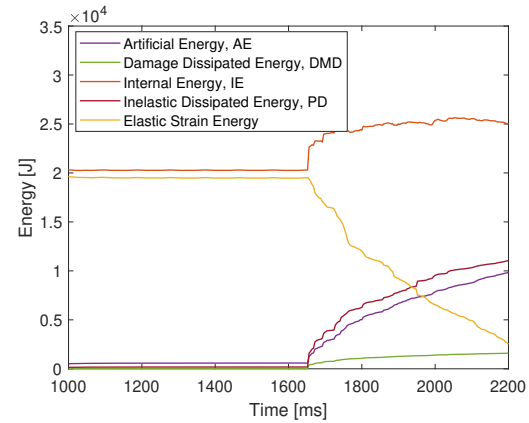


Figure 5.26: Internal energy contributions. [$\alpha = 0.3$ & $H = 3m$]

Comparing the model with and without element deletion, it is clear that when using the element deletion algorithm, the results are changed significantly. In the model without element deletion, all of the kinetic energy was forced to be absorbed into deformation, resulting in a fast drop in kinetic energy, and therefore an increase in internal. With the element deletion model however, the kinetic energy only experiences a small drop in the time of impact, after which it continues to increase caused by the free fall motion of both the slabs. Further inspection of the internal energy differences with and without element deletion reveals that the contribution to artificial energy is now considerably higher when using element deletion, an example can be seen on Figure 5.27 and 5.28.

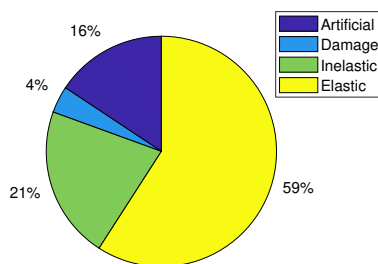


Figure 5.27: Internal energy contributions with Elm-Del [$T_I + 44ms$]

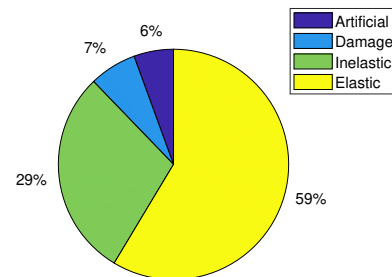


Figure 5.28: Internal energy contributions without Elm-Del. [$T_I + 44ms$]

In general the model without element deletion is seen to give substantially better results in the time of impact, both in estimation of impact forces and in the conversion of kinetic energy to internal energy. The energy does however show the sudden decrease in elastic strain energy, and the credibility of these results is therefore later investigated using a more simple model. Although a numerical model where element deletion is used throughout did not result in usable results, the option of creating hinges where the slab can break as

seen in the Da Vinci failure is possible using this algorithm, and this is further investigated.

5.5 DFS with partwise element deletion

In the design failure scenario without using element deletion, it was found that damaged elements were more concentrated in certain areas, as illustrated on Figure 5.14. These areas suggest that it may be possible for hinges to develop, in which case the response may be very different. This possibility is investigated by inserting strips of elements with the same characteristics as previous, such that the element is removed when enough damage has accumulated. Three simulations are performed with one, two and three strips with element deletion activated, which are placed as shown on Figure 5.29. The choice of placement is based on where most of the initial damage development is seen to appear in the model without element deletion. Figures used to determine the placement of strips is shown in Appendix E.1. In the first model only one strip is used, referred to as "Strip 1", the second model consists of both "Strip 1" and "Strip 2", the last model consists of all of the illustrated strips.

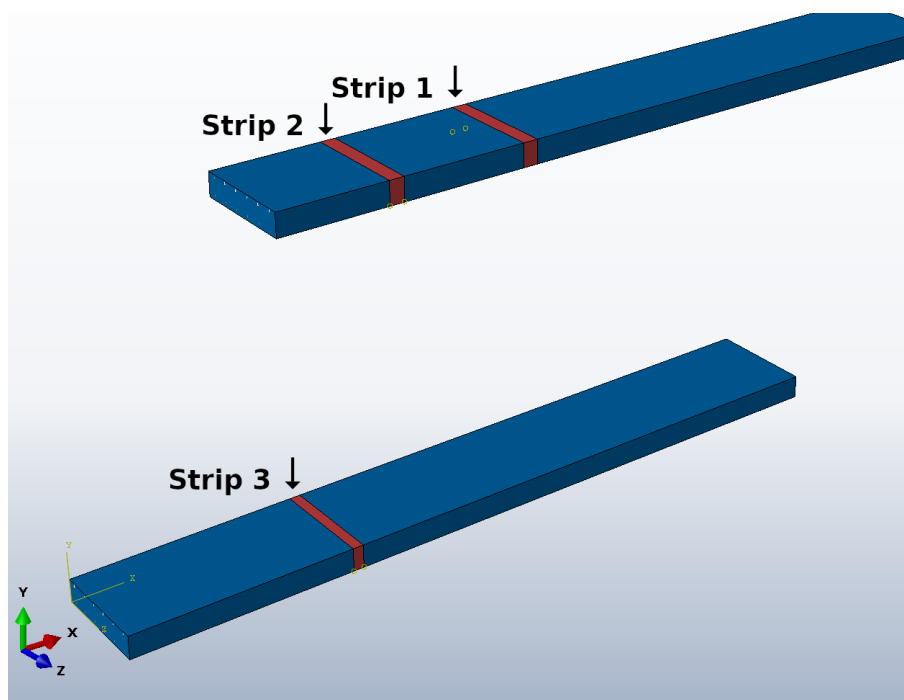


Figure 5.29: Placement of strips which are allowed to be deleted when damaged.

In the simulation of the impact, the strips of element deletion are seen to develop slowly, first initiated because of tensile damage on the underside of the two slabs, as illustrated on Figure 5.30. When the slab reaches peak displacement, a few elements still remain in the top of the strips of both the slabs. When the two slabs begin to move in the upwards direction, hogging moment appears from the pre-tensioned rebars, and this results in tensile damage and therefore removal of the remaining elements, resulting in complete collapse.

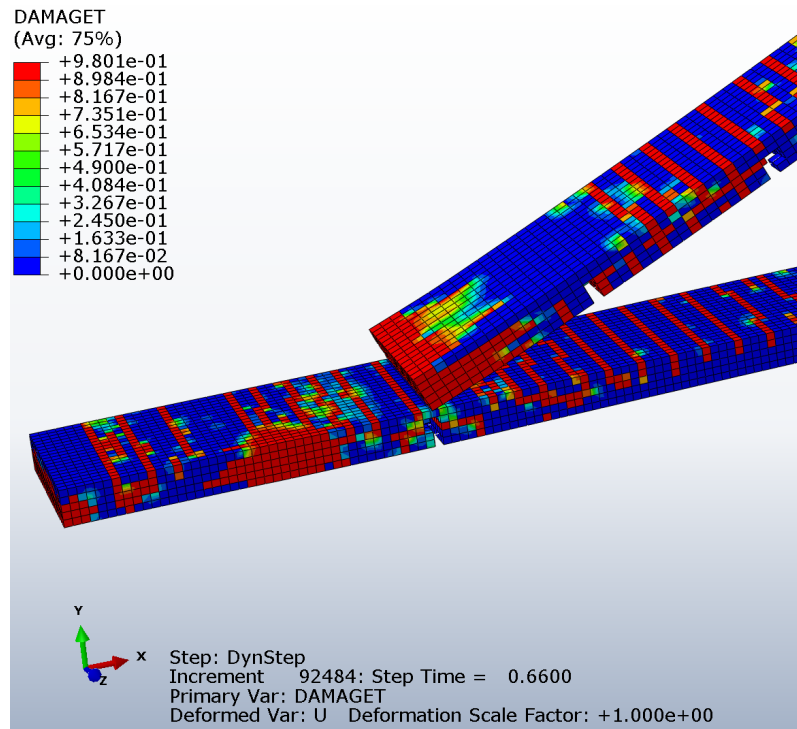


Figure 5.30: Tension damage in the model with 3 strips of element deletion at $T_I + 8\text{ms}$ [$\alpha = 0.3$ & $H = 3\text{m}$]

Abaqus model setup (Figure 5.30)			
Element type	No. of elements	Material	Other
Solid continuum C3D8R	14420	Concrete-02	Partwise element deletion and Contact
Timoshenko beam B31	432	Steel-02	Embedded region
Analysis type:		Explicit dynamic	

The impact and reaction forces for the three models is seen illustrated on Figures 5.31, 5.32 and 5.33 for the impact, left and right reaction respectively. It should be noticed that a Butterworth filter have been used to remove spikes and make the comparison more manageable, the influence of the filter is demonstrated in Appendix D.3. The measured force in the three models can be seen to match rather well, indicating that element deletion has very little effect on the initial forces. Following the first impact the elements does start to be removed, and the forces after this point are different. Even though that the response is different at large time intervals, the deviations in reaction and impact forces are small in the initial impact, and following studies is therefore performed without the use of element deletion.

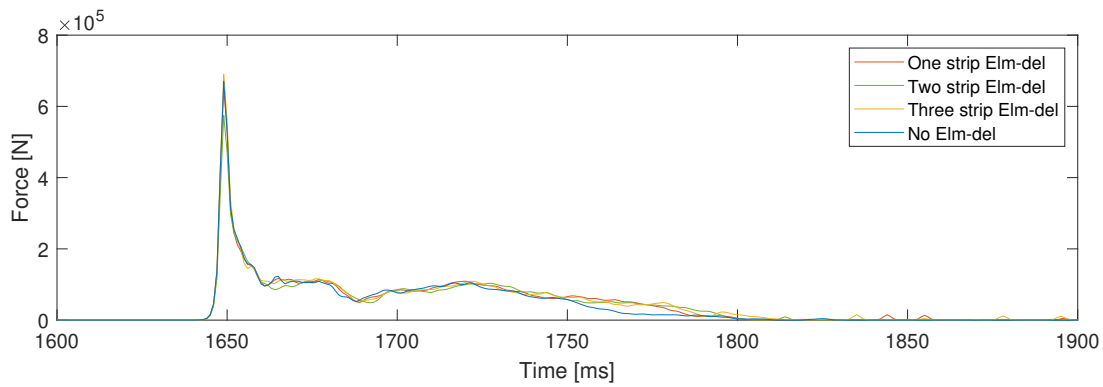


Figure 5.31: Impact force comparison between models with and without partwise deletion.

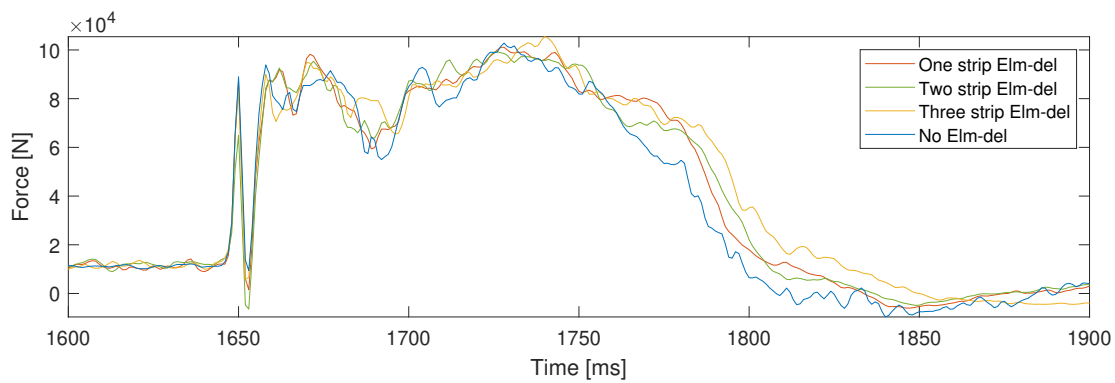


Figure 5.32: comparison of left reaction force, R_{left} , between models with and without partwise deletion.

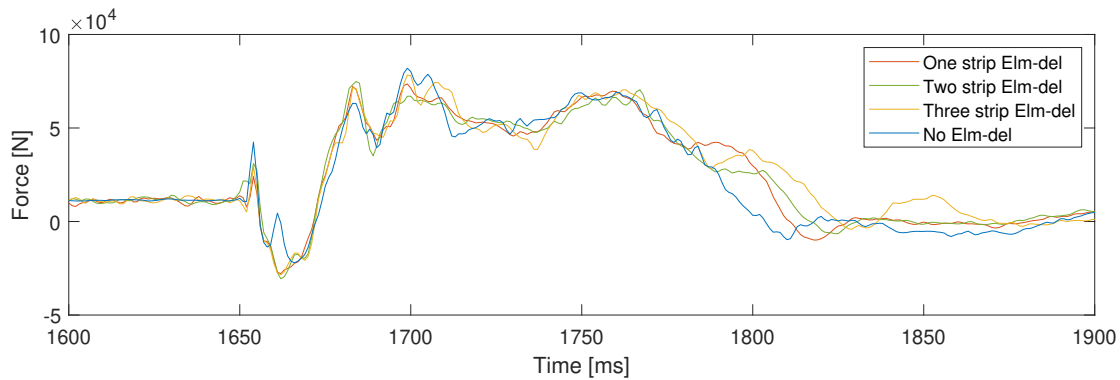


Figure 5.33: comparison of right reaction force, R_{right} , between models with and without partwise deletion.

5.6 Equivalent static loads and parameter study

The impact loads and reaction forces determined previously was only for the specific case of having a fall height of 3m, and an impact position of $\alpha = 0.3$. When building concrete buildings, the floor height may vary depending on the type and use, and the effect of increasing and lowering this may have large influences on the loads applied to the bottom

slab. The influence on the impact force from the change in height is not only critical from a kinetic energy point of view, but also how the stiffness of the slab increases with increasing fall height, as seen on Figure 5.34. Since the increase in drop height will increase the axial deformation, the felt stiffness of the falling slab will increase, with increased drop height. The low drop height simulations will therefore act less stiff, since the axial stiffness is much higher than the transverse for a slab of this length.

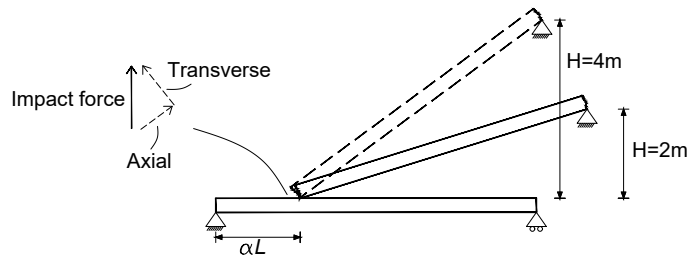


Figure 5.34: Stiffness dependence on drop height H .

Furthermore the influence on dynamic loads from moving the point of impact is investigated. The height, H , and position, α , is defined as shown previously on Figure 5.13

To compare the loads determined from the numerical analysis with the vertical replacement loads suggested by the Danish National Annex, a methodology must be chosen to determine the equivalent static loads. The force is determined as a local equivalent static force, $LESF$, found as the equivalent impulse in the time interval $2 \cdot \Delta t$, determined by equation 5.2, with illustration of the method seen on Figure 5.35

$$LESF = \frac{\int_{-\Delta t}^{\Delta t} F(t) dt}{2 \cdot \Delta t} \quad (5.2)$$

Two time intervals is chosen as being $2\Delta t=25\text{ms}$ & 50ms , such that the effect on duration also can be investigated.

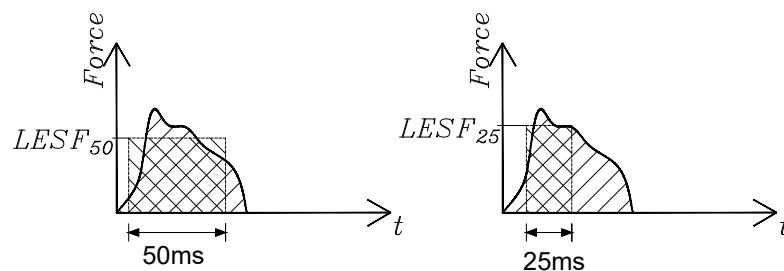


Figure 5.35: Illustration of the equivalent static force.

Five different position parameters and three different heights are investigated, with resulting reaction illustrated on Figure 5.36 and 5.37. Exact values of the measured force and Figures with the 50ms interval can be seen in Appendix E.2. The reaction force is seen to be highly dependent on both the position and height difference between the two slabs. The left support reaction shows that with decreasing distance parameter, the reaction force increases exponentially, which can be explained by how the perceived stiffness and mass of the slab below also increases exponentially as shown in a later section. Furthermore the right reaction force decreases with increasing position parameter, which in this case is increasing the distance to the impacting force.

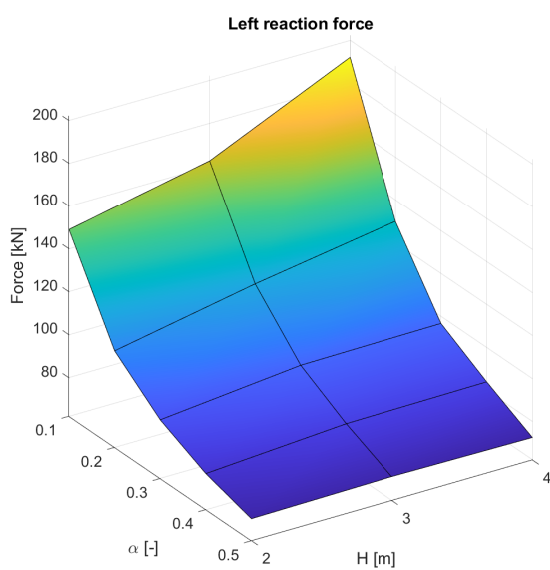


Figure 5.36: *LESF* with time interval $2\Delta t=25\text{ms}$.

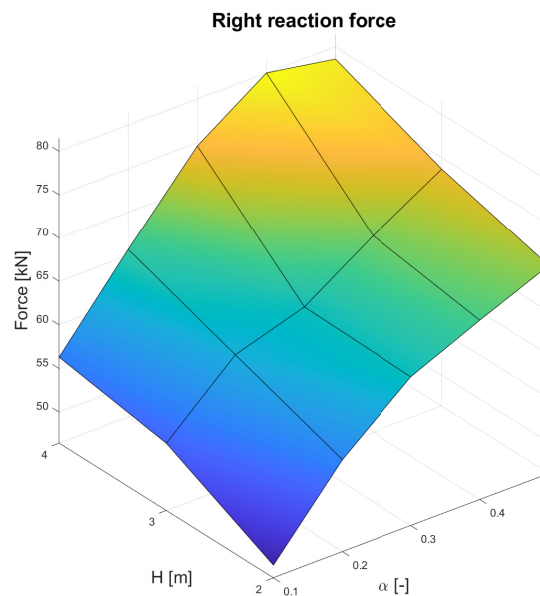


Figure 5.37: *LESF* with time interval $2\Delta t=25\text{ms}$.

The impacting force depending on the position parameter and drop height is illustrated on Figure 5.38. As opposed to the reaction forces, the impact force shows a more coarse pattern. A tendency is still visible with the impact force increasing with increased drop height and decreasing position parameter which also should be expected because of the increasing stiffness and mass of the bottom slab, and increasing kinetic energy with increasing drop height.

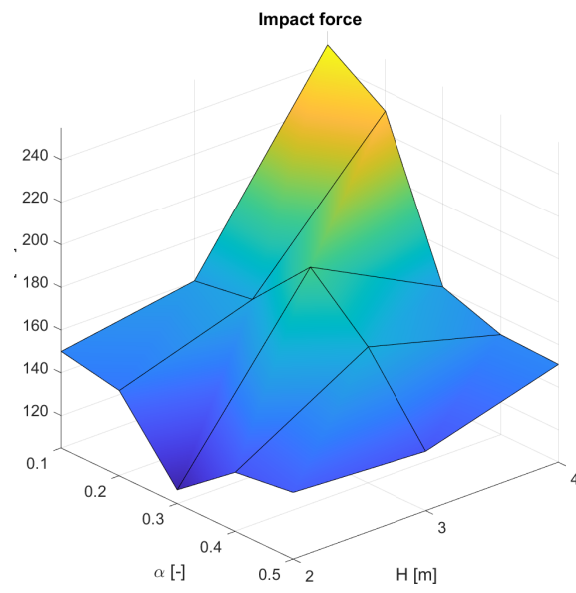
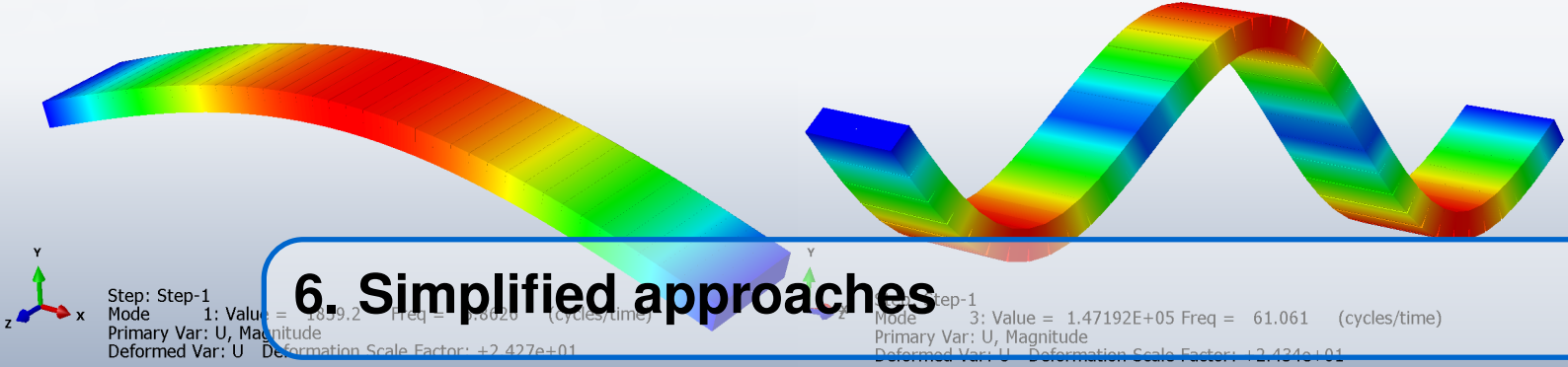


Figure 5.38: *LESF* with time interval $2\Delta t=25\text{ms}$.



6. Simplified approaches

In the previous chapter, several complex models were investigated, and the impact and reaction forces were determined. As long as the most important contributions are included it should be possible to recreate the phenomena seen in the previous chapter with a more simple model. Therefore a simple model is created using beam elements, and the force and energy present is compared with the complex model. Furthermore impact on an elastic beam is investigated using a 2DOF system for the most simple case investigation.

6.1 Beam model in Abaqus

The simplified model created in Abaqus consists of two slabs modelled using Timoshenko beam elements. To recreate the same results as with the complex model, the following is considered;

- The natural frequencies should be approximately the same
- The concrete slab has both a cracked and uncracked spring stiffness.
- More than 30% of the internal energy consists of plasticity and damage.

To ensure that the beam model behaves as the HCS, the natural frequency modes are compared to the full model, as the simplified HCS was in section 4.2.3. Frequency tests are performed in Abaqus and on Figure 6.1 the first and third mode of the simple beam model are shown, which deviate by approximately 2 % and 7 % from the first and third mode of the HCS model respectively.

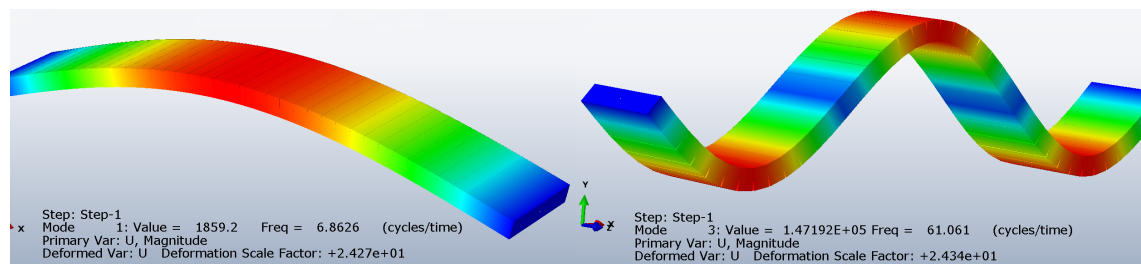


Figure 6.1: The first (left) and third (right) natural frequency and bending mode of the simplified beam model.

Abaqus model setup (Figure 6.1)			
Element type	No. of elements	Material	Other
Timoshenko beam B31	40	PlasticMaterial-01	None
Analysis type:		Frequency analysis	

Even though the behaviour of the natural frequencies are similar, they do not account for plasticity. The plasticity is included by using a constitutive model which consists of linear elasticity followed by hardening plasticity as shown in Table 6.3. A three point bending test is hereafter performed, and the results are compared with the test performed on the HCS model, as seen on Figure 6.2. The simple beam model sufficiently describes the sudden change in stiffness caused by cracking in the HCS model, and is therefore used further in the impact analysis.

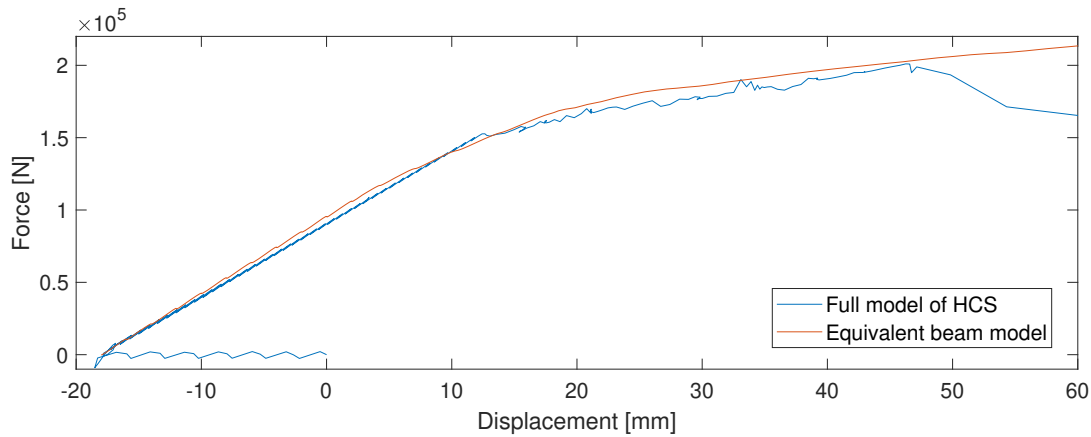
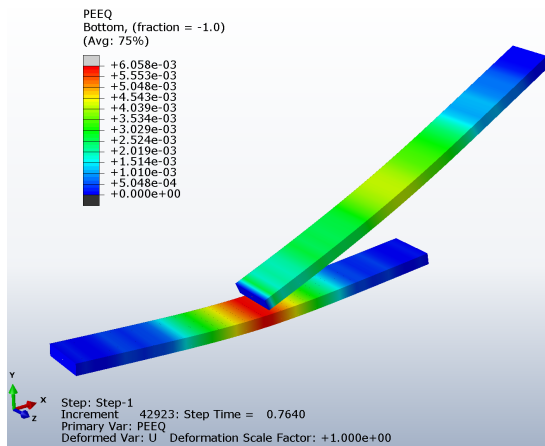


Figure 6.2: The stiffness in the simple beam model is seen to fit well with the spring stiffness in the HCS.

The beam model is then used in the exact same setup as with the complex model, such that the top beam is dropped from rest to simulate a sudden removal of support, and the results are extracted for analysis. Illustration of the plastic deformation at point of maximum deflection is seen on Figure 6.3.

In the beam model a drop height of $H = 3\text{m}$ is used, and three different impact positions is investigated, being $\alpha = 0.5, 0.3$ & 0.1 . To see how the effects change between the point of most compliance of the bottom slab, to the point of greatest stiffness and mass closest to the support. The deflection and moment force for the bottom beam can be seen on Figures 6.4-6.6, with shear force illustrated in Appendix E.3. In the first simulation shown on Figure 6.4, the beam deflection acts as expected, such that in the time of impact it is forced downwards. The moment curve however is because of this dynamic impact seen to experience hogging moment of significant size compared to the mid-span moment in the time of impact, a phenomenon which is further investigated later in this section. Approximately 100ms after the impact, the deflection of the bottom beam reaches its maximum, and at this point the moment curve now resembles a static solution to a point force applied in the middle.



Plasticity parameters	
Yield stress @ 0 plastic strain	9.6 [MPa]
Yield stress @ 0.0276 plastic strain	57.5 [MPa]
Density and elastic parameters	
Young's modulus E	18.29 [GPa]
Poisson ratio ν	0.19 [-]
Density ρ	1521 [kg/m ³]

Figure 6.3 & Table 6.1: Plastic deformation in the beam model at $T_I + 124$ ms. [$H=0.3$ & $\alpha = 0.5$]. Beam material properties: PlasticMaterial-01.

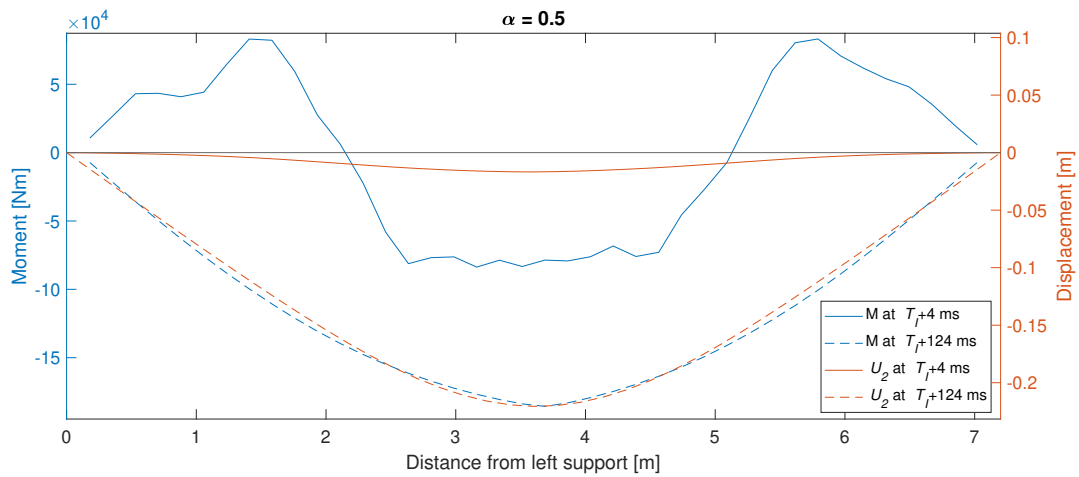


Figure 6.4: Moment and displacement at the time of impact and at point of maximum displacement. [$\alpha = 0.5$]

Simulating the impact with position parameter $\alpha = 0.3$, the same phenomenon is found, with a sagging moment at the point of applied force, and a hogging moment to the right. Furthermore it should be noticed that the moment force felt by the beam is so large that it resembles the moment force at maximum displacement, even though the displacement at the initial impact only is a fraction of the maximum deflection. Approximately 100ms after the impact, the deflection reaches its maximum, and the moment force is seen to resemble a static solution as the $\alpha = 0.5$ case.

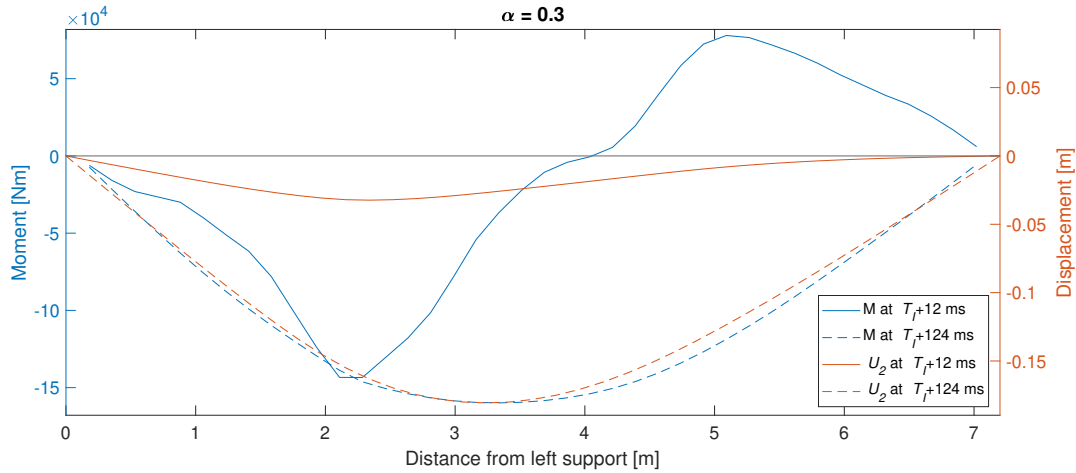


Figure 6.5: Moment and displacement at the time of impact and at maximum displacement. [$\alpha = 0.3$]

With impacts closer to the support at $\alpha = 0.1$, the same behaviour is noticed, where in the time of impact the deflection is low, and moment force is high. In this case it may be noticed that the measured moment force in the beam is higher at the time of impact than at the time of maximum deflection.

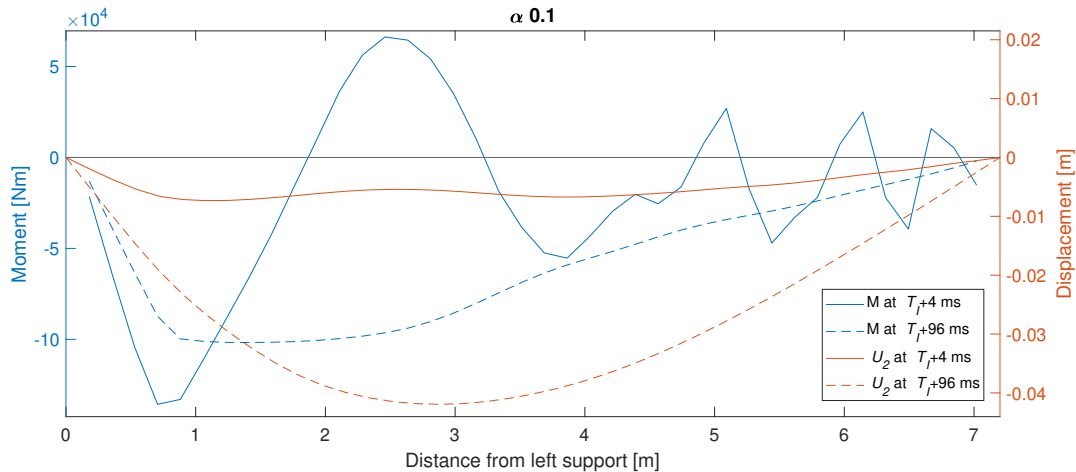


Figure 6.6: Moment and displacement at the time of impact and at maximum displacement. [$\alpha = 0.1$]

In all of the three investigated impacts using the simple beam, a combination of hogging and sagging moment is seen in the time of impact, even though the beam is subjected to a point load and is simply supported. This phenomenon can be explained by the inertia forces of the beam.

Experimental studies and other numerical simulations have shown that in dynamic impacts which span over a few milliseconds, the applied impact force is balanced by the inertia force. The inertia forces present in the beam derives from the fact that during the impact, the beam is accelerated downwards and therefore by newtons 2. law results in an upward force known as the inertia force [Jinlong Guo, 2017].

If the inertia force were to be implemented in a free body diagram, and then compared with the case of a static loaded beam, the results are very different. An example is shown on Figure 6.7, where the static free body diagram is shown on B), and the dynamic is shown on A).

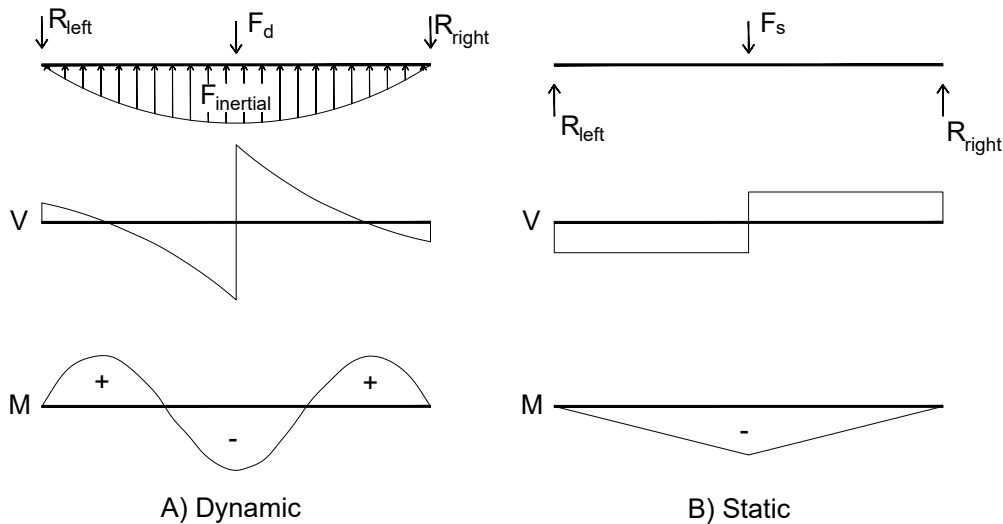


Figure 6.7: Section force diagram for A) Dynamic, B) Static. [Jinlong Guo, 2017]

The inertia force are highly dependent on the stiffness and density of the beam, since these two parameters determine the speed at which the dilational and transverse stress waves propagate. [Thong M.Pham, 2016] A change in stiffness should therefore result in a change of the wave size and how far it has propagated at a chosen time step after impact. The simple beam model is used to investigate this phenomenon, where the time step extracted is with 0.4ms interval. The test is performed with 100%, 50% and 10% of the original Youngs modulus used in the simple beam model, and the results are shown on Figure 6.8. The figure shows a clear difference in the distance that the stress wave have propagated, and explains why the section force at the time of impact shows appearance of both hogging and sagging moment.

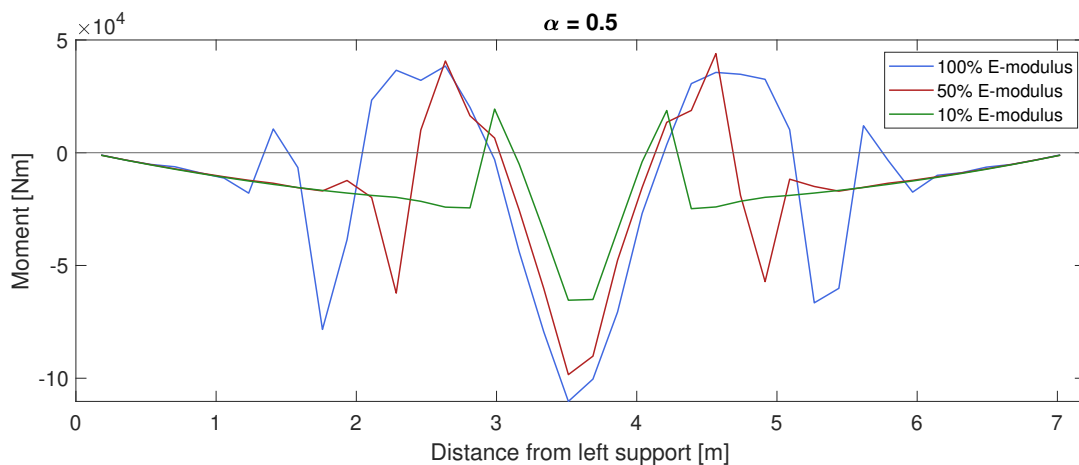


Figure 6.8: Section moment force at time $T_I + 1.2\text{ms}$ using three different Youngs Modulus.

The impact force and reaction forces present in the simulation is furthermore extracted for the three different position parameters to compare with the complex model used in section 5.3. For the mid span impact case the reaction forces is illustrated on Figure 6.9. The reaction forces is for both the complex and simple model seen to have a highly dynamic response in the time of impact. After ≈ 50 ms, the difference in estimated force between the two models is low, and for the mid span impact case, a simple model can sufficiently predict the reaction forces.

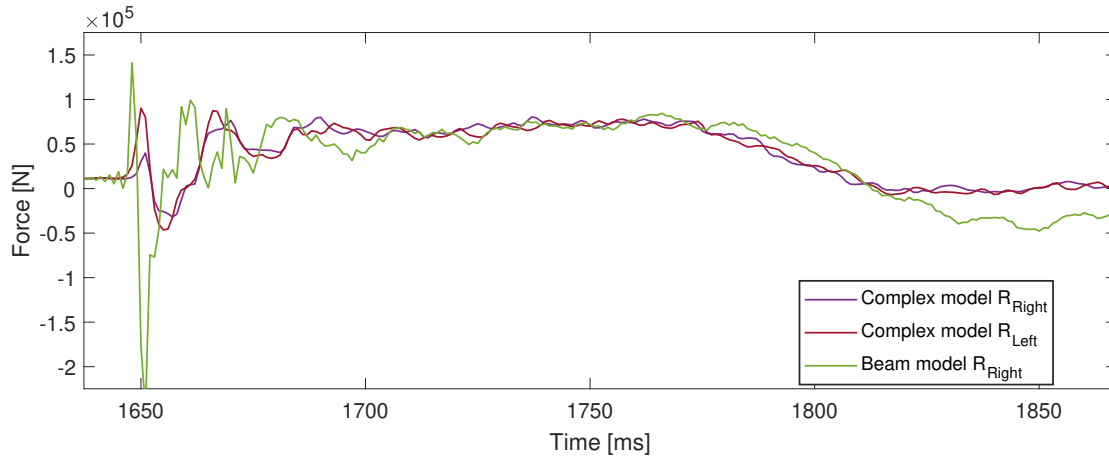


Figure 6.9: Comparison of right reaction force, R_{right} , between complex and beam model.

With decreasing distance to the support, the reaction force determined in the simple model starts to show greater deviation from the complex model. The left and right support reaction for the case $\alpha = 0.3$ & 0.1 is shown on Figure 6.10-6.11 & 6.12-6.13 respectively. The same overall behaviour is found in all of the four figures, but with increasing high-frequent behaviour of the simple model, which can be explained by how the complex model has the ability to dissipate energy through the formation of cracks in the whole model which can appear easily because of the low tension strength, whereas the simple model approximation only can dissipate energy in the form of plasticity which appear only when the stress reaches the yield stress.

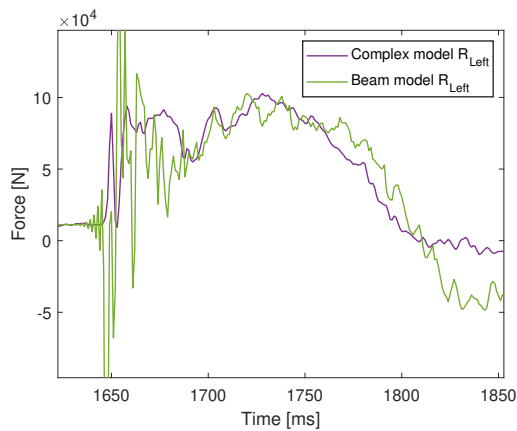


Figure 6.10: Comparison of R_{Left} between complex and simple model. [$\alpha = 0.3, H = 3m$]

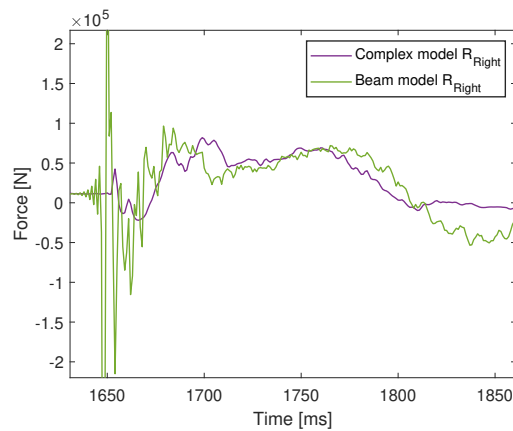


Figure 6.11: Comparison of R_{Right} between complex and simple model. [$\alpha = 0.3, H = 3m$]

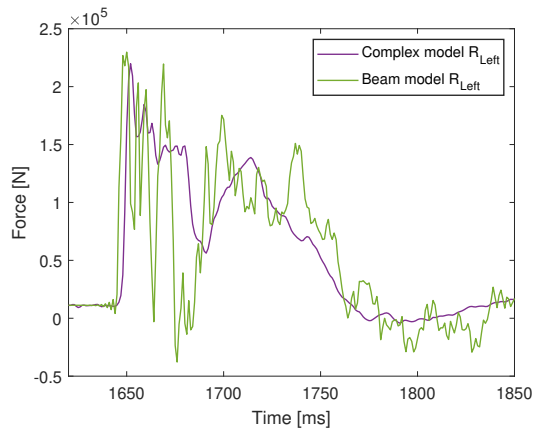


Figure 6.12: Comparison of R_{Left} between complex and simple model. [$\alpha = 0.1, H = 3\text{m}$]

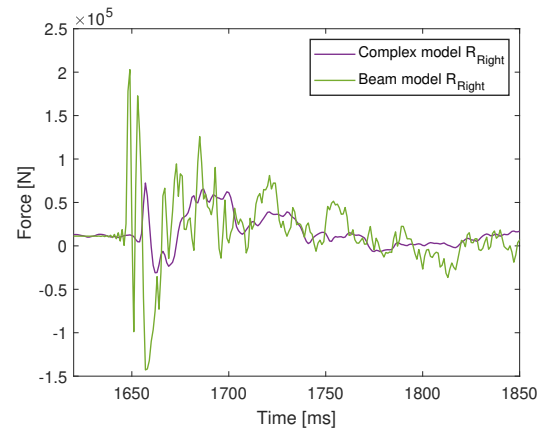


Figure 6.13: Comparison of R_{Right} between complex and simple model. [$\alpha = 0.1, H = 3\text{m}$]

The behaviour of the bottom and top beam during the impact is investigated using the elastic and plastic strain energy seen on Figure 6.14-6.17. From previously investigating the reaction force dependency on position parameter, it was noticed that the time span of applied force decreased with decreasing position parameter, and the size of the force increased. Investigating the elastic strain energy in the bottom beam on Figure 6.15 the same phenomenon can be seen, where the time required to reach maximum internal energy by deflection is doubled between the $\alpha = 0.5$ and $\alpha = 0.1$ case. Besides the increase in time span of increasing elastic energy, the total amount of energy absorbed through elastic deformation is also seen to be more than doubled between the two cases, which is favourable for decreasing the resulting loads felt by the reactions.

Further comparison of the elastic strain energy shows that the bottom and top beam has peak elastic strain energy at two different values of position parameter. For the bottom beam the impact at mid span results in the largest elastic strain energy because of the low stiffness, and for the top beam this is opposite, with the largest elastic strain when impacting close to the support.

Impacting closer to the support will, because of the high stiffness and mass of the bottom beam, result in a case of an elastic object hitting a hard object, such that the energy is mainly conserved in the elastic deformation of the impacting body resembling the Eurocode hard impact definition described in section 5.2. The plastic deformation shows the same tendency, where the plastic strain of the top beam increases with decreasing position parameter, while the bottom beam energy wise seems to show less behaviour of actually feeling the impact.

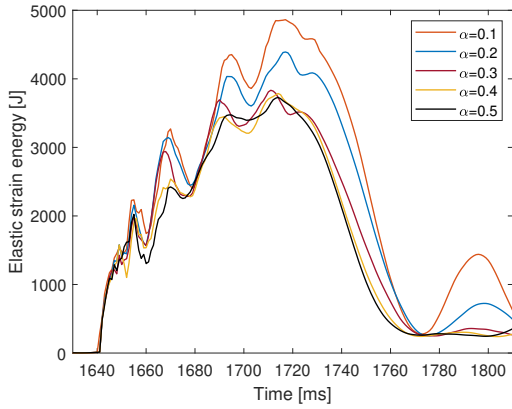


Figure 6.14: Elastic strain energy of the top beam. [H=3m]

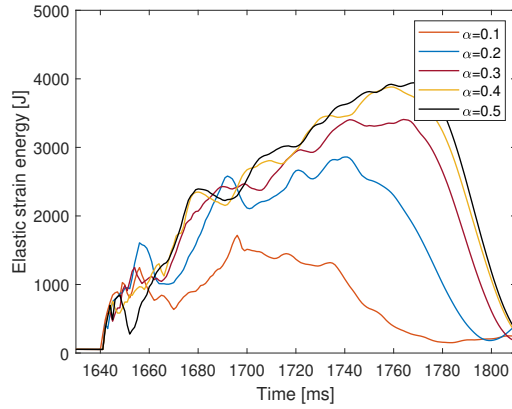


Figure 6.15: Elastic strain energy of the bottom beam. [H=3m]

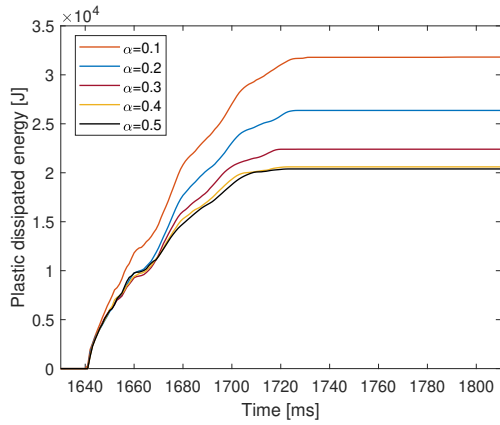


Figure 6.16: Plastic dissipated energy of the top beam. [H=3m]

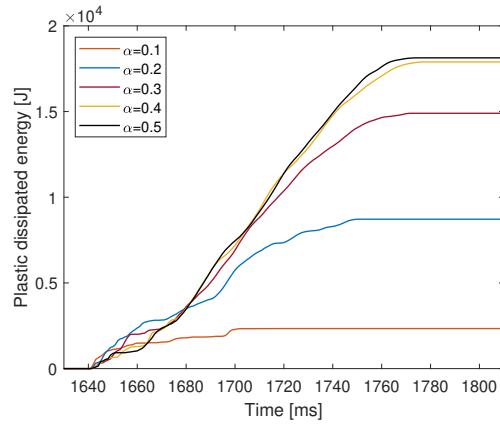


Figure 6.17: Plastic dissipated energy in the bottom beam. [H=3m]

The hard and soft impact behaviour can be illustrated by determining the peaks in plastic and elastic energy from the previous four figures, such that the individual components can be compared, as illustrated on Figure 6.18. The amount of energy dissipated by plasticity and gained in elasticity in the top beam far outweighs the bottom.

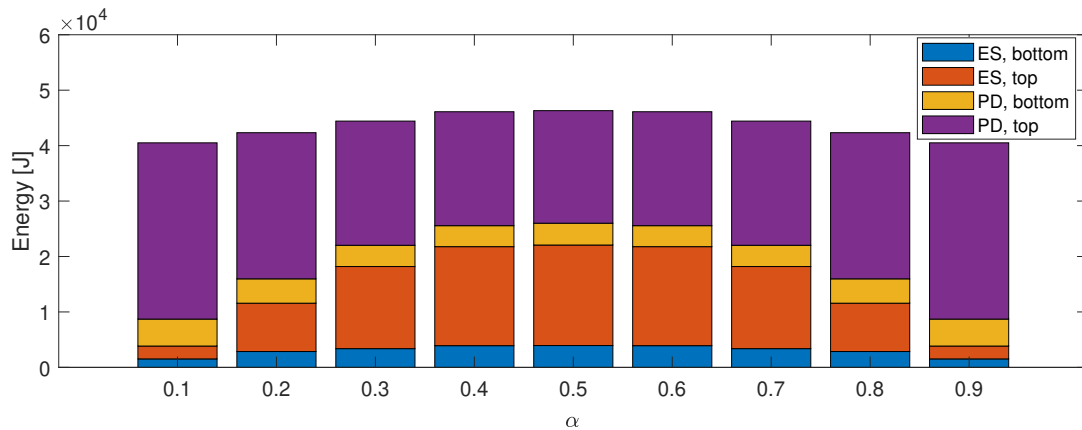


Figure 6.18: Energy dissipation in top and bottom beam. [PD=Plastic dissipated, SE=Elastic strain]

6.2 2DOF approach

In the complex model the forces present was found to be highly dependent on both the position and drop height. Investigation of this dependency is performed using a 2DOF approach as described in Appendix F, where the bottom slab was referred to as the "structure" and is described by Bernoulli-Euler theory. The mass and stiffness of the falling slab, referred to as the "impacting mass" is in this investigation not of high importance, and an assumed value is used in the analysis. In the 2DOF analysis, it was found that the stiffness and mass of the bottom slab increased exponentially when moving towards the reactions, as is illustrated on Figure 6.19. Because of this, the compliance of the structure also decreased dramatically, resulting in very low energy absorption of the structure during the impact, such that the kinetic energy built up in the impacting object were dissipated mostly by strain energy in the impacting object.

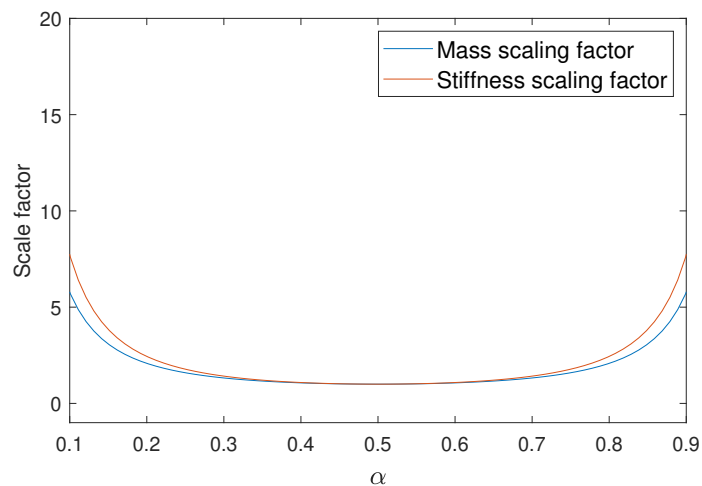


Figure 6.19: Mass and stiffness scale factor normalised to force applied at mid span case.

The same results were found in the simple beam model analysis in Chapter 6, where the plastic and elastic dissipated energy was seen to increase when moving towards the

supports of the bottom slab, and the bottom slab dissipated energy decreased.

In the 2DOF analysis, both the initial velocity of the falling object, and the impact position is changed in a total of 25 times, where in each of the impacts the resulting reaction and impact force is determined, as seen on Figure 6.20, 6.21 and 6.22, for the impact force, left and right reaction force respectively. Since the analysis is performed with only two degree of freedom, the impact force graph is no longer seen to have sudden spike behaviour caused by numerical difficulties, and the dependency on height and position of impact is much easier to see. The reaction forces is also seen to follow the same pattern as the complex model, where the left reaction force increases, and the right decreases with decreasing position parameter.

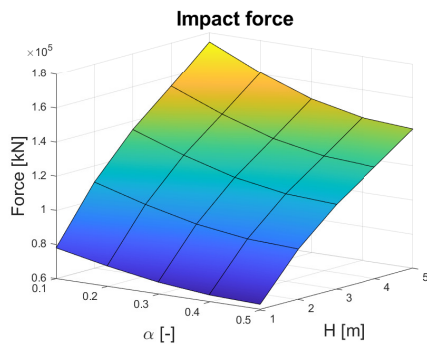


Figure 6.20: Reaction force, R_I , of the impacting mass.

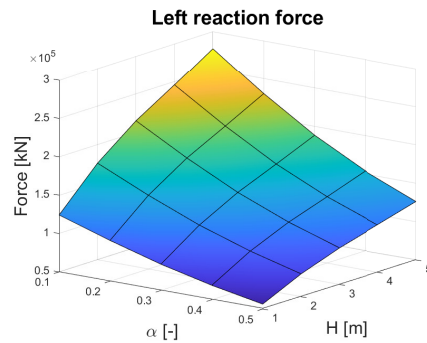


Figure 6.21: Reaction force, R_{left} , of the structure.

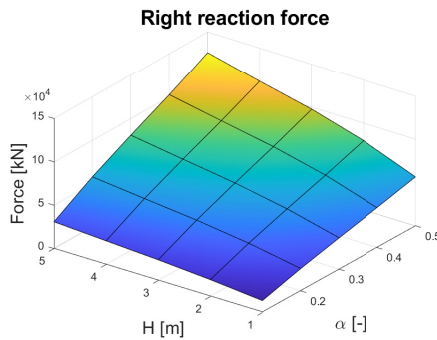
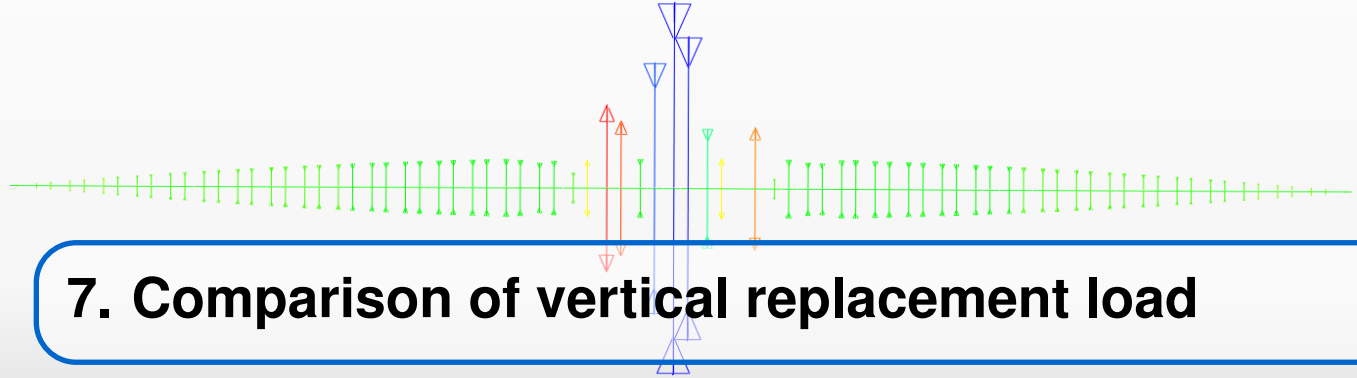
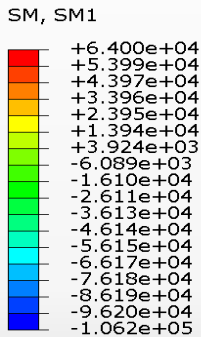


Figure 6.22: Reaction force, R_{right} , of the structure.



The loads determined using the complex numerical model is compared with the vertical accidental load discussed in section 2.4. In the case of a slab with 7.2m span, width of 1m and assumption of storey collapse of 1-2, the resulting section forces can be determined as shown on Figure 7.1.

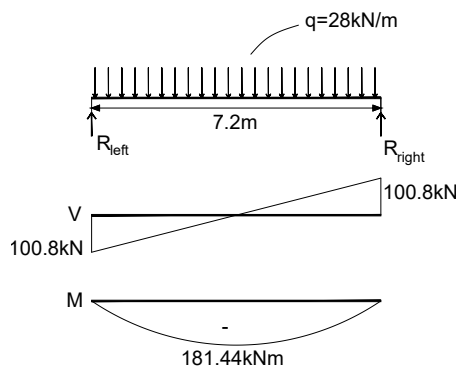


Figure 7.1: Section force diagram when using the Eurocode vertical replacement load for 1-2 storeys.

Comparison between the loads determined in the numerical simulation and the load stated in DS/EN 1990:2019 DK NA is done by investigating both the forces momentarily felt by the slab, and hereafter the forces which are felt by the support.

7.1 Forces at the time of impact

From the simple beam simulation it was found that at the time of impact the forces felt by the bottom beam were large and short in duration. If the forces measured in the beam were to be applied as a static force, a surface load many times the size of the Eurocode mentioned replacement load would be required. This is however not the case since the forces felt right at the time of impact primarily are dissipated through damage of the slab. To further investigate the damage propagation in the slab at the time of peak section forces felt in the beam, 3 steps of 0.4ms are extracted in the complex and simple model. The first step is shown on Figure 7.2 and 7.3, which is extracted 0.4ms after the impact, with the remaining two steps shown in Appendix E.4.

The section moment diagram shown on Figure 7.2 is extracted from Abaqus, where the green arrows show the section moment distribution from gravity loads, and the sudden change towards the mid span is caused by the impact force applied to the beam. At 0.4ms

after the impact, both sagging- (Blue), and hogging-moment (red) appears. Furthermore it is noticed that in the initial time of impact, the supports have not felt the applied force, meaning that even though the applied force is above 1MN, it is purely in equilibrium with the inertia force of the beam.

Inspection of the complex model on Figure 7.3 at the same time step shows the same phenomenon, where damage in the first step only is present as tension cracks below the impact zone, and in the top left and right of the impact.

0.8ms after the impact the stress wave have still not yet reached the support, and the impact force are still in equilibrium with the inertia of the bottom beam, where additional tension cracks develop and starts to propagate towards the support. Only at time 1.2ms the stress wave is close to have reached support, which furthermore was found not to be the case for the complex model, which can be explained by the fact that the damage reduces Young's Modulus in the concrete material model and therefore reduces stress wave velocity.

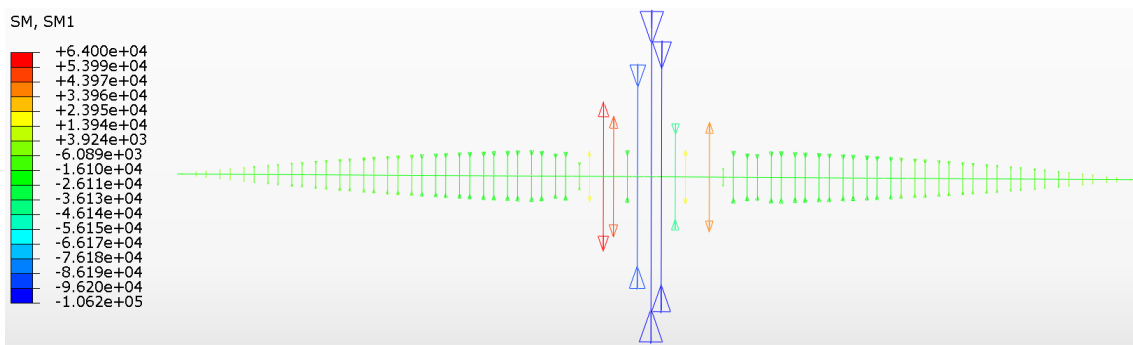


Figure 7.2: Top view of the beam with the section moment distribution at time $T_I + 0.4\text{ms}$ after impact, [$\alpha = 0.5, H = 3\text{m}$]

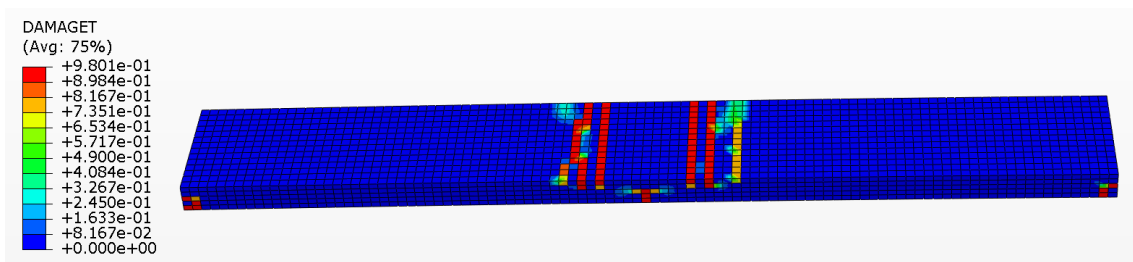


Figure 7.3: Tension crack distribution in complex model at time $T_I + 0.4\text{ms}$ after impact, [$\alpha = 0.5, H = 3\text{m}$].

From each of the impact simulations in the simple model using the five different position parameters, some of the largest measured section forces in the time of impact is measured and compared with the vertical replacement load, VRL, which can be seen on Figure 7.4. The moment section force from a static surface load will inevitably fall short of describing hogging moment in a simply supported beam, and a widespread appearance of tension cracks must therefore be expected in the initial few milliseconds of the impact in both the upper and lower side of the bottom slab, as is illustrated on Figure 7.5 and 7.6.

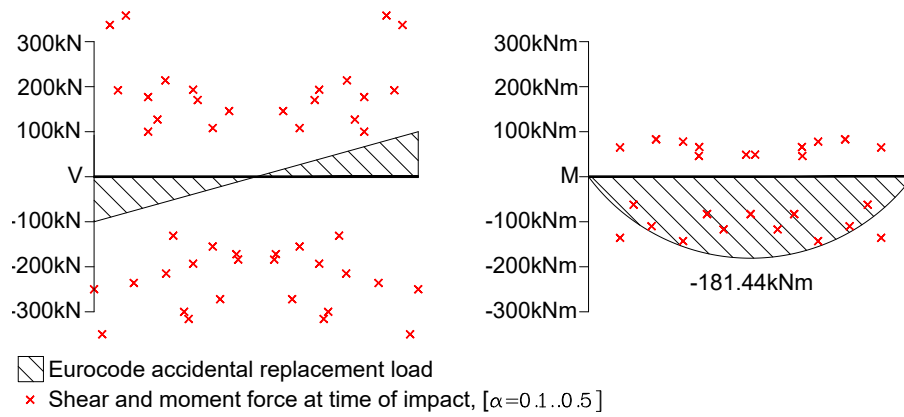


Figure 7.4: Measured section forces at time $t < 2\text{ms}$ after impact compared with section force diagram from VRL.

Comparing the shear section force measured at the time of impact with the accidental replacement load, it is noticed that the shear force present in some cases are more than three times larger. Furthermore a tendency can be seen where the shear force increases towards the support, which is present for lower values of the position parameter. From a static point of view the shear force present will increase linearly when moving the applied force closer to the support, and from a dynamic viewpoint the felt stiffness and mass increases, resulting a lower portion of dissipated energy through deformation. Even though the section force shown on Figure 7.4 in some situations is higher than the vertical replacement load, the force is only felt momentarily in the time of impact, and the displacement found from the Figures 6.4-6.6 reveals that depending on the impact position, it is not yet displaced to such a state that it will collapse. The large forces present at the time $t < 2\text{ms}$ after impact can therefore not be related to a static equivalent load, since they are mainly dissipated through damage and acceleration of the bottom slab.

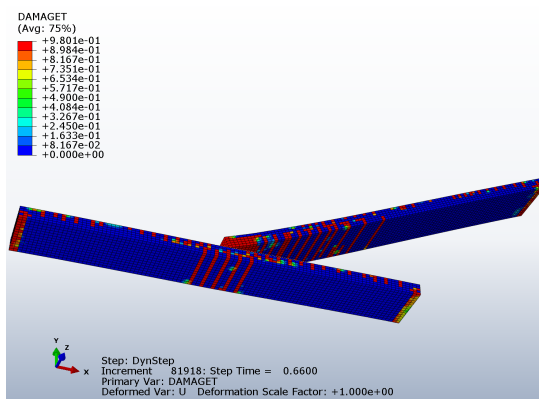


Figure 7.5: Bottom view of tension damage from sagging moment concentrated at mid-span [$T_I + 8\text{ms}$ & $\alpha = 0.5, H = 3\text{m}$]

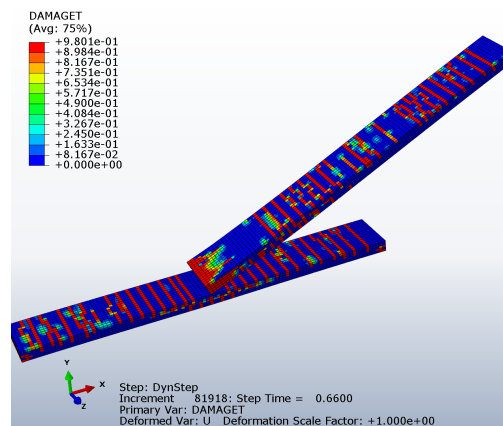


Figure 7.6: Top view of damage caused by hogging moment [$T_I + 8\text{ms}$ & $\alpha = 0.5, H = 3\text{m}$]

7.2 Eurocode comparison with *LESF*

Shortly after the forces and energy from the initial impact are dissipated through deformation of the slab, the force felt by the slab shows a more static behaviour as seen on the previous moment force diagrams from the simple beam case. From the five different position parameters, the section shear and moment force are extracted to be compared with the vertical replacement load, and can be seen on Figure 7.7 and 7.8. From the section moment diagram it can be seen that when the impact position is in the range $0.2 < \alpha < 0.8$, the section force are primarily within the limits of the VRL. When moving towards the support, the moment are seen to increase to values larger than the VRL, which is also seen when investigating the shear force.

The section shear force is as the *LESF* seen to be highly dependent on the impact position, especially when moving towards the support where it increases exponentially.

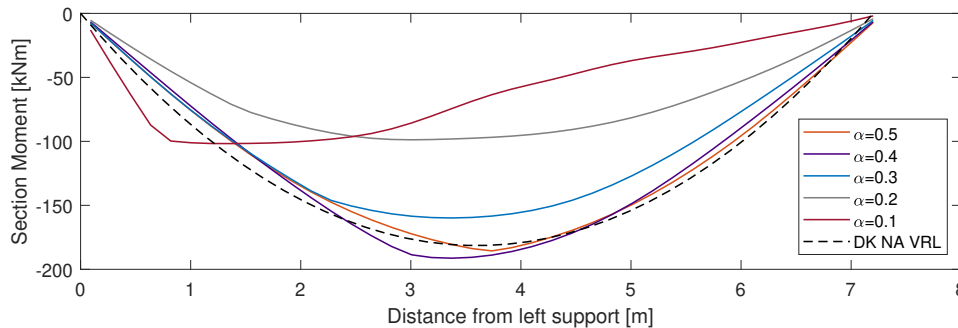


Figure 7.7: Section moment at maximum displacement in simple model compared with VRL.

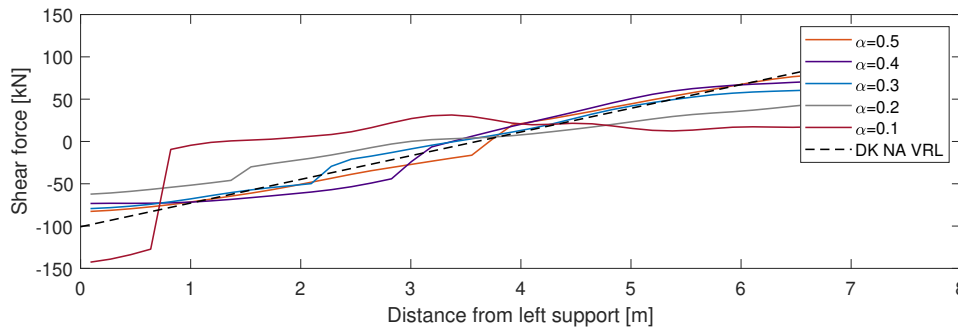


Figure 7.8: Section shear force at maximum displacement in simple model compared with VRL.

A direct comparison between the *LESF* shown on Figure 7.9 and VRL which is illustrated with a grey plane, shows that when the position parameter falls below 3, the DK NA approach is no longer conservative, and the measured load which must be absorbed by the support is higher than the VRL. Because of the very low compliance in the bottom beam when moving the impact towards the support, the resulting increase in forces are high. With high reaction forces and low compliance of the bottom slab, the slab is expected to fail in a shear puncture type failure between the impact position and closest reaction, which is seen to also be indicated by the amount of damage present in the complex model as seen on Figure 7.11 and 7.12. From the two figures, tension damage between the support

and impact position is seen to almost have reached all the way through the slab, which appears shortly after the impact.

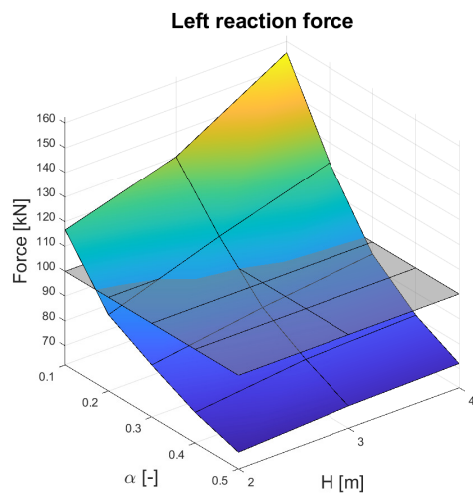


Figure 7.9: LESF with $2\Delta t = 50\text{ms}$ from complex model compared with VRL(Grey plane).

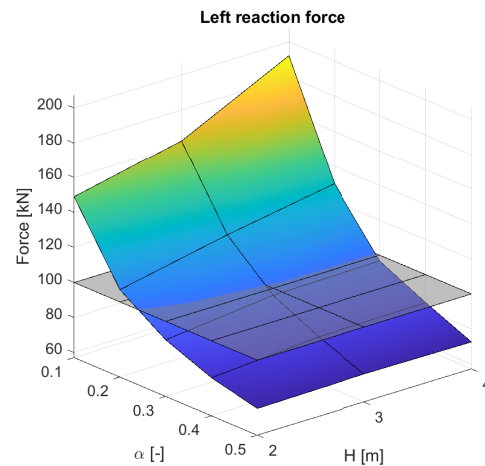


Figure 7.10: LESF with $2\Delta t = 25\text{ms}$ from complex model compared with VRL(Grey plane).

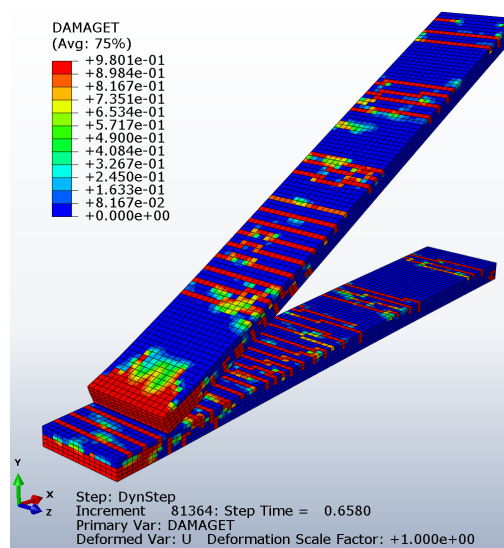


Figure 7.11: Top view of damage concentrated at support [$T_I + 8\text{ms}$ & $\alpha = 0.1, H = 3\text{m}$]

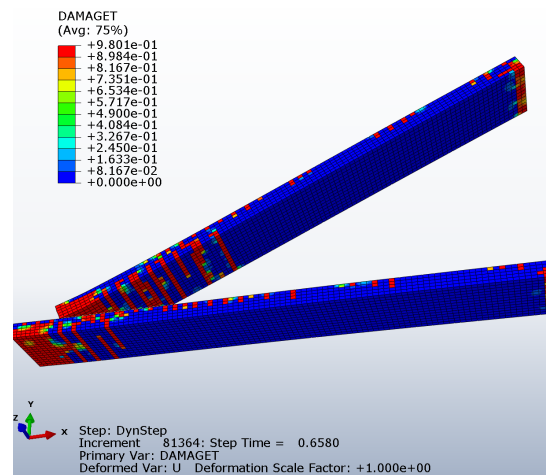


Figure 7.12: Bottom view of damage concentrated at support [$T_I + 8\text{ms}$ & $\alpha = 0.1, H = 3\text{m}$]

Furthermore the previous comparison with the simple beam model showed that the kinetic energy was primarily dissipated through elastic and plastic deformation of the top beam, resembling the definition of the hard impact. If the bottom slab were to be increased in mass and stiffness by e.g. using a solid slab instead of hollow core as shown on Figure 7.13, and with the use of shear reinforcement close to the support to avoid shear puncture,

Chapter 7. Comparison of vertical replacement load

the top slab may fail during the impact and therefore reduce the resulting loads. This will although only work if only the bottom slab is increased in mass and stiffness, and the top slabs contain their hollow core design such that stiffness, mass and therefore energy as a whole present in the impact remains low.

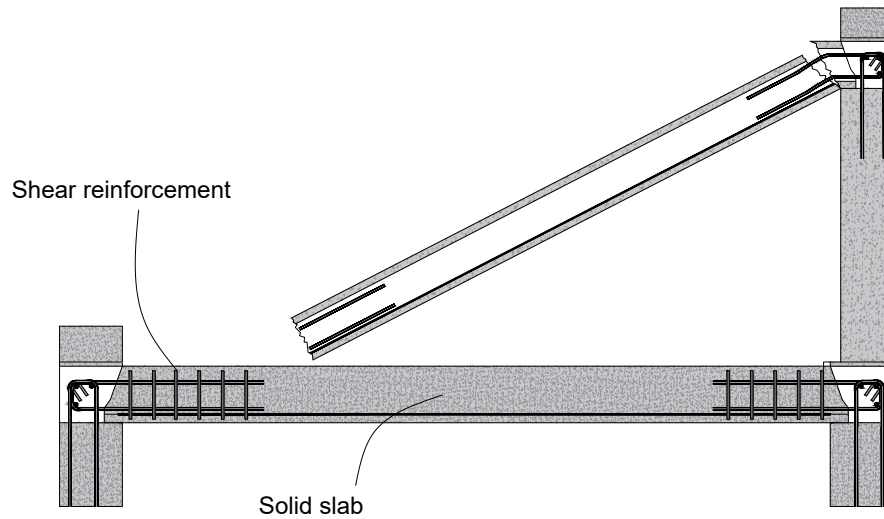
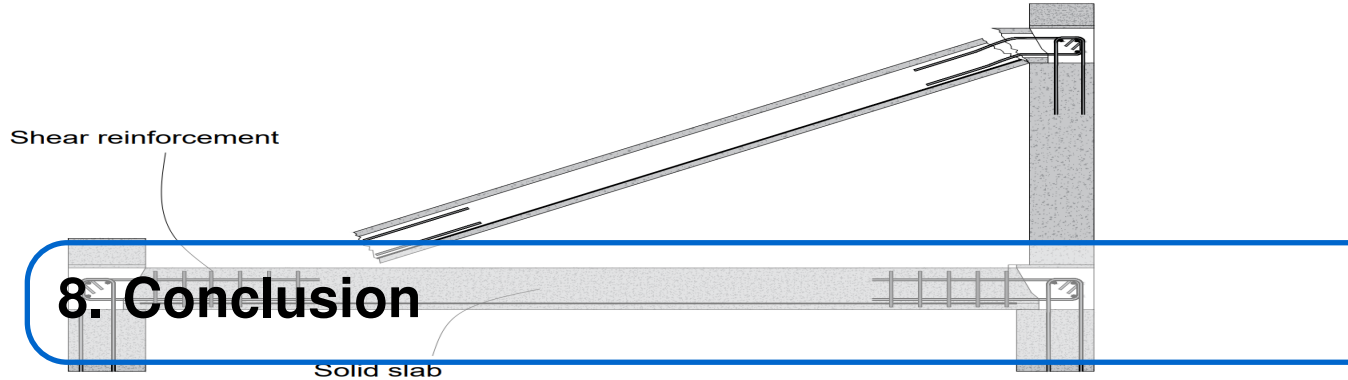


Figure 7.13: Example of increasing mass and implementing shear reinforcement to avoid shear puncture from impact loads close to support.



In this project, the aim was to investigate how the loads present in an impact compared with the vertical replacement load stated by the Danish National Annex. Comparison of these two different load types were performed using an example building referred to as the DPCA-building, in which some of the relevant design failure scenarios were determined, and one of these were chosen for further study.

Modelling of the chosen design failure scenario required the use of complex numerical models, where the behaviour of RC elements in multiple different failure conditions had to be demonstrated to ensure that the final model would give realistic results. Some of the RC elements that was demonstrated are a reinforced concrete beam and a pretensioned hollow core slab. From these two mentioned models, it was found that they behaved in accordance with results from standard bearing capacity calculations, and was therefore deemed suitable in the final numerical model. It was found that the beam was only 1% stronger than expected from the bearing capacity calculations. The hollow core slab could not be compared directly with the informed bearing capacity, but the bearing capacity from the hollow core slab was expected to be within 9.4 % of the real bearing capacity.

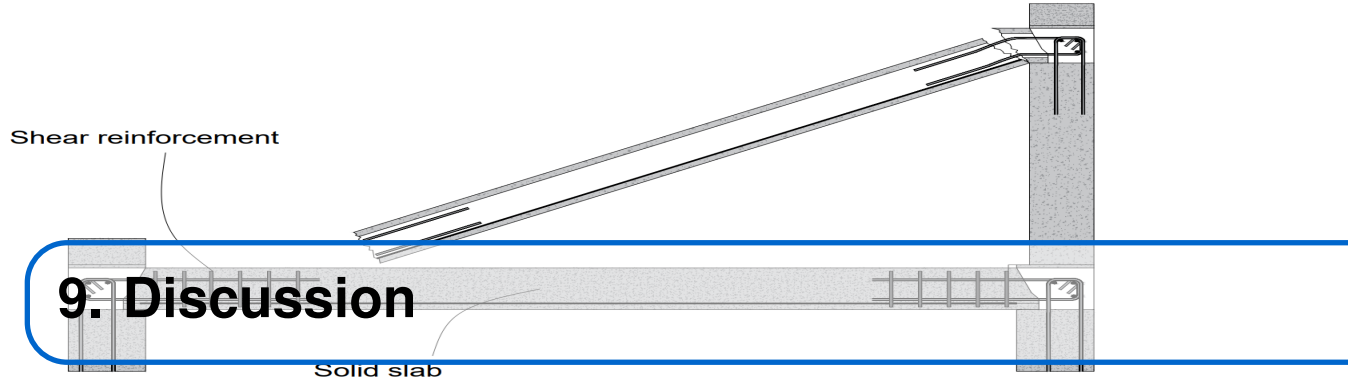
Due to the number of elements needed in the finite element models, it was necessary to create a simplified model to reduce computation time. This model was tested to ensure that it accurately depicted the original full-size model of a hollow core slab so it could be used in a design failure scenario.

From the numerical simulations of the design failure scenario, it was found that the impact forces applied to the bottom slab resulted in complex section force diagrams originating from the effects of inertia, where both hogging and sagging moment were present. These large section forces were present in only a fraction of a second and caused tension cracks to propagate from the point of impact and throughout the slab. Even though large forces were present, the small duration meant that these forces were dissipated quickly through overall damage and plasticity, and the bearing capacity of the beam was in some cases still capable of redistributing the impact load to the supports.

From the complex numerical model, it was found that in the case of mid-span impact, the vertical replacement load was conservative, but this was not the case when the position of impact was closer to the support. Numerical simulations showed that the shear force increased exponentially when moving close to the support, resulting in loads that were twice as large as the vertical replacement load. Because of the limited amount of simulations with the complex numerical model these effects was investigated further by building a simpler model, from which similar results were found.

To ensure that failure caused by large shear forces does not occur, recommendations of

increased mass of the bottom slab and the use of shear reinforcements is described. In the time of failure, the mass and increased loading capacity of the bottom slab will then result in only the top slab failing, such that the kinetic energy built up from the falling motion is dissipated through damage and breakage of the top slab primarily.



In this project, the aim was to investigate what loads would be expected in a design failure scenario in a concrete structure. To determine these loads, complex models were required, which inevitably results in deviations from the real world scenario arising from the assumptions made when building the model. When choosing to model a hollow core slab using a solid slab, focus was to reach the same bending properties using a less computational expensive model, although parameters such as stiffness in shear and compression will differ. In this report crack development near the support were discussed and it could be interesting to study the slab further to see if this crack development could cause complete failure. However, if the model were to estimate the bearing capacity of the hollow core slab it would not be accurate in the case of punching shear failure with the simplified model that is used. This is due to the increase in cross-section area in the solid slab, which will increase the shear bearing capacity of the slab.

In the numerical model, issues emerged when investigating the energy distribution of the model, where the elastic energy decreased to values below zero, and the viscous dissipated energy increased rapidly. Solutions to these phenomenon have later been discussed as being caused by high velocity gradients within the model, and further inspection of this value should therefore be done, to ensure correct behaviour throughout the simulation.

Choosing to model the design failure scenario using pinned and simple support conditions, the effect referred to as catenary action cannot be implemented. This effect may not have a high influence on the loads determined in this project, but as an overall effect when determining the bearing capacity of the bottom slab it has a high effect, and if further studies were to be conducted, the increased bearing capacity from this phenomenon should be investigated.

In the design failure scenario model in Abaqus the slabs are placed on supports that cannot absorb any energy in the form of deflection. This is of course a phenomenon that would be seen in the real world and therefore, in further studies of this topic, could a larger improved model include this deformation in order to improve the estimation of the equivalent static load.

When choosing the design failure scenario from the DPCA-building, a simple slab-impacting-slab scenario was chosen to be compared with the vertical replacement load. In reality there exist a large variety of failure scenarios, and some of them may result in larger loads.



Bibliography

- 1990DK-NA:2019, 2019.** DS/EN 1990DK-NA:2019. *Nationalt anneks til Eurocode 0: Projektteringsgrundlag for bærende konstruktioner*, 2019.
- ASCE, 2016.** ASCE. *Modeling of Steel-Concrete Composite Elements under In-Plane and Out-of-Plane Loads*. <https://ascelibrary.org/doi/10.1061/%28ASCE%29ST.1943-541X.0001554>, 2016.
- Bjarne Chr. Jensen, 2020.** Bjarne Chr. Jensen. *Beton-konstruktioner efter DS/EN 1992-1-1*. Nyt Teknisk Forlag, 2020.
- Bjarne Chr. Jensen, Bent Bonnerup, Carsten Munk Plum, 2009.** Bjarne Chr. Jensen, Bent Bonnerup, Carsten Munk Plum. *Stål-konstruktioner efter DS/EN 1993*. Nyt Teknisk Forlag, 2009.
- Bruce R. Ellingwood and Dusenberry, 2007.** Robert Smilowitz Bruce R. Ellingwood and Donald O. Dusenberry. *Best Practices for Reducing the Potential for Progressive Collapse in Buildings*, 2007. Downloadet: 20-09-2019.
- CHR Concrete, 2020.** CHR Concrete. *Huldæk*, 2020. URL <https://betonelement.dk/betonelementer/daek/huldaek/>.
- Cook et al., 2002.** Robert Cook, David S. Malkus, Michael E. Plesha and Robert J. Witt. *Concepts and applications of finite element analysis*. John Wiley & Sons, Inc., 2002. ISBN: 978-0-471-35605-9.
- Dassault Systèmes, 2020.** Dassault Systèmes. *ABAQUS Simulia User Assistance*. Dassault Systèmes Simulia Corp, United States, 2020.
- DK-NA, 2017.** DS/EN 1992-1-1 DK-NA. *Nationalt anneks til Eurocode 2: Betonkonstruktioner – Del 1-1: Generelle regler samt regler for bygningskonstruktioner*, 2017.
- DS410, 1999.** DS410. *Norm for last på konstruktioner*, 1999.
- DS/EN-1990, 2007.** DS/EN-1990. *Eurocode 0: Basis of structural design*, 2007.
- DS/EN-1991, 2007.** DS/EN-1991. *Eurocode 1: Actions on structures*, 2007.
- DS/EN-1992, 2007.** DS/EN-1992. *Eurocode 2: Design of concrete structures*, 2007.
- DS/INF-146, 2003.** DS/INF-146. *Robustness – Background and principles – Guidance – 2003*, 2003. Downloadet: 16-09-2019.
- Jensen, 2004.** Bjarne Chr. Jensen. *Teknisk Ståbi*, 2004.

- Jensen, 2020.** *Jesper Frøbert Jensen*. Private Communication, 2020.
- Jinlong Guo, 2017.** Wensu Chen Jinlong Guo, Jian Cai. *Inertial Effect on RC Beam Subjected to Impact Loads*, 2017.
- NA:2013, 2013.** DS/EN 1991-1-7 DK NA:2013. *Nationalt anneks til Eurocode 1: Last på bygværker - Del 1-7: Generelle laster - Ulykkeslast*, 2013.
- Nordjyske Stiftstidende, 2019.** Nordjyske Stiftstidende. *Altaner styrtet ned på nybyggeri*, 2019. URL <https://nordjyske.dk/nyheder/aalborg/altaner-styrtet-ned-paa-nybyggeri/745670f4-9aed-488b-b4ab-63a9956049df>. Accessed: 17/04/2020.
- Pearson, 2005.** Cynthia Pearson. *Ronan Point Apartment Tower Collapse and its Effect on Building Codes*, 2005.
- prEN1990:2019, 2019.** prEN1990:2019. *Eurocode 0 — Basis of structural and geotechnical design*, 2019. prEN 1990 Third revised draft.
- Thong M.Pham, 2016.** Hong Hao Thong M.Pham. *Plastic hinges and inertia forces in RC beams under impact loads*, 2016.
- Tomasz and Łodygowski, 2013.** Jankowiak Tomasz and Tomasz Łodygowski. *Identification of parameters of concrete damage plasticity constitutive model*, 2013.
- Uwe Starossek, 2009.** Uwe Starossek. *Progressive collapse of structures*. Thomas Telford Limited, 2009.



Appendix

A	Material modelling	95
A.1	Concrete modelling	
A.2	Testing of material behaviour in Abaqus	
A.3	Shell and solid element RCB	
A.4	Modelling of hollow core slab	
B	Eurocode approach RCB	121
B.1	Analytical RCB model	
C	Abaqus procedures	127
C.1	Contact behaviour in Abaqus	
C.2	Damping in dynamic explicit analysis	
D	Energy and mesh convergence	131
D.1	Da Vinci Failure	
D.2	Mesh convergence	
D.3	Butterworth filter	
E	Design failure scenario	139
E.1	Part-wise element deletion	
E.2	Parameter study	
E.3	Simplified beam shear force diagrams	
E.4	Damage and moment caused by inertia effect	
F	2DOF and Eurocode approach	145
F.1	Stiffness and Mass of the structure.	
F.2	Response to Impact load	
F.3	Eurocode approach of impact loads	
F.4	Hard and soft impact comparison with 2DOF solution.	

A. Material modelling

To investigate how progressive collapse will develop in a precast concrete structure it is essential that a fitting constitutive model is used which describes the most important phenomenons in the material. It is important to be able to model all types of failure and damage of elements that can reduce the stiffness and thus change the dynamic behaviour.

To model the design failure scenario, it is required to model reinforced concrete, meaning that a material model for both steel and concrete is required, which is described in this Appendix.

A.1 Concrete modelling

The behaviour of concrete in the model is described using the Concrete Damage Plasticity model, which was developed by (Lubliner et al., 1989) [Dassault Systèmes, 2020]. The model uses a yield surface f defined in effective stress space $\bar{\sigma}$. The CDP model is based on a modified Drucker-Prager criterion, as illustrated on Figure A.1, where the parameter $K_C = 1$ results in the Drucker Prager yield surface. In a plane stress state, the yield surface is as illustrated on Figure A.2.

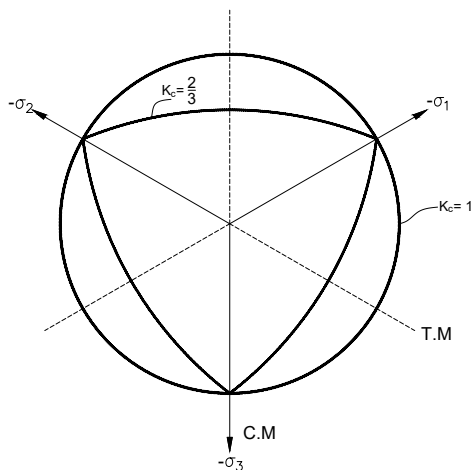


Figure A.1: Yield surface in the deviatoric plane. [Dassault Systèmes, 2020]

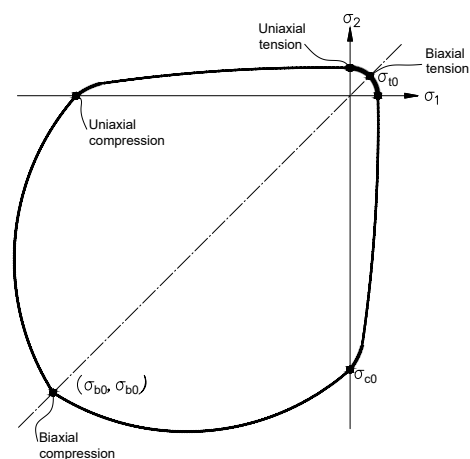


Figure A.2: Yield surface in plane stress state. [Dassault Systèmes, 2020]

The CDP model assumes isotropic damage d and non-associated flow, described by the

Drucker-Prager hyperbolic function, (A.1). The yield surface is described by (A.2).

$$G = \sqrt{(\varepsilon \sigma_{t0} \tan(\psi))^2 + \bar{q}^2} - \bar{p} \tan(\psi) \quad (\text{A.1})$$

$$f = \frac{1}{1-\alpha} \left(\bar{q} - 3\alpha \bar{p} + \beta \left(\bar{\varepsilon}^{\text{pl}} \right) \langle \bar{\sigma}_{\text{max}} \rangle - \gamma \langle -\bar{\sigma}_{\text{max}} \rangle \right) - \bar{\sigma}_c \left(\bar{\varepsilon}_c^{\text{pl}} \right) = 0 \quad (\text{A.2})$$

$$\alpha = \frac{\left(\frac{\sigma_{b0}}{\sigma_{c0}} \right) - 1}{2 \left(\frac{\sigma_{b0}}{\sigma_{c0}} \right) - 1}, \quad 0 \leq \alpha \leq 0.5$$

$$\beta = \frac{\bar{\sigma}_c \left(\bar{\varepsilon}_c^{\text{pl}} \right)}{\bar{\sigma}_t \left(\bar{\varepsilon}_t^{\text{pl}} \right)} (1 - \alpha) - (1 + \alpha) \quad (\text{A.3})$$

$$\gamma = \frac{3(1 - K_c)}{2K_c - 1}$$

where

$\bar{\sigma}_c \left(\bar{\varepsilon}_c^{\text{pl}} \right), \bar{\sigma}_t \left(\bar{\varepsilon}_t^{\text{pl}} \right)$	Effective compressive and tensile cohesion stress
$\bar{\varepsilon}_c^{\text{pl}}, \bar{\varepsilon}_t^{\text{pl}}$	Equivalent plastic strains
\bar{q}	Mises equivalent effective stress
\bar{p}	Hydrostatic pressure stress
$\langle \rangle$	Macauley bracket $\implies \langle x \rangle = \frac{1}{2}(x + x)$
$\bar{\sigma}_{\text{max}}$	Maximum principal effective stress
ψ	Dilation angle
σ_{t0}	Uniaxial tensile yield strength
σ_{b0}	Equibiaxial compressive yield strength
ε	Eccentricity parameter
K_c	Ratio between (T.M) and (C.M) of the second stress invariant

The model assumes that the two main failure modes is tensile cracking and compressive crushing of the concrete material. The yield surface is governed by the two hardening variables $\bar{\varepsilon}_c^{\text{pl}}$ and $\bar{\varepsilon}_t^{\text{pl}}$, described in Figure A.3 and A.4.

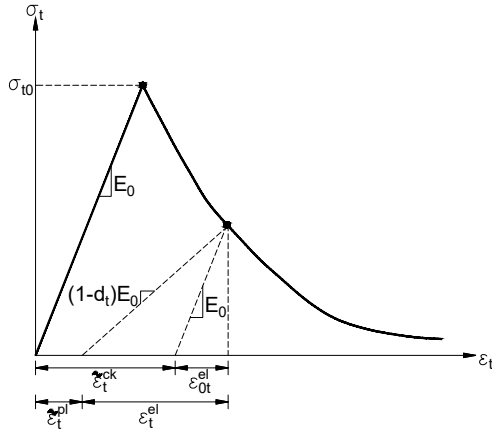


Figure A.3: Stress-strain curve in uniaxial tension [Dassault Systèmes, 2020]

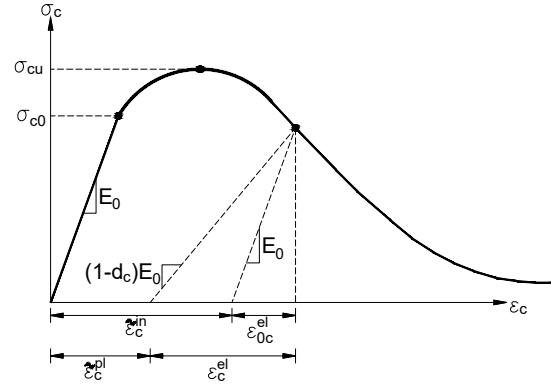


Figure A.4: Stress-strain curve in uniaxial compression [Dassault Systèmes, 2020]

To acquire the data needed in the CDP model, uniaxial compression and tension tests are necessary, along with Kupfer's curve. These tests are not performed in this project, and data from previous tests are used in the model, specifically data acquired from tests on concrete class B50, with characteristic compression strength $f_{ck,cube} = 50\text{MPa}$. The input data needed in the CDP model consists of the inelastic, $\tilde{\epsilon}_c^{in}$, and cracking, $\tilde{\epsilon}_t^{ck}$, strain.

From these parameters, the equivalent plastic strains, $\tilde{\epsilon}_c^{pl}$, $\tilde{\epsilon}_t^{pl}$, is calculated

$$\begin{aligned}\tilde{\epsilon}_t^{pl} &= \tilde{\epsilon}_t^{ck} - \frac{d_t}{1-d_t} \frac{\sigma_t}{E_0} \\ \tilde{\epsilon}_c^{pl} &= \tilde{\epsilon}_c^{in} - \frac{d_c}{1-d_c} \frac{\sigma_c}{E_0}\end{aligned}\tag{A.4}$$

The parameters used in the CDP model is seen in Table A.1, and this material is also referred to as Concrete-01.

Appendix A. Material modelling

Table A.1: Parameters for CDP model - Concrete-01. [Tomasz and Łodygowski, 2013]

Plasticity parameters			Density and elastic parameters		
Dilation angle ψ	38 [deg]		Young's modulus E	19.7 [GPa]	
Eccentricity e	0.1 [-]		Poisson ratio ν	0.19 [-]	
$\frac{\sigma_{b0}}{\sigma_{c0}}$	1.12 [-]		Density ρ	2400 [kg/m ³]	
$K_c = \frac{q_{TM}}{q_{CM}}$	2/3 [-]				
Compressive behaviour			Tensile behaviour		
σ_c [MPa]	Inelastic strain $\tilde{\epsilon}_c^{\text{in}}$ [-]	d_c [-]	σ_t [MPa]	Cracking strain $\tilde{\epsilon}_t^{\text{ck}}$ [-]	d_c [-]
15	0	0	1.99893	0	0
20.19780	7.47307E-05	0	2.842	3.33E-05	0
30.00061	9.88479E-05	0	1.86981	0.00016	0.40641
40.30378	1.54123E-04	0	0.86272	0.00028	0.69638
50.00769	7.61538E-04	0	0.22625	0.00068	0.92039
40.23609	2.55756E-03	0.19540	0.05658	0.00109	0.98009
20.23609	5.67543E-03	0.59638			
5.257557	1.17331E-02	0.89487			

Concrete material subjected to cyclic behaviour will result in continues opening and closing of micro cracks. The CDP model is able to consider this along with the recovered stiffness in each cycle, where e.g. the cycle from tension to compression will result in closure of tensile cracks and therefore recovery of compression stiffness.

The degree of recovery of the stiffness is determined based on the weight factors, w_t and w_c , which control the tension and compression recovery respectively upon load reversal. The effect of the two weight factors is seen illustrated on Figure A.5 for uniaxial behaviour. The values chosen in the numerical model is $w_c = 1$ and $w_t = 0$, such that the compression stiffness is recovered, and tension stiffness is not. [Dassault Systèmes, 2020]

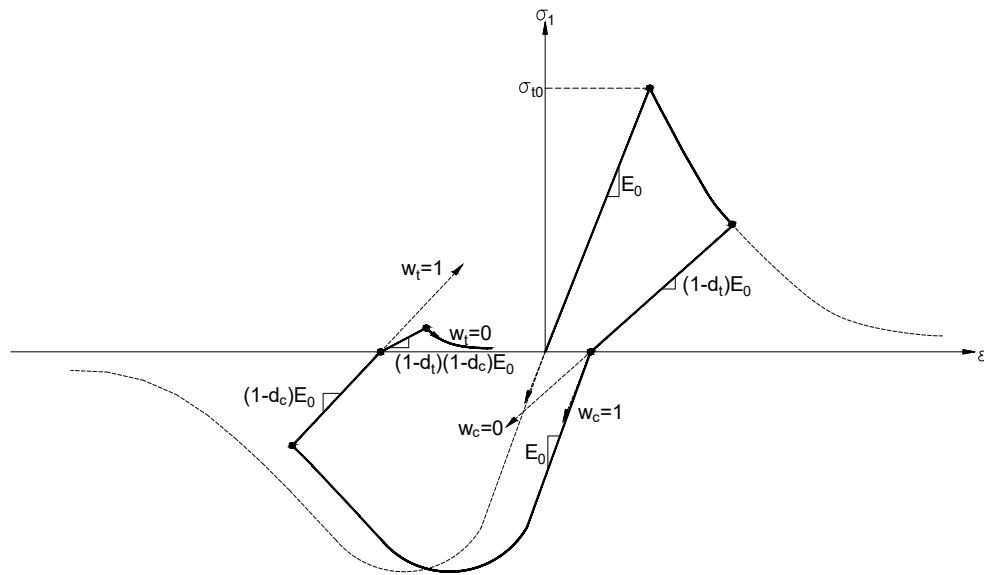


Figure A.5: Cyclic behaviour modelled with weight factors, here shown with uniaxial cyclic test. [Dassault Systèmes, 2020]

A.1.1 Steel material modelling

The behaviour of steel is described using a general procedure described in Dassault Systèmes [2020] where the following needs to be specified:

- Undamaged elastic-plastic response of the material (Classical metal plasticity)

The classic plasticity theory for isotropic metals is based on Von Mises yield criterion. The model uses a yield surface, f , defined in effective stress space, $\bar{\sigma}$, which is shown on Figure A.6.

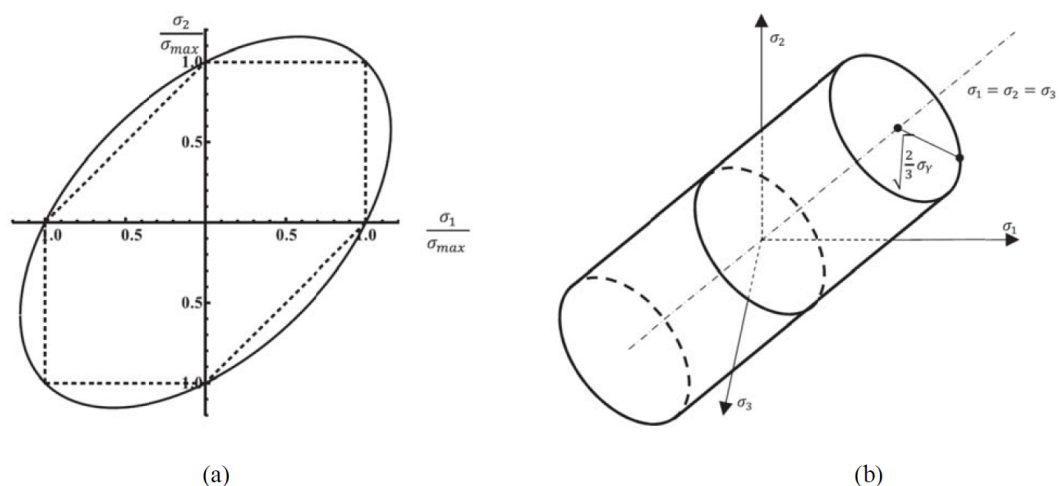


Figure A.6: Von Mises yield surface in 2D and 3D.

For the rebar steel the following material parameters are used and this steel is referred to

as Steel-01 in this report.

Table A.2: Parameters for rebar steel - Steel-01

Plasticity parameters		Density and elastic parameters	
Yield stress @ 0 plastic strain	500 [MPa]	Young's modulus E	210 [GPa]
Yield stress @ 0.1476 plastic strain	550 [MPa]	Poisson ratio ν	0.3 [-]
		Density ρ	7850 [kg/m ³]

A.2 Testing of material behaviour in Abaqus

To ensure correct modelling of the concrete behaviour in bending failure, a quasi-static loading test is performed on a reinforced concrete beam, denoted RCB. In the numerical modelling of the RCB, two models is created, one which uses a fine mesh with solid elements, and one with a coarse mesh using shell elements. The two numerical models is further investigated with a solution based on the Eurocodes, [DS/EN-1992, 2007], described in Appendix B.1. Generally the Abaqus analyses in this report will be performed as explicit dynamic analyses. This is because Abaqus does not allow element deletion for implicit dynamic analysis or static analysis and it is also why some investigations that could in theory be performed as static must be performed quasi-statically. Another reason for using explicit dynamic analysis is that when using a fine mesh with a lot of elements and non-linearity the explicit will solve the problem faster because the stiffness matrix is not factorised. When the stiffness matrix is factorised it refers to a step where the stiffness matrix is inverted for every time step, a very computationally demanding task that is performed in implicit time integration. Since explicit time integration is not unconditionally stable the time step has to be very small for the calculation to not explode and this is an automated process in Abaqus.

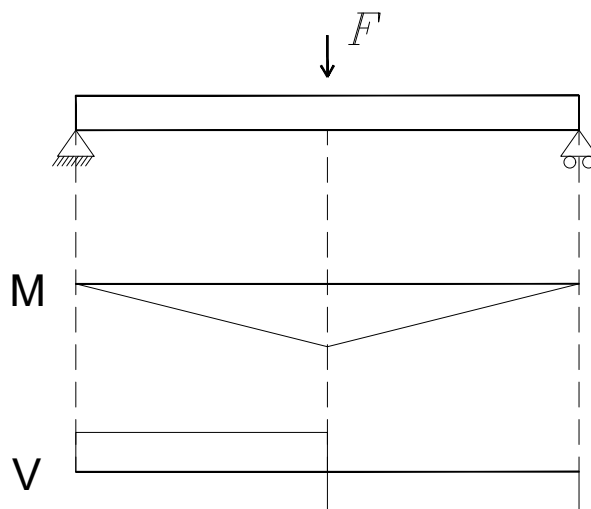


Figure A.7: a) Moment and shear diagram from a three point bending test.

In order to know if the material behave as intended a three point bending test is simulated

as illustrated on Figure A.7. The RCB cross section and overall measures is illustrated on Figure A.8. The RCB is reinforced using two and four rebars in the top and bottom region, respectively. Furthermore the RCB is equipped with shear reinforcement as described in Appendix B.1, to assure that the failure mode is bending. The RCB cross-section and overall dimensions is illustrated on Figure A.8.

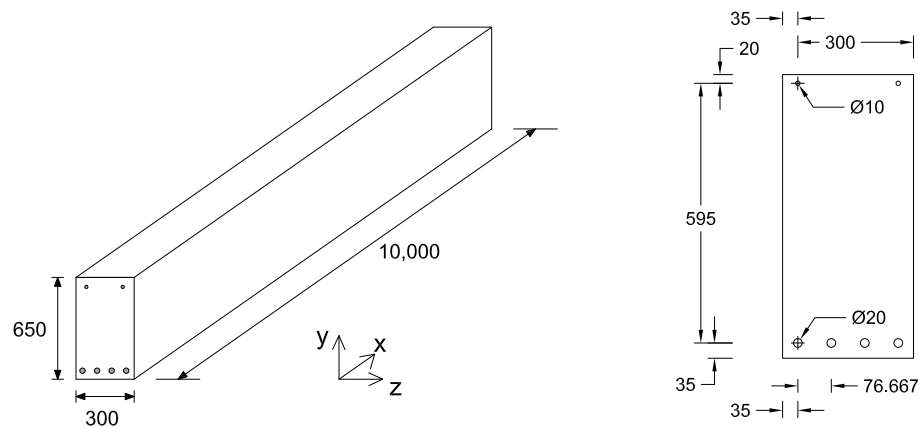


Figure A.8: Cross section of RCB with dimensions used in analytical calculations and FEM simulations. All measurements in [mm]

A.3 Shell and solid element RCB

The RCB is modelled twice, using either shell or solid elements, as described in Table A.3. In the solid element RCB, a fine mesh has been used as illustrated on Figure A.9, and the results are used for comparison to the coarse mesh used in the shell element model illustrated on Figure A.10. Furthermore, to avoid the effects of shear locking in the solid elements, reduced integration has been chosen in the FE-analysis.

Table A.3: FE description.

Element type	Description	Geometric order	2.order accuracy
Shell	8-node quadrilateral in-plane shell	Linear	No
Solid	8-node linear brick	Linear	No

The two RCB models is simulated in an explicit dynamic analysis over 10 seconds. By loading over 10 seconds the dynamic effects is reduced to a point where it can be considered quasi-static. Using the two different types of finite element along with a fine and coarse mesh, the effects of compute time can be compared with the loss in accuracy, as shown in the results.

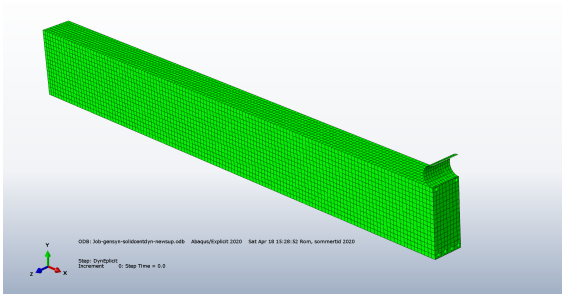


Figure A.9: Element distribution in the solid element RCB.

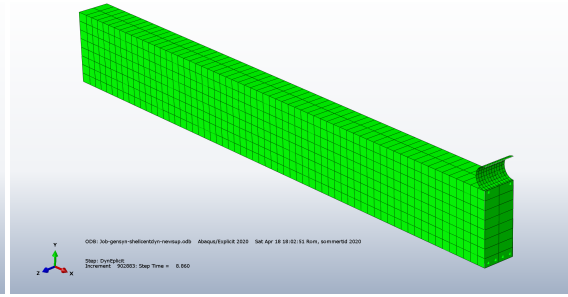


Figure A.10: Element distribution in the shell element RCB.

A.3.1 Results and comparison of simulations

From the three point bending test performed in Abaqus, the reaction force, R_1 and R_2 , along with the displacement, u , is extracted for analysis, as illustrated on Figure A.11. Furthermore, the bottom rebar stress, σ , at the midpoint span is extracted to investigate the yielding behaviour.

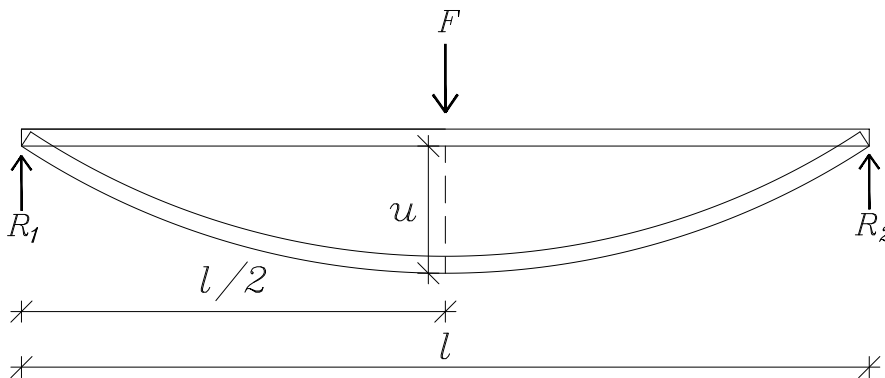


Figure A.11: Displacement, applied force and reaction force definition.

As these simulations are performed as explicit dynamic there can be some dynamic amplification of the reaction and displacement because of the moving RCB mass, these effects are attempted reduced by increasing the force, F , from zero to maximum value over 10 seconds. The load F is applied linearly from zero at time $t = 0s$ until a maximum of 180 kN at time $t = 10s$, reaching just above the analytically determined moment capacity described in Appendix B.1.

Shell model

To illustrate the results from the numerical analysis, two force-displacement curves are obtained as illustrated on Figure A.14. One of the curves illustrate the displacement, u , as function of the applied force, F , which varies linearly with time. The second curve illustrates the dynamic behaviour of the beam, where the displacement is shown as

function of the sum of reaction forces R_1 and R_2 . The two curves behaviour are divided into three zones, being zone *I*, *II* and *III*, where each of the zones have different characteristics.

- Zone *I* The uncracked zone. The first zone is characterised by the linear behaviour of both the reaction and applied force curve, indicating that the beam behaves linear elastic with with the uncracked elastic properties.
- Zone *II* The cracked zone. The first crack occurs as illustrated on Figure A.12, resulting in a sudden drop in bending stiffness.
- Zone *III* Yielding zone. The rebars begin to yield and the residual load capacity is close to zero. Extensive cracking is present as illustrated on Figure A.13

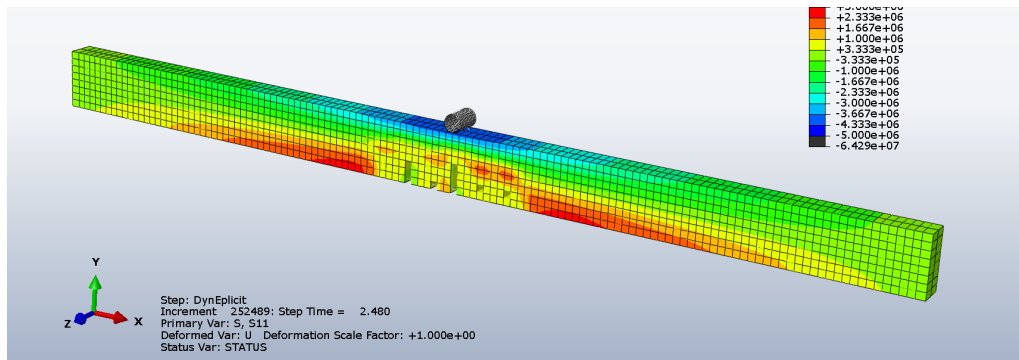


Figure A.12: RC beam with shell elements. First crack development. The stresses shown are averaged for every shell element which is why it does not look like a normal shell where there are different stresses in top and bottom of each element

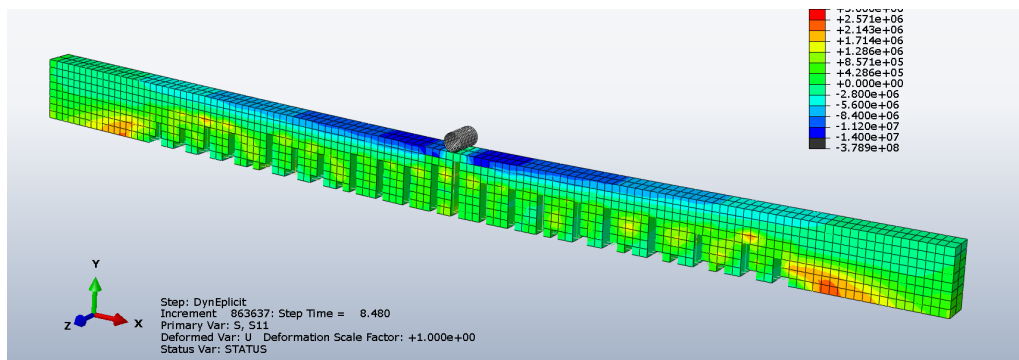


Figure A.13: RC beam with shell elements. Crack development just before failure. The normal stress in the x direction is shown, with red color indicating tension and blue compression.

Abaqus model setup (Figure A.12)			
Element type	No. of elements	Material	Other
Shell continuum SC8R	3586	Concrete-01	Element deletion and Contact
Timoshenko beam B31	1296	Steel-01	Embedded region
Analysis type:		Explicit dynamic	

The initiating deflection, u , of the beam is seen to fit with quasi-static loading conditions

with the linear response until the beams first crack arises at a deflection of $u = 5\text{mm}$. The crack results in a sudden loss of stiffness, which results in a free fall motion of the beam, seen as the decrease in reaction forces on Figure A.14. Followed by the free fall motion, the bending forces are distributed to the cracked cross-section, resulting in a sudden increase in reaction forces $R_1 + R_2$ from the built up inertia in the short free fall of the beam. The phenomenon at the first crack is also visible on the rebar stress curve illustrated on Figure A.15, as the horizontal line at an applied force of $\approx 38\text{kN}$.

The continuous dynamic behaviour throughout the three point bending test can therefore be explained by the continuous occurrence of cracks in the concrete which continues until failure.

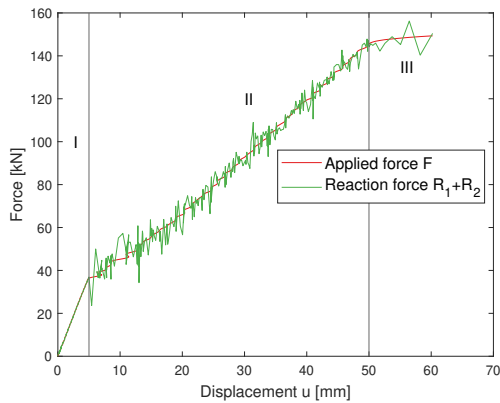


Figure A.14: Force- and reaction-displacement curve (Shell model)

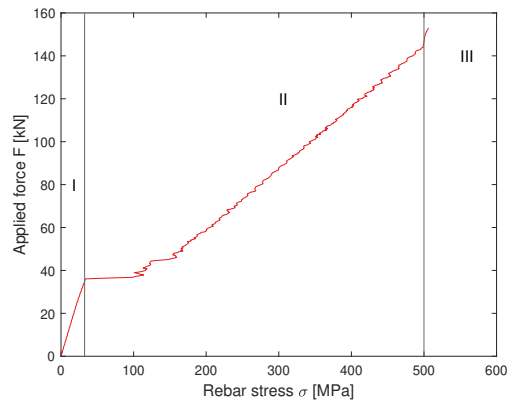


Figure A.15: Bottom rebar stress behaviour at midspan $L/2$ (Shell model)

The bending stiffness of the beam settles to a nearly constant value before and after the crack as shown on A.16. The stiffness of the uncracked beam is called k_1 and the stiffness of the cracked beam is called k_2 . The following values are determined: $k_1 = 7.5 \text{ MN/m}$, $k_2 = 3.0 \text{ MN/m}$.

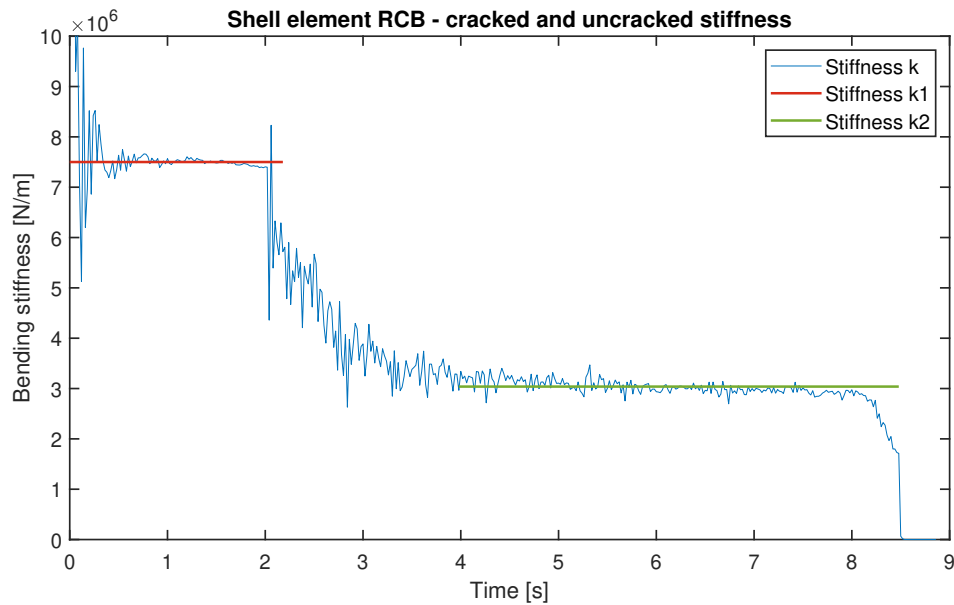


Figure A.16: Stiffness of the shell element beam when loaded to failure over time.

Solid model

In the solid model, the force-displacement curve illustrated on Figure A.18 is seen to follow the same pattern, and can be divided into the same three zones as described in the shell model. In zone *I* the linear elastic pattern is seen to follow the exact path as the shell model, as was expected as the analysis is in the linear elastic stage, and has low complexity. In zone *II*, the first crack has appeared as illustrated on Figure A.19, the shell and solid element model is seen to deviate, with the sudden decrease and increase in reaction forces from initiating crack being twice as high as in the shell model. As well as increased fluctuations in reaction forces $R_1 + R_2$, the bottom rebar stress illustrated on Figure A.18 indicates the same phenomenon with an increased spike in forces at the initial crack, when compared to the shell model rebar stress. Furthermore, the solid model is capable of describing the post rebar yield behaviour illustrated on Figure A.20 with higher accuracy than the shell model, visible by the presence of flexure shear cracks which is not present in the more coarse shell model.

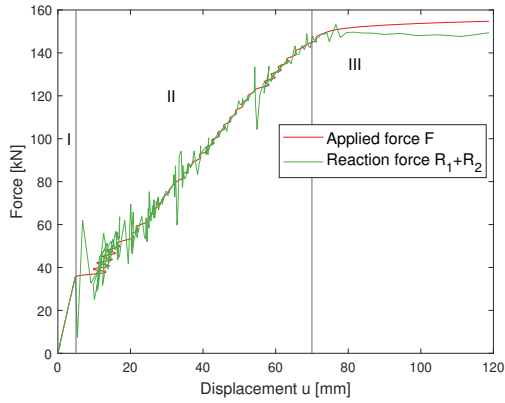


Figure A.17: Force- and reaction-displacement curve (Solid model).

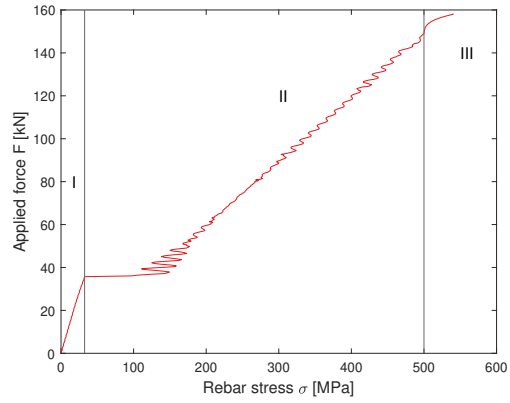


Figure A.18: Bottom rebar stress behaviour at midspan $L/2$ (Solid model).

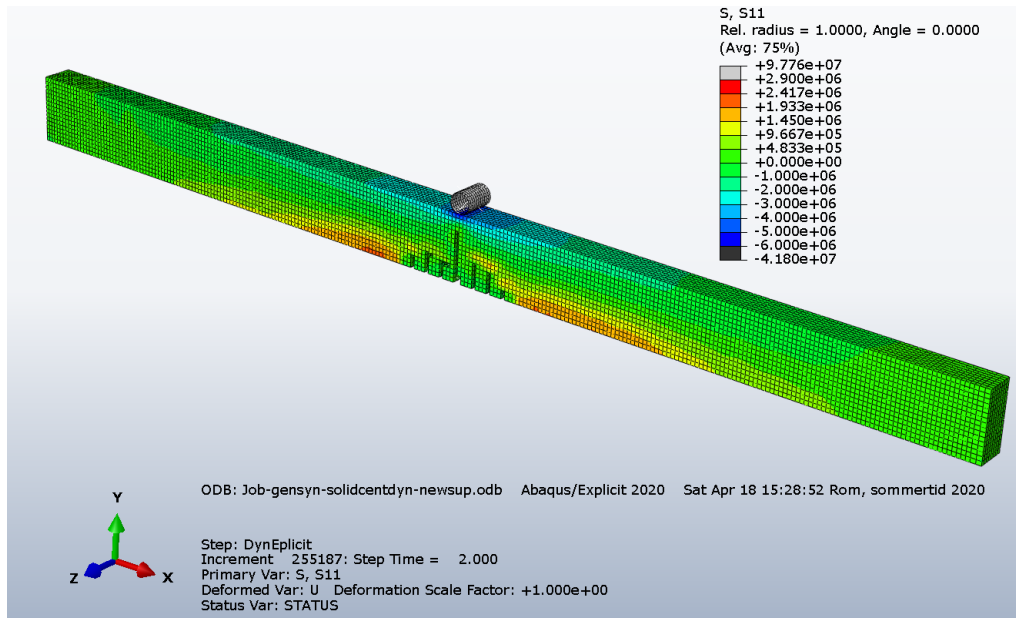


Figure A.19: RCB with solid elements. First crack development. The normal stress in the x direction is shown, with red color indicating tension and blue compression.

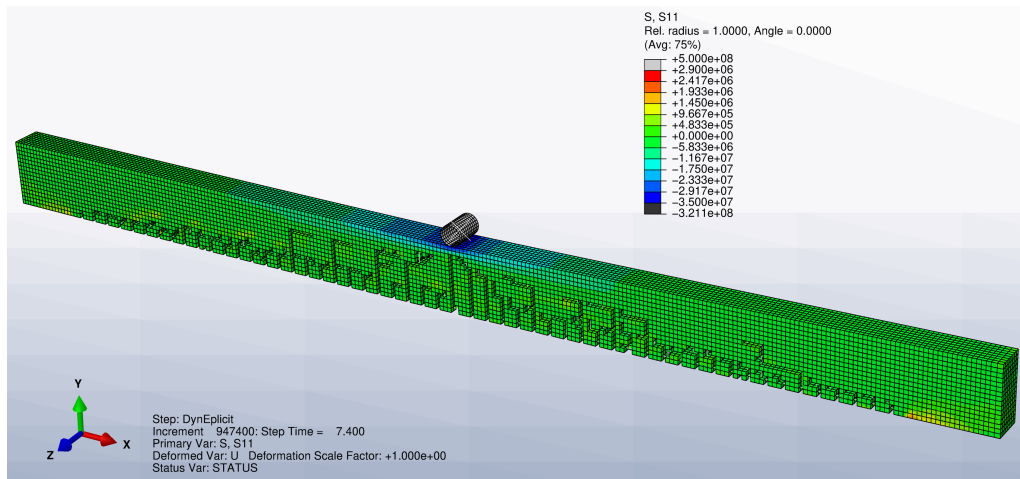


Figure A.20: RCB with solid elements. Crack development just before failure.

Abaqus model setup (Figure A.20)			
Element type	No. of elements	Material	Other
Solid continuum C3D8R	34178	Concrete-01	Element deletion and Contact
Timoshenko beam B31	1296	Steel-01	Embedded region
Analysis type:		Explicit dynamic	

In Figure A.21 the stiffness of the beam with solid elements is shown. As for the shell stiffness, the uncracked beam stiffness is denoted k_1 and the stiffness of the cracked beam is denoted k_2 . The following values are determined: $k_1 = 7.4 \text{ MN/m}$, $k_2 = 2.3 \text{ MN/m}$.

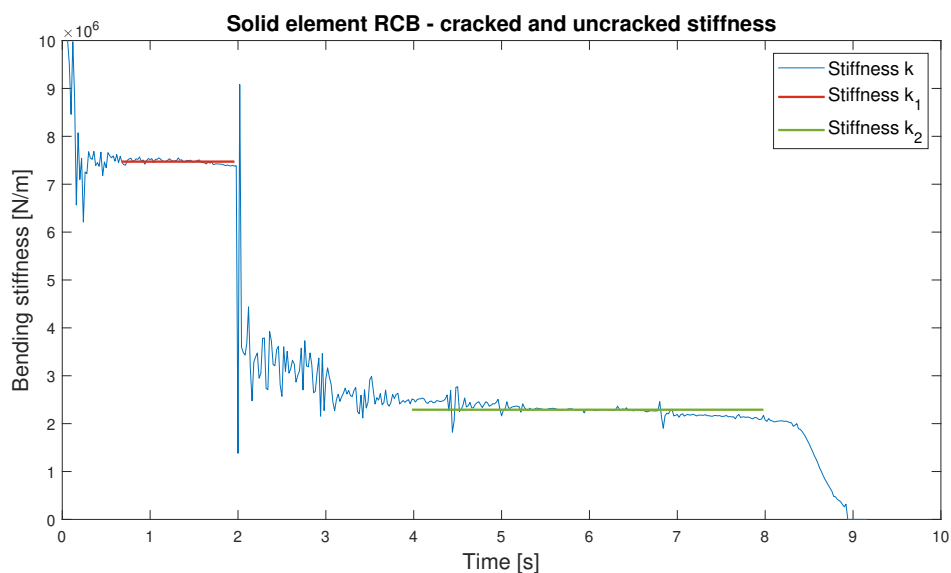


Figure A.21: Stiffness of the beam when loaded to failure over time.

Comparison of Shell, Solid and Analytical beam model

Comparing the shell and solid element model, it can be seen that when using shell elements, the dynamic behaviour is less present. The displacement, u , in the shell model at the start of zone *III* compared to the displacement at the same point in the solid model is smaller, which along with the smaller dynamic impact indicate that shell elements are stiffer. This can however be improved by mesh refinement if the error is deemed too large.

In the analytical calculation, the beam moment capacity is determined as the force at which the bottom rebars reach the yield stress. The comparison between shell, solid and analytical is therefore determined at the point of initial yield in the FE model, which is shown in Table A.4. Both results show a moment capacity that is bit larger than the analytical solution. Taking into consideration that the analytical approach neglects concrete tension strength and therefore is expected to be lower, the FEM results can be concluded to fit well with the analytic moment capacity. The computational effort required to compute the more precise solid element model is in Table A.4 seen to require eight times the cost of running the more simple shell element model. Considering the goal of the project, the solid and shell model differences are considered to be small compared to the difference in computational time, and a model built with shell elements is deemed sufficient to describe the bending failure behaviour of a RC structure.

Table A.4: Moment capacity of RCB calculated with two different element types. Both moments are larger than the analytical solution that showed a moment capacity of 372 kNm.

	Solid	Shell
Moment capacity [kNm]	376.4	379.9
Deviation from analytical solution [%]	1.14	2.08
Computation time [Minutes]	16	134

A.3.2 Quasi-static assumption

As described in the beginning of this section 10 seconds is considered to be quasi-static. This length of time is based on an experiment in Abaqus where a RCB is loaded over four different times, 1 s, 5 s, 10 s, and 20 s, respectively.

On Figure A.22 it is shown how the mid-span displacement varies over time. It is clear that the 1 second case has a significantly more dynamic response than the other times. The 5 second case is seen to show quasi-static behaviour only when uncracked. The 10 and 20 second case has shown to result in close to the exact same behaviour, and therefore the 10 second case is deemed sufficiently close to quasi-static assumption, and can be compared with the Eurocode static approach.

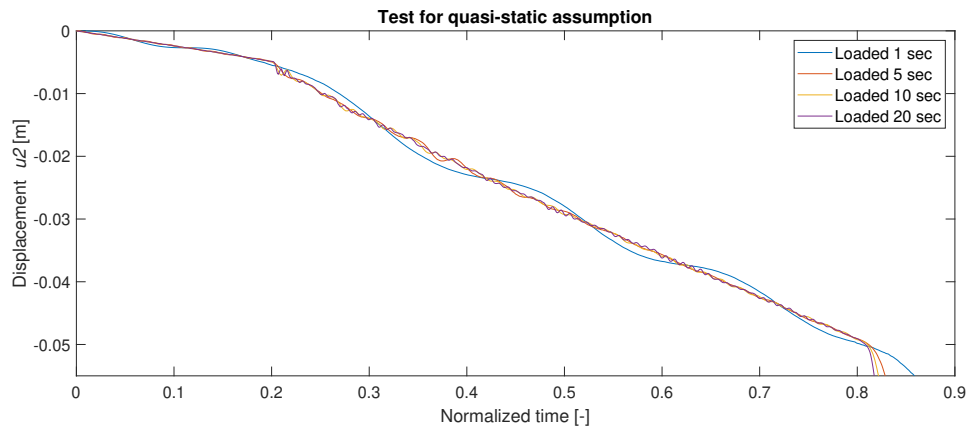


Figure A.22: The RCB is loaded over some time and the displacement at the center, u_2 , is measured. Here the time is normalised in order to compare them.

A.3.3 Testing of rebar embedment method.

Often in failure scenarios with concrete structures, excessive deformation will occur that can lead to rebar being pulled out of the concrete. To investigate how well this actually works in Abaqus, a test is performed with rebar modelled as a beam element which is embedded in a solid element. Force is then applied to the beam element until failure of the concrete.

The reinforcement is modelled with the use of Timoshenko beam elements, resulting in rebars with a circular cross section. To ensure correct concrete-rebar interaction, built-in constraints was used to embed the rebar into the concrete material. The option called "embedded region" in Abaqus takes an element or group of elements and embed it inside a host element, in this case the embedded elements are the rebar and the host element is the concrete structure [Dassault Systèmes, 2020]. The host element can only have translational degrees of freedom, which means it must be continuum elements. The translational degree of freedom of the embedded element nodes are eliminated if they are within the host element, and thus becomes embedded nodes. The geometric relationships between nodes of the embedded elements and the host element is used to interpolate the translational DOFs from the constrained embedded nodes to the corresponding host nodes. Only translational degrees of freedom are constrained and therefore embedded elements like beam elements can retain its rotational DOFs.

According to [Bjarne Chr. Jensen, 2020] the load capacity of a rebar can be calculated with equation (A.5), which is the force required to initiate a slip failure between concrete and rebar.

$$T = 2.25 f_{ctk} 2\pi \varnothing l_b \quad (\text{A.5})$$

The factor 2.25 takes the roughness into account and thus the friction between the two materials. The concrete tensile strength, f_{ctk} used, is the same as the ultimate tensile strength shown in Table A.1. For a rebar with a diameter, \varnothing , of 12.5 mm and an anchorage

length, l_b , of 0.5 m in a concrete block, the needed tensile force to pull the reinforcement out is then 250 kN.

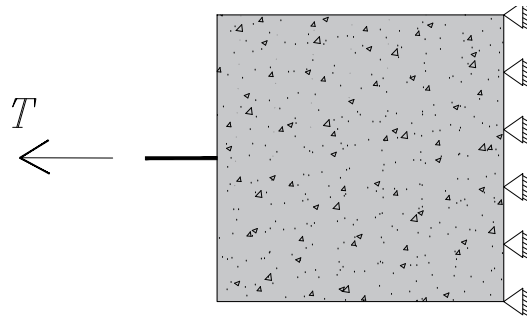


Figure A.23: Abaqus setup for rebar pull test.

The Abaqus setup is illustrated on Figure A.23 and A.24. The rebar is embedded in a cube shaped concrete block which is fixed horizontal and vertical direction using pinned supports on the backside. Equation (A.5) is a semi-empirical equation which is based on rebars with rough surfaces, and therefore is based on a greater failed area resulting in increased capacity T compared to smooth rebars. This is, however, still expected to give reasonable results when compared with the Abaqus model, since the rough mesh will result in a large failed area.

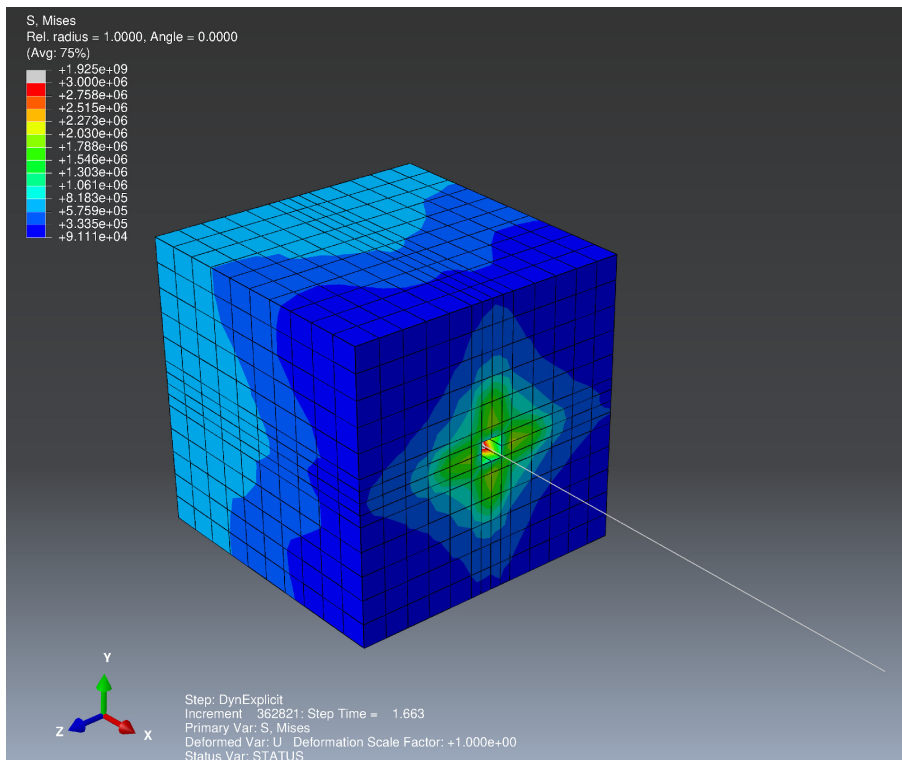


Figure A.24: Rebar pullout test setup in Abaqus, here shown using solid elements.

On Figure A.25 it is seen that the maximum force reaches 220 kN for the block with solid element type and 230 kN for shell element type. The difference is negligible and therefore

this experiment shows that it does not matter what element type is used. The most important outcome of this experiment is to show that it is possible to pull the rebar out of the concrete and the force reaches a level that is considered reasonable when compared to the force calculated with (A.5).

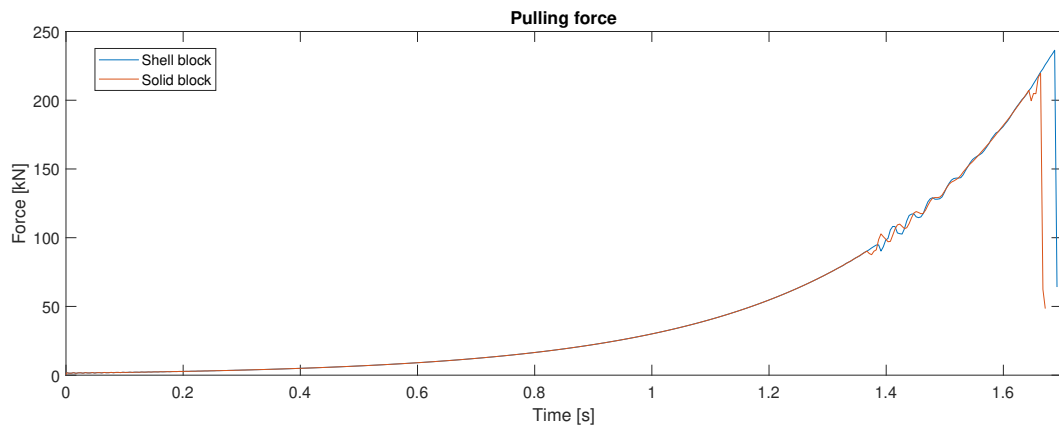


Figure A.25: Here it is seen how the force is applied over time on the rebar

Abaqus model setup (Figure A.25)			
Element type	No. of elements	Material	Other
Solid continuum C3D8R	1960	C01	Element deletion
Timoshenko beam B31	40	S1	Embedded region
Analysis type:		Explicit dynamic	

A.3.4 Testing of shear strength

Another important topic to investigate is the behaviour of reinforced concrete subjected to shear. In Eurocode EC2 [DS/EN-1992, 2007] a formula for the shear capacity without shear reinforcement is provided. Although the formula empirical, it can be expected that the strength should be in the same region. The setup is quite simple; A concrete block with two $\text{\O}10$ rebars and a force applied at the tip, increasing linearly from zero to 50 kN over 5 seconds. The test setup is illustrated on Figure A.26.

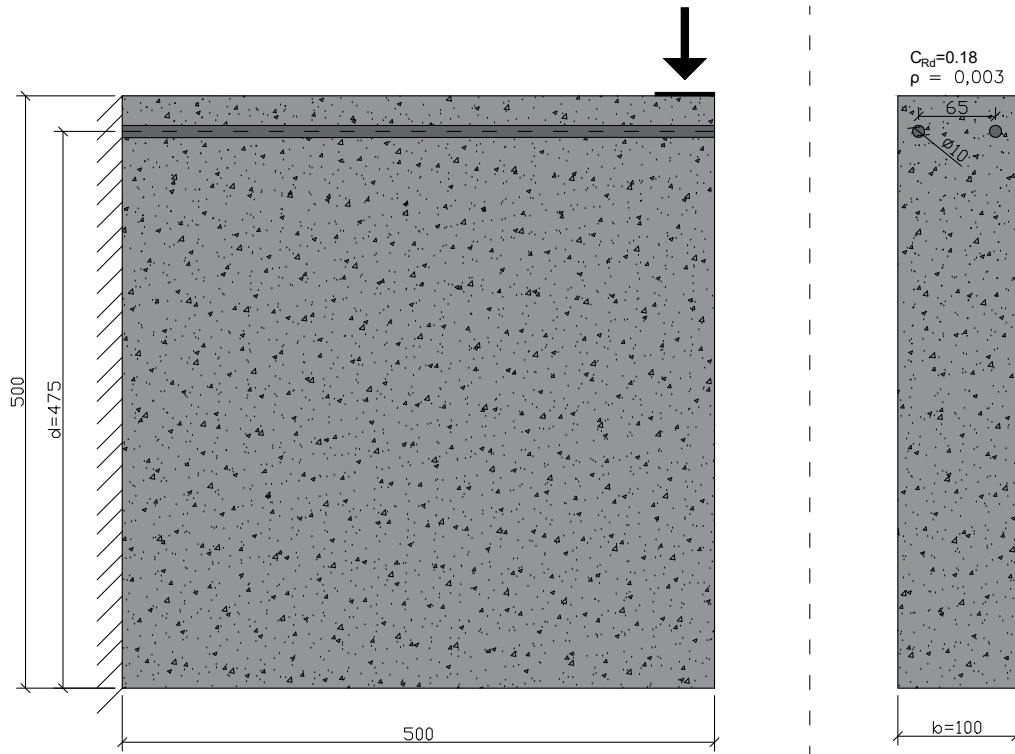


Figure A.26: The setup for the shear test is here illustrated along with the factors used in equation (A.6) All measures in [mm].

The EC2 formula and calculations for shear capacity is shown in (A.6).

$$V_{Rd} = C_{Rd} \left(1 + \sqrt{\frac{200}{d}} \right) (100\rho f_{ck})^{\frac{1}{3}} b d \quad (\text{A.6})$$

$$V_{Rd} = 33.3\text{kN} \quad (\text{A.7})$$

A test was performed with shell elements but because of large thickness and because transverse shear stresses comes from through thickness variation it is seen on Figure A.27 that shell elements does not calculate the shear stress very well. They might perform much better in other applications and this is why they are used in comparison with solid elements in some of the investigations. In this test however the results were bad since the observed shear stress was almost zero and therefore did not accurately show what would happen in reality.

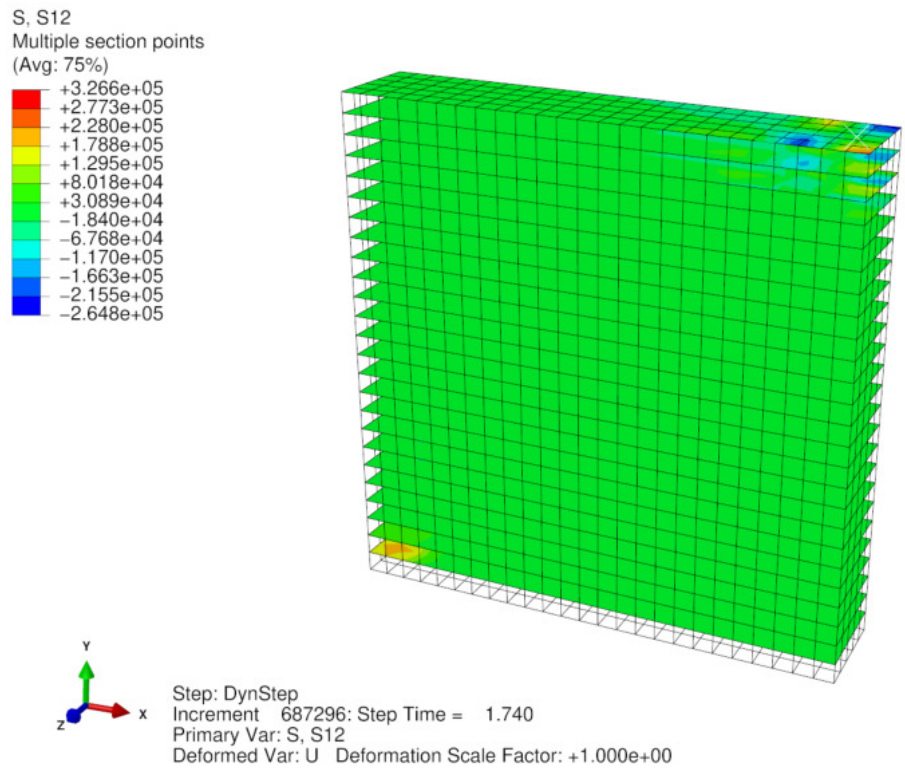


Figure A.27: The shear stress, S12, in the block modelled with shell elements.

Abaqus model setup (Figure A.27)			
Element type	No. of elements	Material	Other
Continuum shell SC8R	3165	C01	Element deletion and Contact
Timoshenko beam B31	40	S1	Embedded region
Analysis type:			Explicit dynamic

On Figure A.28 the final step before failure in for the model with solid elements is shown, with the following steps illustrated on Figure A.29. From the test in Abaqus it is seen that failure happens after 3.67 seconds at a load of 36.7 kN. This is very close to the result from EC2 and thus why it is considered proven that Abaqus accurately can model shear failure with the CDP model when using solid elements.

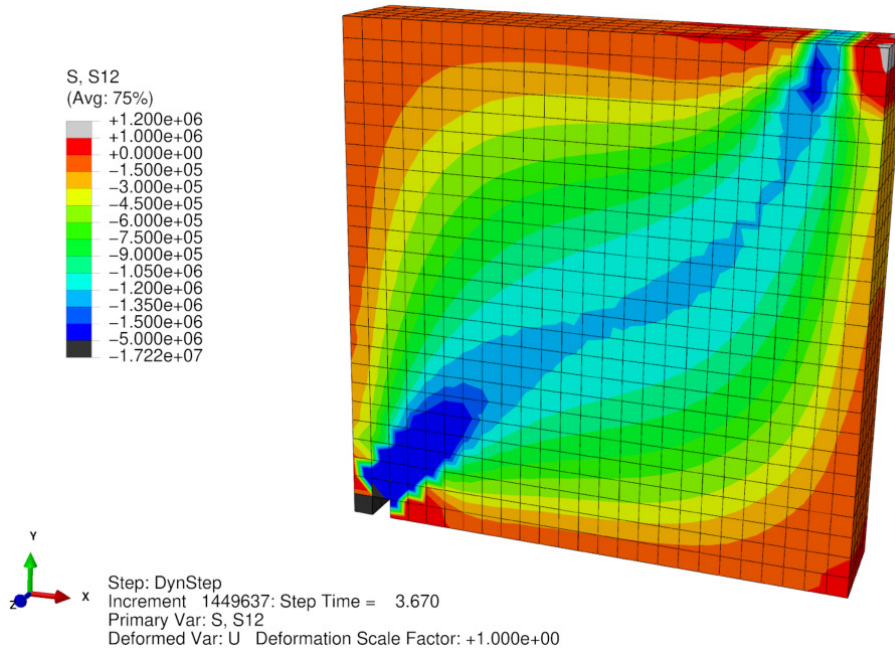


Figure A.28: The shear stress, S12, in the block immediately before it reaches its shear capacity.

Abaqus model setup (Figure A.28)			
Element type	No. of elements	Material	Other
Solid continuum C3D8R	3165	Concrete-01	Element deletion and Contact
Timoshenko beam B31	40	Steel-01	Embedded region
Analysis type:		Explicit dynamic	

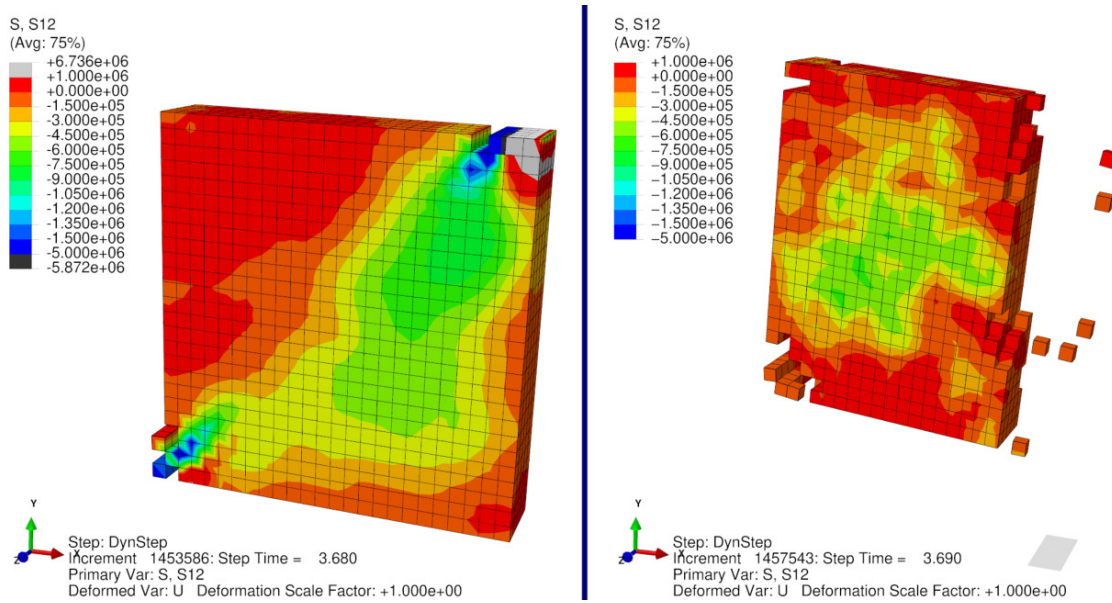


Figure A.29: The shear stress, S12, in the block at 0.01 s and 0.02 s after failure, respectively.

A.3.5 Choice of shell element

The primary reason for comparing the shell and solid meshed beam is to improve performance. However modelling with shell elements is not always preferred and some topics must firstly be considered. Abaqus provide the possibility to use three different types of shell elements, being thin, thick and continuum shell elements. Thin and thick elements are very similar, like all shell elements plane stress is assumed, they both have translational and rotational DOF and the thickness does not vary. In general a shell element is used when 1 dimension is much smaller than the others. General rule of thumb says that thickness, t , must not be larger than $1/15$ of the other dimensions if using thin shell elements. The reason is that the thin elements assumes the effect of transverse shear being negligible, where as thick shell elements takes the transverse shear into account and therefore can be used for $t > 1/15$ of the other dimensions.

So as long as the surfaces remain flat and featureless a thick shell element could be a good choice of element for modelling a RCB. Although problems arise when modelling nonlinear behaviour, in which case the thick and thin shell elements does not perform very well. In this case Abaqus provide a Continuum Shell Element that allow for finite strain and large rotations that makes them very good for nonlinear problems and therefore good for the experiments in this report. Continuum shell elements only have displacement DOFs and therefore, modelling-wise, they look a lot like continuum solid elements, but their kinematic and constitutive behaviour is similar to conventional shell elements.

When using continuum shell elements the transverse shear is not very well described for a single element in the thickness direction, but that can be improved by stacking them as illustrated on Figure A.30.

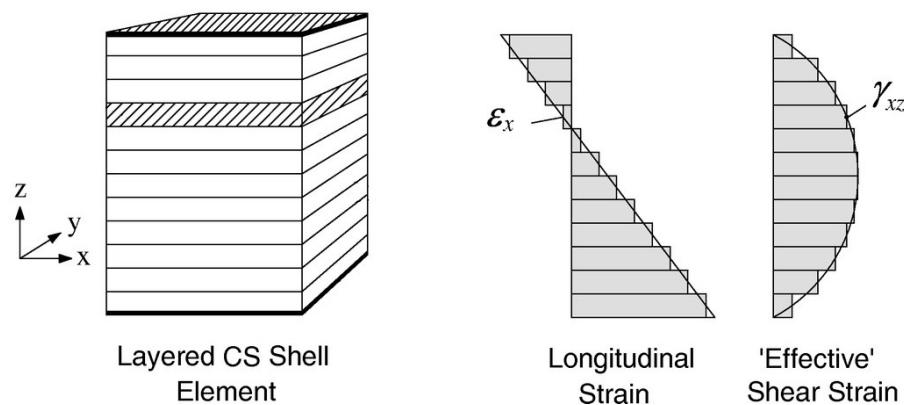


Figure A.30: Stacking in continuum shell [ASCE, 2016]

While stacking increases the number of calculations, continuum shells are in general still more computationally efficient than continuum solids [Dassault Systèmes, 2020]. It is also important to not confuse accuracy of transverse shear and a high resolution transverse shear path. One important difference between continuum solid and continuum shell is the assumption of constant thickness in shell. According to the Abaqus documentation there should be maximum 10 % change in the thickness or else continuum solids should be used instead.

In models with damage, and sometimes element deletion, there can occur big local deformations and therefore these cases will probably be better suited to be modelled with continuum solid elements, but it will be something to consider from case to case.

A.4 Modelling of hollow core slab

As described in section 4.2.3, the hollow core slabs consist of concrete slabs with pre-stressed bottom reinforcement and with longitudinal cylindrical holes to reduce weight.

The HCS model is divided into three steps of analysis in Abaqus, comprising of the following:

- Step 1, the HCS model is created with rebars embedded in the concrete as described in the RCB model
- Step 2, the rebar are pre-stressed by linear cooling and modification of the thermal expansion coefficient
- Step 3, the point load is applied linearly over 10 seconds

The HCS is modelled using solid elements with the same three-point bending setup as the RCB, illustrated on Figure A.11. Furthermore the geometry of the cross section is illustrated on Figure 4.12. The FE-model of the slab can be seen illustrated on Figure A.31 and A.32.

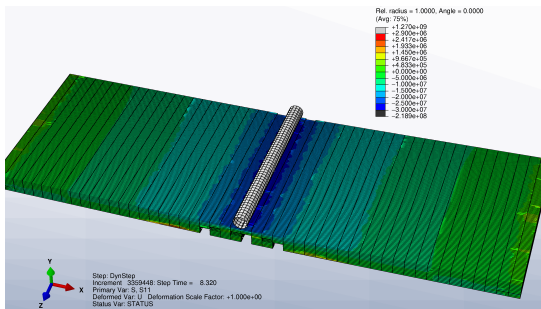


Figure A.31: Top view of HCS before yield in the rebar and therefore before failure. The colours represent normal stresses in the direction of span, S_{11} . Red indicate tension stresses close to yield and blue indicate compression up to 30 MPa.

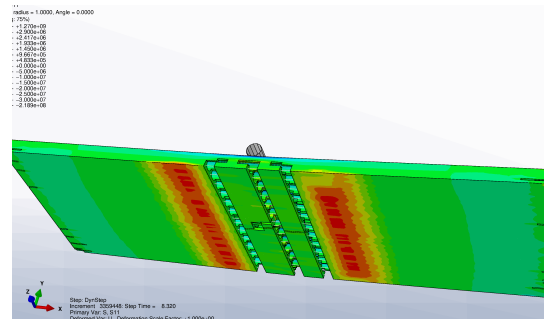


Figure A.32: Bottom view of HCS before yield.

Abaqus model setup (Figure A.31)			
Element type	No. of elements	Material	Other
Solid continuum C3D8R	48800	Concrete-01	Element deletion and Contact
Timoshenko beam B31	504	Steel-02	Embedded region
Analysis type:			Explicit dynamic

The actual use of the HCS is in combination with other construction elements to constructs a design failure scenario for a building, therefore the HCS is investigated for whether

or not it can be simplified to reduce the computational cost. The stiffness of the HCS is important since it can influence the resulting loads, and a simplification of the HCS can change the stiffness. Therefore two investigations has been conducted, where the first investigation is of what influence the pre-tensioned rebars has on the slab bending stiffness, and the second investigation is of what influence the cylindrical holes has on the second order moment of area, and therefore bending stiffness.

The prestressed reinforcement has other material properties than Steel-01 that was used in the analysis of the RCB model and these parameters are chosen based on the information from CHR concrete website [CHR Concrete, 2020]. The prestressed reinforcement has material parameters as described in Table A.5

Table A.5: Parameters for prestressed rebar steel - Steel-02

Plasticity parameters		Density and elastic parameters	
Yield stress @ 0 plastic strain	1660 [MPa]	Young's modulus E	210 [GPa]
Yield stress @ 0.0271 plastic strain	1860 [MPa]	Poisson ratio ν	0.3 [-]
		Density ρ	7850 [kg/m ³]

The two investigations required four different RC slab models, each investigated for the bending stiffness using the force-displacement curve. The resulting force-displacement curve is illustrated on Figure A.33-A.34 for the HCS with and without pretension, respectively. The force-displacement curve is also shown on Figure A.35-A.36 for the solid concrete slab with and without pretension, respectively.

As illustrated on the two pretension-rebar models, A.33 and A.35, the initial displacement is negative, due to the camber from the pretension step previously described. Hereafter the force, F , is applied linearly over 10 seconds, which results in an approximate bi-linear curve until failure when the two curves diverge.

The force-displacement curve of the non pre-tension slab models illustrated on Figure A.34 and A.36 is seen to have a highly dynamic response, caused by the low amount of rebar compared to the cross-section size and mass.

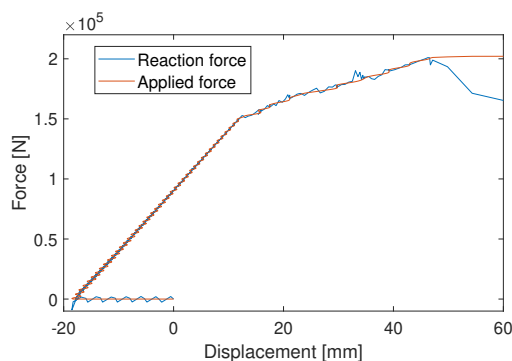


Figure A.33: Force- and reaction-displacement curve from the HCS model with pretension rebars.

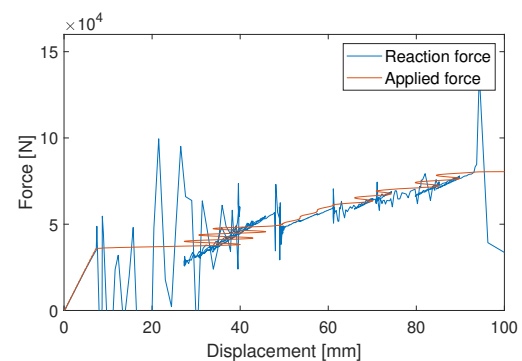


Figure A.34: Force- and reaction-displacement curve from the HCS model with non-pretension rebars.

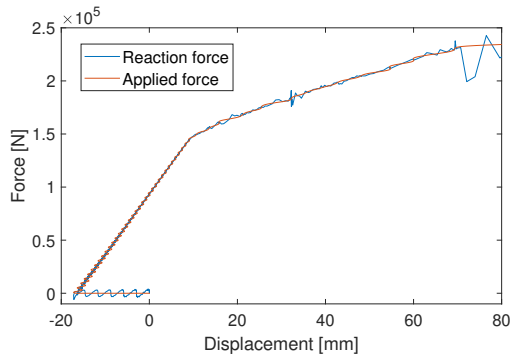


Figure A.35: Force- and reaction-displacement curve from the solid slab model with pre-tension rebars.

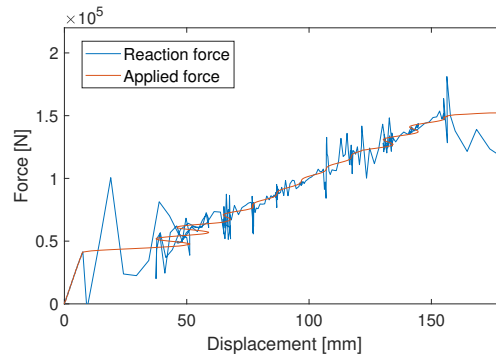


Figure A.36: Force- and reaction-displacement curve from the solid slab model with non-pre-tension rebars.

From the four models four different stiffnesses can be computed as shown in Table A.6. As for the RCB, k_1 is the pre-crack stiffness and k_2 is the post-crack stiffness. The table shows that even though the response is highly dynamic in the non pre-tension models, the resulting stiffness is close to the same value. Considering the low requirements to create pretension in the rebars compared to the excessive dynamic behaviour in the non pretensioned slabs, further studies with HCS is only performed with the use of pre-tension rebars.

Case #	1. HCS w. Pretension	2. HCS w/o Pretension	3. Solid slab w/o Pretension	4. Solid slab w. Pretension
k_1 [MN/m]	5.028	4.886	5.583	5.687
k_2 [MN/m]	1.376	1.025	0.959	1.408

Table A.6: Bending stiffness of the four RC-slab models.

The influence on the bending stiffness from the use of pre-tension rebars and the complex cross-section geometry can be explained by the calculated stiffness deviation in Table A.7. From the table it can be concluded that the uncracked stiffness, k_1 has close to no deviation when comparing the slab models with and without pre-tension, being Case 1 & 2, 3 & 4. Furthermore the cross-section geometry is determined to have close to the same influence on the bending stiffness, with both of the case comparisons being 13-14%.

Table A.7: Influence on stiffness from pre-tension and geometry change.

Stiffness influence Case comparison	Cross-section geometry		Pre-tension	
	Case 1 & 4	Case 2 & 3	Case 1 & 2	Case 3 & 4
Deviation k_1 [%]	13.10	14.26	2.90	1.86
Deviation k_2 [%]	2.32	6.88	34.24	46.81

Further modelling of the slab in the design failure scenario is performed using the solid slab with pre-tension rebars, meaning that only the stiffness deviation originating from the change in geometry is taken into consideration, since the cracked stiffness is independent

of whether the pre-cracked cross-section is solid or not. To replicate the uncracked stiffness from the HCS in a solid slab, the concrete compression young's modulus is modified. Furthermore the mass change from using a solid model is taken into consideration by changing the density of the material.

The generalised bending stiffness of a slab is calculated by (A.8). With this equation it is possible to compare the results from Abaqus with an analytical solution and estimate what the Youngs modulus should be in order for the solid slab to behave as a hollow core slab.

$$k_g = \frac{48EI}{L^3} \quad (\text{A.8})$$

The transformed area moment of inertia, I , for case 4 is calculated with the analytical approach as in [Bjarne Chr. Jensen, 2020]. This results in a generalised stiffness that gives 5.743 MN/m which is 1% larger than the value seen in Table A.6 from Abaqus. The idea was to then set k_g to 5.028 to simulate case 1, however this meant a change of Youngs modulus from 19.70 GPa to 17.05 GPa and this resulted in a too low stiffness. By trial and error in Abaqus the necessary Youngs modulus was found to 18.29 GPa which gave a k_g of 4.996 MN/m and this is used in all models onward involving HCS to imitate the full HCS behaviour.

Based on these investigations a new concrete material is used in Abaqus which is referred to as Concrete-02

The changes parameters compared to Concrete-01 can be seen in Table A.8

Table A.8: Changed parameters from Concrete-01 to Concrete-02

Elastic modulus E	19.7 [GPa] \rightarrow 18.29 [GPa]
Density ρ	2400 [kg/m ³] \rightarrow 1434 [kg/m ³]

A.4.1 Third mode natural frequency for HCS and simple model

The third mode from the natural frequency comparison is shown on Figure A.37 and A.38.

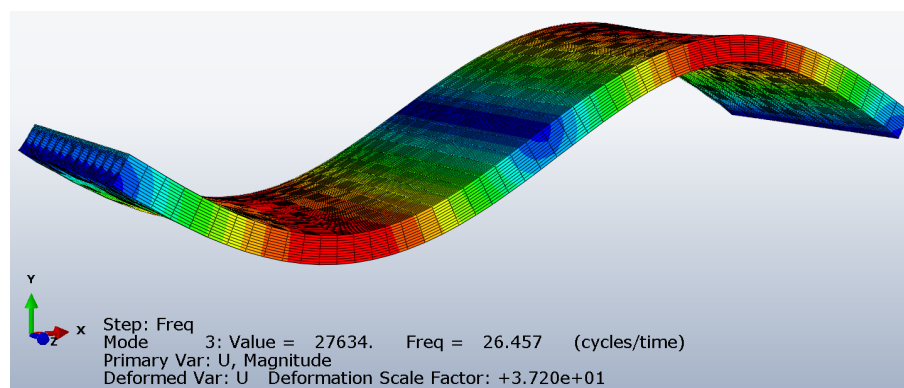


Figure A.37: Third natural frequency of the large model HCS.

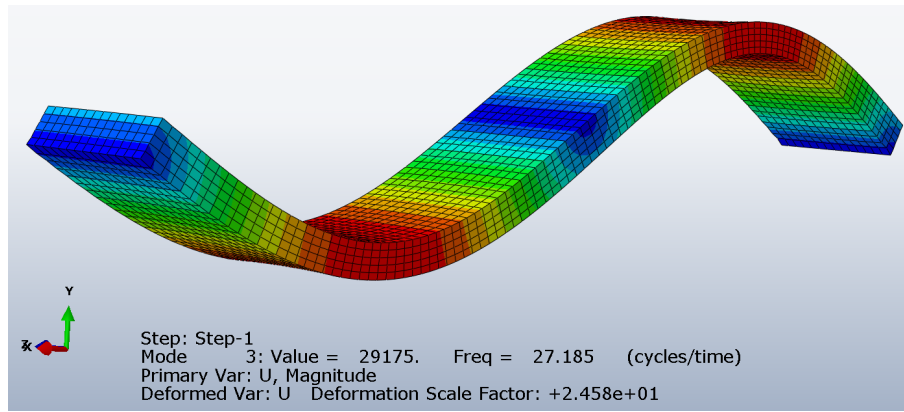


Figure A.38: Third natural frequency of the simplified solid slab.

B. Eurocode approach RCB

This Appendix contains the procedures for determining moment force capacity in a RCB, as well as the shear reinforcement requirement, followed by a method to determine the modulus of elasticity for a solid slab to have equivalent bending stiffness as a hollow core slab.

B.1 Analytical RCB model

The analytical approach is based on the Eurocode for concrete structures [DS/EN-1992, 2007]. The investigated RCB is illustrated on Figure B.1.

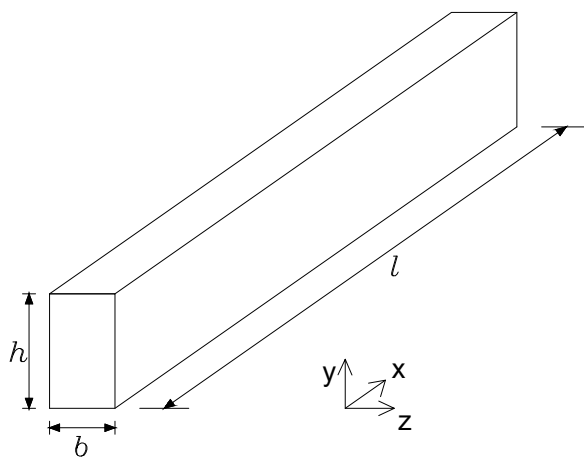


Table B.1: General beam properties.

Height, h	650 [mm]
Width, b	300 [mm]
Length, l	10000 [mm]

Figure B.1: Concrete beam measures and coordinate system definition.

B.1.1 Eurocode approach description

In the Eurocode model, the moment bearing capacity of the beam is determined by the use of equilibrium equations between tension in the reinforcement, and compression in the concrete. Two cross-section types are calculated, first of which has reinforcement placed only in the tension region of the cross section, and the latter with reinforcement in both tensile and compression zone of the cross-section. The calculations are based on [Bjarne Chr. Jensen, 2020], which uses a simplified approach, with the following three assumptions:

- Compression stress-strain curve is Bi-linear with no strain hardening, as illustrated to the right on Figure B.2.

- Concrete is assumed to have no tension strength
- The compressive stresses of the concrete is modelled by an rectangular zone using parameters η and λ , as illustrated on Figure B.3.

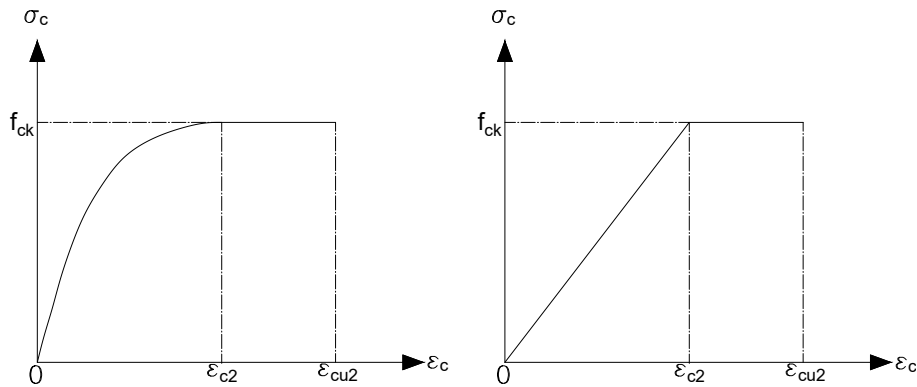


Figure B.2: Bi-linear stress-strain assumption of the concrete compression behaviour.

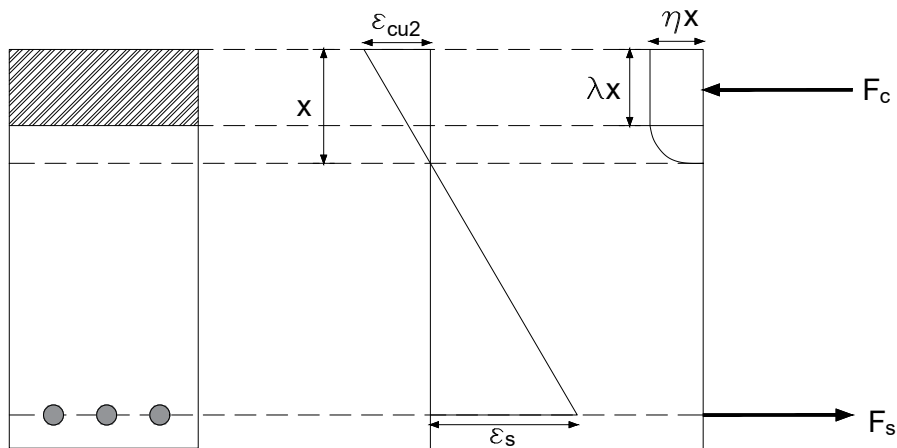


Figure B.3: Illustrated assumption of rectangular stress block.

Tension region reinforced cross-section

The first investigated case is with reinforcement placed in the bottom of the cross-section, as illustrated on Figure B.4, with relevant parameters shown in Table B.2

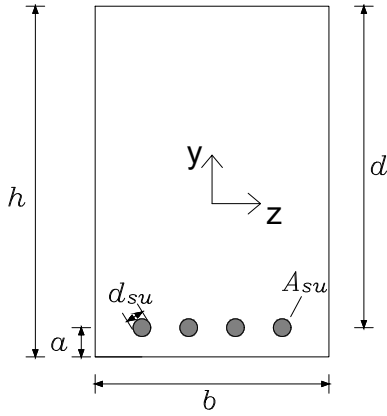


Figure B.4: Cross-section parameters.

Table B.2: Parameters used to calculate moment capacity.

Symbol	Description	Value
A_{su}	Area of rebar [mm ²]	$100 \cdot \pi$
a	Distance to rebars [mm]	35
n_{hu}	Number of rebars [-]	4
λ	Strength parameter [-]	0.8
η	Strength parameter [-]	1
f_{yk}	Yield strength of rebars [MPa]	500
f_{ck}	Yield strength of concrete [MPa]	40
ε_{cu3}	concrete ultimate strain [‰]	3.5
ε_s	rebar yield strain [‰]	1.6
ε_{uk}	Ultimate rebar yield strain [%]	5
f_{ctm}	Mean tension yield strength [MPa]	4.1

To calculate the moment force capacity, the degree of reinforcement is determined by

$$\omega = \frac{n_{hu} \cdot A_{su} \cdot f_{yk}}{b \cdot d \cdot \eta \cdot f_{ck}} \quad (\text{B.1})$$

The degree of reinforcement is introduced to secure proper reinforcement of the cross-section, which is met if condition (B.2) is true. The degree of reinforcement, ω , is used to determine the type of failure of the beam. If the degree of reinforcement is between the two limits stated in (B.2), the cross-section failure will consist of yielding of the rebars, with the compressive stresses being close to the yield limit, f_{ck} , resulting in high utilisation of both concrete and rebar.

$$\omega_{bal} = \lambda \frac{\varepsilon_{cu3}}{\varepsilon_{cu3} + \varepsilon_y} \geq \omega = \frac{n_{hu} \cdot A_{su} \cdot f_{yk}}{b \cdot d \cdot \eta \cdot f_{ck}} \geq \begin{cases} \omega_{min1} & = 0.26 \cdot \frac{f_{ctm}}{f_{yk}} \cdot \frac{f_{yd}}{f_{cd}} \\ \omega_{min2} & = 0.0013 \cdot \frac{f_{yd}}{f_{cd}} \\ \omega_{und} & = \lambda \cdot \frac{\varepsilon_{cu3}}{\varepsilon_{cu3} + \varepsilon_{uk}} \end{cases} \quad (\text{B.2})$$

Complying with (B.2), the moment force capacity, M_{cap} , is found from equilibrium of forces as illustrated on Figure B.3,

$$M_{cap} = b \cdot \lambda \cdot x \cdot \eta \cdot f_{ck} \cdot \left(d - \frac{\lambda \cdot x}{2} \right) \quad (\text{B.3})$$

The moment capacity, M_{cap} , and resulting strain in the rebars, ε_s , is shown in Table B.3

Table B.3: Moment force capacity and resulting bottom reinforcement strain in the single and double reinforced cross-section.

	Single reinforced cross-section
M_{cap} [kNm]	370.0
ε_s [‰]	29.6

Double reinforced concrete beam

The double reinforced cross section is illustrated on Figure B.5. The beam is an exact copy of the Tension region reinforced cross-section evaluated in the previous section, with an additional two rebars placed in the compression area. The additional parameters used in the calculation of moment force capacity is shown in Table B.4

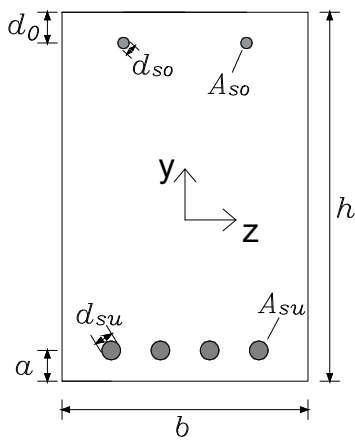


Table B.4: Parameters used to calculate moment capacity.

Symbol	Description	Value
A_{so}	Area of rebar [mm ²]	78.54
d_0	Distance to rebars [mm]	30
E_s	Young's modulus steel [GPa]	210
x	Distance to neutral axis [mm]	49.5361
σ_{so}	Stress in top rebar [MPa]	215.72

Figure B.5: Cross-section parameters.

The distance, x , from the cross-section top to the neutral axis is determined by an iteration procedure (B.4)

$$\begin{aligned} \varepsilon_{so} &= \varepsilon_{cu3} \cdot \frac{x - d_0}{x} \\ \sigma_{so} &= E_s \cdot \varepsilon_{sc} \\ x &= \frac{A_{su} \cdot n_h \cdot f_{yk} - A_{so} \cdot n_{h0} \cdot \sigma_{so}}{\lambda \cdot b \cdot \eta \cdot f_{ck}} \end{aligned} \tag{B.4}$$

Knowing the distance, x , the moment capacity is found by (B.5), which is seen to be identical with the tension region reinforced section, with the contribution of the compressed region rebars. The resulting moment capacity and resulting tension rebar strain is shown in Table B.5. The results show that placing rebars in the compressed zone have close to no influence on the moment capacity.

$$M_{cap} = b \cdot \lambda \cdot x \cdot \eta \cdot f_{ck} \cdot \left(d - \frac{\lambda \cdot x}{2} \right) + n_h \cdot A_{so} \cdot \sigma_{sc} \cdot (d - d_0) \tag{B.5}$$

Table B.5: Moment force capacity and resulting bottom reinforcement strain in the single and double reinforced cross-section.

	Double reinforced beam
M_{cap} [kNm]	372.15
ε_s [‰]	40

Shear reinforcement

The RCB is in the finite element model loaded using a three point bending approach as illustrated on Figure B.6 a), where the point load F , is increased linearly from zero up until complete loss of bearing capacity. The purpose of the FEM analysis is to investigate the flexural failure of RC, and shear reinforcement is therefore required to avoid web- and flexure-shear cracks, as illustrated on Figure B.6 b). The minimum required shear reinforcement needed to avoid these phenomenon is determined in this section.

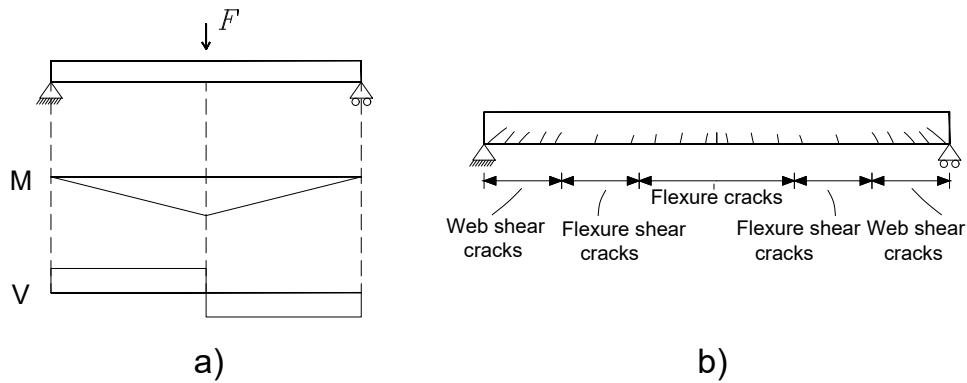


Figure B.6: a) Moment and shear diagram from a three point bending test. b) typical cracks in a RCB.

To secure that the only failure mode present in the three point bending test is bending, the beam is reinforced using transverse rebars. To determine the minimum required shear reinforcement, the shear stress is firstly determined. The approach used is described in [Bjarne Chr. Jensen, 2020].

In the FEM three point bending test described in section 4, the maximum point load applied is 180 kN, resulting in a maximum shear force of $V = 90$ kN at the supports.

The maximum distance between the shear rebars is determined by (B.6)

$$s = \frac{A_{sw} f_y}{\tau b_w} \cot(\theta) \quad (\text{B.6})$$

$$\tau = \frac{V}{b_w z} \quad (\text{B.7})$$

$$z = \left(1 - \frac{1}{2}\omega\right) d \tag{B.8}$$

$$A_{sw} = 2r_s^2 \pi \tag{B.9}$$

where

s	Maximum spacing between shear rebars
A_{sw}	Shear reinforcement area
f_y	Shear reinforcement yield stress
b_w	RCB width
$\cot(\theta)$	Concrete pressure slope
z	Lever arm
ω	Degree of reinforcement
τ	Shear stress
r_s	Shear reinforcement radius

The concrete pressure slope is chosen as the recommended value $\cot(\theta) = 2.5$, the resulting shear stress distribution in the RCB is illustrated on Figure B.7, with a maximum value of $\tau = 0.55$ MPa at the supports, requiring a maximum spacing of $s = 3$ m

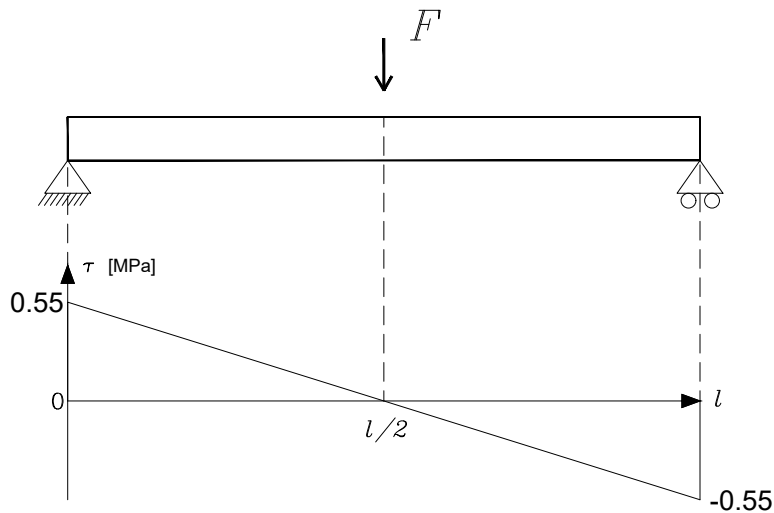


Figure B.7: Shear stress development in RCB.



C. Abaqus procedures

C.1 Contact behaviour in Abaqus

The impact forces determined in the numerical model is determined by the contact definition used in the model, thus having a high influence on the results. In the Abaqus/Explicit model, the contact force behaviour is in this project modelled with the use of "general contact" algorithm, which is available for both Abaqus/Standard and Abaqus/explicit.

The General Contact algorithm can consider multiple types of three dimensional surface contact scenarios, one being the edge-to-surface contact which is present in the DFS.

Using the general contact algorithm, the surface which is expected to be in contact is defined, which in this project is chosen as element-based deformable and rigid surfaces, which is available for both continuum solid and shell elements, and can be defined for both exterior and interior.

Both the interior and exterior surface definition is tested in this project, since two different models are investigated. When doing analysis with element deletion, Elm-Del, on, both interior and exterior surfaces are chosen as contact surfaces, such that contact between the two bodies are possible even after deterioration of the outer element layer. In the models using CDP without Elm-Del on, only the bottom and top surface is marked as being contact surfaces for the top and bottom slab respectively. Since the Elm-Del is off the surface will never disappear and therefore choosing only the two surfaces as contact surfaces, computational expenses are lowered.

The contact constraints are only applied when the clearance between the two surfaces becomes zero. When the clearance reaches zero, pressure is transmitted, and it continues to transfer pressure until separation. When modelling the impact, several contact relationships are available, some being more experimental than others, where the build up pressure can be defined using tabular form pressure depending on clearance and over-closure of the two contact constraints. In this project only the hard contact relationship is chosen, meaning that any contact pressure can be transmitted between the two surfaces, the hard impact method is illustrated on Figure C.1.

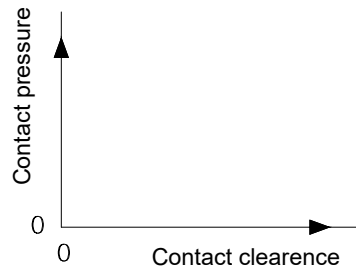


Figure C.1: Hard contact pressure - clearance relationship chosen for modelling contact.

C.2 Damping in dynamic explicit analysis

In Abaqus/Explicit analysis damping is introduced through volumetric straining and bulk viscosity, which is used in the case of high speed dynamic events.

Two types of bulk viscosity is used, being the linear and quadratic form, both of which creates a bulk viscosity pressure, p , which is linear and quadratic respectively. The pressure is a numerical effect only and therefore not included in the constitutive response.

The linear form is used to damp ringing in the highest element frequency. The linear bulk viscosity pressure in the elements is determined by:

$$p_1 = b_1 \rho c_d L^e \dot{\epsilon}_{vol} \tag{C.1}$$

The quadratic form is used only in continuum elements, and furthermore only applies pressure when the volumetric strain rate is compressive:

$$p_2 = \rho (b_2 L^e)^2 |\dot{\epsilon}_{vol}| \min(0, \dot{\epsilon}_{vol}) \tag{C.2}$$

where:

b_1 & b_2		Damping coefficient
ρ		Current material density
L^e		Element characteristic length
$\dot{\epsilon}_{vol}$		Volumetric strain rate
c_d		Current dilatational wave speed

The quadratic form is used to prevent collapse of the elements due to high velocity gradients in the element, meaning that when nodal velocity of the element reaches values near the dilatational wave speed, instead of the element collapsing to zero volume in one time increment, the resisting pressure prevents the element from collapsing. [Dassault Systèmes, 2020]

The damping in each element caused by the bulk viscosity is determined in each of the

elements as a fraction of critical damping:

$$\zeta = b_1 - b_2 \frac{L^e}{c_d} \min(0, \dot{\epsilon}_{vol}) \quad (\text{C.3})$$

The two damping coefficients, b_1 & b_2 , is chosen as the default values, 0.06 & 1.2 respectively, resulting in fraction of critical damping of $\approx 6\%$, which is present in all of the dynamic explicit simulations in this report unless stated otherwise.

D. Energy and mesh convergence

D.1 Da Vinci Failure

The Da Vinci failure is constructed in Abaqus/Explicit using continuum solid elements as illustrated on Figure D.1. The mesh used in the model reflects that behaviour of the two slabs is of interest, which is why the degree of mesh refinement is focused towards the two slabs and not the walls. Numeric model specifics can be seen in the table below Figure D.1, where the rebar mentioned is modelled as non-tensioned, and the slabs are modelled as solid slabs with the concrete material parameters for Concrete-01. The walls in the Da Vinci Failure is in reality constructed using bricks, but since only the slabs are of interest, the same concrete parameters is used as for the slabs. The contact formulation used is the general contact algorithm with hard contact described in Appendix C.1. Furthermore since element deletion is used, both exterior and interior surfaces are chosen as contact surfaces.

The joints seen in the numerical model D.1 is not connected to each other, and interacts therefore only through contact ie. pressure forces.

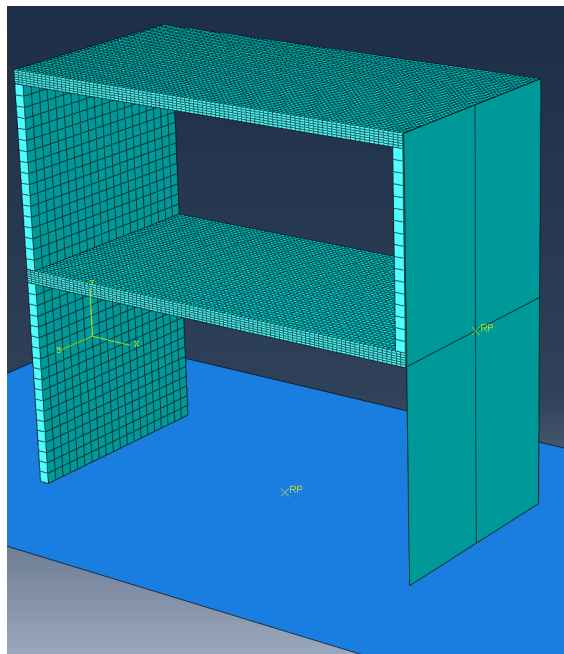


Figure D.1: Da Vinci failure model setup in Abaqus.

Appendix D. Energy and mesh convergence

Abaqus model setup (Figure D.1)			
Element type	No. of elements	Material	Other
Solid continuum C3D8R	49660	Concrete-01	Element deletion and Contact
Timoshenko beam B31	380	Steel-01	Embedded region
Analysis type:		Explicit dynamic	

The model behaviour is investigated through the energy output. In general the total energy of the system should remain constant, and sudden large spikes may be caused by e.g. exceeding the stability limit. Furthermore Abaqus introduces additional energies in the algorithm, to control e.g. hour-glassing phenomenon, and if large parts of the total energy consists of the non-physical energies, refinements should be made to the model.

The total energy in the system is the sum of contributions determined by;

$$E_{total} = E_{IE} + E_{VD} + E_{KE} + E_{WK} = Constant \quad (D.1)$$

Where:

E_{IE}	Internal energy
E_{VD}	Viscous dissipated energy
E_{KE}	Kinetic Energy
E_{WK}	External work

Furthermore, the internal energy consists of several contributions;

$$E_{IE} = E_{AE} + E_{DMD} + E_{PD} + E_{SE} \quad (D.2)$$

where:

E_{AE}	Artificial strain energy
E_{DMD}	Energy dissipated through damage
E_{PD}	Energy dissipated through inelastic deformation
E_{SE}	Elastic strain energy

The energy is extracted during the numerical analysis for the entire model and can be seen illustrated on Figure D.2 and D.3 for equation (D.1) and (D.2) respectively.

The energy varies to some extent as expected. The kinetic energy is seen to increase exponentially as the structure is in free fall motion, furthermore external work increases caused by gravity loads. In the time of impact at ≈ 550 ms, the internal energy increases, with main components E_{AE} and E_{PD} , indicating that both extensive irreversible damage is present, as well as large portions of artificial damage to control hour-glassing phenomenon.

As the simulation continues, all of the contributions to internal energy is seen to increase further, with the ratio remaining close to unchanged.

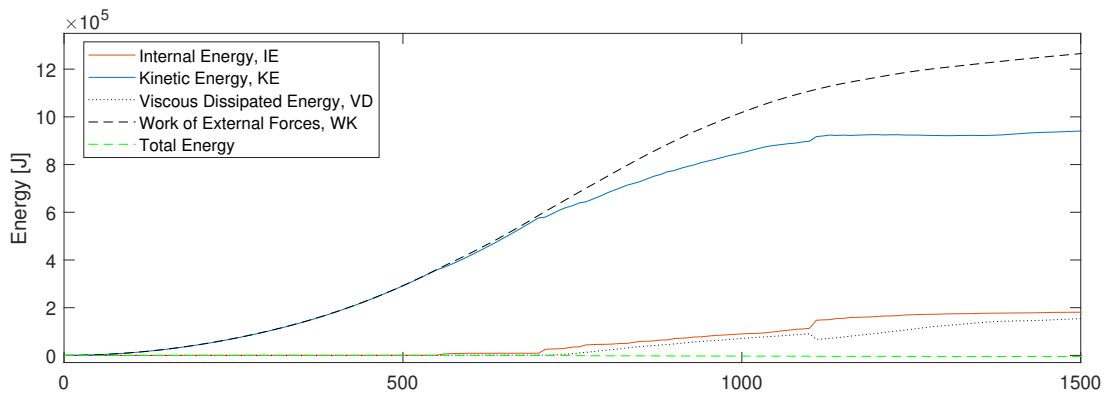


Figure D.2: Total energy contributions of whole model.

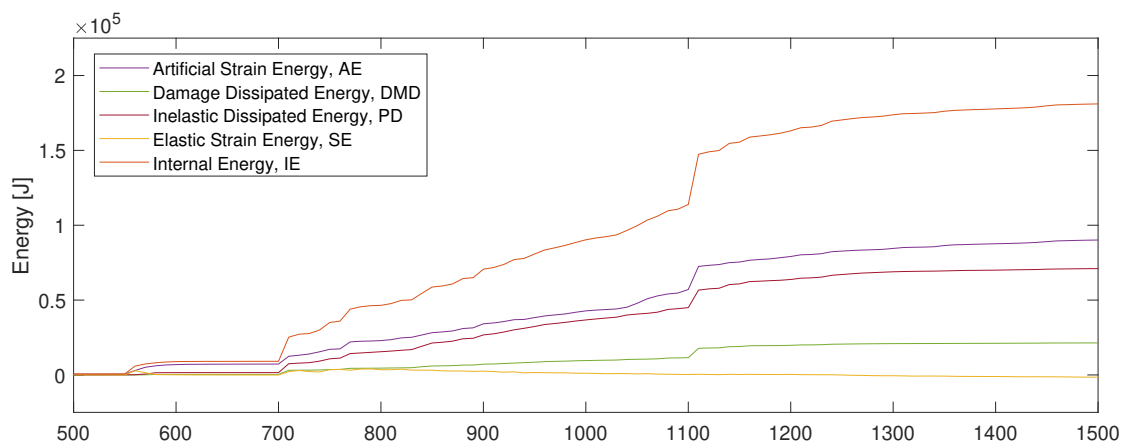


Figure D.3: Internal energy contributions of whole model.

D.2 Mesh convergence

The design failure scenario from the DPCA-building is modelled with four different mesh sizes to investigate the reactions dependence on the chosen mesh. Abaqus provides a range of different meshing techniques, and in most of the models in this report the elements are meshed as a structured mesh with hexahedral shaped elements. The four different mesh sizes are controlled by the Global Size parameter. The Global Size parameter creates a mesh of elements with an approximately even size in all directions, which is good since most of the analyses are explicit dynamic and therefore the time increment depends on the smallest element in the mesh. The simulations would take an unnecessarily long time if one element was much smaller than all the others. An example of a structured mesh with global size 0.07 and a manually chosen different seeding on the corner can be seen on Figure D.4.

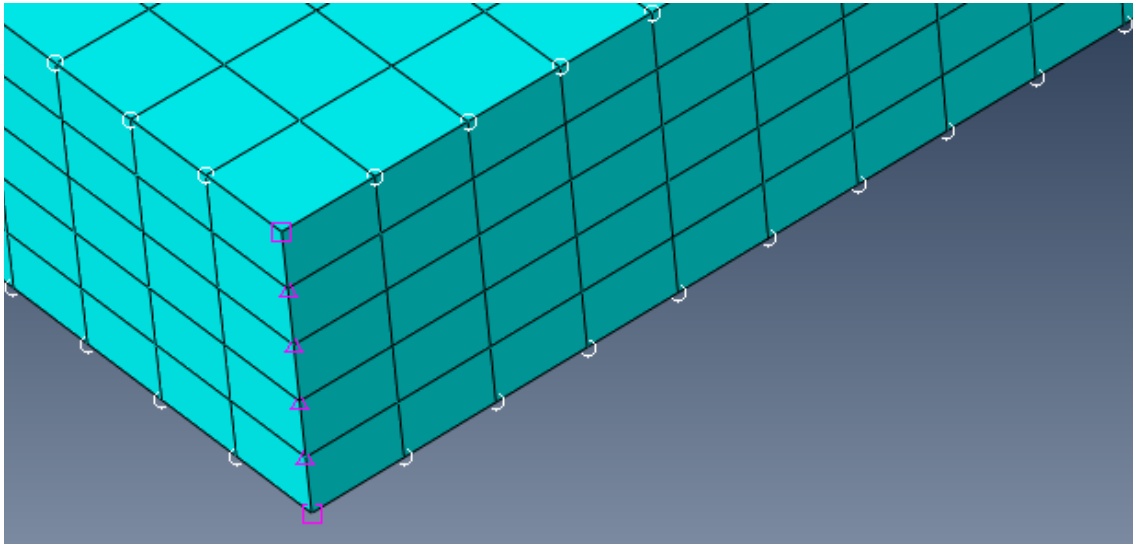


Figure D.4: An example of the seeding in a mesh for a slab. The global size is set to 0.07 but a different seeding is used on the corner, to create more elements in the thickness direction.

The DFS is modelled using continuum solid elements. The numerical model setup and boundary conditions are illustrated on Figure D.5 and D.6.

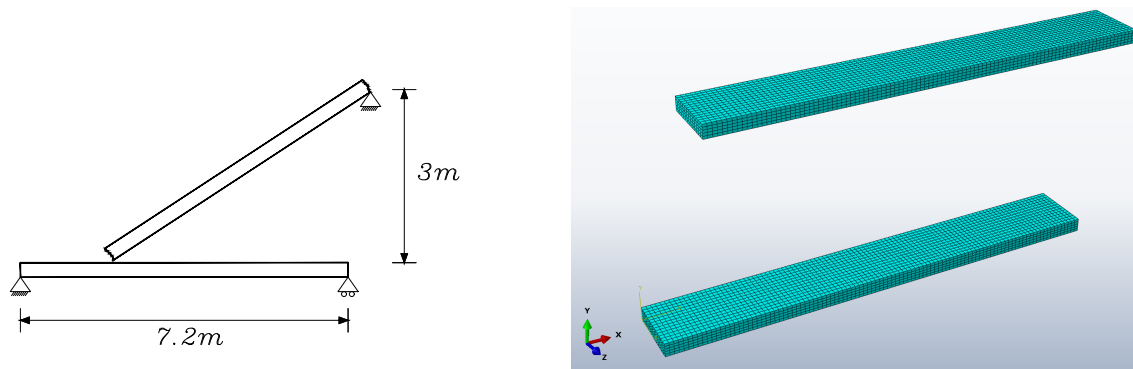


Figure D.5: Setup for the design failure scenario.

Figure D.6: The mesh for DFS with global mesh size set to 0.07.

Four different mesh sizes is investigated, being GS005, 007, 012 and 020 ordered as the most refined and least refined mesh. The differences in mesh is seen in Table D.1

Table D.1: Mesh size characteristics.

GS	Nodes	Elements	Beam elements[rebar]
005	43086	34560	432
007	19176	14420	432
012	7044	5232	432
020	3120	2232	432

Numeric simulations of complex problems such as the impact between two objects can

easily result in errors, which in this case is assessed as being the reason for some of the initial spikes in the reaction forces, and they should not be seen as a reliable description of the real world forces. To secure that the reaction force is visible when plotted, the initial peaks is in some of the figures left out, and the maximum value is instead stated in Table D.2. An overview of the impact force with the four different mesh sizes can be seen on Figure D.7, with the two finest mesh and most coarse seen on Figure D.8 and D.9 respectively.

Table D.2: Maximum measured positive force.

Mesh type	Impact force [kN]	R_{left} [kN]	R_{right} [kN]
GS005	1578	250	105.6
GS007	1819	266.6	118.6
GS012	1817	273.4	99.9
GS020	365.9	179.8	72

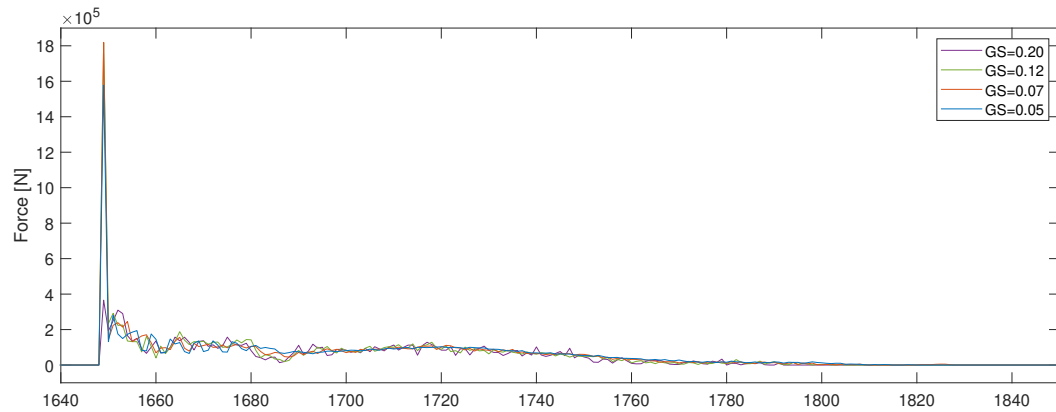


Figure D.7: Impact force for the four different mesh refinements.

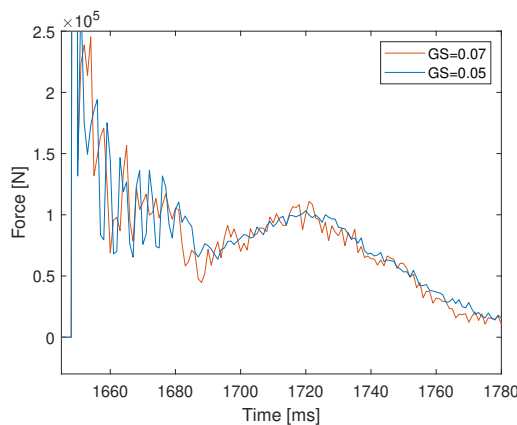


Figure D.8: Impact force for the two most refined models.

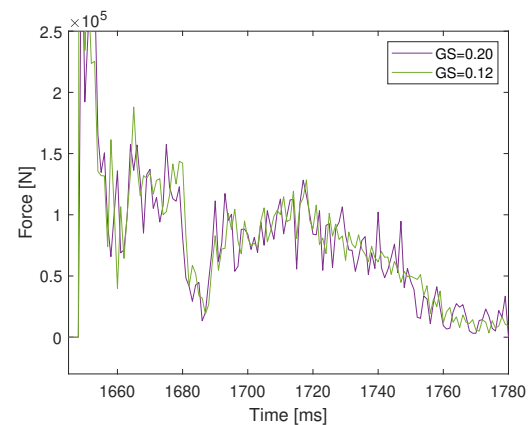


Figure D.9: Impact force for the two least refined models.

An overview of the left reaction force, R_{left} , using the four different mesh refinements is

seen on Figure D.10, with the two most fine and most coarse seen on Figure D.12 and D.11 respectively.

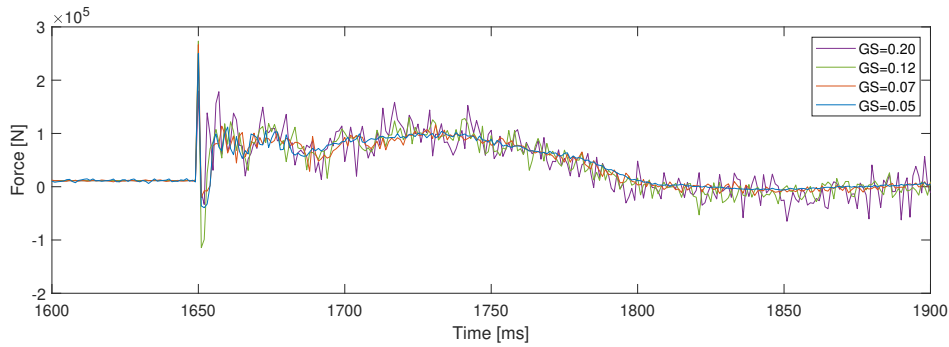


Figure D.10: Left support reaction force, R_{left}

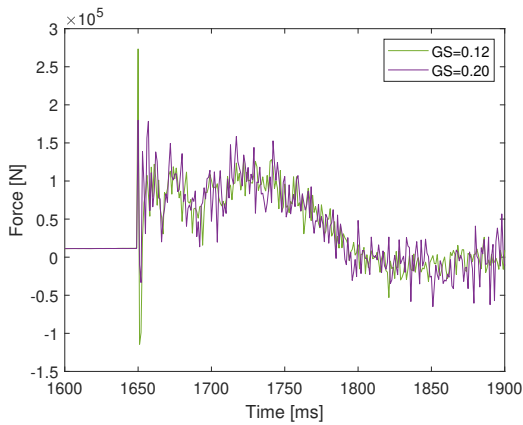


Figure D.11: Left reaction force, R_{left} , for the two least refined models.

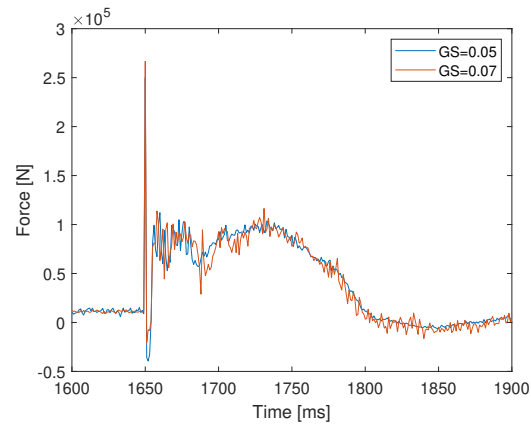


Figure D.12: Reaction force, R_{left} , for the two most refined models.

An overview of the right reaction force, R_{right} , using the four different mesh refinements is seen on Figure D.13, with the two most fine and most coarse seen on Figure D.15 and D.14 respectively.

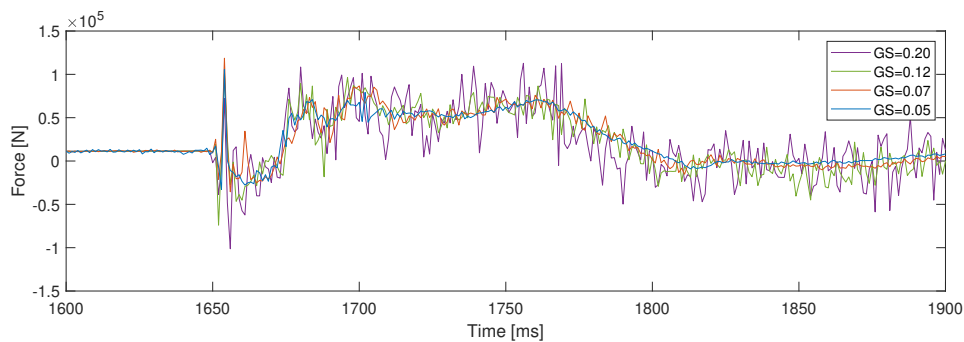


Figure D.13: Right support reaction force, R_{right}

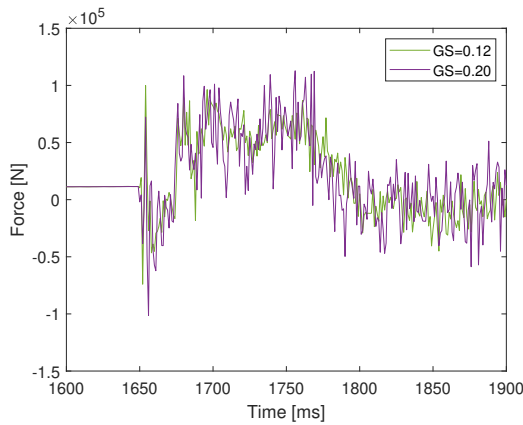


Figure D.14: Reaction force, R_{right} , for the two least refined models.

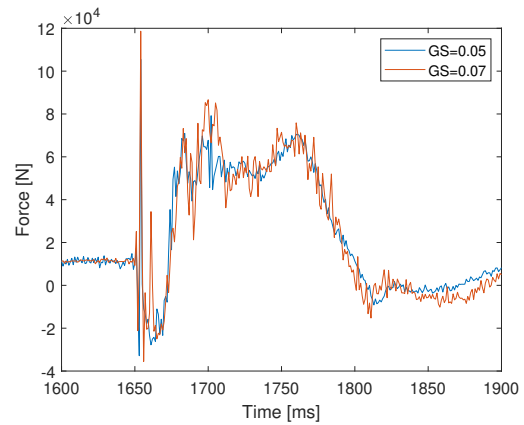


Figure D.15: Reaction force, R_{right} , for the two most refined models.

Investigation of the changes in the internal energies and viscous dissipated energy illustrated on Figures D.16-D.19 shows that the difference between mesh size GS007 and GS005 is small, and further investigations is done using mesh GS007.

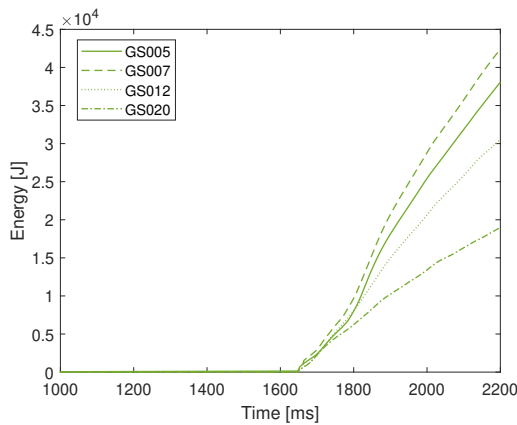


Figure D.16: Energy dissipated by damage using the four levels of mesh refinements.

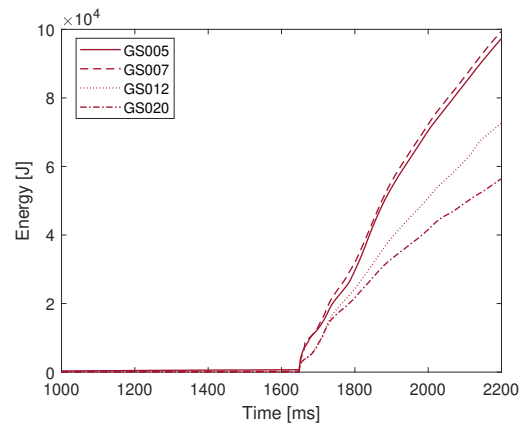


Figure D.17: Inelastic strain energy using the four levels of mesh refinements.

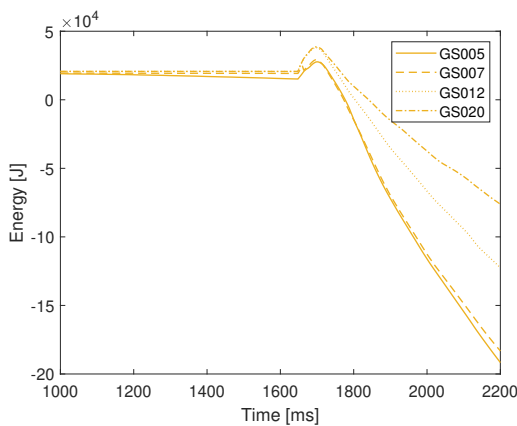


Figure D.18: Elastic strain energy using the four levels of mesh refinements.

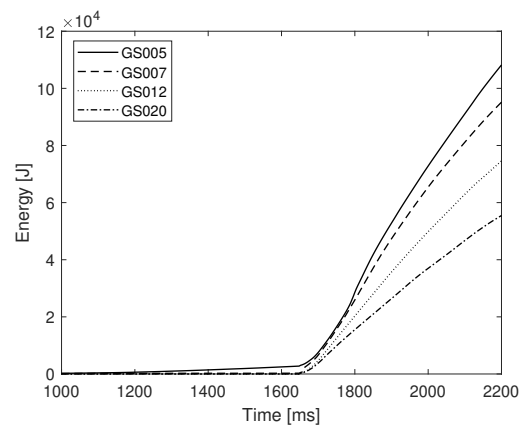


Figure D.19: Energy dissipated through viscosity using the four levels of mesh refinements.

D.3 Butterworth filter

After performing the mesh convergence and the final mesh refinement is chosen, a Butterworth filter is applied when comparing models using the same mesh. The butterworth filter is used to smoothen some of the high frequent response peaks, and make the response easier to compare to different solutions such as the partwise element deletion investigation. An example of the filter is seen on Figure D.20. More precisely filter is the 1st order lowpass digital Butterworth filter with normalised cutoff frequency 0.3.

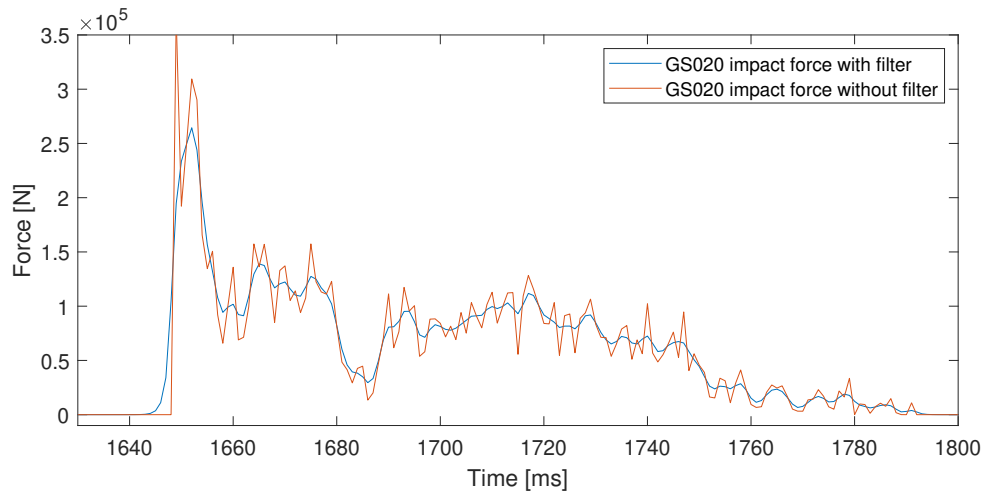


Figure D.20: Illustration of the effect of Butterworth filter.

E. Design failure scenario

E.1 Part-wise element deletion

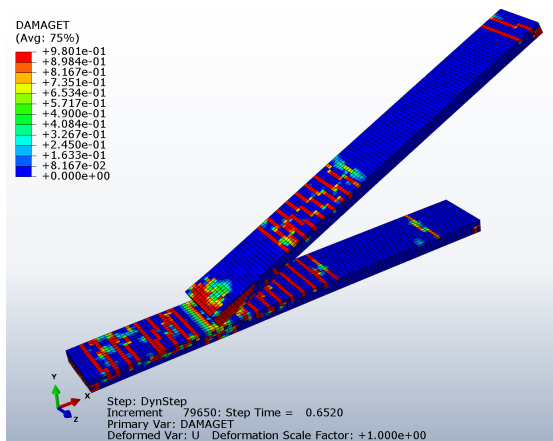


Figure E.1: Tension damage at $T_I + 10ms$

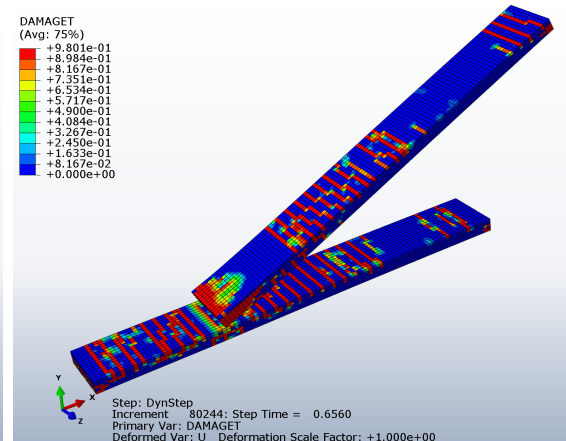


Figure E.2: Tension damage at $T_I + 14ms$

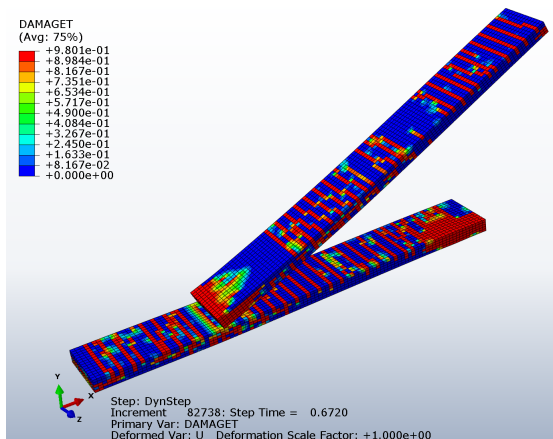


Figure E.3: Tension damage at $T_I + 64ms$

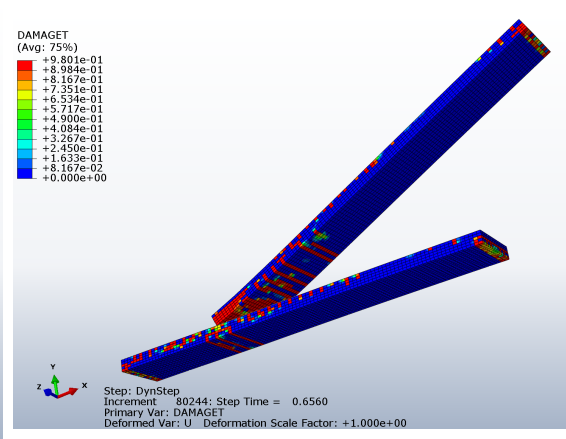


Figure E.4: Tension damage at $T_I + 14ms$

Abaqus model setup (Figure E.1)			
Element type	No. of elements	Material	Other
Solid continuum C3D8R	14420	Concrete-02	Contact
Timoshenko beam B31	432	Steel-02	Embedded region
Analysis type:		Explicit dynamic	

E.2 Parameter study

Figures and tables from the parametric study are shown in the section. The impact force, left and right reaction force for the three different heights and five different position parameters are shown in Table E.1. The belonging Figures for the reaction and impact force depending on the time interval length is seen on Figures E.5-E.7.

Table E.1: Impact force, left and right reaction force from the parametric study

α	H [m]	R_{right} [kN]		R_{left} [kN]		Impact force [kN]	
		25 [ms]	50 [ms]	25 [ms]	50 [ms]	25 [ms]	50 [ms]
0.1	2	47.9	35.8	149.0	116.7	150.0	109.0
	3	54.2	41.0	162.4	130.0	160.4	121.2
	4	56.3	44.6	192.0	155.6	248.6	179.3
0.2	2	57.0	46.0	107.0	93.0	144.7	109.5
	3	61.3	53.5	119.4	108.2	164.7	126.6
	4	65.7	59.6	129.8	121.7	230.5	172.0
0.3	2	63.5	54.0	89.4	83.3	111.3	83.4
	3	63.8	58.5	96.0	90.0	192.8	137.4
	4	74.6	64.6	96.7	95.2	160.9	129.6
0.4	2	67.0	61.0	78.9	74.6	132.5	99.4
	3	69.0	64.8	83.3	79.6	168.5	120.8
	4	80.0	69.0	84.0	81.0	151.6	113.6
0.5	2	70.3	68.2	72.4	69.0	136.1	100.0
	3	73.7	72.7	73.2	71.3	132.7	102.7
	4	78.6	76.6	72.6	72.0	150.7	110.4

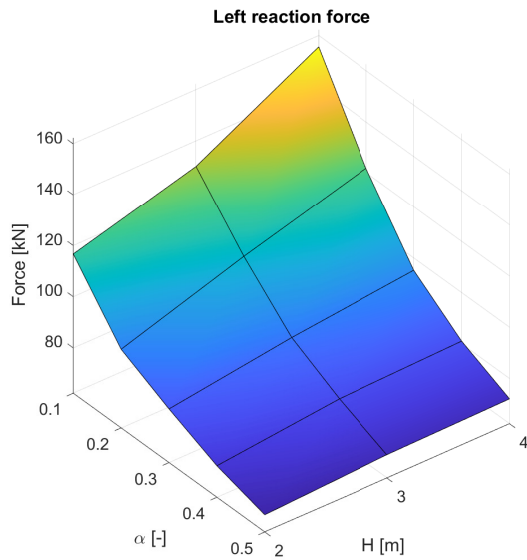


Figure E.5: *LESF* with time interval $2\Delta t=50\text{ms}$.

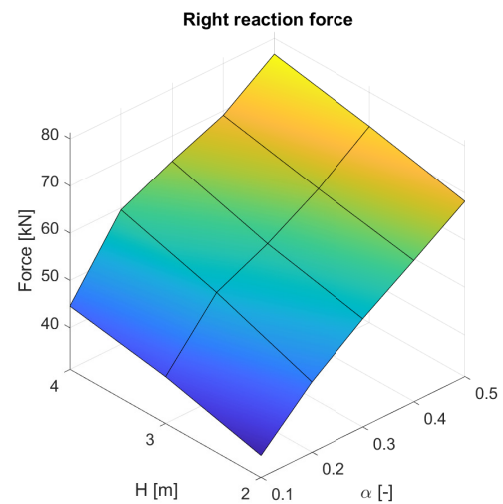


Figure E.6: *LESF* with time interval $2\Delta t=50\text{ms}$.

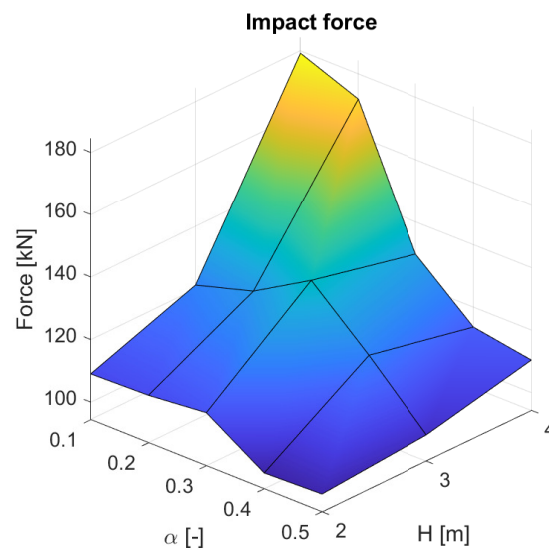


Figure E.7: Impact force with time interval $2\Delta t=50\text{ms}$.

E.3 Simplified beam shear force diagrams

The following images show how the shear force development over time in the dynamic impact between two simplified beams.

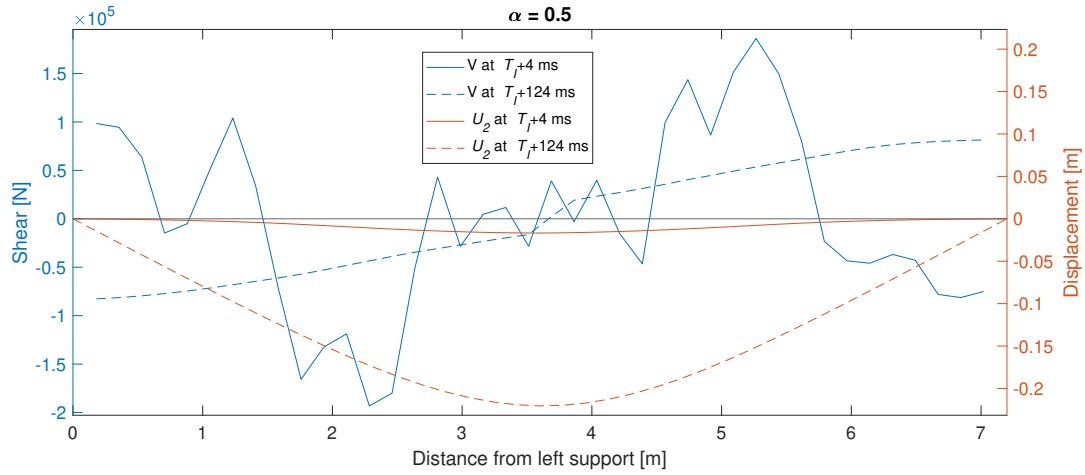


Figure E.8: The shear force is here shown for $\alpha = 0.5$

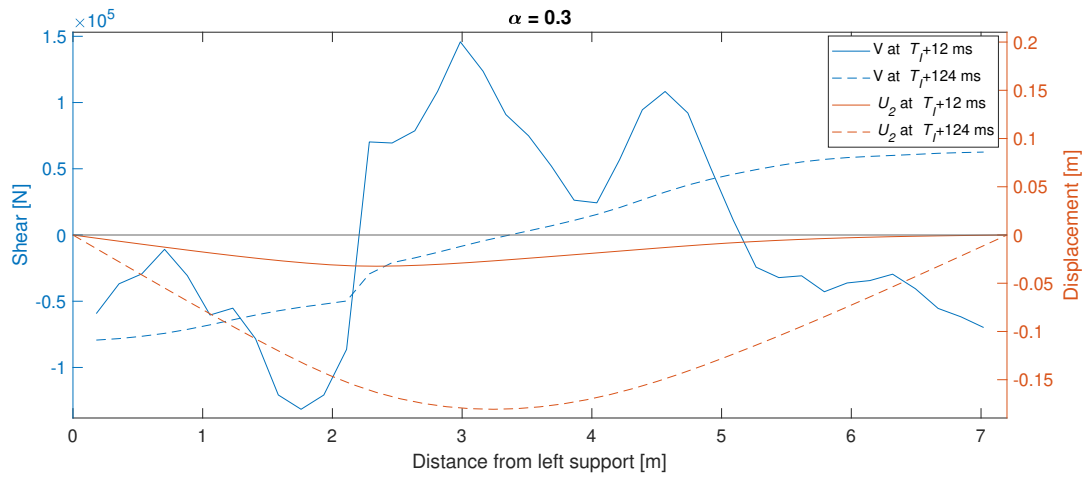


Figure E.9: The shear force is here shown for $\alpha = 0.3$

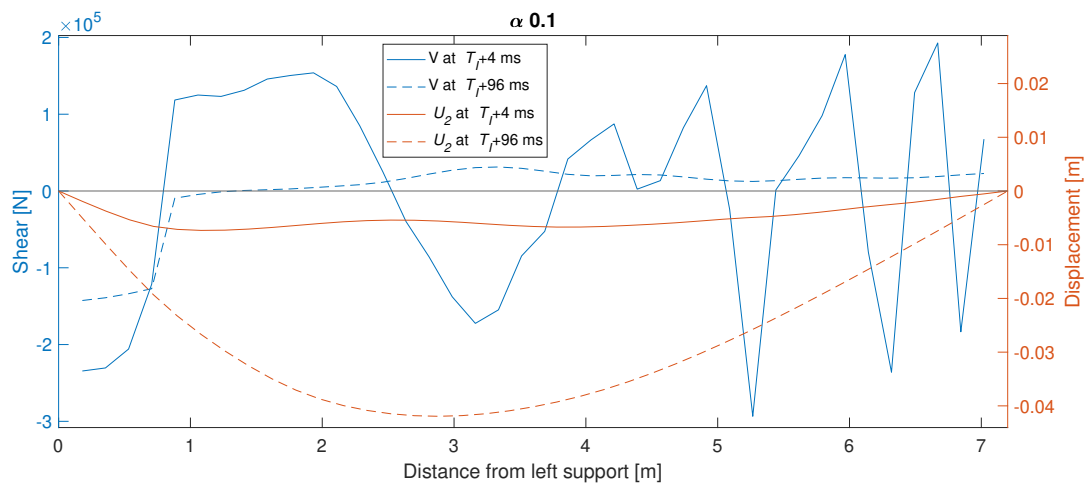


Figure E.10: The shear force is here shown for $\alpha = 0.1$

E.4 Damage and moment caused by inertia effect

The following 4 figures illustrate how the moment propagate through the beam and that this moment causes tension cracks in the top of the slab. The Figures that show moment are obtained with the simplified beam model and the tension crack development is shown with the 1m wide HCS model.

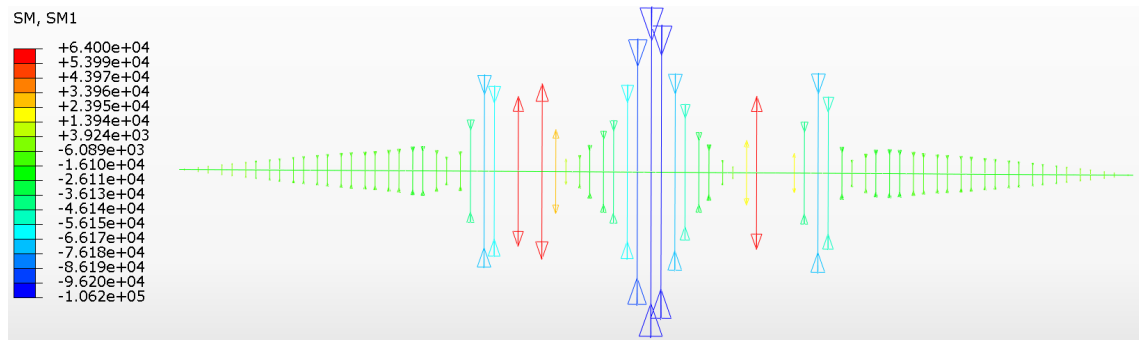


Figure E.11: Moment in the beam at 0.8 ms after impact. Red means tension in the top of the beam and blue means compression.

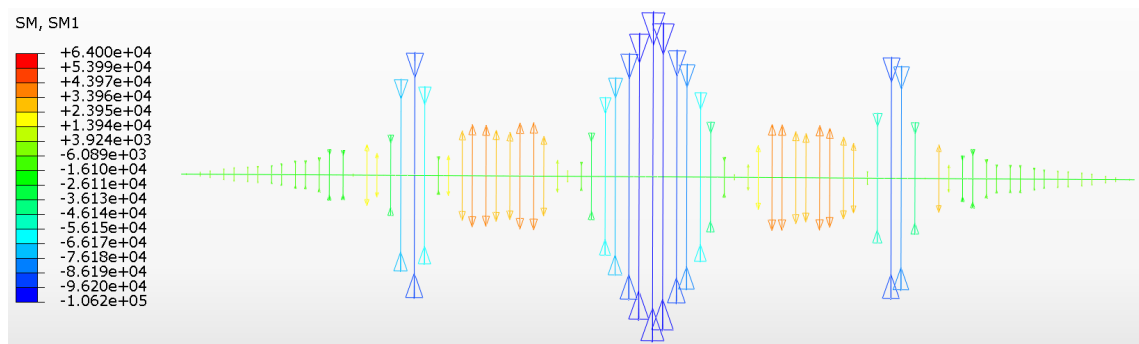


Figure E.12: Moment in the beam at 1.2 ms after impact. Red means tension in the top of the beam and blue means compression.

The tension damage at each of the ends of the slab is caused by the way the prestress is applied.

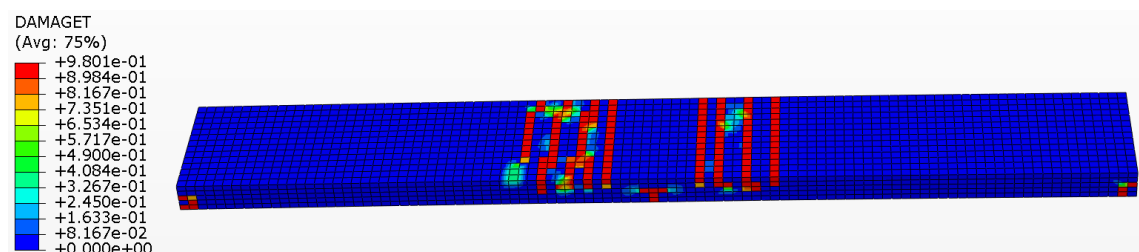


Figure E.13: Tension damage in the slab at $T_I + 0.8ms$ after impact.

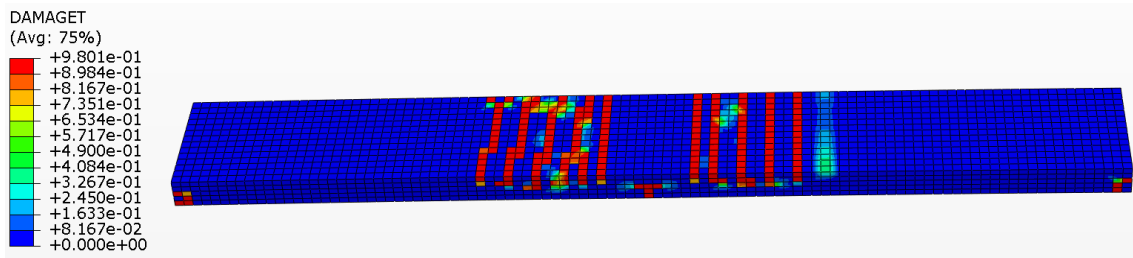


Figure E.14: Tension damage in the slab at $T_I + 1.2\text{ms}$ after impact.

Abaqus model setup (Figure E.13)			
Element type	No. of elements	Material	Other
Solid continuum C3D8R	14420	Concrete-02	Contact
Timoshenko beam B31	432	Steel-02	Embedded region
Analysis type:		Explicit dynamic	

F. 2DOF and Eurocode approach

In this appendix the overall behaviour of impact loads depending on parameters such as drop height and impact placement is investigated using a 2DOF model to see if the behaviour can be recreated using a simple model. Furthermore the Eurocode approach of determining impact loads is used and described.

Throughout this appendix the two objects is referred to as the "impacting mass" with subscript I and the "structure" with subscript s for the falling and stationary object respectively, as illustrated on Figure F.1 and F.2.

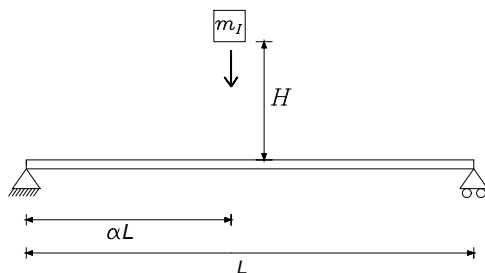


Figure F.1: Illustration of distance parameter which varies with 0.1 intervals between $\alpha=0.1-0.5$.

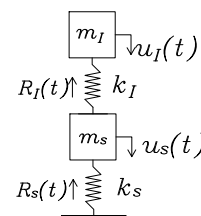


Figure F.2: 2DOF system with deflection, reaction force, mass and stiffness definition.

F.1 Stiffness and Mass of the structure.

The structure is modelled to resemble the slab from the DFS, and the mass and stiffness must therefore be able to vary depending on the impact placement, which is secured through two distance parameters, α & β as shown on Figure F.3.

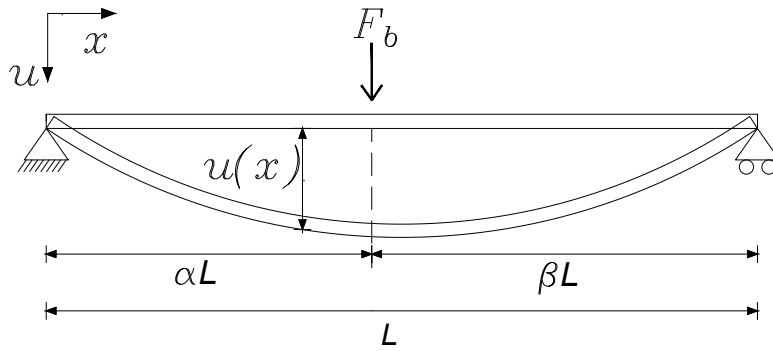


Figure F.3: Displacement of beam subjected to point load.

The deflection of a beam subjected to a point load with varying distance from the supports can be described by (F.1) according to Bernoulli Euler beam theory. [Jensen, 2004]

$$u(x) = \begin{cases} \frac{F_b \beta}{6EI_b} ((1 - \beta^2)l^2x - x^3) & 0 \leq x \leq \alpha l \\ \frac{F_b \alpha}{6EI_b} ((1 - \alpha^2)l^2(l - x) - (l - x)^3) & \alpha l \leq x \leq l \end{cases} \quad (\text{F.1})$$

where:

F_b	Applied point force
I_b	Area moment of inertia of the beam
E	Young's modulus of the beam
αL	Left side distance to applied force
βL	Right side distance to applied force

The maximum deflection of the beam, u_p , is determined by:

$$u_p = \frac{F_b l^3}{3EI_b} \alpha^2 \beta^2 \quad (\text{F.2})$$

Knowing the deflection curve as well as the maximum deflection, the normalised curve can be determined and used to determine the generalised mass [Bjarne Chr. Jensen, Bent Bonnerup, Carsten Munk Plum, 2009]

$$m_g = \int_0^l m(x) (\varphi(x))^2 dx \quad (\text{F.3})$$

The mass scaling factor can then be determined by (F.1), (F.2) and (F.3), along with the fact that $\beta = 1 - \alpha$, and that the mass distribution $m(x)$ is assumed constant.

$$\kappa_m(\alpha) = \frac{(3\alpha^6 - 12\alpha^5 + 14\alpha^4 - 7\alpha^2 + 2)}{105\alpha^2(-1 + \alpha)^4} \quad (\text{F.4})$$

The generalised mass of the beam in the case of load applied at mid span $\alpha = \beta = 0.5$, results in a mass scaling factor of $\kappa_m = 0.486$, implying that only half of the beams mass is used in the equivalent system when impacting the mid span of the beam.

The spring stiffness of the beam is determined by

$$F_b = k_b u_p \quad (\text{F.5})$$

Knowing the displacement at the point of applied force (F.2), the spring stiffness is determined by:

$$k_b(\alpha) = \frac{3 E I_b}{l^3 \alpha^2 (1 - \alpha)^2} \quad (\text{F.6})$$

The change in stiffness of the beam is determined using the stiffness scaling factor, defined as follows;

$$\text{Stiffness scaling factor} = \frac{k_b(\alpha)}{k_b(0.5)} \quad (\text{F.7})$$

$$\text{Mass scaling factor} = \frac{\kappa_m(\alpha)}{\kappa_m(0.5)} \quad (\text{F.8})$$

The resulting mass and stiffness scaling factor dependence on the position parameter, α , is illustrated on Figure F.4.

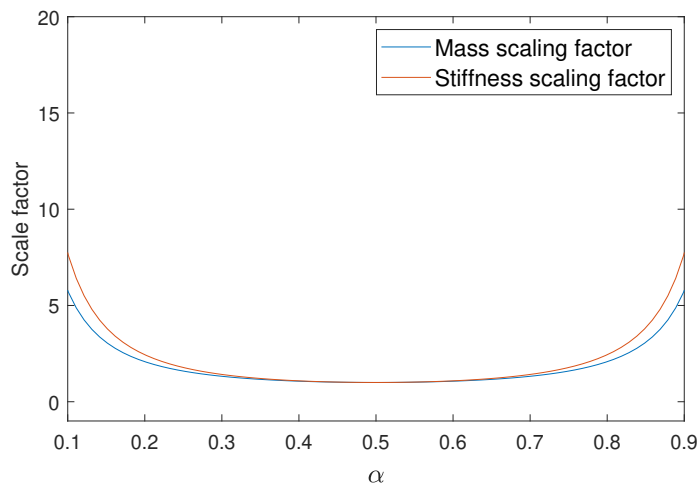


Figure F.4: Mass and stiffness scale factor normalised to force applied at mid span case.

F.2 Response to Impact load

To investigate the beams response to impact loads, a mass and stiffness of the impacting mass must be chosen. The value of this is estimated as 40% of the total beam mass, as well as 1/3 of the stiffness determined for the mid-span case.

$$m_I = \frac{2}{5}hbL\rho = 908.58\text{kg}$$

$$k_I = \frac{1}{3}k_b(0.5) = 0.75\frac{\text{MN}}{\text{m}}$$

$$f_I = \frac{1}{2\pi}\sqrt{\frac{k_I}{m_I}} = 4.56\text{s}^{-1}$$

The response to impact load from the falling object is investigated using five different values of α being 0.5, 0.4, 0.3, 0.2 and 0.1. The generalised stiffness and mass of the two objects is seen in Table F.1. The bending stiffness of the beam, EI , is determined with the use of equation (A.8), and the previously determined stiffness k_g described in Appendix A.4

Table F.1: Mass and stiffness in the 2-DOF system.

α	0.1	0.2	0.3	0.4	0.5
m_I [kg]	908.58	908.58	908.58	908.58	908.58
k_I [MN/m]	0.75	0.75	0.75	0.75	0.75
f_I [Hz]	4.56	4.56	4.56	4.56	4.56
m_s [kg]	6360	2294	1453	1181	1113
k_s [-]	$370.37\frac{EI}{L^3}$	$117.19\frac{EI}{L^3}$	$68.03\frac{EI}{L^3}$	$52.08\frac{EI}{L^3}$	$48\frac{EI}{L^3}$
f_s [Hz]	8.287	7.76	7.42	7.23	7.17

To simulate the impact between the two objects, the equation of motion, (F.9), is solved numerically through time by the use of central difference method as described in [Cook et al., 2002]. When solving the equation of motion, the damping, $[C]$, is neglected since this has no significant influence on the force in the first impact.

$$[M]\{\ddot{u}\} + [K]\{u\} = \{R(t)\} \tag{F.9}$$

Where:

$[\mathbf{K}]$	Stiffness matrix
$[\mathbf{M}]$	Mass matrix
$[\mathbf{C}]$	Damping matrix
$\{\ddot{\mathbf{u}}\}, \{\dot{\mathbf{u}}\}$	Acceleration, Velocity and Displacement vector
$\{\mathbf{R}(t)\}$	Force vector

The response behaviour of the model is divided into three steps as illustrated on Figure F.5. In the first step the mass, m_I , is in free fall motion with constant velocity, $v_{I,0}$, and with the mass m_s being stationary. The second step is described as the time at collision between the two bodies, resulting in the change in velocity of the two masses, m_I and m_s , as function of time $v_I(t)$, $v_s(t)$. In the third step, the two masses are no longer in contact, and the velocity, v_I is constant, whereas the mass m_s is oscillating resulting in a time dependent velocity, $v_s(t)$. When the impacting objects hits the structure, the energy is transferred only through compression forces, and the spring stiffness, k_I , is for that reason set to zero when the reaction force, R_I , is negative, resulting in a constant velocity, v_I , after the impact. Furthermore the equation of motion is solved without external forces acting on the two masses, neglecting the influence of gravity on the interaction behaviour.

When simulating the impact, the velocity of the falling object is of high importance, since this will have a direct influence on the resulting forces. The velocity used in the calculations is determined based on the gravitational acceleration in free fall motion, along with the law of conservation of kinetic and potential energy of an object, assuming that the air resistance has no influence.

$$\frac{1}{2}mv^2 = mgh$$

$$v = \sqrt{2gh}$$
(F.10)

Assuming that gravitational acceleration is 9.82 m/s^2 , along with a floor height of 3 m, and considering that the impacting mass only travels half the distance before impact, the velocity at impact for the mass m_I is $v_{I,0} \approx 5.42 \text{ m/s}$.

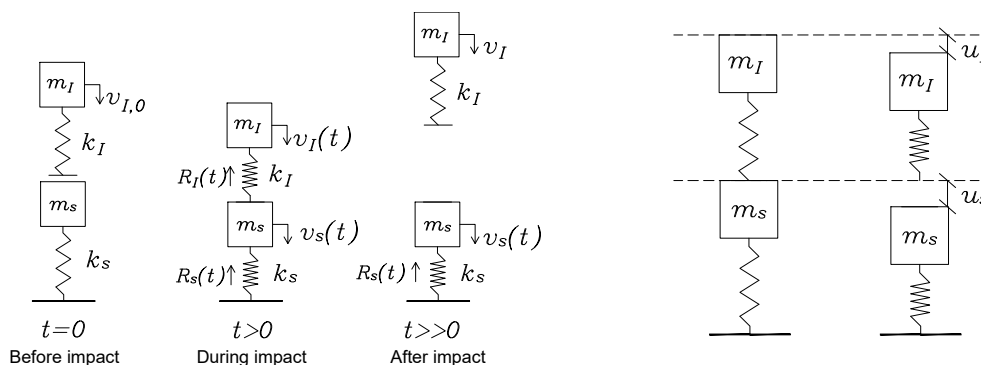


Figure F.5: Three steps in the 2DOF analysis.

Figure F.6: Definition of deflection in 2DOF system.

Knowing the displacement from (F.9), defined as illustrated on Figure F.6, the internal

work can be determined from the change in reaction force and displacement between each time step.

$$\begin{aligned}\Delta W_{I,internal} &= \Delta R_I \cdot \Delta u_I \\ \Delta W_{S,internal} &= \Delta R_S \cdot \Delta u_S\end{aligned}\tag{F.11}$$

As well as the internal work, the external work applied by the impacting mass, m_I , is determined by the use of the structures displacement.

$$\Delta W_{I,external} = \Delta R_I \cdot \Delta u_S\tag{F.12}$$

The change in impulse, I , between both the impacting mass and structure, and the structure and support, can be determined based on the time step, Δt , and reaction force R .

$$\begin{aligned}\Delta I_{R_I} &= \Delta R_I \cdot \Delta t \\ \Delta I_{R_S} &= \Delta R_S \cdot \Delta t\end{aligned}\tag{F.13}$$

The behaviour of the impacting mass and structure is seen on the following figures F.7 - F.20. In each of the figures five curves are illustrated, arising from the five values of position parameter previously described and shown on Figure F.3. From the displacement curve of the impacting object,

The deflection of the two masses can be seen on Figure F.7 and F.8. The displacement is in general seen to be affected by the position parameter in such a way that the time of contact between the two masses increases with increasing position parameter. Furthermore the structure is noticed to be much more compliant when being impacted at the mid-span, which should also be the case since the stiffness and mass of the structure is lowest at this point.

From the velocity and acceleration of the impacting mass, the result from not including gravity forces can be seen, since velocity after impact remains constant, and the acceleration therefore is zero. The structure does however continue to oscillate after impact since this object is constrained by the support.

The impact and reaction force, R_I % R_S is illustrated on Figure F.13 % F.14. The impacting force can here be seen to be lower than the reaction felt by the structure, a phenomenon which is also present in the complex model for some of the position parameters. Furthermore the time span of the impact is seen to be wider when moving towards the support, and peak force increases. Changing the position parameter does however not seem to have a high influence on the structures response.

The internal work, kinetic energy and impulse of the impacting mass and structure is seen on Figures F.15 - F.20. In the time of impact, the internal work of the two objects is seen to increase rapidly caused by the conversion of kinetic energy to deformation energy,

which e.g. can be seen from how the highest peak in internal energy of the impacting mass is present when the kinetic energy reaches zero. Furthermore the impulse of the impacting mass and structure indicates that even though the applied force time span and size changes, the resulting impulse does not.

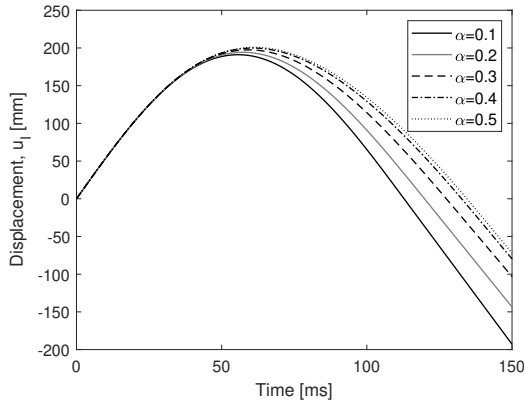


Figure F.7: Deflection of the impacting mass, m_I

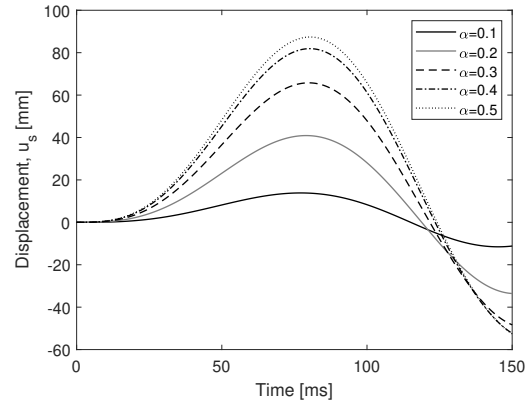


Figure F.8: Deflection of the structure, m_S

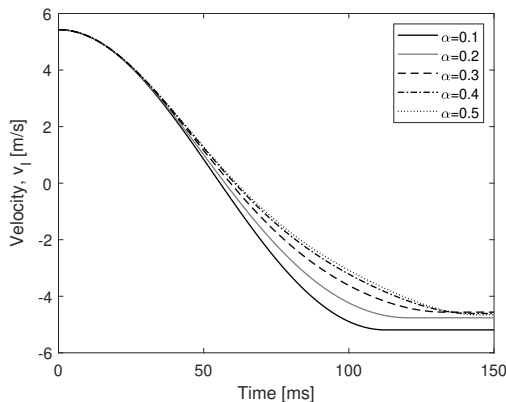


Figure F.9: Velocity of the impacting mass.

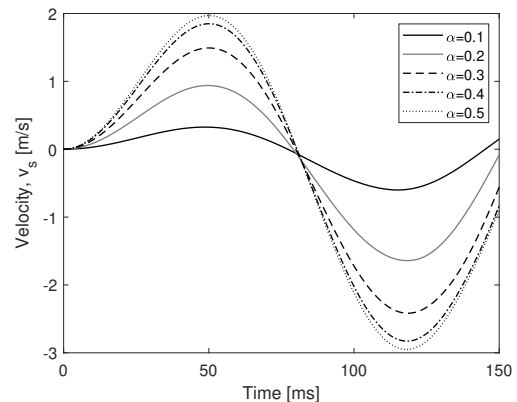


Figure F.10: Velocity of the structure.

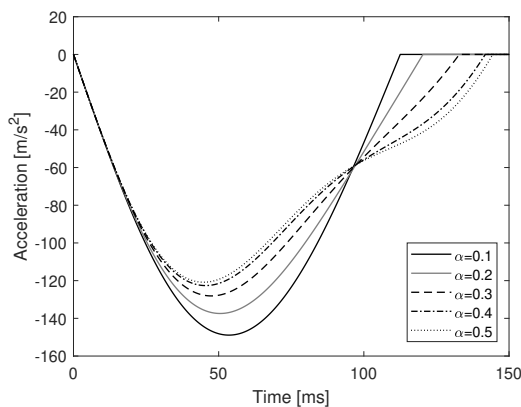


Figure F.11: Acceleration of the impacting mass.

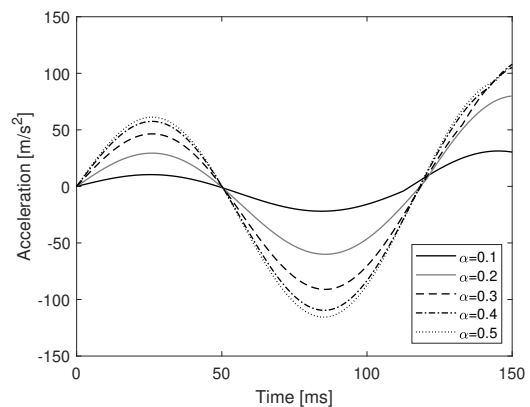


Figure F.12: Acceleration of the structure.

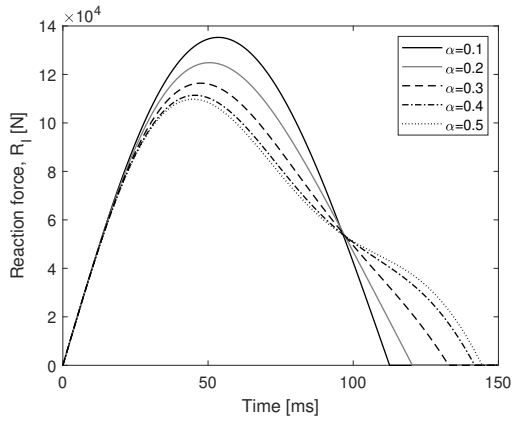


Figure F.13: Impact force, R_I , felt by the impacting mass.

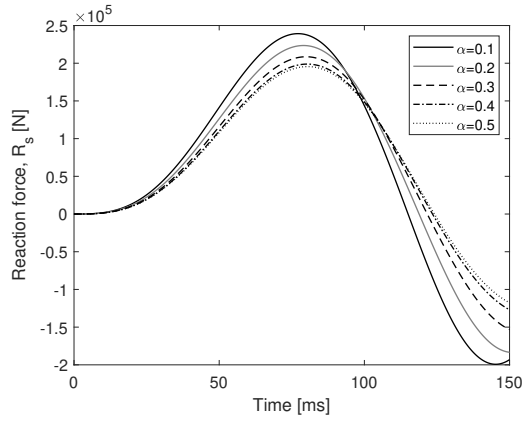


Figure F.14: Reaction force, R_s , of the structure.

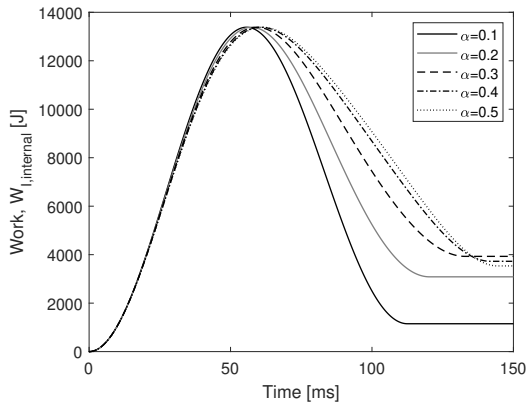


Figure F.15: Internal work in the impacting mass.

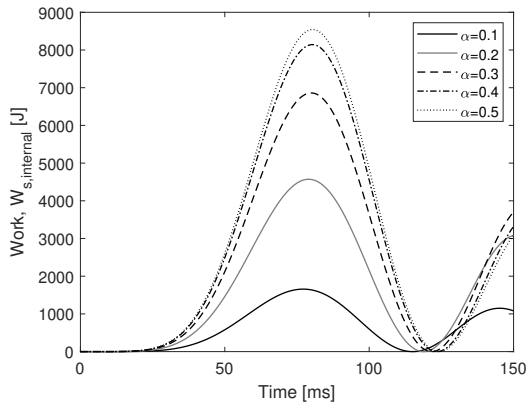


Figure F.16: Internal work in the structure.

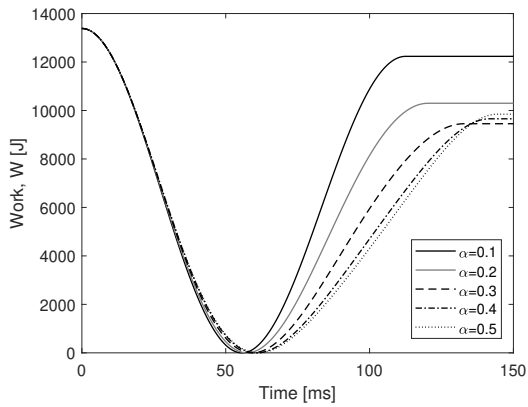


Figure F.17: Kinetic energy of the impacting mass.

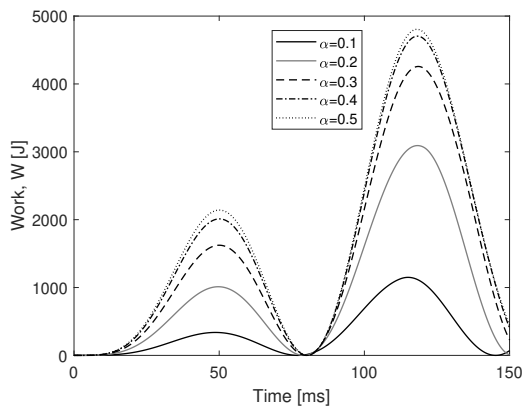


Figure F.18: Kinetic energy of the structure.

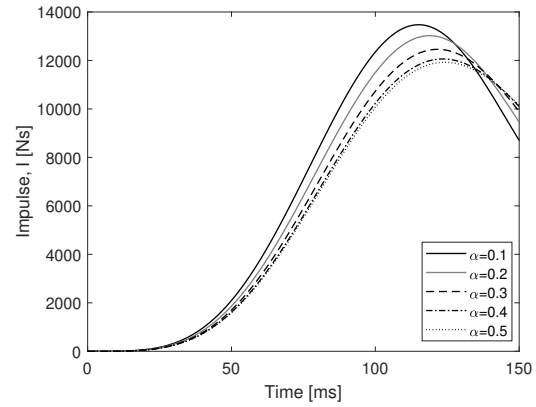
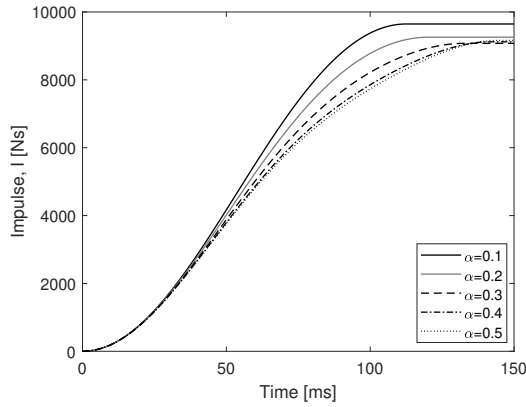


Figure F.19: Impulse from the impact force. **Figure F.20:** Impulse from the reaction force, R_s .

Even though a direct comparison between results from the 2DOF analysis and the numerical model should not be performed, the phenomenons present can be compared. From the numerical model of the DFS described in section 5.3, a tendency was found when adjusting the fall height and the position parameter. This tendency is investigated using five different fall heights, H , and five different position parameters, α . In each of the investigations the reaction force from the impacting object and structure is determined as shown in Table F.2.

Table F.2: Reaction force of structure and impacting object using five different fall heights and positions parameters.

		α				
Height [m]	Reaction	0.1	0.20	0.30	0.40	0.50
5	R_I	174.48	161.03	150.11	143.68	141.60
	R_s	308.52	288.23	269.02	256.46	252.18
4	R_I	154.54	142.63	132.96	127.26	125.41
	R_s	273.26	255.29	238.27	227.15	223.36
3	R_I	135.10	124.68	116.23	111.25	109.64
	R_s	238.89	223.17	208.30	198.57	195.26
2	R_I	110.44	101.93	95.02	90.95	89.63
	R_s	195.30	182.45	170.29	162.34	159.63
1	R_I	78.02	72.00	67.12	64.24	63.31
	R_s	137.95	128.88	120.29	114.67	112.76

Assuming that the reaction force, R_s , can be described by a static shear force diagram as shown on Figure F.21, the right and left reaction force of the structure can be determined for comparison of the complex model, and is shown on Figure F.23 and F.24 along with the impact force, R_I shown on Figure F.22. The reaction forces is seen to show the same behaviour as in the complex model, with increasing reaction force, R_{left} , when decreasing the position parameter and increasing the height.

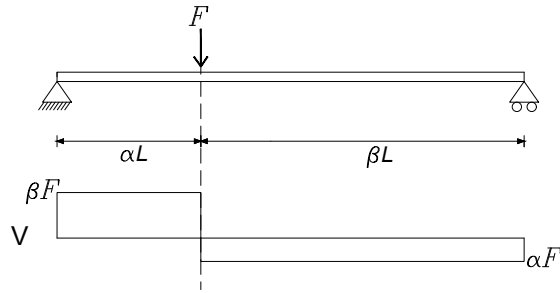


Figure F.21: Reaction force in the 2DOF system based on static assumption.

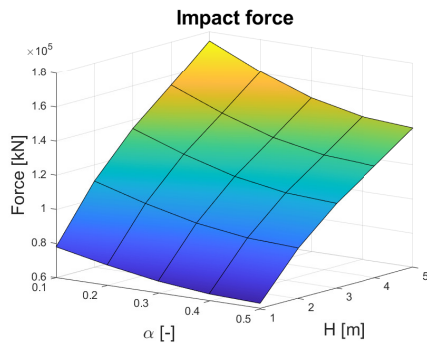


Figure F.22: Reaction, R_I , from the 2DOF model.

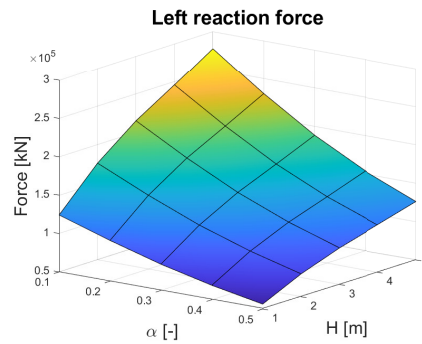


Figure F.23: Reaction force, R_{left} , determined in the 2DOF model.

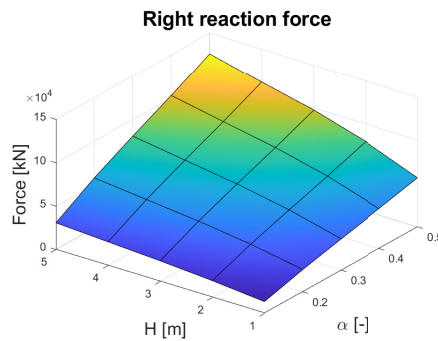


Figure F.24: Reaction force, R_{right} , determined in the 2DOF model.

F.3 Eurocode approach of impact loads

Impact loads between two objects is also described in the Eurocodes, [DS/EN-1991, 2007] and an investigation of this method is performed to see if this is a viable method to determine the impact force, and the reaction forces in the slab.

The Eurocodes divide the determination of impact forces into two approaches, depending on it being either a soft or hard impact, both of which in investigated in the following.

F.3.1 Hard impact

In the hard impact, the energy is assumed dissipated by the impacting object. The maximum dynamic force, F , present in the impact is determined by assuming that the initial kinetic energy, $E_{kinetic}$, is equal to the elastic strain energy of the impacting object, E_{strain} .

$$\begin{aligned} E_{kinetic} &= E_{strain} \\ \frac{mv^2}{2} &= \frac{F^2}{2k} \\ F &= v\sqrt{km} \end{aligned} \quad (F.14)$$

Where:

F	Maximum dynamic force
v	Velocity at impact
k	Equivalent elastic stiffness of the object
m	Mass of impacting object

The Eurocodes assumes a rectangular impulse on the structure as illustrated on Figure F.25, where the duration, Δt , is determined by the use of conservation of momentum condition:

$$F \Delta t = m v \quad (F.15)$$

Which when combined with the dynamic force, F , in (F.14) results in:

$$\begin{aligned} v\sqrt{km} \Delta t &= m v \\ \Delta t &= \sqrt{\frac{m}{k}} \end{aligned} \quad (F.16)$$

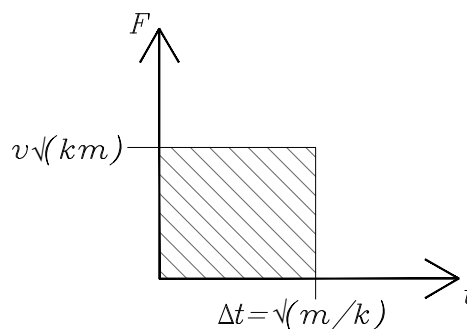


Figure F.25: Shape of the Eurocode approach impulse in hard impact.

With the use of equation F.14, the maximum dynamic force on the surface of the structure can be obtained, which can be compared with reaction force, R_I . The forces felt in the structure past the surface, previously referred to as R_s , varies depending on the impulse time and shape. If the impulse is applied suddenly as shown in Figure F.25, the resulting dynamic load factor is 2.0, whereas if the impulse maximum value is not applied suddenly, amplification factors below 1 and up to 1.8 is expected.

In the Eurocode approach, no method of calculating the dynamic load factor is shown, only a recommendation that a direct dynamic analysis should be used.

F.3.2 Soft impact

In the soft impact, the energy is absorbed through elastic-plastic material behaviour of affected structural components, such that the deformations of the impacting body is neglected. Examples of such structures are the road restraint systems built to absorb the kinetic energy of the vehicle, such that the driver experiences as little force as possible.

The force of the impulse is determined using the same expression as (F.14), where the stiffness, k , is replaced with the stiffness of the structure.

F.4 Hard and soft impact comparison with 2DOF solution.

Comparing the Eurocode approach with the 2DOF solution described previously in this chapter, the impulse force, F , illustrated on Figure F.25 can be determined and compared to the five impact scenarios. Parameters needed to determine the force, F , is shown in Table F.1, resulting in

$$F_{hard} = 5.42 \frac{\text{m}}{\text{s}} \cdot \sqrt{0.75 \cdot 10^6 \frac{\text{N}}{\text{m}} \cdot 908.58\text{kg}} = 141.1 \text{ kN} \quad (\text{F.17})$$

$$F_{soft, \alpha=0.5} = 5.42 \frac{\text{m}}{\text{s}} \cdot \sqrt{2.24 \cdot 10^6 \frac{\text{N}}{\text{m}} \cdot 908.58\text{kg}} = 244.4 \text{ kN} \quad (\text{F.18})$$

The hard and soft impact approach shows large differences in the calculated maximum dynamic interaction force, F . Reasons for the big difference is explained through the assumptions, which for hard impact states that the impacting object absorbs all of the kinetic energy, and for soft impact assumes that the structure absorbs all of the kinetic energy. Comparison between the soft and hard impact force, F , with the 2DOF solution is seen in Table F.3. Comparing the soft impact force, F , to the reaction force, R_I , illustrated on Figure F.13, convergence behaviour is observed, with the deviation decreasing with increasing values of α . Reason for this can be found in the assumption made in the soft impact calculation, in which all of the energy is dissipated through the beam deflection. The deflection of the beam increases exponentially when moving towards the mid span of the beam, and therefore more in compliance with the soft impact assumptions.

The hard impact comparison to reaction force, R_I , illustrated on Figure F.13 is seen to show the opposite convergence behaviour, with lower values of α resulting in higher stiffness and mass of the structure, such that the impacting object conserves to a greater extent the kinetic energy, as the assumption made in the hard impact approach.

Table F.3: Eurocode hard and soft approach compared with 2DOF solution.

α		0.1	0.2	0.3	0.4	0.5
Hard Impact, (F.14)	[kN]	141.1	141.1	141.1	141.1	141.1
Soft Impact, (F.14)	[kN]	678.9	381.9	291.0	254.6	244.4
R_I , (F.13)	[kN]	135.1	124.6	116.2	111.2	109.6
R_s , (F.14)	[kN]	238.8	223.1	208.3	198.5	195.2
Deviation, Hard/ R_I	[%]	4.44	13.1	21.4	26.8	28.7
Deviation Soft/ R_I	[%]	402.6	206.3	150.3	128.8	122.9
Dynamic Load Factor, R_s/R_I	[-]	1.77	1.79	1.79	1.78	1.78

The simplifications made in the hard and soft impact approach results in a general overestimation of the impact force between the impacting object and structure. Furthermore the Eurocode approach only mentions methods to determine the impacting force, meaning that without knowing the dynamic load factor, the response of the structure remains unknown. The results from the 2DOF approach is based on assumed values of stiffness and mass of the falling object, and therefore only the phenomenons found are used, and not the determined impact and reaction forces.